Thesis submitted for the degree of Doctor by

L'UNIVERSITÉ DE BORDEAUX AND

LA UNIVERSITAT AUTÒNOMA DE BARCELONA

PhD programs: Physical chemistry of condensed matter and Materials science

Optical metamaterials: design, up-scalable fabrication and characterization

By Mayte Gómez Castaño

Under the supervision of: Serge Ravaine and Agustín Mihi

Tutor: Jordi Hernando Campos

Centre de Recherche Paul Pascal

Institut de Ciència de Materials de Barcelona

June 2020

"If you only do what you can do,
you'll never be better than what you are"

Master Shifu, Kung Fu Panda 3

A mi abuela Juanita,

Table of contents

Acknowledgments

This thesis is the result of a great and enriching collaboration between the Centre de Recherche Paul Pascal (CRPP) and the Institut de Ciència de Materials de Barcelona (ICMAB), within the frame of an IdEx fellowship and CSIC and ERC projects. This international teamwork has allowed me to develop my work and grow both scientifically and personally. I would therefore like to thank the priceless help and support of the people that have shared with me this adventure.

Firstly, I would like to express my thanks to my supervisors, Serge Ravaine and Agustín Mihi, for giving me this opportunity, for their incentive, ideas, guidance, availability for Skype meetings and, of course, help with the infinite paperwork. I want to thank Serge for his always-open door (even at 7pm on Fridays), for his exhaustive analysis and discussions, and for providing me all the necessary tools for developing properly my work: from conferences to countless visits to Placamat within the same week. To Agustín, I give my thanks for his enthusiasm, for always looking for the best solution and for pushing further and further until obtaining results at the cutting edge. His motivation and support during these years have inspired me more than once and I sincerely appreciate them.

I would like also to thank two very important people (VIP) without whom more than half of this thesis could not have been accomplished. I am thankful to Renaud Vallée for teaching me the physics and French terms behind our systems, for his always positive attitude and for including me in parallel projects that have contributed to the final development of the thesis. I want to thank as well Juan Luis García Pomar, for his help with the simulations and for his patience while I was trying to absorb a small piece of his vast and admirable knowledge. Thanks also for the good moments shared in the office, always providing unbelievable breaking news all around the world.

La première partie de cette thèse a été effectuée au sein du CRPP, où j'ai eu la chance de trouver une ambiance de travail et un personnel extraordinaires. Tout d'abord je voudrais remercier la direction et l'administration pour leur accueil et toute leur aide: Cécile Zakri, Corinne Amengual, Béatrice Dupin, Elisabeth Hortolland, Evangéline Lounissi et, plus particulièrement, Caroline Legrand pour son impeccable gestion de la bourse IdEx.

Je remercie les personnes du laboratoire qui m'ont permis de me former sur des différents instruments et qui ont été toujours disponibles pour mes infatigables et impatientes demandes. Un grand merci à Isabelle Ly pour m'avoir initiée à la microscopie électronique, à Xavier Brilland pour les formations sur n'importe quel spectrophotomètre et à Joanna Giermanska pour son aide avec le spin-coater.

Merci à Sandrine Maillet et Jean-Luc Laborde pour tous les outils informatiques qu'ils m'ont fournis pour gérer cette cotutelle. Je ne peux pas oublier Nathalie Touzé à l'accueil pour apporter les meilleurs ingrédients pour bien commencer la journée.

Je remercie également les personnes de Placamat qui ont contribué à l'acquisition des images de MEB à haute résolution : Sophie Agard, Michel Martineu et, en particulier, Philippe Legros pour m'apprendre les secrets de la microscopie électronique à balayage. Merci à Wiljan Smaal et Sokha Khiev de'ElorprintTec pour la formation sur le « plasma etcher » et les quelques images de MEB faites en pleine crise de microscopie au campus.

At CRPP and Bordeaux in general I had the chance of meeting many people whose friendship turned these places into my second home. I want to thank specially the Serge team for the great ambience in and out the lab. I thank Petra for being like a big sister and great friend (despite it was me who got the molkky). Merci à Hervé pour son soutien, visites au sous-sol et les bons moments partagés en France et en Espagne. « Tu vois qui est … ? » Merci également à Pierre-Etienne, Sophie, Eliott, Sharvina, Stéphanie, Bin, Rawan et Andréa pour leur aide avec les activités quotidiennes au labo.

Je remercie aussi la petite famille française qui m'a accompagnée pendant cet an et demi au laboratoire, aux soirées jeux ou à la plage. Je pense à ma « co-bureautrice » Hélène, Artem, Maxime, Rafael, Nathassia, Florian, Romain, Marie-Charlotte, Julien, Kébo, Antoine et Valentine. Merci à vous tous pour faire partie des très bons moments qui resteront toujours dans ma mémoire.

I am also grateful to the international family that filled my daily life with lots of fun and laughs. Special words to Raj for his support and for being the best company ever for having dinner at Crous restaurants. I also want to thank Laura, Fernando, Teo, Xuan, Carlotta, Valentina, Marco, Franco, Katerina, Denize, Aurélie, Armand, Said, Ferdinand, Julia, Marie F., Marie H., Juan, Ricardo, Goce, Rajam, Simone, Etienne, Rémi, Manu, Lachland, Maëva, Yun, Hongwei, Quentin, Romain, Ale, Flavia, Arantza, Sara, Sarah, Junjin and all the people that contributed to that amazing environment.

Enfin, merci à l'équipe de running du CRPP sous la direction d'Ahmed Bentaleb pour leur accueil, la soif de dépassement et pour être une source de déconnexion.

La experiencia en un gran instituto como el ICMAB no iba a ser menos y me ha permitido conocer y trabajar con personas de la mejor calidad humana y profesional. En primer lugar, me gustaría agradecer la gran labor de la administración, en especial a Sonia Roldán y Pietat Sierra por conseguir cerrar mi contrato antes incluso de que llegara.

Gracias igualmente a Javier Rubio por la gran gestión de mi ordenador portátil francés, a pesar de todos los dolores de cabeza que le haya podido ocasionar.

También quiero agradecer la ayuda con las medidas de SEM a Anna Esther Carrillo, del ICMAB, así como al equipo del ICN2. Igualmente, gracias a Luigi Morrone, de la sala blanca, por los depósitos hechos por ALD.

Gracias también a Anna May por picarme con el gusanillo de la divulgación y por crear grandes ocasiones para tomar perspectiva del mundo de la ciencia en general.

Millones de gracias al grupo de Enlightment, por todo el conocimiento intercambiado, por las ideas y por el genial ambiente tanto en el laboratorio como fuera de él. A Cristiano por enseñarme todo sobre el hard/soft PDMS, for pillars, for holes, for wait… Era al revés. A Camilla por encontrar siempre una solución buena, rápida y efectiva. A Pau por ser un gran amigo siempre dispuesto a perder apuestas (#sestafeiraforever). Al David (Davit), per ser el millor company possible per fer hard PDMS. A Denise, por su buena onda e inestimable apoyo, wey. A Luis, por siempre encontrar un hueco para satisfacer mis ansias de medir con ángulo. Y a André, Leo y Nicolás, por sus buenos consejos y discusiones científicas.

Mis agradecimientos se extienden indudablemente al grupo de Nanopto. A los bosses, gracias por crear un ambiente de tal envergadura donde crecer y aprender cada semana. Igualmente, gracias al resto de estudiantes de doctorado y postdocs del grupo. Moltes graciès al Martí per les seves boges però grans idees per les meves mostres i per ser el meu professor oficial de català. I also want to thank Adri, Quique, Rana, Minghua, Osnat, Fatma, José, Valentina, Nadia, Xabi, Albert, Iván, Jinhui, Kai, Alex, Laura, Bernhard, Miquel, Carmen, Aurélien… for the good moments shared in the lab, during lunch, playing board games or at the multiple barbecues.

Gracias igualmente a Cris, Sohini, Bego, Edu, Isa, Uri, Juanan, Cristina, Javi, Timo, Raúl, Juan, Romain, Fendi, Javi P. y todas aquellas personas que me han acompañado durante esta bonita aventura en Barcelona.

Quiero darles también las gracias a Jose Luis Pau y Eduardo Ruíz por acogerme de vuelta unos días en el lab de Microelectrónica de la UAM y ayudarme con los depósitos por CVD.

Aprovecho este momento para agradecerles a mis amigos todo su apoyo e interés durante estos años a pesar de los cientos de kilómetros que nos separaban. A mis non-quantum amigas de la uni: Miriam, Irene, Ana y Eva; por supuesto a Mariano (ya en poco nos dedicamos a nuestra verdadera pasión: la jardinería); a mis amigos del barrio y derivados: Alba, Diego, Nu, Sandra, Ali, Pablo, Chechu, David y, sobre todo, a Guille y Álvaro, por ser los mejores amigos que una podría tener.

Mis más sinceras gracias a Andrés, por tus ánimos, tus consejos, por tus ganas de aprender cada curiosidad que te pueda contar, por los millones de viajes aquí y allá, por aquella primera tortilla en Burdeos, por creer en mí y, sobre todo, por siempre aportar luz cuando todo parece oscuridad.

Por último y más importante, me dirijo al gran pilar de mi vida: mi familia. Gracias a todos vosotros por vuestro cariño, apoyo y por las eternas preguntas de "¿cuánto te quedas?", "¿qué tal va la tesis?", "¿te parece bien si vamos a verte tal finde?". A la familia hispano-peruana-boliviana, por vuestras siempre calurosas bienvenidas llenas de palomitas. A los más viajeros, grupo al que me siento enormemente orgullosa de pertenecer, por vuestro infalible humor desde allí donde quiera que estéis. A los Castaños, porque… "esto no es un grupo, es mi familia", a pesar de lo que diga la policía turística. A Guillermo y Javi, por traer siempre un contagioso aire fresco y divertido. A mis abuelos, para mí fuentes de inspiración, superación y cariño.

Y finalmente, gracias a mis padres. Por haber sido siempre un soporte incondicional y más aún, cuando empezó esta aventura. Porque sólo unos pocos conocen las maravillosas cazadoras de Burgos, las carreteras del País Vasco o lo que es verdaderamente importante en nuestras vidas. Gracias por los miles de paquetes enviados, por las sorpresas a distancia, por aquella traumatizante mudanza y por llenarme de tappers cada vez que bajaba. Porque sin vosotros, ninguna de estas páginas habría sido posible. Gracias.

Abstract

Metamaterials are artificially structured materials, thoroughly designed for achieving electromagnetic properties not observed in nature. In the last years, the field of metamaterials has exponentially grown due to the exceptional possibilities that they offer to manipulate light. One of the most attractive phenomena is the negative refractive index, which may enable resolution imaging beyond the diffraction limit.

Nowadays, one of the main challenges of negative-index metamaterials is the transition from the laboratory to real applications. However, the vast majority of metamaterials still rely on low-throughput and expensive techniques that hamper this progression. Therefore, this thesis is devoted to the development of up-scalable negative-index metamaterials with the aim of facilitate their implementation in actual devices. We focus on the fishnet design because of its efficient behavior at optical wavelengths.

Firstly, we develop a bottom-up fishnet design by combining colloidal lithography and electrodeposition. The system consists of a double-fishnet made of gold layers separated by air gaps and supported by dielectric particles. We study experimentally and theoretically the optical dependence on the main structural parameters. Their proper control gives rise to metamaterials whose refractive index can be easily tailored from positive to negative values in the near infrared, with a minimum value of -1 at 940 nm.

Secondly, we study fishnet metamaterials made by nanoimprint lithography and electrodeposition. The infiltration of several metallic layers through templates of pillars leads to multilayered fishnet structures made of gold and air gaps. The accurate design leads to strong negative indices, from -1.2 at 700 nm to -2.8 at 910 nm. We thoroughly analyze their optical response and study their performance as optical sensors when filling the gaps with different liquids.

Finally, inspired by the cost-effective approaches of colloidal lithography and nanoimprinting, we investigate the fabrication of nanostructured metallic substrates for the observation of collective spontaneous emission. We develop large-area plasmonic crystals whose resonances can boost the emission rate of ensembles of dye molecules.

Resumen

Los metamateriales son materiales artificialmente estructurados, minuciosamente diseñados para obtener propiedades electromagnéticas inobservables en la naturaleza. En los últimos años, el campo de los metamateriales ha crecido exponencialmente debido a las excepcionales posibilidades que ofrecen para manipular la luz. Uno de los fenómenos más atractivos es el índice de refracción negativo, con el que se podrían obtener resoluciones ópticas más allá del límite de difracción.

Hoy en día, uno de los mayores desafíos de los metamateriales es el salto del laboratorio a las aplicaciones reales, pues la gran mayoría de ellos todavía depende de técnicas de bajo rendimiento y alto coste que obstaculizan esta transición. Por ello, esta tesis está dedicada al desarrollo de metamateriales de índice negativo fácilmente escalables, con el objetivo de facilitar su implementación en dispositivos reales. Nos centramos en el diseño tipo «fishnet» por su funcionamiento efectivo a frecuencias ópticas.

En primer lugar, desarrollamos un diseño «bottom-up» de metamateriales fishnet combinando la litografía coloidal y el electrodepósito. El sistema consiste en una fishnet doble hecha de capas de oro separadas por cavidades de aire y soportadas por partículas dieléctricas. Estudiamos la respuesta óptica al variar los principales parámetros estructurales. Demostramos que un control adecuado da lugar a metamateriales cuyo índice de refracción puede variar fácilmente desde valores positivos hasta negativos en el infrarrojo cercano, obteniendo un mínimo de -1 a 940 nm.

En segundo lugar, estudiamos metamateriales fishnet hechos por nanoimpresión y electrodepósito. La infiltración de múltiples capas metálicas a través de patrones de pilares da lugar estructuras fishnet multicapas de oro y aire. El riguroso diseño de estas estructuras da lugar a grandes índices negativos, desde -1.2 a 700 nm hasta -2.8 a 910 nm. Analizamos en detalle su respuesta óptica y estudiamos su aplicación como sensores ópticos al infiltrar distintos líquidos entre las cavidades de aire.

Por último, inspirados por la facilidad de procesado de la litografía coloidal y de la nanoimpresión, investigamos la fabricación de sustratos metálicos nanoestructurados para la observación de emisión espontánea colectiva. Desarrollamos cristales plasmónicos cuyas resonancias pueden aumentar el ritmo de emisión de moléculas fluorescentes.

Résumé long

Les métamatériaux sont des matériaux structurés artificiellement, soigneusement designés pour obtenir des réponses électromagnétiques inobservables dans la nature. Leurs propriétés ne proviennent pas seulement des matériaux constitutifs mais sont surtout déterminées par la géométrie et la disposition des composants.

L'origine des métamatériaux est associé aux travaux pionniers de Veselago (1968) sur la propagation de la lumière dans un matériau hypothétique de permittivité et perméabilité négatives.[1] Il a montré que dans un tel milieu la lumière obéit toujours aux lois de Maxwell mais se comporte différemment que dans les matériaux conventionnels, avec des propriétés exotiques comme un indice de réfraction négatif. Cependant, le sujet n'a pas attiré l'attention pendant plus de 30 ans[2] faute d'un matériau possédant une permittivité et une perméabilité négatives simultanément. Le fait que cette combinaison électromagnétique n'existe pas dans les substances naturelles a donné lieu au terme de métamatériaux.

Au cours de ces dernières années, le domaine des métamatériaux a connu une croissance exponentielle grâce aux possibilités exceptionnelles qu'ils offrent pour manipuler la lumière. Entre autres, on peut nommer le magnétisme à fréquences optiques, la chiralité artificielle ou la réfraction négative. L'indice de réfraction négatif suscite toujours un grand intérêt en raison de l'obtention potentielle de résolutions optiques au-delà de la limite de diffraction.

Aujourd'hui, un des principaux défis des métamatériaux à indice de réfraction négatif est la transition du laboratoire au marché. Ce passage implique quelques prérequis tels que compatibilité avec de grandes surfaces ou des processus de fabrication à faible coût, en préservant à tout moment une réponse optique de qualité. A ce jour, la plupart des métamatériaux dépendent de techniques peu performantes qui empêchent leur utilisation dans des applications comme la superlentille.[3,4]

Afin de faciliter leur mise en place dans des dispositifs réels, cette thèse porte sur le développement de métamatériaux à indice négatif pouvant être réalisés à grandes échelles. Nous détaillons ci-dessous les principaux sujets et résultats développés au cours de ces travaux.

Tout d'abord, le **Chapitre 1** présente les notions générales sur l'interaction lumière-matière qui sont à la base du comportement des métamatériaux. Ceci inclut les propriétés optiques des métaux et des diélectriques ainsi que le couplage de la lumière avec des interfaces entre de ces deux types de matériaux. Les ondes électromagnétiques qui se propagent à ces interfaces sont appelées plasmons-polaritons de surface et sont à l'origine des propriétés des métamatériaux dans le domaine du visible et l'infrarouge. L'excitation de ces ondes superficielles et l'ingénierie des résonances plasmoniques donnent lieu à la possibilité de concentrer et guider la lumière à l'échelle nanométrique. Les métamatériaux profitent de cette interaction lumière-matière exaltée. En effet, l'excitation et l'hybridation des plasmons de surface au sein des composites métal-diélectrique est responsable du caractère extraordinaire des métamatériaux.

Les métamatériaux sont généralement réalisés à partir de l'assemblage de briques élémentaires complexes, aussi nommées méta-atomes, dont la taille est plus petite que la longueur d'onde de la lumière. Ainsi, même si les propriétés inhabituelles des métamatériaux proviennent de l'interaction électromagnétique avec les méta-atomes, l'ensemble peut être décrit comme un milieu homogène avec des paramètres macroscopiques effectifs.

On distingue différent types de métamatériaux en fonction de ces paramètres et des designs proposés pour les réaliser. Parmi les métamatériaux à indice négatif, plusieurs structures ont été étudiées théoriquement et expérimentalement afin d'obtenir un tel indice, de la gamme des microondes jusqu'au visible. La condition pour pouvoir observer un tel comportement est l'existence d'une réponse électrique et magnétique simultanée, c'est-à-dire à la même longueur d'onde. Etant donnée la réponse électrique des métaux, le but principal est de designer des architectures qui présentent un magnétisme artificiel.

Les structures de type « fishnet » constituent l'approche la plus prometteuse pour les gammes du visible et de l'infrarouge,[5] ce design permettant un contrôle indépendant des réponses magnétique et électrique. D'une part, le magnétisme est obtenu à partir de bandes métalliques parallèles au champ magnétique incident et séparées par une couche diélectrique. Si les bandes métalliques sont suffisamment proches, les plasmons de surface excités à chaque interface métal-diélectrique s'hybrident et donnent lieu à des courants électriques antiparallèles. Ceux-ci induisent à leur tour un moment magnétique artificiel dans la structure. D'autre part, la réponse électrique est générée grâce à des bandes métalliques perpendiculaires aux premières et orientées parallèlement au champ

électrique. Elles agissent comme un métal dilué avec une fréquence plasma plus faible qui confère la réponse électrique aux métamatériaux, notamment une permittivité négative.[6] En résumé, le design « fishnet » peut être vu comme une structure multicouche perforée par des trous périodiques.

Dans les dernières années, plusieurs groupes de recherche ont travaillé sur la fabrication ce de type de structures en utilisant divers matériaux constitutifs, différentes épaisseurs de couches ou formes des trous pour obtenir des valeurs d'indice de réfraction négatives aux fréquences optiques. A la fin du premier chapitre, nous présenterons l'état de l'art concernant les métamatériaux à indice négatif selon leur taille, la longueur d'onde de travail et les valeurs d'indice atteintes. Comme précédemment discuté, on constate que la grande majorité de ces métamatériaux a été fabriquée avec des méthodes difficilement compatibles avec les grandes surfaces nécessaires pour leur mise en œuvre au sein de dispositifs opérationnels.

Le **Chapitre 2** présente les techniques utilisées au cours de cette thèse pour fabriquer des matériaux de type fishnet à faible coût, sur des grandes surfaces et avec une réponse optique comparable à celles atteintes avec les processus « classiques » plus coûteux. A cette fin, nous avons utilisé la lithographie colloïdale, la lithographie par nanoimpression et l'électrodéposition.

La lithographie colloïdale permet d'obtenir d'une manière simple et rapide des monocouches de nanoparticules bien ordonnées dont le diamètre peut être modifié sans affecter l'ordre du réseau. Dans cette thèse, nous avons utilisé l'assemblage à la surface de l'eau pour obtenir des monocouches de sphères de polystyrène sur des surfaces de quelques centimètres. Nous présentons ensuite les avantages de la lithographie par nanoimpression, notamment la possibilité de répliquer plusieurs motifs nanométriques avec une grande fiabilité. La fabrication des moules flexibles qui ont été utilisés est détaillée et le protocole d'électrodéposition est également précisé.

A la fin de ce chapitre, sont présentées les techniques de caractérisation structurale et optique employées, ainsi que la méthode de différences finies dans le domaine temporel (FDTD) qui a été utilisée pour simuler les propriétés optiques des métamatériaux fabriqués.

Le **Chapitre 3** est dédié à la conception, à la fabrication et à la caractérisation de métamatériaux de type « fishnet » par une voie « bottom-up ». Nous avons combiné les

avantages de la lithographie colloïdale et de l'électrodéposition pour réaliser des matériaux « double fishnet » composés de deux couches d'or séparées par une cavité d'air et perforées de manière périodique par une monocouche de sphères de polystyrène. En premier lieu, nous présentons l'influence des paramètres les plus importants dans ces structures : le diamètre des particules et l'épaisseur de la couche d'air entre les couches métalliques. Nous montrons qu'en diminuant la taille de ces deux paramètres, on obtient des indices de réfraction plus négatifs ainsi qu'un décalage vers le rouge de la longueur d'onde de résonance.

Ces études préliminaires ont servi à la fabrication de métamatériaux avec un indice de réfraction facilement réglable. Le processus suivi commence par le dépôt d'une monocouche de particules de polystyrène de 480 nm sur un substrat de nickel. Le diamètre des particules est réduit à l'aide d'un plasma d'oxygène, ce qui donne lieu à des monocouches colloïdales non compactes au sein desquelles des couches d'or et de nickel sont électrodéposées de manière séquentielle. La dissolution sélective ultérieure des couches sacrificielles de nickel permet d'obtenir des métamatériaux constitués par deux couches d'or séparées par une cavité d'air et percées par les particules de polystyrène. En plus, cette étape de dissolution permet de transférer les matériaux obtenus sur des substrats transparents, permettant leur caractérisation optique.

Nous avons étudié les propriétés optiques de ces structures et avons démontré leur qualité grâce au bon accord entre les spectres expérimentaux et les simulations. A partir de ces calculs, on a extrait les propriétés macroscopiques effectives, qui montrent que l'indice de réfraction des métamatériaux réalisés varie entre valeurs positives, valeurs proches de zéro et valeurs négatives dans le proche infrarouge. La valeur minimale d'indice obtenue est de -1 à une longueur d'onde de 940 nm, avec une bande de valeurs négatives qui s'étale sur 100 nm.

Les simulations de la distribution des champs électromagnétiques montrent que l'origine de ce comportement est liée à la résonance magnétique excitée dans la cavité d'air, conformément à la théorie. La validité des paramètres extraits a également été confirmée en substituant les systèmes par des milieux effectifs qui donnent la même réponse macroscopique. De la même façon, la modélisation d'un prisme réalisé à partir du métamatériau d'indice -1 a montré la possibilité d'obtenir une réfraction négative avec ces structures.

Le **Chapitre 4** est consacré à une autre voie d'élaboration des métamatériaux de type « fishnets », basée sur la combinaison de la lithographie par nanoimpression et l'électrodéposition. Dans ce cas, nous avons utilisé différents réseaux de piliers diélectriques dont la périodicité varie entre 200 et 500 nm. L'infiltration de multicouches d'or et de nickel autour des piliers puis la dissolution sélective du nickel a permis de montrer la possibilité de fabriquer des métamatériaux de type « fishnets » constitués de multicouches d'or et d'air. Ces structures sont préparées sur des substrats conducteurs et transparents, donc permettant la réalisation directe de dispositifs optiques.

Ce protocole permet d'obtenir une large gamme des métamatériaux en contrôlant les aspects structuraux tels que la périodicité, le diamètre et la hauteur des piliers, l'épaisseur des couches d'or, la séparation entre elles ou le nombre de couches métalliques. Le rigoureux design de ces géométries a conduit à des valeurs d'indice de réfraction négatives dans le visible et infrarouge, avec des valeurs de -1.2 à 700 nm ou -2.8 à 910 nm. De même que précédemment, il a été montré que la résonance magnétique a lieu entre les couches d'or.

On a également montré que pour les structures avec plus de deux couches d'or l'indice effectif présente une discontinuité prononcée, passant d'une valeur négative à une valeur positive. Cela est dû au changement du mode électromagnétique dominant dans la structure. La distribution des champs varie donc entre les branches d'indice négatif et positif.

La réponse optique des métamatériaux est influencée par le nombre de couches qui les composent. Par exemple, en augmentant ce nombre, l'absorption diminue et la zone de travail se décale vers les longueurs d'onde plus petites. Le faible décalage observé pour les métamatériaux de périodicité plus petite suggère une convergence de leur comportement avec celui d'un matériau massif, où la réponse optique ne dépend plus du nombre de couches ou l'angle d'incidence de la lumière.

Enfin nous démontrerons l'accessibilité de la porosité des métamatériaux en étudiant les changements des propriétés optiques qui se produisent quand on infiltre différents liquides au sein des couches métalliques. La dépendance linéaire de la longueur d'onde de résonance avec l'indice de réfraction du milieu infiltré démontre le potentiel des métamatériaux comme capteur optiques.

Inspiré par la possibilité d'obtenir des motifs nanométriques par des voies faciles à mettre en œuvre et reproductibles, le **Chapitre 5** aborde la fabrication de substrats métalliques nanostructurés pour l'étude de l'émission spontanée collective. Dans ce projet, nous avons développé trois types des plateformes métalliques dont la configuration peut exalter le taux d'émission d'un ensemble de molécules fluorescentes. Ces plateformes sont des systèmes où les molécules sont placées à une certaine distance de la surface métallique. Les trois types correspondent à un film de métal plat, un réseau plasmonique unidimensionnel et un réseau plasmonique bidimensionnel.

Pour la configuration plate, nous avons démontré théoriquement et expérimentalement l'existence de deux régimes d'émission (collective et individuelle) et leur forte dépendance avec la distance entre les molécules et la surface métallique ou avec le nombre d'émetteurs.

Finalement, nous avons utilisé les techniques de nanoimpression et de lithographie colloïdale pour fabriquer des cristaux plasmoniques. La superposition spectrale de leurs résonances avec l'émission des molécules montre la possibilité d'exalter pas seulement le taux de fluorescence mais aussi le comportement collectif.

Références

1. V. G. Veselago. The electrodynamics of substances with simultaneously negative values of ε and μ. *Sov. Phys. Uspekhi* **1968**, *10*, 509–514.

2. D. R. Smith, W. J. Padilla, D. C. Vier, S. C. Nemat-Nasser and S. Schultz. Composite medium with simultaneously negative permeability and permittivity. *Phys. Rev. Lett.* **2000**, *84*, 4184–4187.

3. J. B. Pendry. Negative refraction makes a perfect lens. *Phys. Rev. Lett.* **2000**, *85*, 3966–3969.

4. G. Yoon, I. Kim and J. Rho. Challenges in fabrication towards realization of practical metamaterials. *Microelectron. Eng.* **2016**, *163*, 7–20.

5. C. M. Soukoulis and M. Wegener. Past achievements and future challenges in the development of three-dimensional photonic metamaterials. *Nat. Photonics* **2011**, *5*, 523–530.

6. J. Valentine, S. Zhang, T. Zentgraf and X. Zhang. Development of bulk optical negative index fishnet metamaterials: Achieving a low-loss and broadband response through coupling. *Proc. IEEE* **2011**, *99*, 1682–1690.

List of abbreviations

CL	Colloidal lithography
EM	Electromagnetic
FDTD	Finite difference time domain
FOM	Figure of merit
FTIR	Fourier transform infrared spectroscopy
GSP	Gap surface plasmon
ITO	Indium-doped tin oxide
MIM	Metal-insulator-metal
NIL	Nanoimprint lithography
NIM	Negative index metamaterial
NA	Numerical aperture
NIR	Near infrared
PS	Polystyrene
PMMA	Polymethyl methacrylate
RI	Refractive index
RIE	Reactive ion etching
RT	Room temperature
SEM	Scanning electron microscopy
SPP	Surface plasmon polariton
SPR	Surface plasmon resonance
SRR	Split-ring resonator
TE	Transverse electric
TM	Transverse magnetic
TCO	Transparent conducting oxide
UV	Ultraviolet
Vis	Visible
WE	Working electrode

Chapter 1

Introduction

1.1 Light-matter interaction

From radio waves to gamma rays, light has inspired scientists for centuries and undoubtedly influenced our daily life and progress. The interaction of light with matter has become an essential tool for research and development in physics, chemistry, biology or medicine. Yet, the exploration of light propagation, engineering of optical properties and the innovation in electromagnetic communications make light-matter interaction as one of the most vibrant areas of science.[1,2]

The emergence and enormous advances of nanotechnology in the last decades have led to new perspectives for light manipulation.[3] The study of light coupling to nanostructured materials has rapidly blossomed because of the countless applications in optical technologies such as imaging,[4] sensing,[5] energy harvesting,[6] or lightning.[7] Specifically, nano- and micro-patterned metal-dielectric interfaces attract great attention for confining light, upgrading the performance of classical devices or attaining unprecedented electromagnetic phenomena.

This is the case of metamaterials, artificially structured materials providing exotic optical responses. Typically made of periodic composite arrays, metamaterials generate unique electromagnetic properties mostly governed by the geometry rather than the constituent materials. Therefore, they can be engineered to exhibit electromagnetic behaviors beyond the natural limits such as optical magnetism or negative refractive index. The exploitation and practical implementation of these properties could revolutionize the field of optics with fascinating devices such as super-resolution lenses or invisibility cloaks.[8]

In this chapter, we will introduce the main theoretical aspects of light-matter interaction behind metamaterials. Starting with the fundamentals of light propagation through a medium, we will later focus on the coupling at metal-dielectric interfaces. This photonic framework will be the support for introducing the concept of metamaterials, the

types so far developed and, more importantly, the key ingredients for realizing negative-index metamaterials (NIMs). Finally, we will review some of the most relevant works in this field as well as the main challenges towards the practical implementation of NIMs working at optical frequencies.

1.1.1 Electromagnetic wave propagation

The spatial and temporal propagation of an electromagnetic (EM) wave within a material is described by Maxwell's equations:

$$\nabla \cdot \vec{D} = \rho \tag{1.1}$$

$$\nabla \cdot \vec{B} = 0 \tag{1.2}$$

$$\nabla \times \vec{E} = -\frac{\partial \vec{B}}{\partial t} \tag{1.3}$$

$$\nabla \times \vec{H} = \frac{\partial \vec{D}}{\partial t} + \vec{J} \tag{1.4}$$

where $\vec{D}$ is the electric displacement, $\vec{B}$ the magnetic induction, $\vec{E}$ the electric field, $\vec{H}$ the magnetic field, ρ the free charge density and $\vec{J}$ the current density. For a linear and isotropic medium, $\vec{D}$ and $\vec{B}$ are related to $\vec{E}$ and $\vec{H}$ by the constitutive relations:

$$\vec{D} = \varepsilon_0 \vec{E} + \vec{P} = \varepsilon_0 \varepsilon \vec{E} \tag{1.5}$$

$$\vec{B} = \mu_0 \vec{H} + \vec{M} = \mu_0 \mu \vec{H} \tag{1.6}$$

where ε_0 is the vacuum electric permittivity, μ_0 the vacuum magnetic permeability and $\vec{P}$, $\vec{M}$ the polarization and magnetization induced in the material by the external fields. The overall response can be expressed in terms of the relative permittivity ε and permeability μ of the medium. These are unitless and complex numbers that depend on the radiation frequency. The real parts describe the polarization or magnetization strength while the imaginary parts account for the absorption losses or the gain in the material.

$$\varepsilon = \varepsilon' + i\varepsilon'' \tag{1.7}$$

$$\mu = \mu' + i\mu'' \tag{1.8}$$

Therefore, the interaction of an EM wave with a medium is determined by these macroscopic parameters, which significantly vary between dielectrics, semiconductors and metals. Two related parameters are also used to describe the electromagnetic response of the medium: the refractive index n and the wave impedance z. The former is the ratio

between the speed of light in vacuum and in the medium, while the latter characterizes the material resistance to the wave propagation.

$$n = \sqrt{\varepsilon\mu} \tag{1.9}$$

$$z = \sqrt{\mu/\varepsilon} \tag{1.10}$$

Similarly to ε and μ, depending on the material and frequency, n and z might be complex, the imaginary part being the absorptive component. These values govern the classical interactions of light and matter such as absorption, reflection or refraction.

1.1.2 Optical properties of dielectric and metals

At optical frequencies, the magnetization of a medium is much weaker than the electric counterpart and can be neglected. Therefore, the magnetic induction approaches the free space regime, the relative permeability can be taken as $\mu = 1$ and the refractive index is simplified to $n = \sqrt{\varepsilon}$. Contrarily, the permittivity not only differs from the vacuum limit but acquires remarkable different values for metals and dielectrics.

On one hand, from the blue to the mid-infrared, dielectrics are mostly characterized by a positive and nearly constant permittivity with a negligible imaginary part. Light is slowed down but not absorbed within the medium. This is why dielectrics are commonly used in optical components, since they display high transparency.[8]
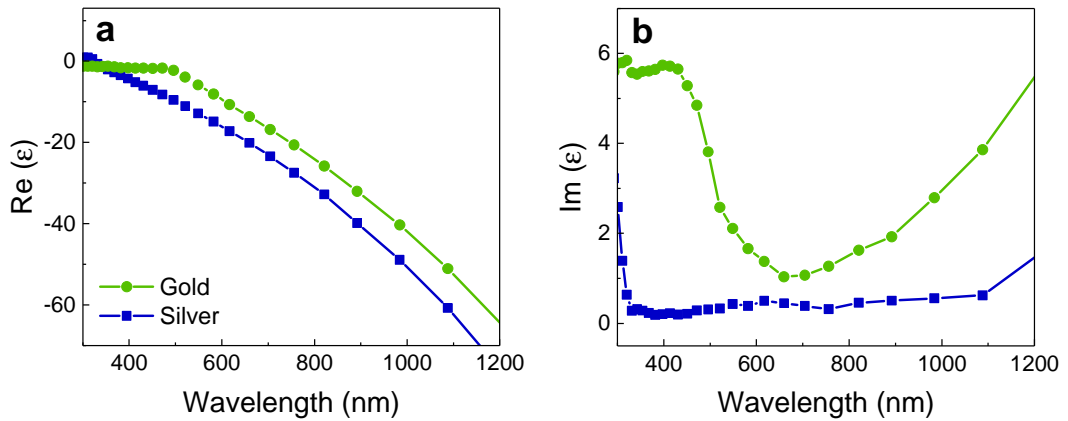
Figure 1.1 Comparison of the permittivity: **a** real part and **b** imaginary part of silver and gold at optical frequencies. Adapted from Johnson and Christy measurements.[9]

On the other hand, the optical properties of metals are governed by their plasma frequency ω_p, which accounts for the oscillations of the free electrons cloud and typically falls in the ultraviolet (UV) range. Below this value, the real part of the permittivity is

characteristically negative. This is one of the most important attributes of metals as far as optical properties are concerned. It implies that the electrons oscillate out of phase with the external field, screening the EM wave and leading to a reflectivity close to 1. Besides, metals present non-negligible losses coming from electronic collisions and band transitions that should be considered when designing optical structures. Figure 1.1 shows the permittivity of the most commonly used metals in optics: silver and gold, both presenting negative real parts that substantially decrease with the wavelength.

1.1.3 Surface plasmon polaritons

The sharp contrast between metals and dielectrics is the key for obtaining unusual electromagnetic properties such as the ones of metamaterials. They typically rely on the interaction of light with metal-dielectric interfaces. When the impinging light is coupled to such boundaries, it excites electromagnetic surface waves called surface plasmon polaritons. Since most of our research derives from this excitation, we will briefly introduce the basic properties of such plasmonic waves.

Propagating surface plasmon polaritons or simply called surface plasmon polaritons (SPPs) are hybrid photon-electron excitations travelling at the interface between a dielectric and a metal. They arise from the coupling of an EM wave with a longitudinal charge density oscillation at the metallic surface (Figure 1.2). Interestingly, while SPPs can propagate along the interface, they are evanescently confined in the perpendicular direction, with penetration depths of the order of hundreds of nanometers in the dielectric and tens of nanometers in the metal.[10]
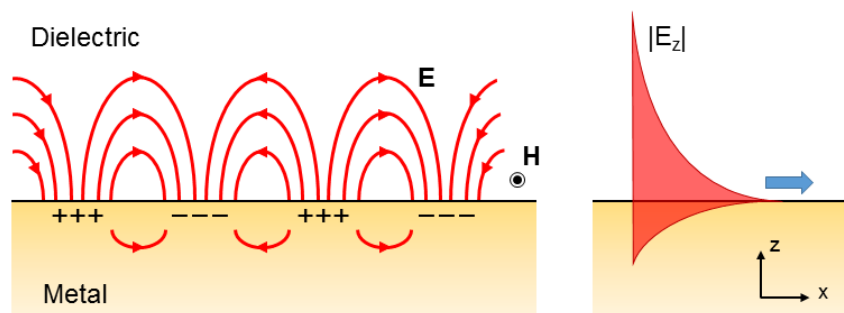
Figure 1.2 (Left) Combined electromagnetic and charge density waves of surface plasmon polaritons propagating at the metal-dielectric interface. (Right) Decay of the perpendicular electric field intensity inside the dielectric and the metal.

The nature of surface plasmons lies on the opposite sign of the permittivities ε involved. As previously discussed, this situation is fulfilled for dielectric and metals above

UV wavelengths, where the metal permittivity ε_m turns negative and rapidly decreases with the wavelength, whereas the dielectric permittivity ε_d remains constant. From Maxwell's equations it can be demonstrated that SPPs only exist for the transverse magnetic (TM) polarization, this is, with the magnetic field perpendicular to the propagation plane. Under these boundary conditions, the dispersion relation of SPPs results in:

$$k_{||} = \frac{\omega}{c} \sqrt{\frac{\varepsilon_d \varepsilon_m}{\varepsilon_d + \varepsilon_m}} \tag{1.11}$$

where $k_{||}$ is the wavenumber parallel to the surface, ω the wave frequency, c the speed of light in vacuum and

$$\frac{\omega}{c} = k_0 = \frac{2\pi}{\lambda_0} \tag{1.12}$$

being k_0 the vacuum wavenumber and λ_0 the corresponding vacuum wavelength. In the same dielectric, however, light follows the linear dispersion relation:

$$k_{||} = \frac{\omega}{c} \sqrt{\varepsilon_d} \tag{1.13}$$

which means that the SPP wavenumber is always higher than the wavenumber in the dielectric or free space. Hence, light impinging at a dielectric-metal interface cannot directly excite SPPs because of the momentum mismatch and additional in-plane momentum is needed.

There exist several methods for providing the missing momentum and exciting SPPs through light. These methods include light coupling through a prism by total internal reflection, scattering from a surface defect such as protrusions or holes, or diffraction from gratings.[11] The latter is of great interest because of the direct incorporation of the coupling mechanism into the structure. The absence of external items facilitates the application of plasmonic behaviors in optical devices.

SPPs are excited on a grating if their wavenumber matches the momentum of the impinging light plus the reciprocal lattice vectors of the array as follows:[12]

$$\left|\vec{k}_{SPP}\right| = \left|\vec{k}_0 \sin\theta + m\vec{G}_m + n\vec{G}_n\right| \tag{1.14}$$

where $\vec{k}_{SPP}$ is the wavevector of SPP derived from equation (1.11), $\vec{k}_0 \sin\theta$ is the in-plane wavevector of light, $\vec{G}_m$, $\vec{G}_n$ are the lattice vectors and $m, n = 0, \pm1, \pm2, \ldots$ In the simplest case where light impinges normally to the surface ($\theta = 0$), this expression is simplified to

the contribution of the reciprocal lattice vectors $\vec{G}_{m,n}$. For the most common periodic geometries, the module of these lattice vectors, and so of $\vec{k}_{SPP}$, is given by the following expressions, where L denotes the lattice constant.

Linear:
$$\left|\vec{k}_{SPP}\right| = \left|\vec{G}_m\right| = \frac{2\pi}{L}m \tag{1.15}$$

Squared:
$$\left|\vec{k}_{SPP}\right| = \left|\vec{G}_{m,n}\right| = \frac{2\pi}{L}\sqrt{m^2 + n^2} \tag{1.16}$$

Hexagonal:
$$\left|\vec{k}_{SPP}\right| = \left|\vec{G}_{m,n}\right| = \frac{4\pi}{\sqrt{3}L}\sqrt{m^2 + n^2 + mn} \tag{1.17}$$

Thus, when this momentum matches the dispersion relation of equation (1.11), light is coupled to SPPs propagating at the metal-dielectric interface.

Figure 1.3 depicts the excitation of SPPs at normal incidence thanks to the in-plane momentum provided by a periodic array ($G_{m,n}$). The frequency at which the momentum matching is satisfied is known as surface plasmon resonance (SPR). In this situation, the energy of the incident light is efficiently transferred to the SPP wave, with a drastic effect on the optical response typically manifested as a fall in the reflection spectra.
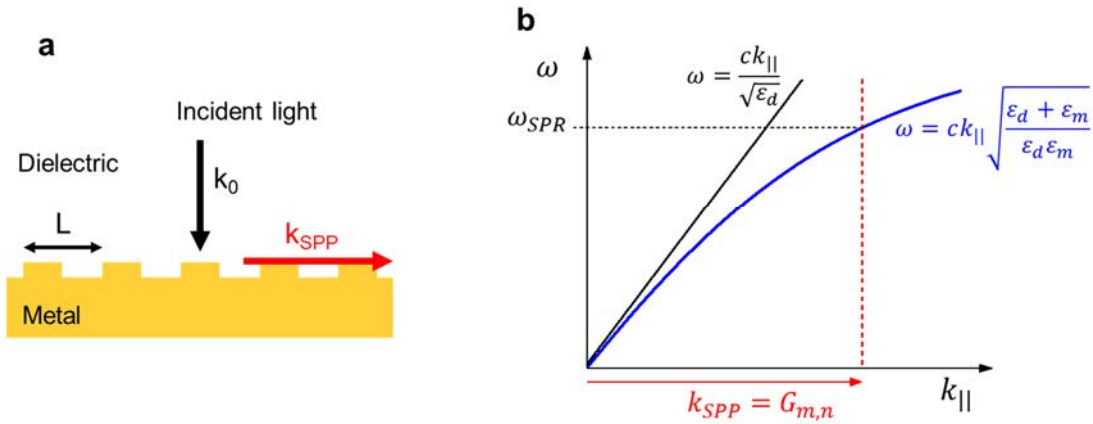
Figure 1.3 a Excitation of SPPs on a metal-dielectric grating at normal incidence. **b** Dispersion relation of SPP (blue) and light in the same dielectric (black). The red vector represents the momentum provided by the grating, matching the SPP dispersion at a free space frequency ω_{SPR}.

The excitation of SPPs and derived plasmonic resonances implies the possibility of concentrating and channelling light at the nanoscale. Metamaterials are one of the current fields benefiting from such enhanced light-matter interaction. As we will discuss later, the excitation and hybridization of SPPs in metal-dielectric composites is responsible for the extraordinary character of many metamaterials.

1.2 Metamaterials

1.2.1 Tailoring ε and μ

The origin of metamaterials is associated with the seminal paper of Veselago (1968) about the behavior of light through a hypothetical material with negative permittivity and permeability.[13] He found that in such medium light would still obey Maxwell's equations but would behave inversely to conventional materials, with exotic properties such as negative refraction. However, the subject was left aside for more than 30 years[14,15] due to the lack of natural materials with simultaneous negative permittivity and permeability for proving the phenomenon. The fact that such combined electromagnetic response is not found in naturally occurring substances coined the famous term of metamaterials.

Metamaterials (from the Greek prefix $\mu\varepsilon\tau\alpha$ (meta-), beyond) are artificially engineered structures exhibiting properties not attainable with ordinary media. Made from the arrangement of subwavelength units, the properties of metamaterials do not derive from their chemical composition but rather from their physical structure. The basic units, sometimes called meta-atoms, are composites of conventional materials whose complex geometry can lead to exotic properties compared to the individual constituents.
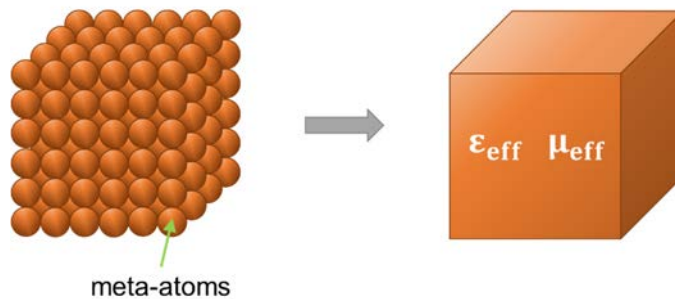
Figure 1.4 Principle of the homogenization method. The composite metamaterial can be described as an effective medium.

The scales of the units, typically their thickness and lattice constant in periodic arrays, are considerably smaller than the wavelength of interest so that the whole system can be described as a uniform media. Therefore, although the unusual properties of metamaterials arise from the intricate EM interaction, light macroscopically sees a homogeneous medium. This approximation enables the description of the metamaterial as an effective medium with macroscopic effective parameters such as permittivity, permeability, refractive index and impedance (Figure 1.4).[8] Properly designing the geometry, size and media involved in a metamaterial, it is possible to engineer the overall electromagnetic

response. For instance, artificial magnetism can be achieved from non-magnetic constituent materials.[16]
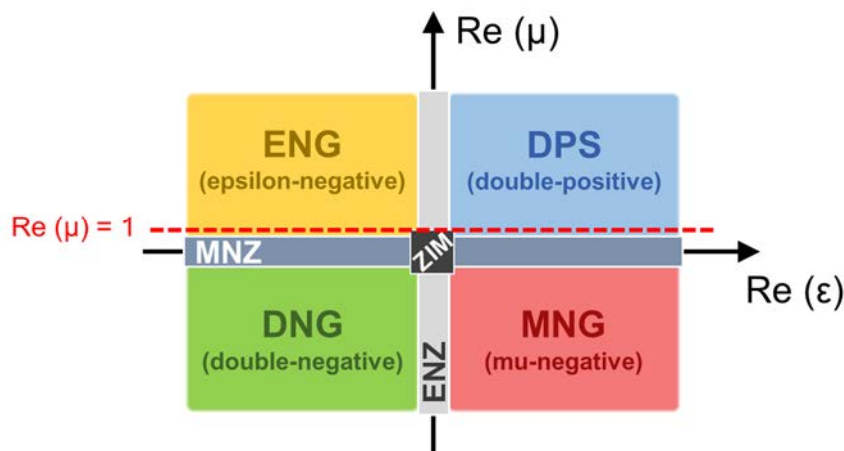
Figure 1.5 Materials classification as a function of the real parts of the permittivity ε and permeability μ. The red dashed line represents natural media at optical frequencies, for which Re (μ) = 1.

Natural and human-made materials can be classified according to the real part of the parameters ε and μ (Figure 1.5).[17,18] If both the permittivity and the permeability are positive numbers, like in most dielectrics and magnetics materials, the media are called double-positive (DPS). In contrast, if both parameters are negative, materials are referred as double-negative (DNG). To date, such response has not been observed in nature, and so this type of materials have become one of the most intriguing metamaterials, particularly since the first experimental realizations.[19] When the permittivity becomes negative but the permeability remains positive, materials are called epsilon-negative (ENG). This group embraces plasmas, metals below the plasma frequency and some doped semiconductors.[20] The opposite situation, this is, materials with positive permittivity and negative permeability are named mu-negative (MNG). Though unusual, this response has been observed in some ferrites at microwave frequencies.[21] In opposition to double-negative materials, ENG and MNG are often comprised in a single category called single-negative (SNG). Below the unity values, materials are specifically known as epsilon-near-zero (ENZ) or mu-near-zero (MNZ). Deeper in this category, materials with both parameters near-zero have been termed near-zero or just zero-index materials (ZIM) in relation to the linked refractive index.

Nevertheless, the electromagnetic map is extremely reduced when working with conventional materials at optical wavelengths due to the lack magnetism. At this range, from metals to dielectrics, materials present a relative permeability equal to 1 (red dashed

line of Figure 1.5). This limitation is indeed the main motivation of metamaterials research: designing and implementing materials beyond the natural framework.[22,23]

1.2.2 Types of metamaterials

Theoretical investigations together with the continuous development of nanotechnology have led to a feasible tailoring of ε and μ from positive to zero and negative values. As a result, the metamaterials field has rapidly grown and led to different branches of study according to the sought properties and elementary building blocks.
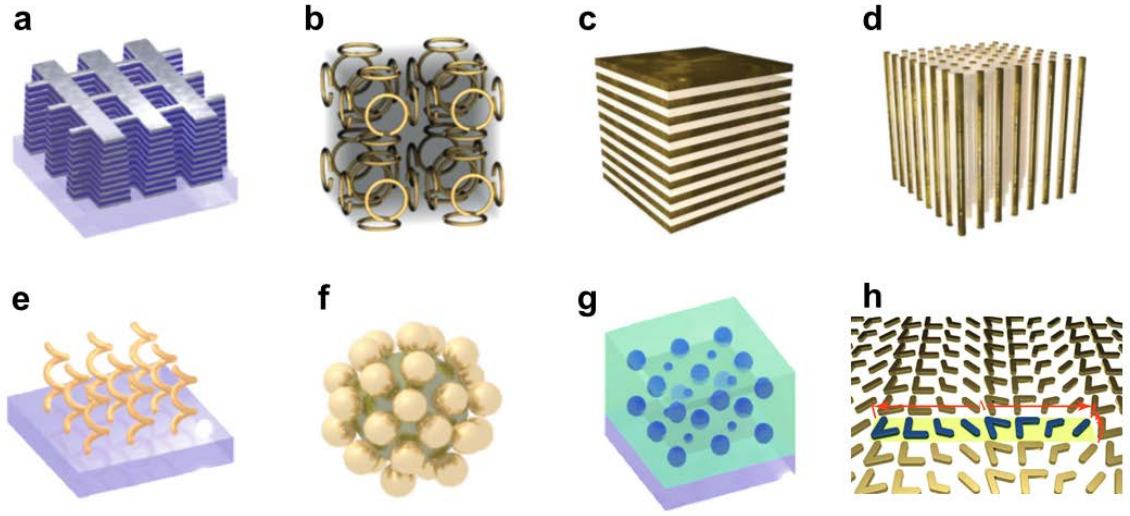
Figure 1.6 Types of optical metamaterial structures. **a** Multilayered fishnet negative-index metamaterial.[24] **b** Arrangement of split-ring resonators for artificial magnetism.[25] **c** Laminated and **d** nanowire hyperbolic metamaterials.[26] **e** Chiral metamaterial made from a helix array.[24] **f** Raspberry-like magnetic nanocluster made from metal-dielectric particles.[27] **g** All-dielectric negative-index metamaterial from inclusions of high refractive index dielectric spheres.[24] **h** Nanoantenna array metasurface for negative reflection and refraction.[28]

Among the different types, we should highlight negative-index metamaterials,[8,24] likely the most extended structures for historical reasons and focused on attaining negative refractive indices through artificial magnetism; hyperbolic metamaterials,[26] which present an anisotropic permittivity; and chiral metamaterials,[29] aimed at obtaining strong optical activity. Other types include colloidal nanoresonators,[30,27] displaying also an artificial magnetic response; or all-dielectric metamaterials,[31] similar to the previous classes but avoiding the common use of plasmonic resonances because of the inherent metallic losses. In addition, there exists an increasing interest in the so-called metasurfaces,[32] planar metamaterials primarily used in wavefront engineering. Figure 1.6 presents some of the most studied systems in these fields, largely dominated by plasmonic resonances.

The effective electromagnetic design of these structures has made possible the development and improvement of optical systems such as invisibility cloaks, super-resolution lenses, nanoantennas, absorbers, polarizers, sensors, non-linear devices or even anti-counterfeiting methods.[14,28,33–40]

Thanks to the academic advances, metamaterials have successfully moved beyond the laboratory scale to high-volume applications. Companies such as Kymeta or Evolv Technology already commercialize meta-antennas for high-performance satellite communications or security scanners, respectively. The start-up Metaboards enables charging portable electronic devices across large surfaces without the need for alignment, providing flexible and functional wireless power solutions (Figure 1.7a). Although more challenging because of the reduced dimensions, the meta-technology has been also extended to the optical regime. The company Lumotiv has developed a beam steering technology based on a liquid crystal metasurface for automotive light detection and ranging, LIDAR (Figure 1.7b). Similarly, Metamaterial Inc. (META) applies nanopatterned composites to boosted biosensors through impedance matching or to green light anti-reflection glasses. The latter, patented as MetaAir and co-developed with the aerospace corporation Airbus, offers a balanced combination of laser protection with high colour transparency (Figure 1.7c).
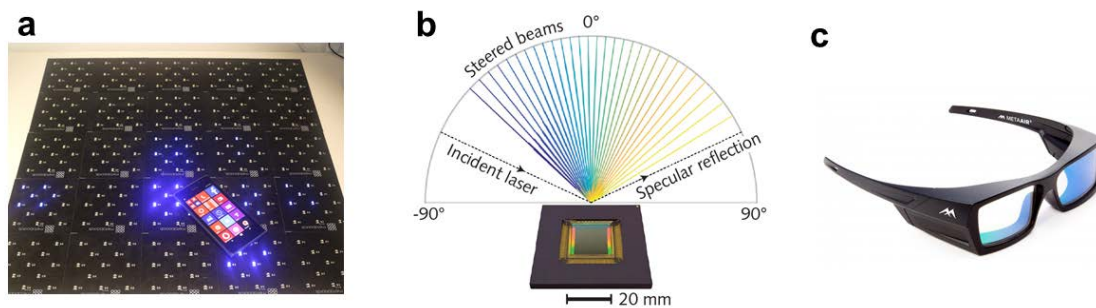
Figure 1.7 a Photograph of a mobile phone charging on a Metaboards surface.[41] **b** Beam steering from the liquid crystal metasurface developed by Lumotive.[42] **c** Photograph of the MetaAir aviation glasses from Metmaterial Inc.[43]

These companies are just some examples of the promising future of metamaterials in everyday life devices. For this reason, nowadays a significant part of the research community works on developing metamaterials that can easily satisfy the requirements needed for commercialization. Among the types above discussed, negative-index metamaterials are still one of them.

1.3 Negative-index metamaterials

1.3.1 Negative refraction

The refractive index n is one of the most important and used parameters for describing light propagation through media. Defined as:

$$n = c/v \qquad (1.18)$$

being v the phase velocity in the medium, it describes how fast light travels through the material. Most common optical materials present refractive indices ranging from 1 to 2.5 at visible and infrared frequencies.[44]

When a light ray travels across two different media, it gets bent owing to the change in refractive index. This phenomenon, refraction, explains why a straw immersed in a glass of water may appear broken. Thanks to refraction, the light path can be adjusted and focused in glasses, magnifying lenses or microscopes. Because of this strong influence of n in daily life, the concept of a negative index of refraction is an attractive new domain of light manipulation with revolutionary impact in current optical technologies.
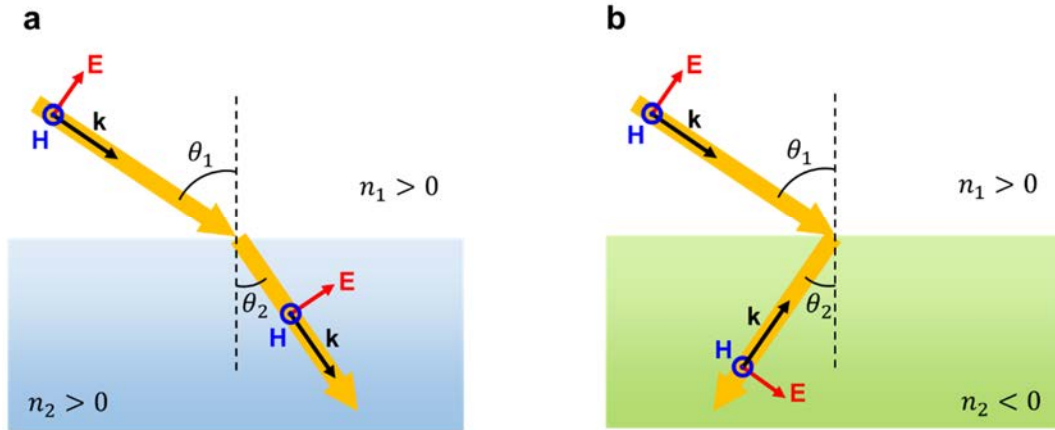
Figure 1.8 a Positive and **b** negative refraction, along with the wavevectors and EM fields.

The most intuitive result of negative-index metamaterials is negative refraction. As expressed by Snell's law

$$n_1 \sin \theta_1 = n_2 \sin \theta_2 \qquad (1.19)$$

light passing from a positive index material (n_1) to a NIM (n_2) will bend in a negative angle θ_2, oppositely to conventional materials (Figure 1.8). Furthermore, in NIMs the wavevector $\vec{k}$ will be oriented in the opposite direction to the energy propagation, forming a left-handed system with the field vectors $\vec{E}, \vec{H}$. Because of this, NIMs are also known as

left-handed materials, unlike natural right-handed materials. Such property implies as well a negative phase velocity inside the metamaterial with related phenomena such as reversed Doppler effect or Cerenkov radiation.[13]

One of the most remarkable applications of NIMs might be the so-called perfect lens (Figure 1.9).[14] Taking advantage of the negative refraction of these materials, it would be possible to focus light without the need of common curved surfaces. Moreover, the evanescent waves would be amplified through the NIM slab, compensating the decay outside the material and recovering the original intensity at the focus plane. Since the evanescent waves carry the subwavelength information of an object, it would be possible to overcome the diffraction limit of light and reconstruct a super-resolved image. This extraordinary light bending introduced new prospects for optical space engineering, leading to striking devices such as invisibility cloaks.[33,45]
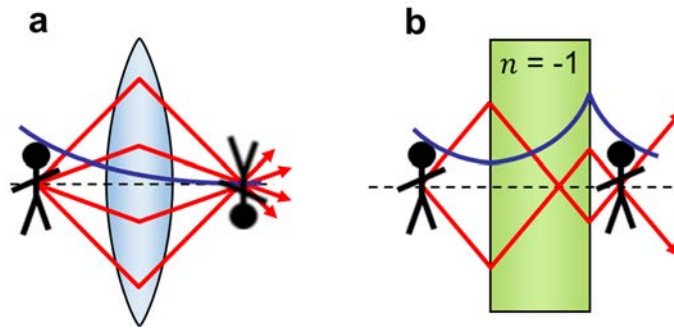
Figure 1.9 Imaging with **a** a conventional convex lens and **b** perfect lens with refractive index of -1. Red and blue lines illustrate the propagating direction and evanescent intensity, respectively.

1.3.2 Designs for negative-index metamaterials

Although Veselago first stated that simultaneous negative ε and μ were needed to achieve NIMs, it was later demonstrated that in dissipative media the strict necessary condition is given by[46]

$$\varepsilon'\mu'' + \varepsilon''\mu' < 0 \tag{1.20}$$

Therefore, one could achieve negative indices in a SNG medium, with just ε' or μ' negative. Yet, this condition implies the existence of an electric and magnetic response at the same wavelength, this is, ε and μ different from passive media.[8] The losses in these metamaterials are often characterized by the figure of merit (FOM):

$$\text{FOM} = \frac{|n'|}{n''} \tag{1.21}$$

where n' and n'' denote the real and imaginary parts of the refractive index, respectively. Thus, the higher the FOM, the better the metamaterial performance is.

In the last decades, several approaches have been worldwide developed for the realization of NIMs working from microwave to visible frequencies. Given the electrical response of metals, the main motivation has been to design intriguing architectures showing artificial magnetism. The key point for such goal is the creation of current loops within the structure components that can induce magnetic dipoles. The combination of the induced magnetic response with the electrical nature of metals is the most common strategy for achieving negative refractive index.

Split-ring resonators

The first experimental demonstration of NIMs was provided by a metallic and non-magnetic array of straight wires combined with split-ring resonators (SRRs).[15] In these meta-atoms, the incident light can excite an oscillating electric current along the metallic SRRs that in turn induces a local magnetic field perpendicular to the SRR plane (Figure 1.10a). Since the direction of the current loop varies following the EM oscillation, the generated magnetic field will as well oscillate, leading to an artificial magnetic dipole.

Though efficient at low frequencies, its implementation at optical wavelengths encounters several issues such as miniaturization limitations or, more importantly, saturation of the working wavelength and decrease of the magnetic dipole strength.[47]
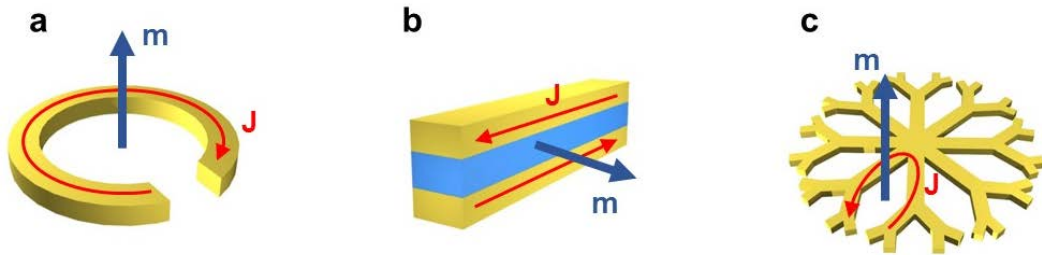
Figure 1.10 Examples of meta-atoms for negative-index metamaterials. **a** Split-ring resonator. **b** Cut-wire pair. **c** Dendritic design. The electrical current J loop induces a magnetic dipole m from non-magnetic constituent materials.

Cut-wire pairs

The restrictions found with SRR pushed the design of alternative resonant meta-atoms such as metallic pairs of rods or plates, known as cut-wire pairs.[48,49] The EM resonances in these metamaterials arise from the SPPs excited along the rods. If two rods are

brought together, the plasmonic resonance will hybridize into a symmetric and an anti-symmetric mode. The impinging electric field oriented parallel to the rods will induce symmetric currents between the rods, whereas the perpendicular magnetic field will generate antiparallel currents.[50] Analogous to the SRRs, the latter will create a magnetic dipole (Figure 1.10b), responsible for the artificial magnetism. However, an accurate geometrical design is needed so that both electric and magnetic resonances overlap and lead to a negative refractive index.

Dendrites

Designs based on dendritic or fractal unit cells present similar operation to the previous models. In these metallic systems, the magnetic response is induced by current loops generated in the branches in the same manner as for SRRs (Figure 1.10c).[51] Nonetheless, like for the cut-wire pairs, the electric response appears at a different frequency so that a fine design is required for obtaining both resonances at the same wavelength. The spectral difference is the major obstacle that these structures experience.

Fishnet design

The fishnet design breaks this limit thanks to the combination of a magnetic resonance with a non-resonant but rather background electric response (Figure 1.11).
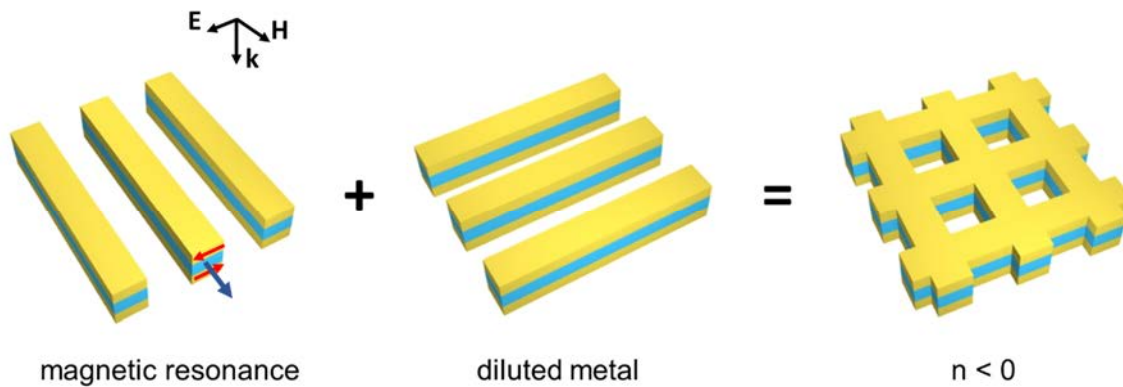
Figure 1.11 Components of the fishnet structure.

The magnetic response is achieved through metallic strips oriented along the incident magnetic field and separated by a dielectric layer. In the same manner as previous designs, the metallic wires support antiparallel currents that induce a magnetic moment in the structure. The origin of these currents lies on the coupling of the SPPs propagating at both metal-dielectric interfaces. When the metallic layers are close enough, their evanescent fields overlap and lead to the formation of gap surface plasmons (GSPs),[52] Figure

1.12. Metallic strips parallel to the electric field provide the electric counterpart. They work effectively as a diluted metal with a lower plasma frequency that gives a background electric response, namely negative permittivity.

Bringing together both components (Figure 1.11), the fishnet metamaterial can be viewed as a metal-insulator-metal (MIM) stack drilled with dielectric holes. Since the magnetic response is generated in the insulator, the effective permeability will mainly depend on the thickness and refractive index of this film. On the other hand, the effective permittivity will be governed by the cut-off frequency of the waveguide mode supported by the holes in the metal layers. Above the cut-off wavelength, the effective permittivity will become negative.[53] Therefore, the fishnet design enables an independent control of both responses while simplifying their operation at the same wavelength.
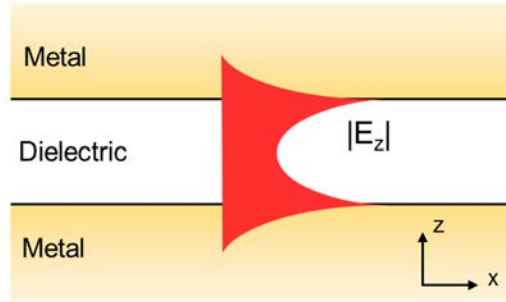
Figure 1.12 Evanescent waves coupling of SPPs leading to gap-surface plasmons.

1.3.3 Fishnet metamaterials at optical frequencies

In 2011, Soukoulis et al. reported the advances towards optical NIMs, showing the promising approach of the fishnet design to visible wavelengths (Figure 1.13).[24] Compared to its partners, fishnet metamaterials stand out for the easier overlap of the magnetic and electric response and for their continuous structure, which is highly compatible with current nanopatterning techniques.

Numerous groups have developed fishnet metamaterials with the motivation of getting a strong magnetic resonance, highly negative refractive index, visible operation, polarization independency, low losses or large-area implementations. All systems based on perforated MIM stacks, they have made use of different materials, layers thicknesses, hole shapes or lattice lengths for obtaining a broad range of NIMs at optical frequencies.
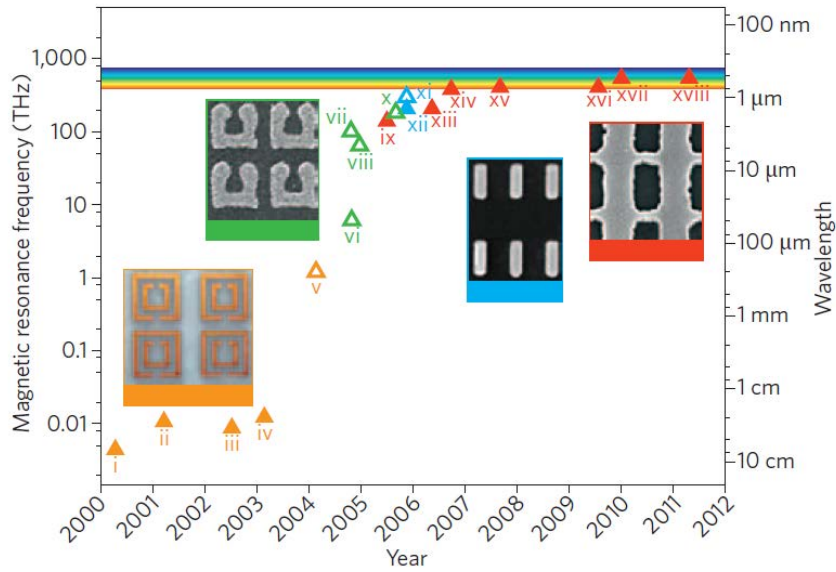
Figure 1.13 Advances in metamaterials operating frequency over the first decade.[24] Orange: structures based on double SRRs; green: U-shaped SRRs; blue: cut-wire pairs; red: double-fishnet structures. The insets show optical or electron micrographs of the four types of designs.

Figure 1.14 summarizes the main fishnet metamaterials developed to date as a function of the wavelength at which the most negative effective refractive index n_{eff} has been achieved. The colour bar marks the scale of the systems, showing that the vast majority of fishnet NIMs working at optical frequencies still rely on low-throughput nanofabrication (yellow and greenish colours).
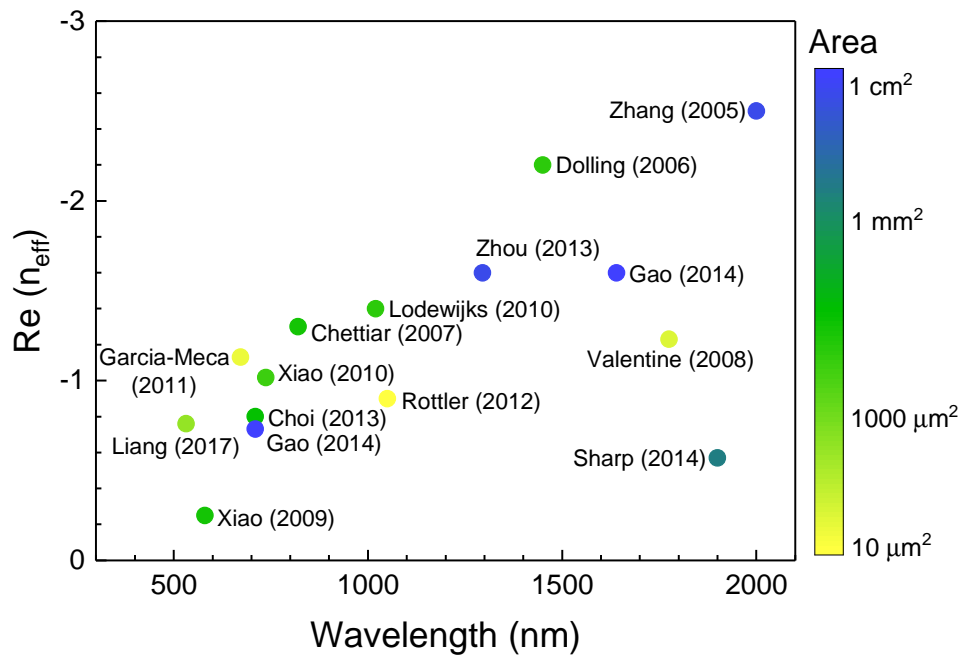
Figure 1.14 State of the art at the beginning of this thesis. Main fishnet metamaterials fabricated to date as a function of the most negative effective refractive index n_{eff}, the operation wavelength and the area. Data extracted from references [54-67].

In 2005, Zhang et al.[54] demonstrated the experimental achievement of NIMs through a pair of gold layers separated by aluminium oxide. With a lattice period of about 800 nm made by interferometric lithography, this pioneering double-fishnet exhibited a refractive index of -2.5 at 2 μm with a FOM of 0.7. Since then, most of works focused on fabricating NIMs with fewer losses and working at shorter wavelengths, from the NIR to the visible. However, as observed in Figure 1.14, this parametric reduction came at costs of smaller areas and less negative n_{eff}.

For instance, Dolling et al. fabricated fishnets of silver and magnesium fluoride (MgF$_2$) working at 1450 and 780 nm, with refractive index of -2.2 and -0.6, respectively.[55,68] Xiao et al. presented for the first time a yellow-light fishnet metamaterial, made from a Ag-MgF$_2$-Ag stack with a periodicity of 220 nm and displaying an index of -0.25 at 580 nm.[58] Their low FOM was remarkably improved from 0.3 to 26 with the incorporation of a gain medium within a NIM working at 737 nm with a refractive index around -1 (Figure **1.15**).[59]
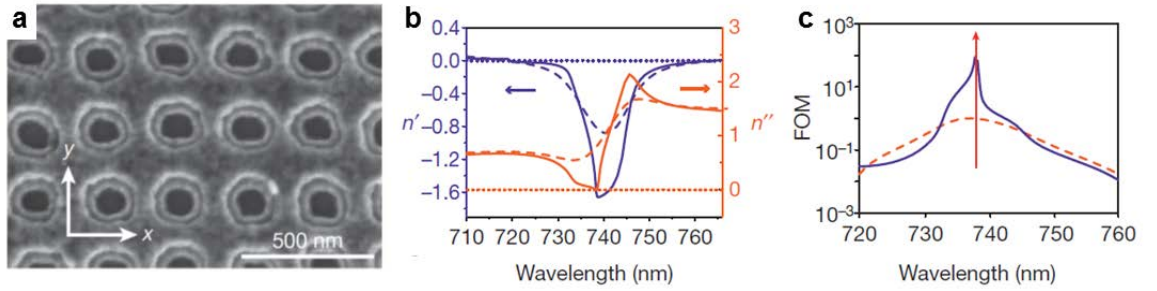
Figure 1.15 a Scanning electron microscopy (SEM) image of the silver double-fishnet metamaterial made by Xiao et al.[59] **b** Retrieved effective refractive index with (solid) and without (dashed) the gain. **c** Figure of merit with (solid) and without (dashed) gain.

Valentine et al. reported a three-dimensional (3D) fishnet metamaterial made of several MIM stacks perforated by ion beam milling (Figure 1.16).[57] They proved that such systems converged to a bulk metamaterial regime and directly measured negative refraction of light in a prism made of the multilayered fishnet structure. Following these studies, later works successfully developed 3D NIMs with significant characteristics such as flexible substrates[63] or record values of -1.13 at 670 nm[61] and -0.76 at 532 nm.[67]

However, these structures were based on sophisticated fabrication processes such as electron beam lithography or focused ion beam. Although highly accurate, these technologies suffer from complex equipment and long processing that restrict the fabricated NIM areas to a hundred of microns. For the implementation of fishnet metamaterials in

actual devices like the ones presented in Figure 1.7, requirements such as large-scale, homogeneous optical response or low-cost production have to be fulfilled.
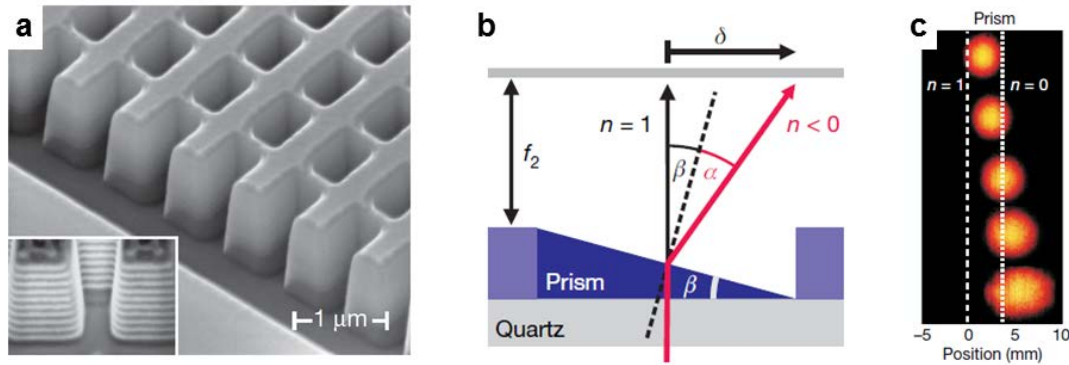
Figure 1.16 a SEM images of a multilayered fishnet structure made of Ag and MgF$_2$. **b** Geometry diagram of the negative angle (α) and beam shift (δ) measurement through a NIM prism. **c** Beam shift resulting from the bending of light at the prism at various wavelengths.[57]

Alternatively, Lodewijks et al. proposed an approach based on colloidal lithography.[60] Instead of engraving through low-throughput techniques, they used a self-assembled colloidal monolayer as mask for creating hexagonal double fishnet structures, made of gold and silicon dioxide (SiO$_2$). Their method led to NIMs with -1.4 refractive index at 1020 nm (Figure 1.17a,b). Gong et al. used the same concept for developing a low-cost route based on colloidal lithography and electrodeposition, with a minimum value of -0.5 at 560 nm (Figure 1.17c-e).[69]
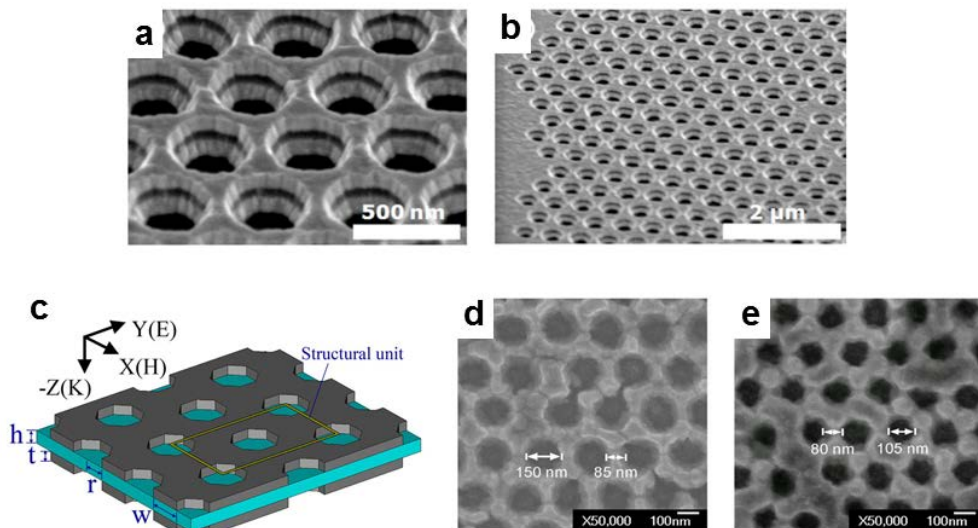
Figure 1.17 Fishnet metamaterials made by colloidal lithography. **a,b** SEM images of Au-SiO$_2$-Au sputtered layers drilled following a colloidal mask.[60] **c** Scheme and **d,e** SEM views of fishnets made by colloidal lithography and silver electrodeposition, working at visible wavelengths.[69]

In the same line of scalable manufacturing, Chanda et al. proposed the use of nanoimprint lithography and transfer printing for fabricating metamaterials with a record index of -7.8 at 2.4 μm over centimeter-sized surfaces (Figure 1.18a-c).[70] With a similar method, Gao et al. reduced the size of the unit cell for developing NIMs working at visible. Their structures displayed negative index over 181 nm, with a minimum value of -0.73 at 710 nm (Figure 1.18d,e).[65]
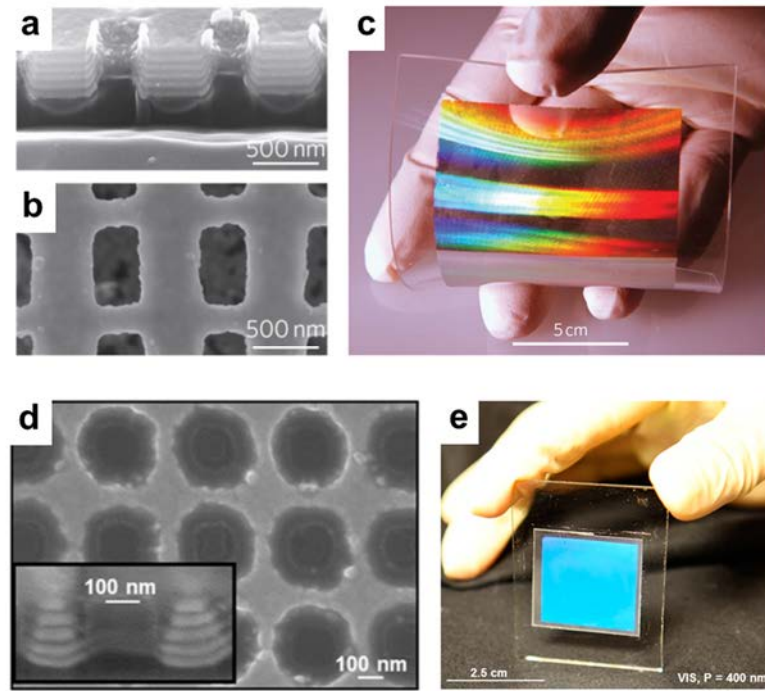
Figure 1.18 Fishnet metamaterials based on nanoimprint lithography. **a** Side and **b** top SEM views of a multilayered Ag-MgF$_2$-Ag stack after transfer printing. **c** Macroscopic optical image of the same structure.[70] **d** SEM image of a similar MIM stack operating at visible wavelengths. **e** Photograph of the sample.[65]

Thanks to their scalability and low-cost manufacturing, colloidal lithography and nanoimprinting are promising tools for the achievement of nanostructured metamaterials. As proved by the latest studies and recent technological advances, these lithographies can enable the mass production and implementation of metamaterials in real NIM devices.[71] In addition, in terms of the absolute values achieved, there is still room for improvement for large-are NIMs in order to reach the performance obtained by low-throughput approaches.

Hence, this thesis will make use of colloidal lithography and nanoimprinting for providing improved fabrication procedures of fishnet metamaterials, with properties comparable to the ones obtained by the typical short-range methods.

1.4 References

1. J. Weiner and F. Nunes. *Light-matter interaction: Physics and engineering at the nanoscale*, 2nd ed.; Oxford University Press, New York, USA, 2017.

2. X. Luo. Subwavelength artificial structures: Opening a new era for engineering optics. *Adv. Mater.* **2019**, *31*, 1804680.

3. J. W. Haus. *Fundamentals and applications of nanophotonics*; Woodhead Publishing, UK, 2016.

4. S. Lee, Y. Sun, Y. Cao and S. H. Kang. Plasmonic nanostructure-based bioimaging and detection techniques at the single-cell level. *TrAC Trends Anal. Chem.* **2019**, *117*, 58–68.

5. Y. Xu et al. Optical refractive index sensors with plasmonic and photonic structures: Promising and inconvenient truth. *Adv. Opt. Mater.* **2019**, *7*, 1801433.

6. S. Linic, P. Christopher and D. B. Ingram. Plasmonic-metal nanostructures for efficient conversion of solar to chemical energy. *Nat. Mater.* **2011**, *10*, 911–921.

7. Y. Li et al. Tailor-made nanostructures bridging chaos and order for highly efficient white organic light-emitting diodes. *Nat. Commun.* **2019**, *10*, 2972.

8. W. Cai and V. Shalaev. *Optical metamaterials: Fundamentals and applications*; Springer, New York, USA, 2010.

9. P. B. Johnson and R. W. Christy. Optical constants of the noble metals. *Phys. Rev. B* **1972**, *6*, 4370–4379.

10. W. L. Barnes. Surface plasmon–polariton length scales: A route to sub-wavelength optics. *J. Opt. A Pure Appl. Opt.* **2006**, *8*, S87–S93.

11. A. V Zayats and I. I. Smolyaninov. Near-field photonics: Surface plasmon polaritons and localized surface plasmons. *J. Opt. A Pure Appl. Opt.* **2003**, *5*, S16–S50.

12. T. W. Ebbesen, H. J. Lezec, H. F. Ghaemi, T. Thio and P. A. Wolff. Extraordinary optical transmission through sub-wavelength hole arrays. *Nature* **1998**, *391*, 667–669.

13. V. G. Veselago. The electrodynamics of substances with simultaneously negative values of ε and μ. *Sov. Phys. Uspekhi* **1968**, *10*, 509–514.

14. J. B. Pendry. Negative refraction makes a perfect lens. *Phys. Rev. Lett.* **2000**, *85*, 3966–3969.

15. D. R. Smith, W. J. Padilla, D. C. Vier, S. C. Nemat-Nasser and S. Schultz. Composite medium with simultaneously negative permeability and permittivity. *Phys. Rev. Lett.* **2000**, *84*, 4184–4187.

16. J. B. Pendry, A. J. Holden, D. J. Robbins and W. J. Stewart. Magnetism from conductors and enhanced nonlinear phenomena. *IEEE Trans. Microw. Theory Tech.* **1999**, *47*, 2075–2084.

17. A. Alu, N. Engheta, A. Erentok and R. W. Ziolkowski. Single-negative, double-negative, and low-index metamaterials and their electromagnetic applications. *IEEE Antennas Propag. Mag.* **2007**, *49*, 23–36.

18. Y. Liu and X. Zhang. Metamaterials: A new frontier of science and technology. *Chem. Soc. Rev.* **2011**, *40*, 2494–2507.

19. W. J. Padilla, D. N. Basov and D. R. Smith. Negative refractive index metamaterials. *Mater. Today* **2006**, *9*, 28–35.

20. G. V Naik and A. Boltasseva. A comparative study of semiconductor-based plasmonic metamaterials. *Metamaterials* **2011**, *5*, 1–7.

21. K. Bi et al. Negative and near zero refraction metamaterials based on permanent magnetic ferrites. *Sci. Rep.* **2014**, *4*, 4139.

22. T. Tanaka and A. Ishikawa. Towards three-dimensional optical metamaterials. *Nano Converg.* **2017**, *4*, 34.

23. X. Fu and T. J. Cui. Recent progress on metamaterials: From effective medium model to real-time information processing system. *Prog. Quantum Electron.* **2019**, *67*, 100223.

24. C. M. Soukoulis and M. Wegener. Past achievements and future challenges in the development of three-dimensional photonic metamaterials. *Nat. Photonics* **2011**, *5*, 523–530.

25. M. Kadic, G. W. Milton, M. van Hecke and M. Wegener. 3D metamaterials. *Nat. Rev. Phys.* **2019**, *1*, 198–210.

26. P. Huo, S. Zhang, Y. Liang, Y. Lu and T. Xu. Hyperbolic metamaterials and metasurfaces: Fundamentals and applications. *Adv. Opt. Mater.* **2019**, *7*, 1970054.

27. V. Ponsinet et al. Self-assembled nanostructured metamaterials. *EPL* **2017**, *119*, 14004.

28. X. Ni, N. K. Emani, A. V Kildishev, A. Boltasseva and V. M. Shalaev. Broadband light bending with plasmonic nanoantennas. *Science* **2012**, *335*, 427.

29. Z. Wang, F. Cheng, T. Winsor and Y. Liu. Optical chiral metamaterials: A review of the fundamentals, fabrication methods and applications. *Nanotechnology* **2016**, *27*, 412001.

30. M. Fruhnert, S. Mühlig, F. Lederer and C. Rockstuhl. Towards negative index self-assembled metamaterials. *Phys. Rev. B* **2014**, *89*, 1–6.

31. S. Jahani and Z. Jacob. All-dielectric metamaterials. *Nat. Nanotechnol.* **2016**, *11*, 23–36.

32. X. Luo. Subwavelength optical engineering with metasurface waves. *Adv. Opt. Mater.* **2018**, *6*, 1701201.

33. D. Schurig et al. Metamaterial electromagnetic cloak at microwave frequencies. *Science* **2006**, *314*, 977–980.

34. A. Martínez, C. García-Meca, R. Ortuño, F. J. Rodríguez-Fortuño and J. Martí. Metamaterials for optical security. *Appl. Phys. Lett.* **2009**, *94*, 251106.

35. T. Chen, S. Li and H. Sun. Metamaterials application in sensing. *Sensors* **2012**, *12*, 2742–2765.

36. X. Ni, Z. J. Wong, M. Mrejen, Y. Wang and X. Zhang. An ultrathin invisibility skin cloak for visible light. *Science* **2015**, *349*, 1310–1314.

37. J. Kaschke and M. Wegener. Optical and infrared helical metamaterials. *Nanophotonics* **2016**, *5*, 510–523.

38. S. RoyChoudhury, V. Rawat, A. H. Jalal, S. N. Kale and S. Bhansali. Recent advances in metamaterial split-ring-resonator circuits as biosensors and therapeutic agents. *Biosens. Bioelectron.* **2016**, *86*, 595–608.

39. P. Yu et al. Broadband metamaterial absorbers. *Adv. Opt. Mater.* **2019**, *7*, 1800995.

40. J. G. Webster, J. Y. Yin and T. J. Cui. Metamaterial lenses. *Wiley Encycl. Electr. Electron. Eng.* **2019**, 1–16.

41. Metaboards: Getting rid of the wires, 2018 https://www.alumni.ox.ac.uk/quad/article/getting-rid-wires.

42. G. M. Askelrod. Optics for automotive lidar: Metasurface beam steering enables solid-state, high performance lidar, 2019 https://www.laserfocusworld.com/optics/article/14036818/metasurface-beam-steering-enables-solidstate-highperformance-lidar.

43. MetaAir laser glare protection eyewear, https://www.meta-air.com.

44. E. Hecht. *Optics*, 4th ed.; Addison Wesley, San Francisco, USA, 2002.

45. S. Mühlig et al. A self-assembled three-dimensional cloak in the visible. *Sci. Rep.* **2013**, *3*, 2328.

46. R. A. Depine and A. Lakhtakia. A new condition to identify isotropic dielectric-magnetic materials displaying negative phase velocity. *Microw. Opt. Technol. Lett.* **2004**, *41*, 315–316.

47. M. W. Klein, C. Enkrich, M. Wegener, C. M. Soukoulis and S. Linden. Single-slit split-ring resonators at optical frequencies: Limits of size scaling. *Opt. Lett.* **2006**, *31*, 1259–1261.

48. V. A. Podolskiy, A. K. Sarychev and V. M. Shalaev. Plasmon modes in metal nanowires and left-handed materials. *J. Nonlinear Opt. Phys. Mater.* **2002**, *11*, 65–74.

49. V. M. Shalaev et al. Negative index of refraction in optical metamaterials. *Opt. Lett.* **2005**, *30*, 3356–3358.

50. M. A. Noginov and V. A. Podolskiy. *Tutorials in Metamaterials*; CRC Press, Taylor & Francis Group, USA, 2011.

51. X. Zhao. Bottom-up fabrication methods of optical metamaterials. *J. Mater. Chem.* **2012**, *22*, 9439–9449.

52. R. Ortuño, C. García-Meca, F. J. Rodríguez-Fortuño, J. Martí and A. Martínez. Role of surface plasmon polaritons on optical transmission through double layer metallic hole arrays. *Phys. Rev. B* **2009**, *79*, 075425.

53.   A. Mary, S. G. Rodrigo, F. J. García-Vidal and L. Martín-Moreno. Theory of negative-refractive index reponse of double-fishnet structures. *Phys. Rev. Lett.* **2008**, *101*, 103902.

54.   S. Zhang et al. Experimental demonstration of near-infrared negative-index metamaterials. *Phys. Rev. Lett.* **2005**, *95*, 137404.

55.   G. Dolling, C. Enkrich, M. Wegener, C. M. Soukoulis and S. Linden. Low-loss negative-index metamaterial at telecommunication wavelengths. *Opt. Lett.* **2006**, *31*, 1800–1802.

56.   U. K. Chettiar et al. Dual-band negative index metamaterial: Double negative at 813 nm and single negative at 772 nm. *Opt. Lett.* **2007**, *32*, 1671–1673.

57.   J. Valentine et al. Three-dimensional optical metamaterial with a negative refractive index. *Nature* **2008**, *455*, 376–380.

58.   S. Xiao, U. K. Chettiar, A. V Kildishev, V. P. Drachev and V. M. Shalaev. Yellow-light negative-index metamaterials. *Opt. Lett.* **2009**, *34*, 3478–3480.

59.   S. Xiao et al. Loss-free and active optical negative-index metamaterials. *Nature* **2010**, *466*, 735–740.

60.   K. Lodewijks, N. Verellen, W. Van Roy, G. Borghs and P. Van Dorpe. Self-assembled hexagonal double fishnets as negative index materials. *Appl. Phys. Lett.* **2011**, *98*, 091101.

61.   C. García-Meca et al. Low-loss multilayered metamaterial exhibiting a negative index of refraction at visible wavelengths. *Phys. Rev. Lett.* **2011**, *106*, 67402.

62.   A. Rottler et al. Rolled-up nanotechnology for the fabrication of three-dimensional fishnet-type GaAs-metal metamaterials with negative refractive index at near-infrared frequencies. *Appl. Phys. Lett.* **2012**, *100*, 151104.

63.   M. Choi, J. H. Choe, B. Kang and C. Choi. A flexible metamaterial with negative refractive index at visible wavelength. *Curr. Appl. Phys.* **2013**, *13*, 1723–1727.

64.   Y. Zhou et al. Fabrication of large-area 3D optical fishnet metamaterial by laser interference lithography. *Appl. Phys. Lett.* **2013**, *103*, 123116.

65.   L. Gao et al. Nanoimprinting techniques for large-area three-dimensional negative index metamaterials with operation in the visible and telecom bands. *ACS Nano* **2014**, *8*, 5535–5542.

66.   G. J. Sharp, S. I. Khan, A. Z. Khokhar, R. M. de la Rue and N. P. Johnson. Negative index fishnet with nanopillars formed by direct nano-imprint lithography. *Mater. Res. Express* **2014**, *1*, 045802.

67.   Y. Liang, Z. Yu, N. Ruan, Q. Sun and T. Xu. Freestanding optical negative-index metamaterials of green light. *Opt. Lett.* **2017**, *42*, 3239–3242.

68.   G. Dolling, M. Wegener and S. Linden. Negative-index metamaterial at 780 nm wavelength. *Opt. Lett.* **2007**, *32*, 53–55.

69.   B. Gong et al. A visible metamaterial fabricated by self-assembly method. *Sci. Rep.* **2014**, *4*, 4713.

70.   D. Chanda et al. Large-area flexible 3D optical negative index metamaterial formed by nanotransfer printing. *Nat. Nanotechnol.* **2011**, *6*, 402–407.

71.   G. Yoon, I. Kim and J. Rho. Challenges in fabrication towards realization of practical metamaterials. *Microelectron. Eng.* **2016**, *163*, 7–20.

Chapter 2

Fabrication, characterization and simulation methods

2.1 Introduction

As discussed in the previous chapter, achieving optical metamaterials demands the fabrication of complex architectures of just a few hundred of nanometers. At this scale, however, conventional patterning techniques such as photolithography or interferometric lithography encounter the diffraction limit when aiming to provide high-density structures with reduced dimensions. Consequently, the fabrication of metamaterials at optical frequencies has been intensively based on techniques like electron beam lithography or focused ion beam milling.[1-6] Although these technologies can generate arbitrary patterns of high quality and resolution, their expensive and time consuming processes typically limit the active area to micrometer sizes. This small scale is the major bottleneck for mass production and practical applications of metamaterials.

Recent advances in nanofabrication have revealed the potential of unconventional nanopatterning methods such as colloidal lithography and nanoimprint lithography (NIL). The large-area, high-throughput and cost-effective processing of these techniques promises an effective approach for the technological implementation of complex photonic architectures like metamaterials.[7,8]

The low-cost manufacturing can be extended likewise to the deposition process through inexpensive techniques such as electrodeposition. This method does not depend on complex vacuum systems and enables the fabrication of a broad variety of nanostructures.[9]

Along this chapter, we introduce the principles and procedures used for colloidal lithography, nanoimprinting and electrodeposition, which compose the backbone of the work. We later describe the structural and optical techniques employed for characterizing the structures fabricated along the thesis. Finally, we present the fundamentals of the numerical method used for modelling the optical properties,

providing a better comprehension of the studied systems. The details of additional techniques used through the manuscript will be briefly explained when mentioned.

2.2 Colloidal lithography

During the past years, colloidal self-assembly has emerged as an attractive bottom-up route for the fabrication of well-defined micro and nanostructures. At its most general conception, colloidal self-assembly can lead to single or multilayer colloidal crystals, hierarchical superstructures or even complex clusters of particles of different shapes or compositions.[10-12]

Interestingly, when deposited on a substrate, two-dimensional (2D) colloidal crystals can work as masks for surface patterning. This is the base of colloidal lithography (CL), also known as nanosphere lithography. Typically, the particles used for the formation of these colloidal monolayers are made of silica of polystyrene (PS) because of their easy synthesis, self-assembly control and compatibility with further modifications. Besides, since the particle size can vary from microns to hundreds of nanometers, a broad range of templates can be achieved. Being a low-cost, large-area and versatile approach, colloidal lithography has become a powerful alternative to the complex procedures of top-down lithographies.

There exist several techniques for fabricating colloidal crystals, mainly differentiated by the forces driving the assembly. Typical interactions between submicron spheres include capillary action, electrostatic repulsion, van der Waals attraction or external stimuli such as gravity, centrifugation or electromagnetic fields.[13,14] The balance of the implied forces generally leads to hexagonal packed colloidal crystals, where the monodispersity in size and in shape of the particles is of crucial importance for achieving high quality crystals. Therefore, the use of one particular technique will depend on the particle material, surface functionalization, dispersion medium and desired structure. Commonly assembly techniques include drop casting, vertical deposition, spin-coating, electrophoretic self-assembly or interface self-assembly.[14,15]

Using the latter method, Gao et al. showed the notable scalability of CL beyond the laboratory frame.[16] Based on the self-assembly at the water-air interface, they developed a micro-propulsive injection method for the high-throughput fabrication of 1 m² monolayer of PS spheres (Figure 2.1a,b). Taking a similar monolayer as starting point, Vogel et al. demonstrated the facile achievement of non-closed packed monolayers of PS

beads by reducing the particle size with a controlled oxygen plasma step (Figure 2.1c).[17] Oppositely, one can also finely reduce the voids between particles by a controlled annealing of the material (Figure 2.1d).[18] More complex structures such as binary colloidal crystals are also feasible (Figure 2.1e). In this case, colloidal particles of two different sizes are assembled together in a complementary array, where their relative amounts determines the final structure.[19,20] Furthermore, colloidal self-assembly does not restrict to spherical beads but has been extended to anisotropic particles with shapes like ellipsoids,[21] cubes[22] or red blood cells (Figure 2.1f).[23,24]
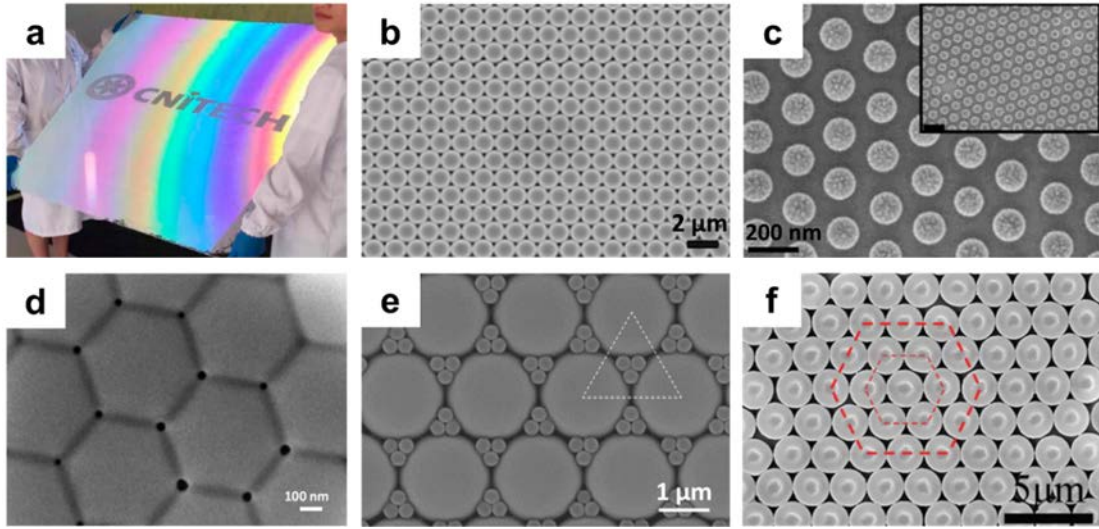
Figure 2.1 Advances in colloidal templates made with polystyrene particles. **a,b** Photograph and SEM image of 1 m² colloidal monolayer.[16] **c** Non-closed packed array obtained after oxygen plasma etching. Scale bar of the inset: 500 nm.[17] **d** Colloidal monolayer after annealing at 110 °C.[18] **e** Binary colloidal crystal made of 350 nm and 2µm spheres.[19] **f** Self-assembled anisotropic red blood cell-like colloidal particles.[23]

The diverse geometries reachable through CL together with further etching or deposition steps have drawn the attention of researchers working in the fields of metamaterials,[25,26] light emission devices,[27] wettability[28] or multiple sensors[29,30] where a large-scale periodic pattern can enhance the targeted performance. In the same way, we have applied CL to the fabrication of optical metamaterials. The method employed for the pattern fabrication is now described.
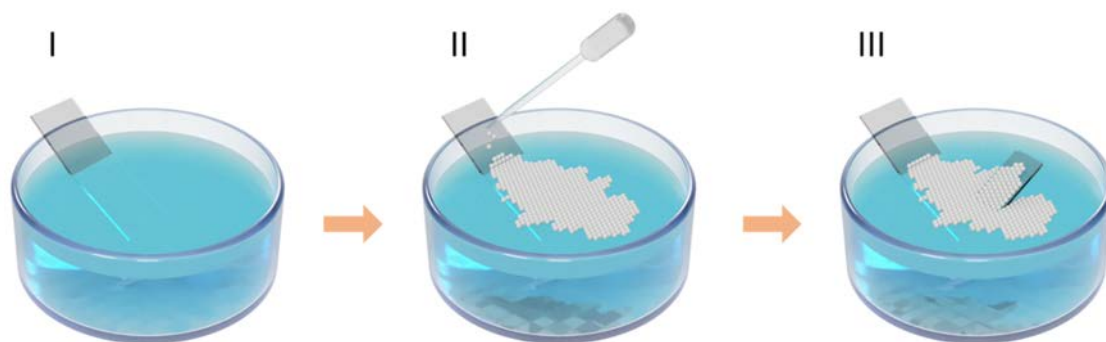
2.2.1 Self-assembly of monolayers on the water surface

We fabricated colloidal monolayers by the well-known method of self-assembly at the water-air interface.[17-31] Based on the controlled spreading of particles and their

packing on the water surface, this method stands out for its simplicity and rapid deposition while presenting high quality arrangements.

We made use of submicron polystyrene latex particles previously synthesized in our laboratory by emulsion polymerization.[32] The concentration of the PS suspension in distilled water was initially adjusted to 12 g/L. Then, an equal volume of ethanol was added in order to reduce the surface tension of the solution, being 1:1 the final mixture of water and ethanol.

Substrates of glass, gold or nickel were cleaned by ultrasounds for 20 min in acetone, 20 min in ethanol and dried by air blowing. They were subsequently treated with UV ozone in order to render the surface highly hydrophilic.

Figure 2.2 Steps of the self-assembly process on the water surface and transfer onto a substrate: **I** immersion of a glass slide into the water, **II** spreading of the suspension, **III** deposition of the monolayer onto a substrate.

Figure 2.2 depicts the formation of a closed-packed monolayer on the water surface. (I) A cleaned glass is immersed in a crystallizing dish half filled with distilled water and fixed to the crystallizer wall at approximately 45° using scotch tape. This glass will be used for spreading the PS suspension, as a bridge to the water surface. Next, around 30 drops of 2 wt% sodium dodecyl sulfate (SDS, Sigma Aldrich) were added to the water before spreading the particles in order to promote the ordering. (II) 20 μL of the colloidal suspension were spread on the inclined glass slide by moving steadily the pipette so that the particles descended evenly to the water and orderly assembled in the minimum energy configuration: a hexagonally packed monolayer. The presence of the surfactant counteracts van der Waals and capillary attractions between particles, increasing their time available to find the most stable configuration and thus, increasing the order of the monolayer. A proof of the correct packing on the water surface are the colourful reflections arising from Bragg diffraction (Figure 2.3a). If the suspension, on

the contrary, freely spreads through the water forming white clouds, more SDS surfactant is needed since the particles are not arranging into large-area monolayers.
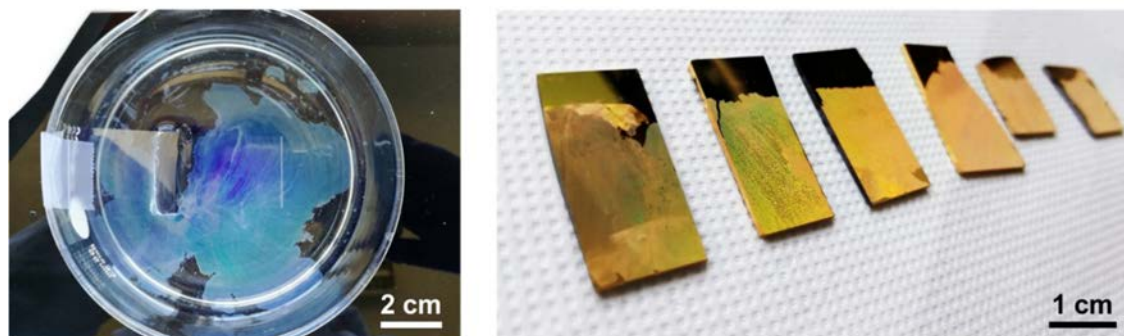
Figure 2.3 a Top-view photograph of a self-assembled monolayer of 480 nm PS spheres on the water surface. **b** Photograph of monolayers of PS beads deposited on centimeter-sized substrates.

(III) Once centimeter-sized assemblies are formed on the water surface, a cleaned substrate is immersed into the water through a point free of particles. It is positioned under the region of interest and lifted out at a shallow angle to pick up the monolayer. It is worth mentioning that a hydrophobic surface might repel the water drops and break the monolayer. The covered substrate is finally let out for drying vertically so that the excess of water slides and dry off. This process is repeated with the remaining self-assembled area so that multiple samples can be made from the same floating monolayer (Figure 2.3b).
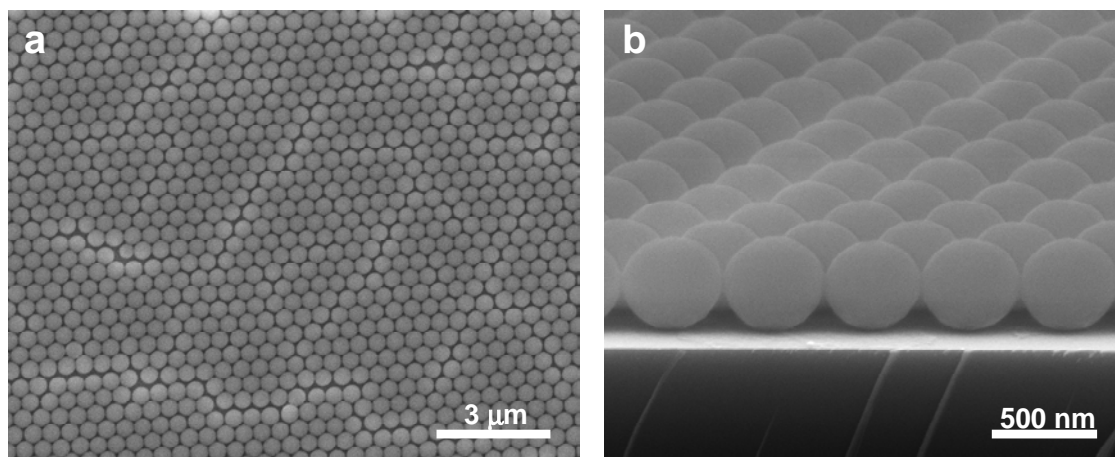
Figure 2.4 a Top view and **b** cross-section SEM images of a self-assembled monolayer of 480 nm polystyrene particles.

In this thesis, we have worked with 480 nm PS particles because of their optical response in the visible-NIR range and well-ordered monolayers. Figure 2.4 shows SEM images of the high quality self-assembled monolayers. These large-area arrays will be used as templates for the fabrication of more complex structures in Chapters 3 and 5.

2.3 Nanoimprint lithography

The concept of imprinting for replicating a mold is one of the oldest manufacturing techniques used by human civilizations. Coins production, leather embossing or letterpress printing are just some examples. However, the first replica at the nanoscale only arose in 1995 when Chou et al. proved the high-resolution imprinting of sub-25 nm features (Figure 2.5a).[33]

Similar to other lithographies, the principle of nanoimprint lithography (NIL) consists of transferring an initial pattern to a target substrate. It uses a mold to deform plastic materials through pressure, creating a negative replica on the target. Although the fabrication of the initial mold might depend on conventional lithographies, NIL is considered one of the most promising patterning approaches in future nanotechnology because of its high-throughput and large-area performance.[34,35] Furthermore, the repeatability of the process from the same mold significantly reduces the costs and times so far required for producing submicron patterns. These are the reasons why numerous works investigate its adaptability to materials such as resists, biopolymers or perovskites (Figure 2.5).[36-39] The advances in high resolution and mass production patterns like these examples have made a breakthrough not only in the metamaterials community[7,40-42] but also in the fabrication of devices such as solar cells,[43] nanofluidic chips[44] or supercapacitors.[45]
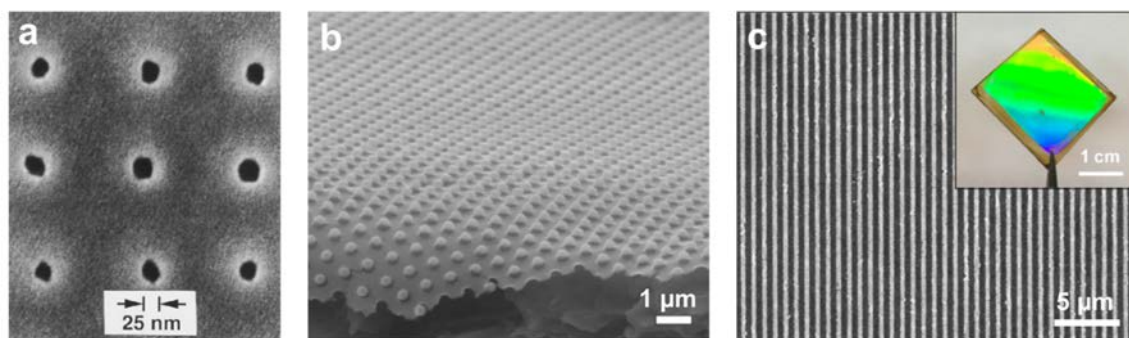
Figure 2.5 Versatility of nanoimprint lithography over various materials and shapes. **a** PMMA film patterned with 25 nm wide holes.[33] **b** Array of pillars printed on hydroxypropyl cellulose.[37] **c** Imprinted lines on inorganic halide perovskites. Inset: photogaph of the structure.[39]

Regarding the process used for nanoimprinting, NIL can be divided in two main categories: thermal NIL and ultraviolet NIL.

- o Thermal NIL, also known as hot-embossing, relies on the compression of a softened thermoplastic material. Typically, the target material is heated above its

glass transition temperature (T_g) and the mold is pressed against it, so that the material flows through the pattern reliefs. The system is then cooled down, the thermoplastic material solidifies with the new negative shape and the mold is removed. This technique enables patterning a broad variety of polymers at temperatures around 100 ºC.[46]

o   In UV NIL, a liquid photoresist is used for imprinting a pattern that is later cured with UV light. For this reason, at least one of the substrates involved in the imprinting must be transparent at these wavelengths. Compared to thermal NIL, this method eliminates fracture defects coming from the different thermal expansion between the mold and the resist.[47] However, a photocurable material is needed.

In addition, NIL is also classified in three different techniques depending on the stiffness of the stamp used: hard, soft or hybrid molds.[48]

o   Historically, the first nanoimprinted replicas were made from hard molds such as silicon or quartz because of the high definition of the patterns,[33] with Young's modulus of the order of GPa.[34] The process requires high pressure and temperature to achieve conformal contact with the target material. Moreover, the rigidity of the molds presents several drawbacks that can harm the imprinted structure. These issues include the formation of air bubbles between the stamp and the resist, the easy damage of the mold or even the breakage when applying pressure.

o   Soft nanoimprinting is characterized by the use of flexible molds such as polydimethylsiloxane (PDMS) or polyethylene terephthalate (PET). The flexibility of these materials presents two main advantages. First, a longer working life thanks to their easy manipulation and re-use. Second, a conformal contact between the mold and the substrate, which prevents surface defects and enables imprinting curved surfaces. In fact, soft nanoimprint lithography has been extended to the mass-production technique of roll-to-roll, facilitating the fabrication of large and flexible patterned surfaces.[49] However, the low Young's modulus of soft molds (~2 MPa) often results in the deformation or collapsing of the features, limiting the patterns to short aspect ratio structures.

o   Hybrid molds merge the advantages of hard and soft stamps. With intermediate values of the Young's modulus, they display high-resolution features while keeping a degree of flexibility that make them a potential tool for fabrication at the nanoscale. This type include composites of PDMS or photocurable resists such as Ormostamp.[48,50]

In this thesis, we have employed hybrid molds for the steady fabrication of patterns with high definition nanofeatures. Starting from a hard silicon master, we have transferred the patterns to working molds of PDMS, from which the final imprinted templates have been created.

2.3.1 Master replication

1 cm² silicon masters of holes and lines with submicron diameters and periodicities were fabricated using e-beam lithography by Eulitha (Switzerland) and Naitec (Spain). Figure 2.6 describes the replication process for obtaining working soft stamps with the same features as the initial silicon master. As detailed, we made use of the intermediate photoresist Ormostamp (Micro resist technology).
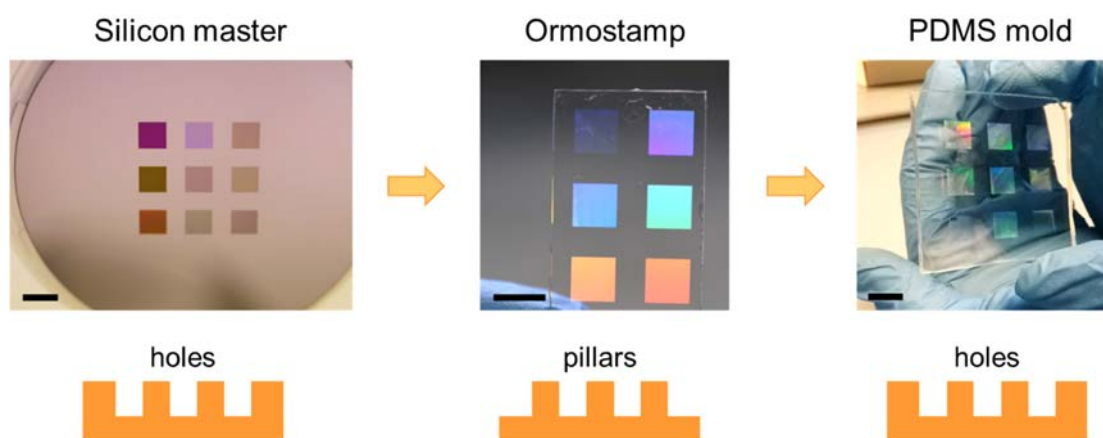
Figure 2.6 Replication process from the original Si master to obtain working molds of PDMS. Scale bars: 1 cm.

First, the silicon masters were silanized in order to provide a molecular anti-sticking layer between the master and the Ormostamp. 5 μL of 1H,1H,2H,2H-perfluorooctyl-trichlorosilane (PFOTS) (97%, Alfa Aesar) were dropped into a 4 L desiccator together with the masters and let under vacuum for 30 min. During this time, the silane molecules evaporated and covalently linked to the silicon surfaces. The masters were later heated at 150 °C for 20 min and rinsed with isopropanol to remove the excess of silane.

A few drops of Ormostamp photoresist were then poured onto the silicon masters and covered with previously cleaned and UV ozone activated glass slides. If bubbles are formed, the glass cover can be gently pressed to facilitate the Ormostamp spreading while the air is squeezed out. The resist was cured with a commercial UV lamp placed at 10 cm distance for 5 min, adopting the inverse pattern of the initial master. A post-bake treatment of 130 °C for 30 min increased the thermal stability of the new stamps and assisted the physical separation fom the silicon substrates. After carefully demolding to not damage the patterns, both surfaces were cleaned with acetone and isopropanol.

The new Ormostamp/glass masters of pillars were also silanized prior the replication into working PDMS stamps. Hybrid molds made of a thin layer of hard-PDMS and a support layer of soft-PDMS were fabricated following a previous method.[51] As explained, this composite would provide simultaneously high-resolution patterns and conformal contact. For the hard layer, we used a hard PDMS kit purchased from Gelest (USA). Stirring after each step, we mixed 1.7 g of vinyl prepolymer (VDT-731) with 9 µL of Pt catalyst (SIP6831.2), 0.05 g of modulator (SIT7530.0) and 0.5 g of hydrosilane prepolymer (HMS-301). 1.55 g of toluene were lastly added to decrease the viscosity of the mixture. This was casted on the Ormostamp masters and spread over the entire surface by air blowing until a homogeneous cover was achieved. The hard-PDMS was let at room temperature (RT) for 1 hour to ensure it dried and finally cured at 60 °C for 1 h.

The soft-PDMS layer was fabricated by thoroughly mixing base and curing agent (Sylgard184, Dow Corning, USA) in a 10:1 ratio. After degassing for 2 hours, the mixture was poured onto the hard-PDMS film and cured at 80 °C for 3 hours. Once cooled down, the Ormostamp template was released, leading to a PDMS mold with high-resolution holes (or lines) on a flexible support. These properties enabled the fabrication of a wide variety of templates, as it is next explained.

2.3.2 Soft nanoimprinting

Cleaned glasses and indium tin oxide coated glasses (Ossila) were used as substrates. Thin layers of 5-7 wt% SU8 photoresist (MicroChem 2000.5) were spin-coated (Polos Spin150i) at 2000 rpm for 12s. These conditions led to 150-270 nm thick SU8 layers for imprinting different patterns.

Soft nanoimprinting on SU8 was done by combining hot embossing with UV exposure. Figure 2.7 depicts the main steps of the imprinting process. The previously fabricated PDMS molds with patterned areas of 1 cm² were pressed onto the SU8 layers at 90 °C (T_g = 55 °C) for 10 s. After this time, the SU8 had adopted the negative shape of the mold and the whole system was let to cool down until 40 °C for demolding. The structure was cross-linked by 10 min of UV light and hardened with a post-bake at 160 °C for 30 min.
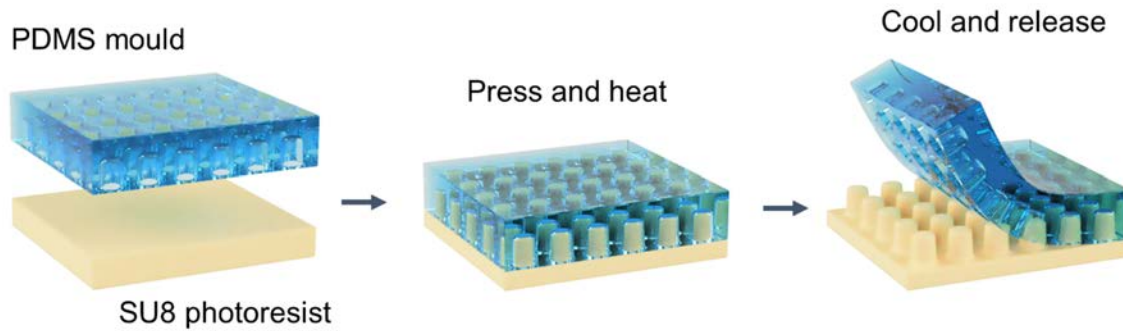
Figure 2.7 Hot embossing procedure for imprinting nanostructures from soft molds.

This process was mainly applied to the fabrication of SU8 arrays of pillars, whose lattice parameter (L) ranged from 200 nm up to 500 nm. Figure 2.8 presents SEM images of some of the imprinted patterns, showing the versatility to produce from 100 nm wide features (Figure 2.8a,b) to 330 nm tall pillars (Figure 2.8c). It is worth noting that pillars taller than the initial SU8 layer are attainable thanks to the resist filling into the pattern.

These large-area templates will be the base for the structures developed in Chapter 4. Moreover, the process will be applied for the fabrication of shallow lines in Chapter 5.
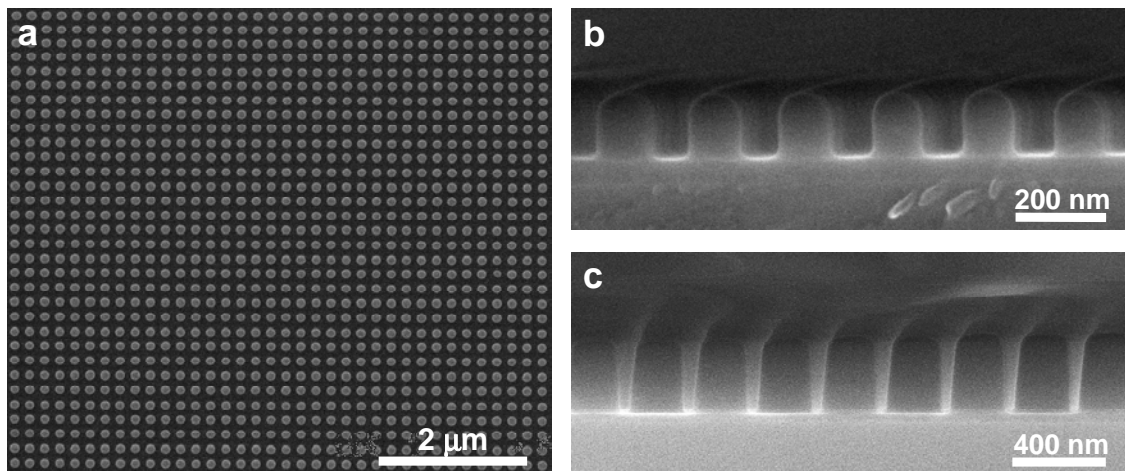
Figure 2.8 a,b SEM top and cross-section views of periodic arrays of pillars with L = 200 nm. **c** Cross-section of a similar pattern of L = 400 nm.

2.4 Electrodeposition

Metallic electrodeposition, also known as electroplating, consists on the reduction of metal ions from an electrolyte onto a conductive surface. It is typically performed in a three-electrode cell that includes the sample to coat, known as cathode or working electrode (WE), an anode or counter electrode (CE) and a reference electrode (RE) (Figure 2.9). In potentiostatic mode, a constant potential controlled by the RE is applied between the WE and CE. The metallic cations of the electrolyte migrate towards the working electrode and eventually reduce on the conductive parts of the substrate.
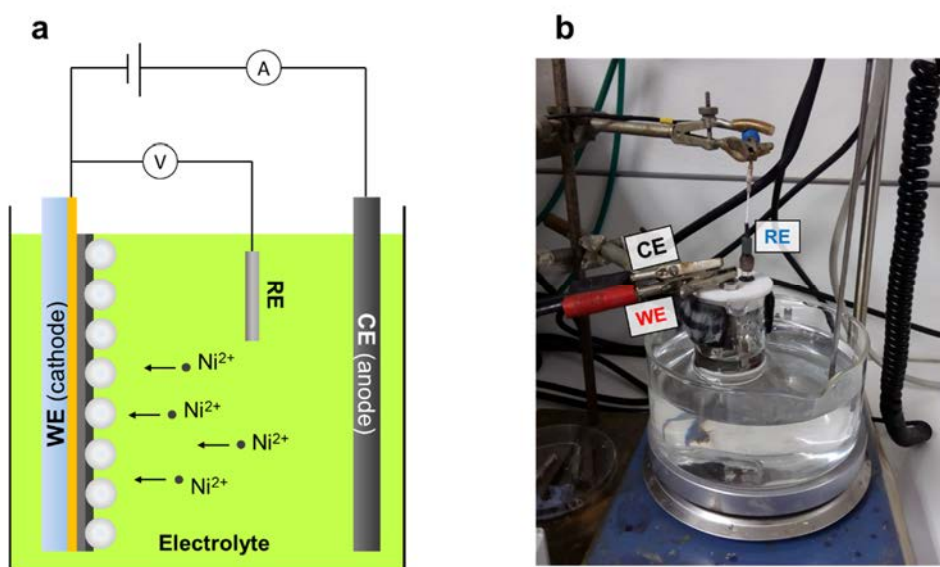
Figure 2.9 a Scheme of a three-electrode cell, mainly composed by an electrolyte, a working electrode (WE), counter electrode (CE) and referene electrode (RE). **b** Photograph of the experimental set up used in this thesis.

Electrodeposition presents several attributes that make it stand out over other deposition methods. Firstly, it can be performed over large areas at RT from water-based electrolytes. It enables a precise control of the composition, morphology and thickness of the deposits just by adjusting experimental parameters such as potential, time, temperature, pH, etc. Furthermore, since electrodeposition starts from the bottom of the substrate, it is an exceptional technique for plating curved surfaces or creating three-dimensional architectures.

In industry, electrodeposition is a well-established surface modification tool for improving properties such as wear resistance, hydrophobicity or passivation against corrosion.[52] Nowadays, with the increasing interest in miniaturized and complex

devices, electrodeposition offers a unique approach for building nanostructures from particles to films and hierarchical architectures.[9]

Of particular interest is the so-called template-assisted electrodeposition, where the deposit takes place through a micro- or nanopatterned structure. This approach limits the area for nucleation and growth, enabling a controlled structuring of the material. Commonly applied for the fabrication of nanowires through alumina membranes,[53] in the last years templated electrodeposition has emerged as an attractive complement for low-cost patterning techniques such as NIL and CL. Large-area arrays of magnetic nanodots, nanodendrite sensors or metal-dielectric nanowires for photocatalysis are some examples of its combination with NIL.[54-56] Furthermore, the metallic infiltration through colloidal crystals have led to intringuing geometries not achievable with top-down techniques such as metallic inverse opals, dendritic metamaterials or diabolo-like nanopillars among others.[18,57-60]

Following these latter results, in this work, we have applied the infiltration of metallic layers of gold and sacrificial nickel through colloidal and pillar-based templates for the fabrication of fishnet metamaterials. The technical details of the process are now described.

Prior to electrodeposition, we delimited the electroactive area with commercial nail varnish, on top of which no deposition would take place because of its insulating character. In this way, we avoided electroplating on unpatterned areas, ensuring the homogeneity of the deposition through the templates.

The electrodeposition step was carried out in a three-electrode cell, using the samples as working electrodes, a 3 mm thick glassy carbon plate (Alfa Aesar) as counter electrode and a Ag/AgCl electrode (3 M NaCl, Alvatek) as reference. The surface of the counter electrode was at least two times bigger than the working electrode to avoid a current flow limitation by the CE. Both, WE and CE were placed parallel to ensure a homogeneous growth across the surface. Commercial cyanide-free gold plating bath (Metalor ECF60) and nickel plating solution (Alfa Aesar, bright finish) were used as electrolytes. The temperature of the cell was controlled through a water bath set at 25 °C unless otherwise stated. The electric current flow was monitored using an Autolab PGSTAT 20 potentiostat (EcoChemie) working with the GPES 4.9 software.

Cyclic voltammetry was used to estimate the optimal reduction potentials on gold-coated glass substrates (Figure 2.10). From this analysis and following previous works, the reduction of Au^+/Au and Ni^{2+}/Ni was performed at constant potentials of -0.7 V and -0.9 V (vs Ag/AgCl), respectively.[61,62]
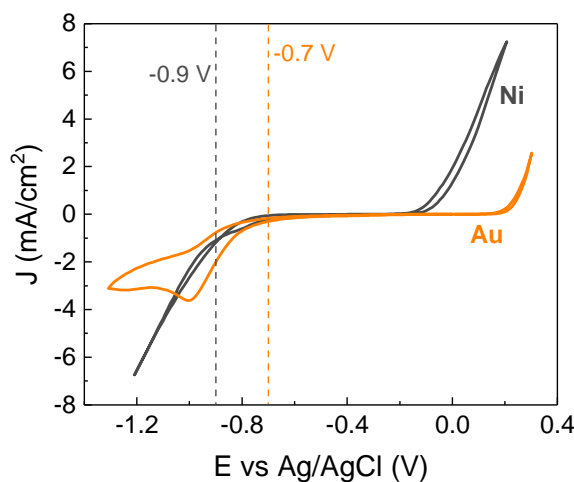
Figure 2.10 Cyclic voltammograms of gold and nickel solutions on gold-coated glasses as working electrodes. Dashed lines indicate the potentials used for electrodepositing gold and nickel.

2.5 Scanning electron microscopy

Scanning electron microscopy (SEM) has been extensively used in this work to observe the arrangement and dimensions of the submicron features. The collection of secondary and backscattered electrons has supplied essential information about the structures and the materials distribution.

We have mainly used two high-resolution SEM equipment depending on the laboratory where the experiments were being carried out: a JEOL 6700F or a Quanta FEI 200 FEG-ESEM microscope. In both cases, the acceleration voltage was kept between 5 and 10 kV, which avoided sample charging and provided clear surface information.

2.6 Optical characterization methods

The way a structure reflects, transmits, absorbs or emits light is of crucial importance in material science. These properties can provide deep information about the composition, arrangement or electromagnetic resonances of the structure. In other words, they allow for a deep understanding of physical and chemical phenomena

occurring within the material. In this thesis, three main techniques working at vis-NIR frequencies were used to characterize the optical properties of the samples.

2.6.1 Visible-infrared spectroscopy

The optical properties of the structures were mainly studied by recording vis-NIR transmittance and reflection spectra under normal incidence. Two commercial equipment were used depending on the current laboratory where the measurements were performed. In both cases, silver mirrors (≥ 96% reflectivity) and air were taken as references for reflectance and transmittance measurements, respectively.

In first place, we employed a CRAIC 2020 microspectrophotometer working with a 10x objective and a spatial aperture of 50 x 50 μm². Secondly, a Bruker Vertex 70 FTIR spectrophotometer attached to a Bruker Hyperion optical microscope was used. The spectra were recorded with a 4x objective, being the spot size 400 x 400 μm².

2.6.2 Angle-resolved spectroscopy

A home-built setup was used for measuring reflection at oblique angles of incidence θ (Figure 2.11). A tungsten halogen lamp (Ocean Optics, HL-2000 HP) was used as light source. After passing through a linear polarizer, the light was focused on the sample with a lens of numerical aperture (NA) of 0.125. The sample was mounted on a goniometer-coupled holder aligned to the rotation axis so that the sample surface was kept at the same position independently of the rotating angle. The reflected light was finally collected through a NA = 0.125 lens using a fiber-coupled spectrophotometer (Ocean Optics, QEPro-FL), placed in specular configuration.
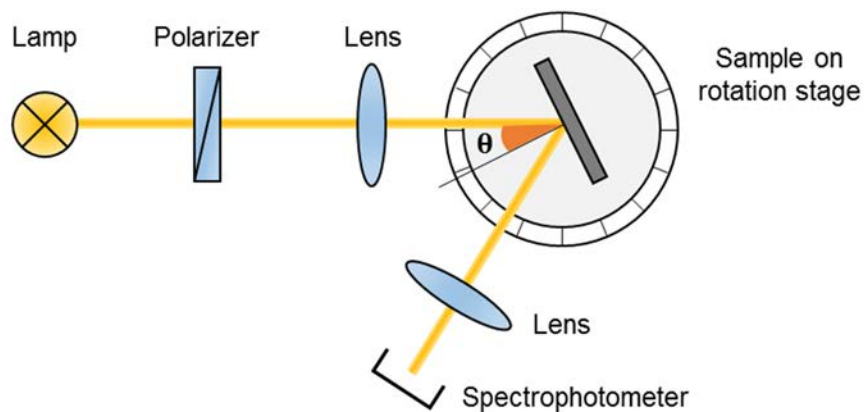
Figure 2.11 Scheme of the setup for angle-resolved reflectance measurements.

This setup was used in Chapter 4 for characterizing the angular response of multilayered fishnet metamaterials made by NIL and electrodeposition.

2.6.3 Time-resolved fluorescence microscopy

We used a custom-made setup for measuring the fluorescence decays of the plasmonic structures developed in Chapter 5 (Figure 2.12). Pulses of 70 ps width from a laser operating at 654 nm (EPL-Edinburgh Instrument) provided the excitation light. Keeping the peak power at 120 mW, the repetition rate was varied between 1 kHz and 1 MHz to get a proper signal/noise ratio. The pulses were directed to the sample through a dichroic mirror and a 100x objective with NA = 0.9 (Zeiss EC Epiplan-Neofluar, 422392-9900). The emitted signal was then collected through the same objective and sent to the detector (ID Quantique, ID100 single detection module) through two emission filters (Omega, 710QM80 and Semrock, 664 nm RazorEdge ultrasteep long-pass edge filter, LP02-664RU-25). The detector was equipped with a Time Correlated Single Photon Counting (TCSPC) Card (ID Quantique, ID800) registering photons one by one in order to reconstruct the decay profiles afterwards.
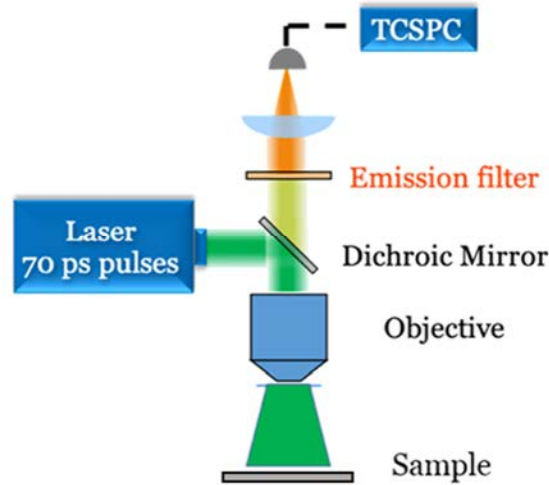
Figure 2.12 Scheme of the experimental setup for fluorescence decay measurements.

2.7 Finite-difference time-domain simulations

The optical response of the structures has been simulated by finite-difference time-domain (FDTD) calculations. FDTD is a well-extended method for solving Maxwell's equations over time in a given volume. Over the last decade, it has become a powerful tool in computational electromagnetism because of its robust implementation and easy handling of composite geometries and materials.[63,64]

The FDTD method discretises Maxwell's equations on a spatial and temporal grid using central difference approximations. Firstly, the technique divides three-dimensional

geometries into a mesh composed by the so-called Yee cells (Figure 2.13). In these rectangular or cubic units, the location of the electric and magnetic field components satisfy classical boundary conditions. The fields are then calculated at discrete time steps with a leapfrog algorithm. This means that the electric field is solved at a given instant, then the magnetic field at the next time instant, and the process is repeated until reaching an electromagnetic steady-state.
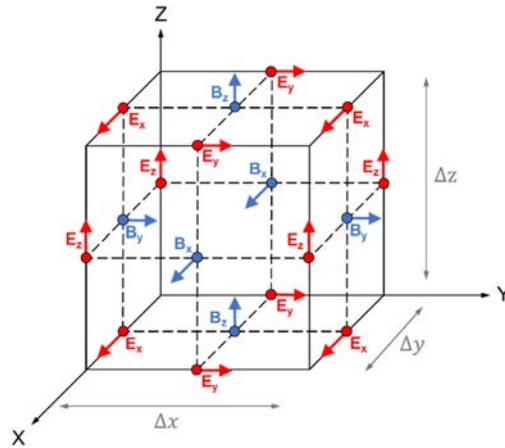
Figure 2.13 Position of the electric and magnetic field components in a Yee cell.

The spatial mesh size ($\Delta x,\Delta y,\Delta z$) should be fine enough to well reproduce the structure, considering both the geometry and the electromagnetic parameters of the materials. Although the proper mesh depends on the smallest feature size and vary for each system, when working with plasmonic structures at optical wavelengths a minimum resolution of 10 nm is typically required. Moreover, the time step (Δt) should satisfy the Courant condition for numerical stability:

$$c\Delta t \leq \frac{1}{\sqrt{\frac{1}{\Delta x^2} + \frac{1}{\Delta y^2} + \frac{1}{\Delta z^2}}} \tag{2.1}$$

where c is the speed of light in vacuum. One should not forget that high resolutions come at the costs of large memory requirements and simulation times. Therefore, if similar results are obtained for different mesh sizes, it is advisable to use the larger one.

The simulations shown in this manuscript were done using the Lumerical FDTD solutions software. The structural dimensions were based of the SEM analysis and more precisely fitted to the optical spectra. Mesh sizes between 2 and 5 nm were used to resolve the modelled structures, while the program automatically adjusted the time step

to avoid instabilities. Thanks to the periodicity of the systems, memory and time were saved through EM (anti)symmetric boundary conditions on the sides of the simulation. Perfectly matched layers were placed above the structure and on the semi-infinite substrate to absorb the incoming light with minimal reflections. After illuminating the system with a linearly polarized planar wave, reflection and transmission coefficients were collected through power monitors. Similarly, profile monitors were included to obtain electromagnetic field distributions at a given wavelength. For the angular dispersion calculations, the broadband fixed angle source technique was used. In general, the calculations stopped when the energy in the simulation volume dropped to 5×10^{-7} of the energy injected.

Regarding the materials modelling, the gold dispersion was taken from Johnson and Christy,[65] nickel from Palik[66] and ITO from Sopra SA database (France). The dielectric materials were considered to have constant refractive indices of 1.46 for silica glass, 1.59 for polystyrene and 1.65 for SU8.

2.8 References

1.   U. K. Chettiar et al. Dual-band negative index metamaterial: Double negative at 813 nm and single negative at 772 nm. *Opt. Lett.* **2007**, *32*, 1671–1673.

2.   G. Dolling, M. Wegener and S. Linden. Negative-index metamaterial at 780 nm wavelength. *Opt. Lett.* **2007**, *32*, 53–55.

3.   S. Xiao, U. K. Chettiar, A. V Kildishev, V. P. Drachev and V. M. Shalaev. Yellow-light negative-index metamaterials. *Opt. Lett.* **2009**, *34*, 3478–3480.

4.   C. García-Meca et al. Low-loss multilayered metamaterial exhibiting a negative index of refraction at visible wavelengths. *Phys. Rev. Lett.* **2011**, *106*, 67402.

5.   M. Choi, J. H. Choe, B. Kang and C. Choi. A flexible metamaterial with negative refractive index at visible wavelength. *Curr. Appl. Phys.* **2013**, *13*, 1723–1727.

6.   Y. Liang, Z. Yu, N. Ruan, Q. Sun and T. Xu. Freestanding optical negative-index metamaterials of green light. *Opt. Lett.* **2017**, *42*, 3239–3242.

7.   A. M. Urbas et al. Roadmap on optical metamaterials. *J. Opt.* **2016**, *18*, 093005.

8.   G. Yoon, I. Kim and J. Rho. Challenges in fabrication towards realization of practical metamaterials. *Microelectron. Eng.* **2016**, *163*, 7–20.

9.   F. Nasirpouri. *Electrodeposition of nanostructured materials*; Springer, Switzerland, 2017.

10.   M. A. Boles, M. Engel and D. V. Talapin. Self-assembly of colloidal nanocrystals: From intricate structures to functional materials. *Chem. Rev.* **2016**, *116*, 11220–11289.

11.   Y. Wang, M. Zhang, Y. Lai and L. Chi. Advanced colloidal lithography: From patterning to applications. *Nano Today* **2018**, *22*, 36–61.

12.   X. Liang, R. Dong and J. C. Ho. Self-assembly of colloidal spheres toward fabrication of hierarchical and periodic nanostructures for technological applications. *Adv. Mater. Technol.* **2019**, *4*, 1800541.

13.   Y. S. Lee. *Self-assembly and nanotechnology: A force balance approach*; John Wiley & Sons, USA and Canada, 2008.

14.   Z. Xu, L. Wang, F. Fang, Y. Fu and Z. Yin. A review on colloidal self-assembly and their applications. *Curr. Nanosci.* **2016**, *12*, 725–746.

15.   H. Zheng and S. Ravaine. Bottom-up assembly and applications of photonic materials. *Crystals* **2016**, *6*, 54.

16.   P. Gao et al. Large-area nanosphere self-assembly by a micro-propulsive injection method for high throughput periodic surface nanotexturing. *Nano Lett.* **2015**, *15*, 4591–4598.

17.   N. Vogel, S. Goerres, K. Landfester and C. K. Weiss. A convenient method to produce close- and non-close-packed monolayers using direct assembly at the air-water interface and subsequent plasma-induced size reduction. *Macromol. Chem. Phys.* **2011**, *212*, 1719–1734.

18.   H. Zheng et al. Morphological design of gold nanopillar arrays and their optical properties. *J. Phys. Chem. C* **2016**, *120*, 1178–1185.

19.   Z. Dai, Y. Li, G. Duan, L. Jia and W. Cai. Phase diagram, design of monolayer binary colloidal crystals, and their fabrication based on ethanol-assisted self-assembly at the air/water interface. *ACS Nano* **2012**, *6*, 6706–6716.

20.   J. L. Russell, G. H. Noel, J. M. Warren, N. L. L. Tran and T. E. Mallouk. Binary colloidal crystal films grown by vertical evaporation of silica nanoparticle suspensions. *Langmuir* **2017**, *33*, 10366–10373.

21.   T. Ding, K. Song, K. Clays and C.-H. Tung. Fabrication of 3D photonic crystals of ellipsoids: Convective self-assembly in magnetic field. *Adv. Mater.* **2009**, *21*, 1936–1940.

22.   L. Rossi et al. Cubic crystals from cubic colloids. *Soft Matter* **2011**, *7*, 4139–4142.

23.   L. Song, X. Du, L. Zhong, X. Zhang and Z. Cheng. Self-assembly of anisotropic red blood cell (RBC)-like colloidal particles. *Soft Matter* **2018**, *14*, 7954–7957.

24.   L. Song et al. Non-close-packed particle arrays based on anisotropic red blood cell (RBC) like particles via stretching deformation method. *Langmuir* **2019**, *35*, 9044–9049.

25.   K. Lodewijks, N. Verellen, W. Van Roy, G. Borghs and P. Van Dorpe. Self-assembled hexagonal double fishnets as negative index materials. *Appl. Phys. Lett.* **2011**, *98*, 091101.

26.   B. Gong et al. A visible metamaterial fabricated by self-assembly method. *Sci. Rep.* **2014**, *4*, 4713.

27.   S. Mariana et al. Vertical GaN nanowires and nanoscale light-emitting-diode arrays for lighting and sensing applications. *ACS Appl. Nano Mater.* **2019**, *2*, 4133–4142.

28.   P. Xue et al. Ordered micro/nanostructures with geometric gradient: From integrated wettability "library" to anisotropic wetting surface. *Small* **2017**, *13*, 1601807.

29.   X. Zhang et al. Ultrasensitive SERS performance in 3D "sunflower-like" nanoarrays decorated with Ag nanoparticles. *Nanoscale* **2017**, *9*, 3114–3120.

30.   Y. Zhang et al. Flexible and highly sensitive pressure sensor based on microdome-patterned PDMS forming with assistance of colloid self-assembly and replica technique for wearable electronics. *ACS Appl. Mater. Interfaces* **2017**, *9*, 35968–35976.

31.   G. D. Moon et al. Assembled monolayers of hydrophilic particles on water surfaces. *ACS Nano* **2011**, *5*, 8600–8612.

32.   A. Désert et al. High-yield preparation of polystyrene/silica clusters of controlled morphology. *Polym. Chem.* **2012**, *3*, 1130.

33.   S. Y. Chou, P. R. Krauss and P. J. Renstrom. Imprint of sub-25 nm vias and trenches in polymers. *Appl. Phys. Lett.* **1995**, *67*, 3114.

34.   W. Zhou. *Nanoimprint lithography: An enabling process for nanofabrication*; Springer, Germany, 2013.

35.   D. Wu, N. S. Rajput and X. Luo. Nanoimprint lithography - the past, the present and the future. *Curr. Nanosci.* **2016**, *12*, 712–724.

36.   C. Schuster, F. Reuther, A. Kolander and G. Gruetzner. mr-NIL 6000LT-epoxy-based curing resist for combined thermal and UV nanoimprint lithography below 50 °C. *Microelectron. Eng.* **2009**, *86*, 722–725.

37.   A. Espinha et al. Hydroxypropyl cellulose photonic architectures by soft nanoimprinting lithography. *Nat. Photonics* **2018**, *12*, 343–348.

38.   Y. Jiang, B. Luo and X. Cheng. Enhanced thermal stability of thermoplastic polymer nanostructures for nanoimprint lithography. *Materials.* **2019**, *12*, 545.

39.   B. Jeong et al. Polymer-assisted nanoimprinting for environment- and phase-stable perovskite nanopatterns. *ACS Nano* **2020**, *14*, 1645–1655.

40.   I. Bergmair et al. Single and multilayer metamaterials fabricated by nanoimprint lithography. *Nanotechnology* **2011**, *22*, 325301.

41.   D. Chanda et al. Large-area flexible 3D optical negative index metamaterial formed by nanotransfer printing. *Nat. Nanotechnol.* **2011**, *6*, 402–407.

42.   L. Gao et al. Nanoimprinting techniques for large-area three-dimensional negative index metamaterials with operation in the visible and telecom bands. *ACS Nano* **2014**, *8*, 5535–5542.

43.   A. Mihi, F. J. Beck, T. Lasanta, A. K. Rath and G. Konstantatos. Imprinted electrodes for enhanced light trapping in solution processed solar cells. *Adv. Mater.* **2014**, *26*, 443–448.

44.   X. Chen and L. Zhang. Review in manufacturing methods of nanochannels of bio-nanofluidic chips. *Sensors Actuators B Chem.* **2018**, *254*, 648–659.

45.   S. Lochmann et al. Nanoimprint lithography of nanoporous carbon materials for micro-supercapacitor architectures. *Nanoscale* **2018**, *10*, 10109–10115.

46.   H. Schift. Nanoimprint lithography: An old story in modern times? A review. *J. Vac. Sci. Technol. B Microelectron. Nanom. Struct. Process. Meas. Phenom.* **2008**, *26*, 458–480.

47.   M. C. Traub, W. Longsine and V. N. Truskett. Advances in nanoimprint lithography. *Annu. Rev. Chem. Biomol. Eng.* **2016**, *7*, 583–604.

48.   B. Kwon and J. H. Kim. Importance of molds for nanoimprint lithography: Hard, soft, and hybrid molds. *J. Nanosci.* **2016**, *2016*, 6571297.

49.   N. Kooy, K. Mohamed, L. Pin and O. Guan. A review of roll-to-roll nanoimprint lithography. *Nanoscale Res. Lett.* **2014**, *9*, 320.

50.   S. Hosaka. *Updates in advanced lithography*; IntechOpen, Rijeka, Croatia, 2013.

51.   T. W. Odom, J. C. Love, D. B. Wolfe, K. E. Paul and G. M. Whitesides. Improved pattern transfer in soft lithography using composite stamps. *Langmuir* **2002**, *18*, 5314–5320.

52.   N. Kanani. *Electroplating: Basic principles, processes and practice*; Elsevier, Berlin, Germany, 2004.

53.   D. Wang, A. Mukhtar, K. Wu, L. Gu and X. Cao. Multi-segmented nanowires: A high tech bright future. *Materials.* **2019**, *12*, 3908.

54.   C. H. Lee et al. Fabrication and characterization of Co-Pt nanodot arrays by nanoimprint lithography and electrodeposition. *Microelectron. Eng.* **2010**, *87*, 2085–2090.

55.   S. Wang et al. Space-confined fabrication of silver nanodendrites and their enhanced SERS activity. *Nanoscale* **2013**, *5*, 4284–4290.

56.   H. Eom et al. Strong localized surface plasmon resonance effects of Ag/TiO$_2$ core–shell nanowire arrays in UV and visible light for photocatalytic activity. *Nanoscale* **2014**, *6*, 226–234.

57.   N. Sapoletova et al. Controlled growth of metallic inverse opals by electrodeposition. *Phys. Chem. Chem. Phys.* **2010**, *12*, 15414–15422.

58.   X. Zhao. Bottom-up fabrication methods of optical metamaterials. *J. Mater. Chem.* **2012**, *22*, 9439–9449.

59.   A. Karajić et al. Bottom-up generation of miniaturized coaxial double electrodes with tunable porosity. *Adv. Mater. Interfaces* **2015**, *2*, 1500192.

60.   A. Ngamaroonchote, T. Muangnapoh, N. Aroonyadet, P. Kumnorkaew and R. Laocharoensuk. Plasma-etched nanosphere conductivity-inverted lithography (PENCIL): A facile fabrication of size-tunable gold disc array on ITO-coated glass. *Adv. Mater. Interfaces* **2018**, *5*, 1800477.

61.   A. Karajić. Development of electrode architectures for miniaturized biofuel cells, University of Bordeaux, 2015.

62.   H. Zheng. Design and bottom-up fabrication of nanostructured photonic / plasmonic materials, University of Bordeaux, 2016.

63.   K. Yee. Numerical solution of initial boundary value problems involving Maxwell's equations in isotropic media. *IEEE Trans. Antennas Propag.* **1966**, *14*, 302–307.

64.   A. Z. Elsherbeni and V. Demir. *The finite-difference time-domain method for electromagnetics with matlab simulations*, 2nd ed.; SciTech Publishing, United States, 2015.

65.   P. B. Johnson and R. W. Christy. Optical constants of the noble metals. *Phys. Rev. B* **1972**, *6*, 4370–4379.

66.   E. D. Palik. *Handbook of optical constants of solids*; Academic Press, Boston, 1998.

Chapter 3

Fishnet metamaterials made by colloidal lithography

3.1 Introduction

In the recent years, self-assembly has emerged as a stimulating approach for the mass production of metamaterials thanks to the easy and low-cost processesing. The rational organization of subwavelength building blocks can give rise to unconventional electromagnetic properties at visible and NIR frequencies without the need of expensive and time consuming top-down lithographic techniques.[1–3]

Self-assembly enables the synthesis of colloidal nanoresonators, which are subwavelength elements formed by the controlled organization of metallic nanoparticles into complex clusters. These systems are commonly studied for achieving phenomena such as cloaking,[4] optical magnetism,[5] negative refractive index[6] or chirality.[7] The fabrication of self-assembled metamaterials directly on surfaces is also feasible by approaches such as block copolymer organization. In this case, different patterns are within reach by adjusting the volume fraction of the polymers involved in the composite. The resulting templates can be lately employed for the fabrication of chiral,[8,9] tunable refractive index[10] or hyperbolic metamaterials.[11] In the same way, colloidal lithography supports the formation of highly ordered and complex architectures such as the ones needed in periodic metamaterials.

For instance, the spherical particles typically used in CL have attracted great interest in developing circular SRRs over large surfaces. By using colloidal monolayers as shadow masks, SRRs operating at the NIR have been achieved when depositing metals by thermal evaporation[12] or electrodeposition.[13] Similar approaches have served for the creation of elliptical shapes[14] or even 3D systems by stacking several layers of split rings.[15] Metallic dendritic designs have been also reported as left-handed metamaterials with an entirely bottom-up route such as CL and electrochemical deposition.[16,17]

Furthermore, nanosphere lithography has been proposed as an alternative route for the fabrication of fishnet metamaterials motivated by the large area, inexpensive and fast character of the approach. Lodewijks et al. showed the feasibility of using nanosphere lithography for NIMs working at NIR frequencies with refractive indices up to -1.4 and FOM of the order of 1.[18] However, their process still implied subsequent ion beam milling that hindered the scalability of their method. Less complex procedures were based on the direct MIM deposition onto the beads, which acted as masks and led to holey fishnet structures after their removal.[19] Gong et al. reported a bottom-up method based on electroplating silver films through PS monolayers working as templates.[20] The structures showed a minimum refractive index of -0.5 at 560 nm. Further works included a gain medium within the same metamaterial to compensate the optical losses coming from the metal absorption at these frequencies.[21] However, these last designs suffered from lateral misalignment of the holes in the metallic layers, inhibiting the achievement of both strong negative index values and high FOMs.
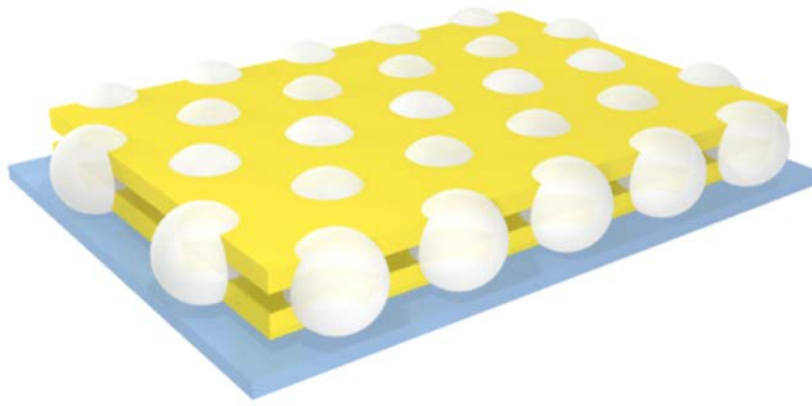
Figure 3.1 Illustration of the proposed double fishnet structure based on colloidal lithography.

In this chapter, we present a new fishnet design based on such bottom-up combination of colloidal lithography and electrodeposition, two well-known scalable and low-cost techniques. The proposed scheme follows the basic geometry of a double fishnet structure (Figure 3.1). It is composed by two gold layers separated by an air gap and symmetrically perforated by a monolayer of polystyrene spheres on top of a glass substrate. We study the dependence of the optical response on structural parameters such as the diameter of the particles and the air gap width in between the metallic layers. The possibility of tuning the effective refractive index by properly controlling these structural dimensions is explored.

3.2   Tuning the effective refractive index

As described in Chapter 1, the electric and magnetic responses of a metamaterial depend on the shape, size and materials of which it is made. The fishnet design allows and independent control of the permittivity and the permeability at a specific wavelength.[22] In the effective medium approximation, the electric response can be described from holey metallic layers, where the metal plasma frequency is replaced by the cut-off frequency of the fundamental mode of a hole waveguide.[23] This value determines the maximum wavelength at which the electric field is guided through the holes. For wavelengths above the cut-off wavelength λ_c, SPP waves dominate the propagation through the structure and the effective permittivity becomes negative.[24,25] In the case of circular holes, λ_c depends on the diameter D and the refractive index n_a of the apertures.[26]

$$\lambda_c = \frac{\pi D}{1.841} n_a \qquad (3.1)$$

Two regimes can be found concerning this value:[24] as long as λ_c is higher than the lattice parameter L of the structure, a decrease of the diameter will involve more negative ε_{eff} and therefore, more negative n_{eff}. However, if λ_c becomes smaller than L, the light will not effectively couple to the periodic structure and less negative values will be obtained. For this reason, the following studies have focused on the first situation, this is, on diameters D sufficiently large so that $\lambda_c > L$.

The magnetic behavior is induced by the excitation of gap surface plasmons within the MIM cavity. If the metallic layers are sufficiently close, the SPPs propagating at the internal faces will interact due to the overlapping of their evanescent fields, creating a GSP.[27] For two non-perforated metallic films of thickness t separated by a dielectric width w, the GSP dispersion relation at low frequencies can be described by the linear approximation[28,29]

$$k_{GSP} = k_0 n_d \left[\frac{w}{w + 2\lambda_p \coth\left(\frac{2\pi t}{\lambda_p}\right)} \right]^{-1/2} \qquad (3.2)$$

where k_0 is the vacuum wave vector, n_d the refractive index of the dielectric spacer and λ_p the plasma wavelength of the metal. Even though this equation corresponds to flat and continuous layers, the dispersion when considering an array of holes perforating

the films presents a similar dependence.[30] In fact, GSPs may be generated only if the momentum matching is satisfied, which in the fishnet design can be achieved thanks to the grating structure. An interesting property of these cavities is the dependence of the resonant wavelength with the width *w* of the dielectric spacer. Considering a structure where all the other parameters remain constant and the light impinges at normal incidence, the GSP excitation wavelength λ_0 can be expressed as:

$$\lambda_0 = A\left(1 + \frac{B}{w}\right)^{1/2} \tag{3.3}$$

where *A* and *B* are constants depending on the geometrical parameters and the materials that compose the structure. It is therefore expected that λ_0 increases when decreasing the dielectric width *w*.
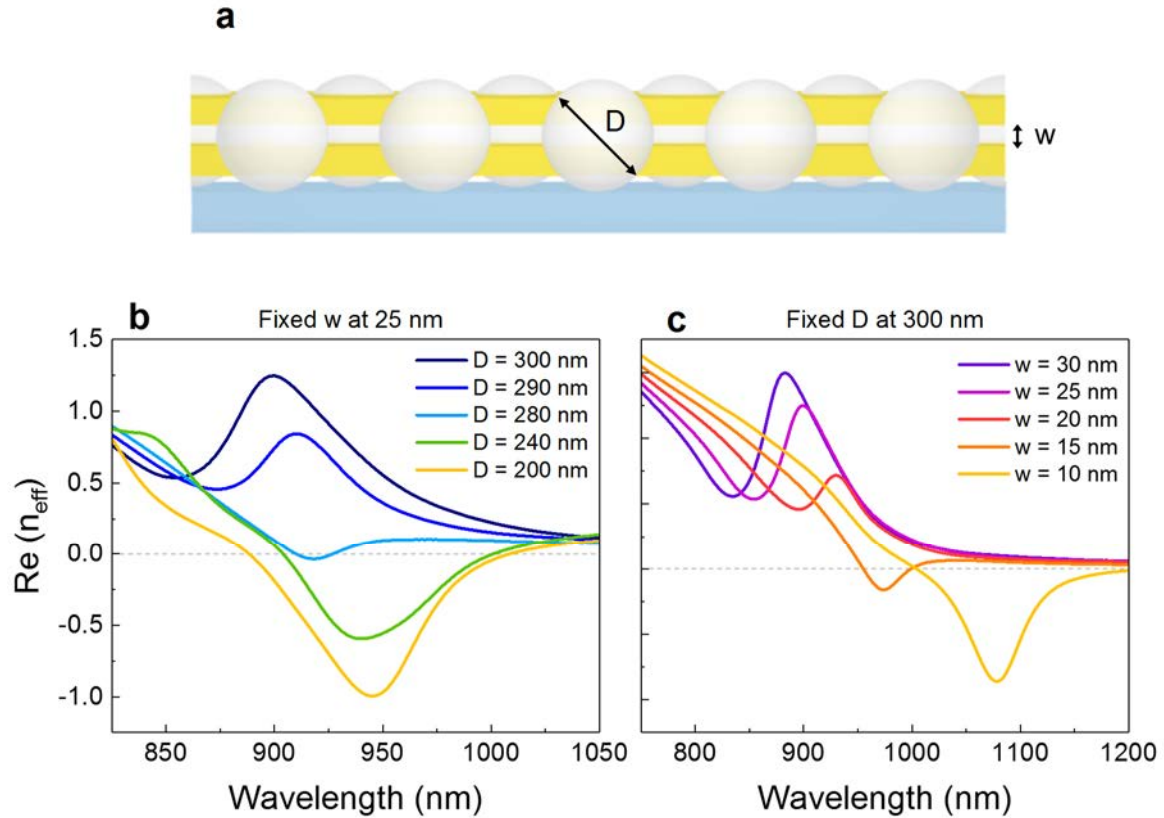
Figure 3.2 a Cross-sectional scheme of the modelled fishnet metamaterial, where *D* denotes the diameter of the spheres and *w* the gap width separating the metallic layers. Simulations of the real part of the effective refractive index when varying **b** the diameter of particles and **c** the air gap width.

In the light of these discussions, numerical simulations were performed by FDTD to study the evolution of the effective refractive index n_{eff} when tuning two main parameters of our design: the diameter of the beads and the air gap width (Figure 3.2a).

The structure was considered to have a lattice spacing L of 480 nm, two 50 nm thick gold layers and to be placed on top of a semi-infinite glass substrate. The refractive index of PS was taken as n_{PS} = 1.59. The real parts of n_{eff} for different diameters and gap widths are plotted in Figure 3.2b and c, respectively. As can be observed, by separately tuning one of the two parameters, the value of the refractive index changes, moving from positive to negative and red shifting when decreasing either D or w. In particular, small decreases in w produce large redshifts of the operating wavelength of the structure, in accordance with equation (3.3) and previous studies.[31] The lowering of n_{eff} when decreasing w can be explained as an enhancement of the GSP coupling as the gold layers come closer. On the other hand, reductions in D primarily result in more negative values of n_{eff}, in agreement with the above discussion. Therefore, the sizes of D and w act as turning knobs that enable the achievement of metamaterials featuring positive, zero and negative refractive indices.

3.3 Fabrication of double fishnet metamaterials by colloidal lithography

Double-fishnet structures were fabricated over centimeter-sized areas by a complete bottom-up route, based on the combination of colloidal lithography and electrodeposition. Figure 3.3 summarizes the whole fabrication procedure, which will be explained in detail throughout the following sections.
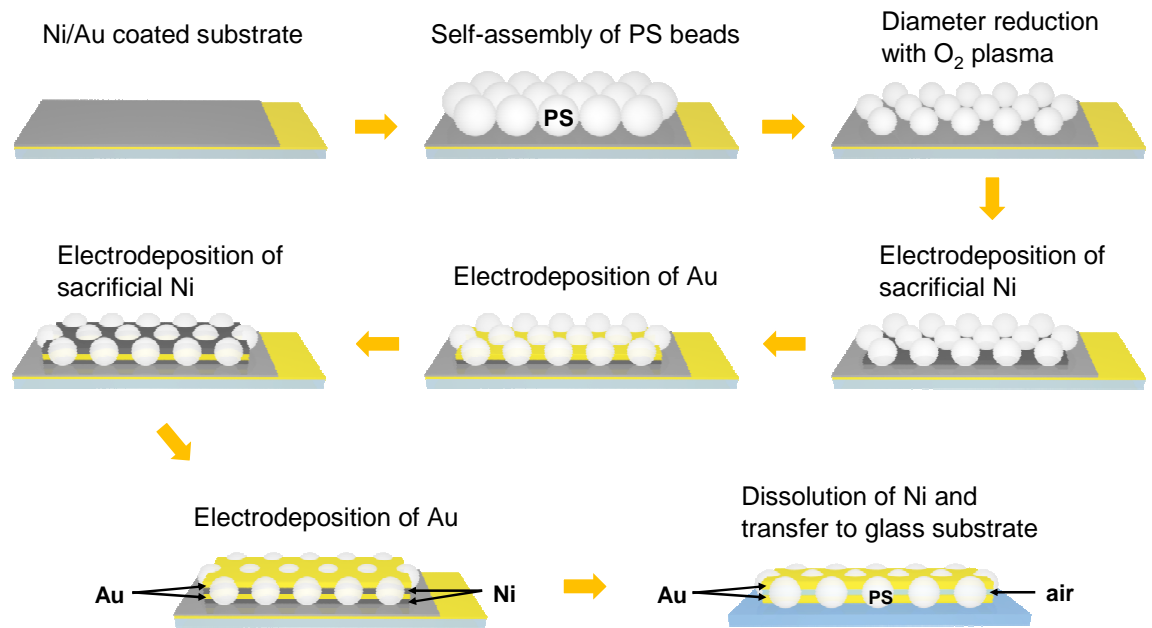

Figure 3.3 Scheme of the bottom-up fabrication process to obtain double fishnet metamaterials.

3.3.1 Preparation of non-closed-packed templates

Closed-packed monolayers of 480 large PS spheres were prepared on nickel-plated gold-coated substrates following the self-assembly procedure described in Chapter 2. We chose such diameter because of the high quality of the formed monolayers and relatively small size, which would give an optical response in the visible-NIR range. The conductive surfaces will serve as working electrodes during the electrodeposition step as will be explained in Section 3.3.2.

Since the fishnet structure is composed by isolated dielectric perforations, the particles diameter had to be reduced while keeping the original lattice parameter of the array. Being an organic material, polystyrene can be easily etched by an oxygen plasma treatment. The oxygen ions and radicals in the plasma react with the polymer leading to volatile products that are then removed by the vacuum system.[32] Therefore, it is possible and easy to obtain non-closed-packed colloidal templates by varying the diameter of PS spheres with plasma parameters such as etching time, power or gas flux.
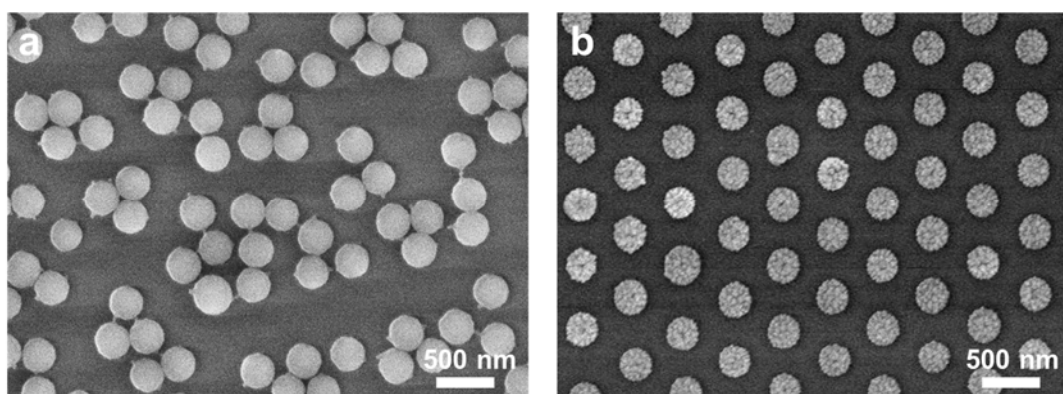
Figure 3.4 Comparison of the particles position after etching when the substrate is placed at **a** RT and **b** -15 ⁰C.

Conserving the periodic order of the array is a crucial aspect when doing colloidal lithography. If the particles move or detach from the substrate during the plasma treatment, the final properties coming from the grating will be lost. Thermal annealing prior to plasma etching can help to increase the contact area with the substrate and well fix the particles.[33] Another important aspect to consider is the substrate temperature during the process.[34] An uncontrolled temperature not only can affect the reliability of the experiments but also softens and plastically deforms the particles, which combined with large size reductions leads to a displacement from the original position[35] as can be observed in Figure 3.4a. On the other hand, under a controlled and sufficiently low

temperature, the particles stay rigid and keep their initial place as presented in Figure 3.4b.

For these reasons, before the plasma etching, the samples were sintered in a conventional oven for 1 hour at 90 ⁰C, slightly below the glass transition temperature of polystyrene (T_g = 107 ᵒC).[36] This short step helped to mechanically consolidate the PS array, it did not modify their shape but rather increased the contact area with the substrate and fixed their position. The diameter was then reduced by an isotropic oxygen plasma etching using a Plasma Etch PE100 equipment, at ElorprintTec facilities. The working conditions were 10 sccm flow of O_2, a plasma power of 80 W and a cooling temperature of the sample stage of -15 ⁰C. Figure 3.5 illustrates the evolution of the particles diameter with processing time and how the initial periodicity of the array is kept even for approximately 40% smaller particles. The samples were finally rinsed with distilled water to remove the eventual organic residues that could remain on the surface.
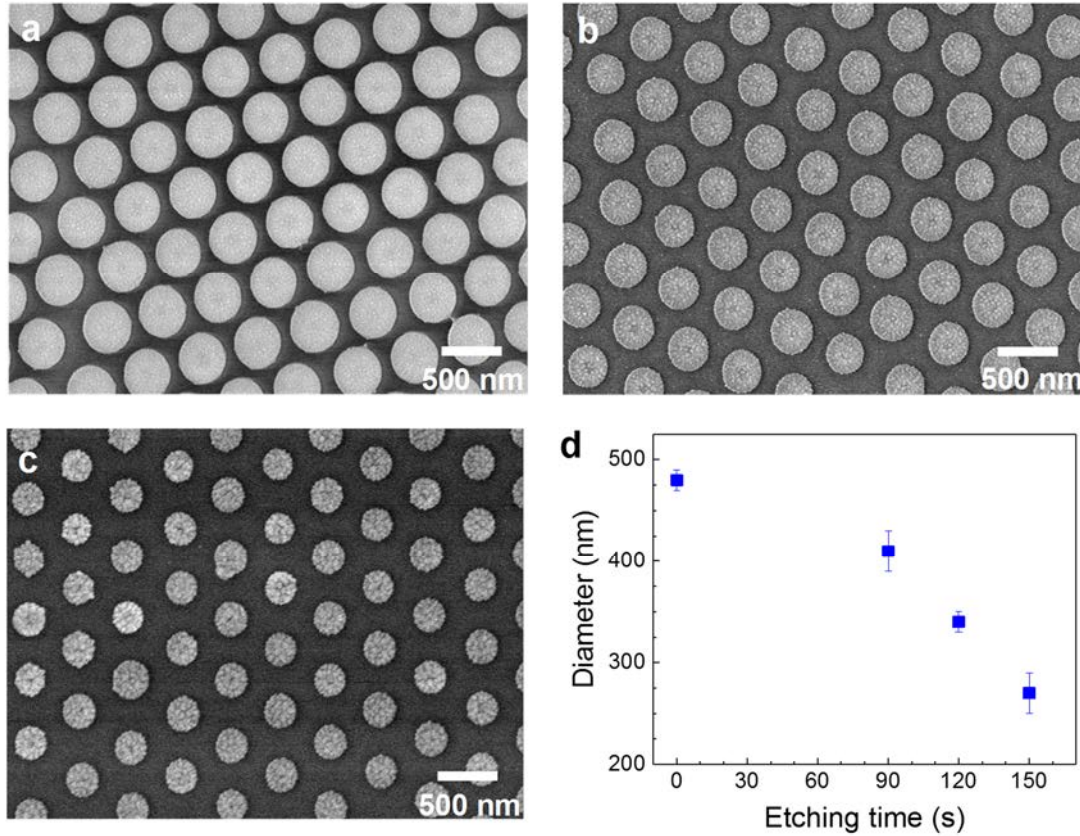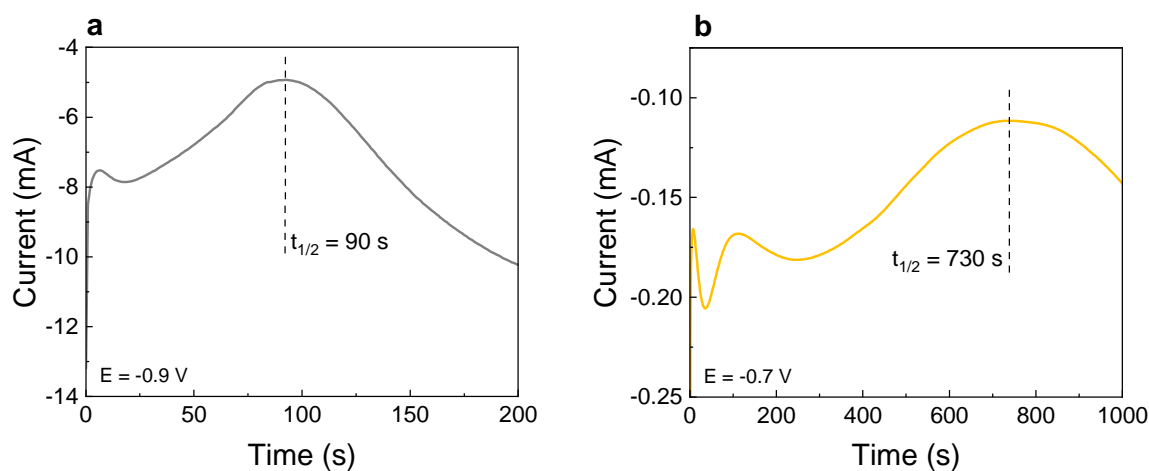

Figure 3.5 SEM images of non-closed-packed monolayers of PS beads after etching times of **a** 90 s, **b** 120 s and **c** 150 s. **d** Evolution of the particles diameter with the oxygen plasma etching duration.

3.3.2 Multilayer electrodeposition through a colloidal template

The double-fishnet geometry was accomplished by electrodepositing gold layers through the non-closed-packed monolayer templates. Sacrificial nickel layers were as well electrodeposited in between serving as supports and spacers for the gold layers.

A very interesting property of combining electrodeposition and CL is the on-time control of the electrodeposited thickness. Under a constant potential, the electric current varies accordingly with the electroactive area: larger areas imply higher electrodeposition currents flowing through the electrolytic cell. Therefore, the deposited thickness through three-dimensional templates such as ours can be determined by monitoring the current variations.[37,38] Such phenomenon was initially verified by electrodepositing nickel and gold through closed-packed monolayers of 480 large PS spheres. As can be observed in Figure 3.6, after some initial fluctuations, the current reaches a minimum in absolute value. This stage is linked with the smallest electroactive area where the ions reduction occurs, which corresponds with half the height of the monolayer. Knowing the time that takes to deposit half a monolayer and assuming a constant electrodeposition rate, one could calculate the time required for any desired thickness.

Figure 3.6 Chronoamperometric curves of **a** nickel and **b** gold electrodeposition through a closed-packed monolayer of 480 nm large polystyrene particles.

However, this behavior was not observed for non-closed-packed arrays. The absence of current variations was attributed to the small difference in cross-sectional area across the template height. When the diameter is reduced, the particles are no longer touching each other, the space between them becomes larger and the transversal area does not change sufficiently so that a current variation is observed. It was then

considered that the metals grew approximately at the same rate as on an open surface. The deposition rate for both metals was determined by SEM on gold-coated substrates, being 0.97 ± 0.09 nm/s for nickel reduced at -0.9 V, and 0.34 ± 0.03 nm/s for gold reduced at -0.7 V. The slow deposition rates allowed us to finely control the thickness of each metallic layer.

In order to obtain the targeted symmetric structure (Figure 3.7), the thickness of the first nickel layer x was adjusted according to the relation between the height h of the monolayer and the desired thicknesses for the gold layers y and the nickel spacer z.

$$x = \frac{h - 2y - z}{2} \tag{3.4}$$
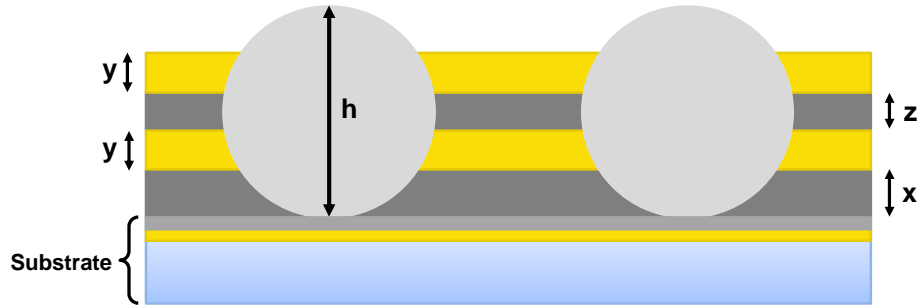
Figure 3.7 Scheme of the targeted multilayered structure surrounding the colloidal template.

A short sintering step of 102 ^{0}C for 15 min was always done before the process in order to improve the adhesion of the particles and ensure that they stayed fixed at their positions during the electroplating. Lower temperatures might have implied longer sintering treatments whereas with higher temperatures we risked to considerably deform the particles because of the proximity to the polystyrene T_g. Without this mechanical adhesion, while the deposition occurred, the metallic layers could push up the particles because of their low density.[39]

Subsequent electrodeposition of nickel, gold, nickel and gold through the PS templates produced two 50 nm thick gold layers, symmetrically placed regarding the equatorial axes of the monolayer and separated by a variable sacrificial nickel spacer. Figure 3.8 presents the multilayered structure after the whole electrodeposition process over a template of etched spheres with D = 340 nm. One can clearly distinguish the PS particles embedded in a nickel-gold stack, while preserving the high quality of the periodic array over centimeter-sized areas. These images attest to the successful multi-

electrodeposition through colloidal templates, without damaging the structure and accurately controlling the thickness and position of each metallic layer.
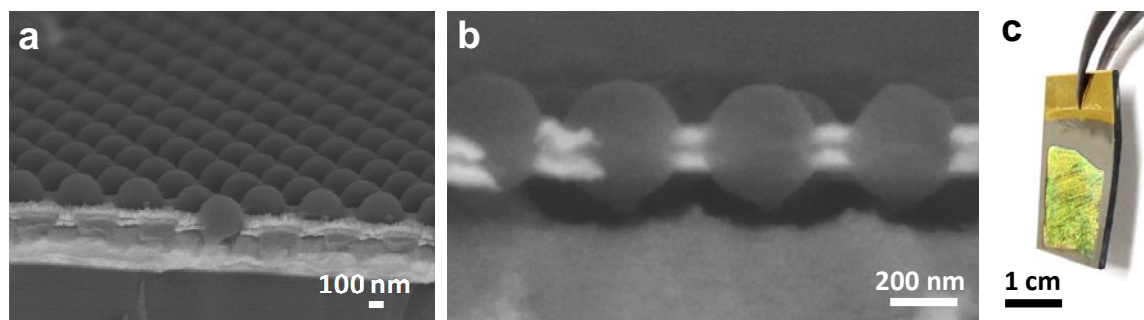
**Figure 3.8 a** SEM image of a multilayered nanostructure composed by 340 nm large PS particles, two 50 nm thick Au layers symmetrically placed and a 70 nm thick Ni spacer separating them. **b** Close-up view of the same structure. **c** Photograph of the sample, where the iridescent region corresponds to the multilayered grating.

3.3.3 Nickel dissolution and transfer to transparent substrate

Once we created a multilayered structure through non-closed-packed templates, the last step was to dissolve the nickel parts. Such removal is needed to achieve the proper designed fishnet metamaterial, where the MIM structure is composed of gold-air-gold. To fully characterize, understand and make them suitable for practical applications, the samples should be placed on a transparent surface. For this purpose, we planned to detach the fishnet structures from the current substrate, transfer them to water and recover them with a glass slide as we initially did with just the monolayer. This is the reason why our substrates were initially plated with a 400 nm thick Ni layer. When chemically etching the nickel parts, the top layer of the substrate may be also dissolved and the sample can be detached.

Nickel parts were removed by immersion in 10 wt% nitric acid (HNO$_3$) aqueous solution for 15 minutes. Although after 3 minutes it could be seen by naked eye that the top substrate-nickel layer was removed, we let the samples a few minutes more to ensure a complete removal. Despite the dissolution of such initial layer, the fishnet structure did not detach, but still presented a strong physical adhesion to the original substrate by van der Waals forces. The sample was then slowly re-immersed at a grazing angle so that the fishnet structure separated from the original substrate thanks to the directional liquid infiltration. While floating on the diluted acid-air interface, the fishnet structure was scooped on a new glass slide (Figure 3.9d) and allowed to dry in air. The detachment and transfer steps were always carefully performed so that the layered

sample did not break into several pieces. Still, some optimizations or alternative ways of detachment might be studied in order to preserve the structure integrity. Figure 3.9a presents a close view of a double fishnet metamaterial obtained after nickel removal, where one can easily recognize the two gold layers, separated by the expected air gap and supported by the PS particles. Although a slight decrease in the particle size and air gap is observed, the arranged particles still conserved their high quality order after the HNO_3 treatment (Figure 3.9b). Our approach enables the fabrication of free-standing membranes (Figure 3.9c), illustrating the flexibility and potential adaptability of the structures to different kind of substrates over centimeter-sized areas (Figure 3.9d).
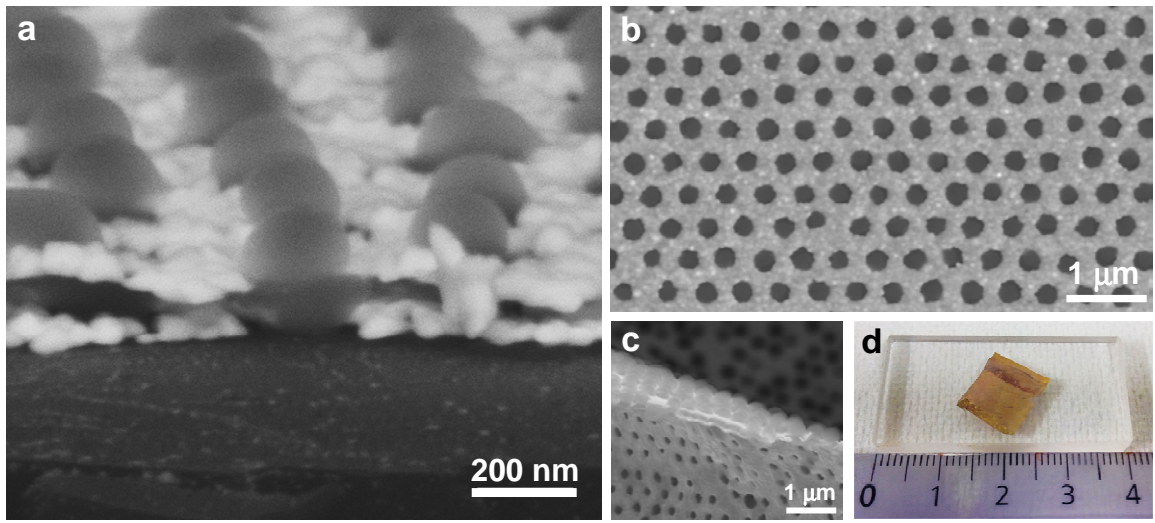
Figure 3.9 a SEM tilted and **b** top views of the hexagonally ordered double fishnet structures after nickel dissolution. **c** Close up view of a free-standing metamaterial membrane. **d** Photographs of a sample on a glass substrate after the transfer.

3.4 Optical characterization of the fishnet structures

In order to ensure the most reliable reproduction of the optical properties, the samples were optically characterized and compared to FDTD simulations before and after nickel dissolution as a quality test of the fabrication procedure. The experimental curves shown are an average of several measured points on each sample by microspectrophotometry.

3.4.1 Colloidal monolayers embedded in a stack of metallic layers

Figure 3.10 shows the measured and simulated reflectance spectra of samples with different diameters *D* after all the electrodeposition steps. For all the cases, the composition of the metallic stack consisted of two 50 nm thick Au layers separated by a

Ni spacer of 70 nm. The thickness of the first nickel layer was adjusted for each particle size so that the gold films were at the correct height of the monolayer. The modelled structure also considered the nickel substrate, similarly to the experiment.
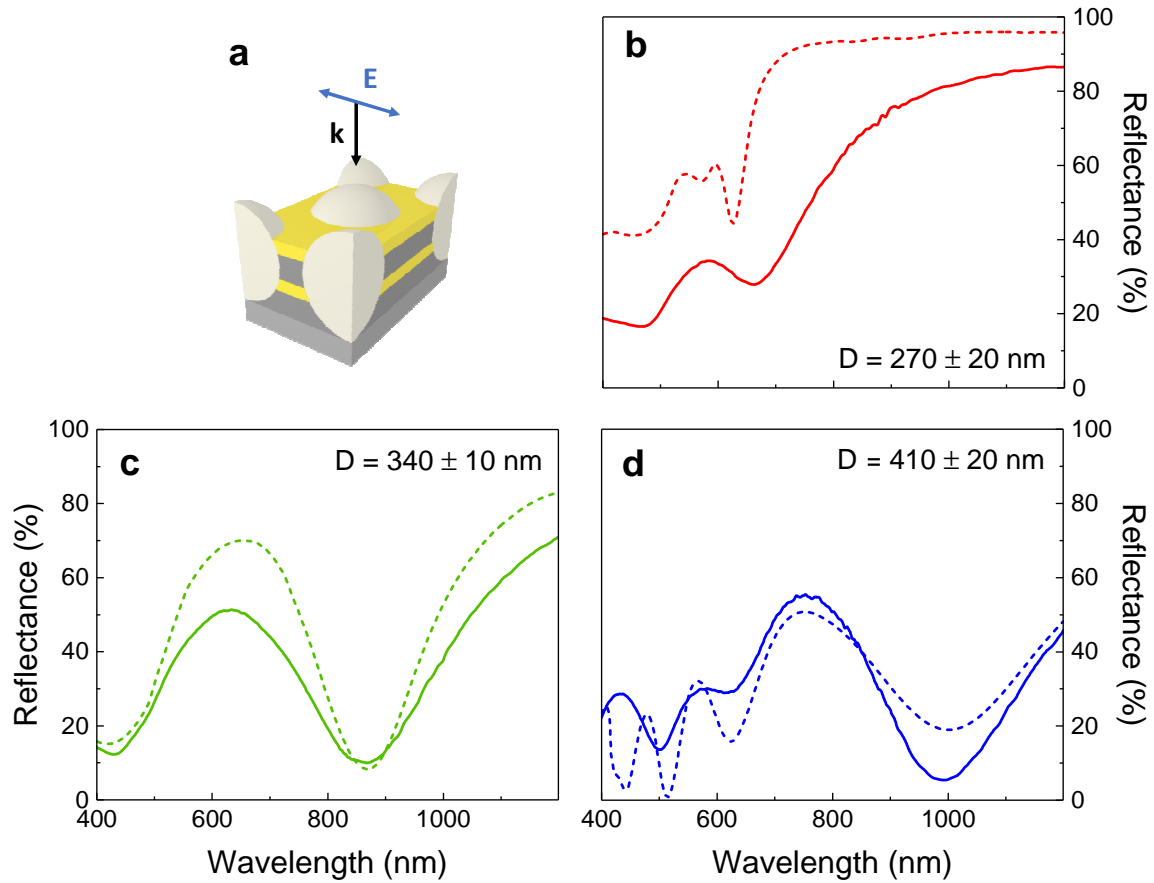
Figure 3.10 a Scheme of the simulated unit cell, where *E* denotes the polarization of the electric field and *k* the direction of the incident wave. Measured (solid) and simulated (dashed lines) reflectance spectra of Ni-Au-Ni-Au films perforated by PS particles with diameters of **b** 270 ± 20 nm, **c** 340 ± 10 nm and **d** 410 ± 20 nm.

A very good correlation between the experimental and the simulated curves can be appreciated, which confirms the successful deposition through the colloidal templates. Nevertheless, some discrepancies exist whose explanation was found with further simulations. For instance, in Figure 3.10b, the broader experimental dip shown at around 660 nm comes from the slight inhomogeneity of the particles size *D*. When numerically averaging over the error range of diameters (270 ± 20 nm), the simulated sharp dip disappears and a smoother curve is obtained like in the measurements (Figure 3.11a). A small disagreement appears as well in Figure 3.10d at short wavelengths. In particular, at 440 nm, we experimentally obtained a reflectance peak in contrast with a numerical dip. We ascribe such discrepancy to our experimental set up. On one hand, the simulations

were performed with a normally incident wave regarding the structure surface. On the other hand, the measured reflectivity was acquired by both exciting and collecting the signal through an objective with NA = 0.2, which implies light impinging with angles in the range of 0–12^0. Figure 3.11b illustrates a better agreement between the experimental spectrum and the average of the simulated curves within this range of incident angles.
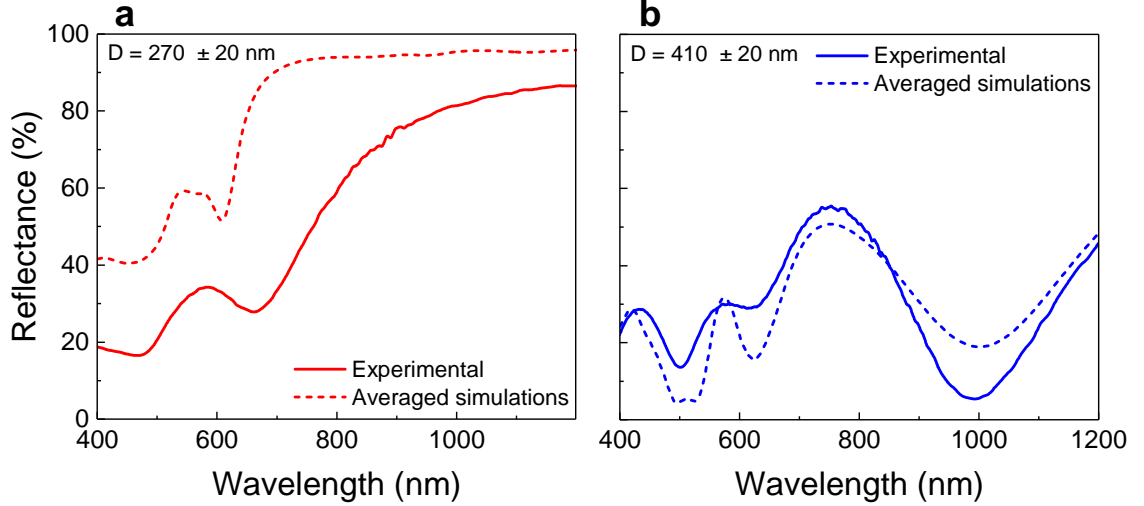
Figure 3.11 Measured (solid) and averaged simulations (dashed lines) reflectance spectra of Ni-Au-Ni-Au films with embedded PS particles. The simulated curves correspond to an average over **a** the error range of D = 270 nm and **b** over angles of incidence ranging from 0 to 12^0 for the sample with D = 410nm.

Close inspection of the spectra of Figure 3.10 points out that the main valley redshifts as the diameter increases, being located at around 660 nm, 870 nm and 990 nm for D equal to 270, 340 and 410 nm, respectively. This observation confirms the dependence of the optical response with the diameter.

In order to better understand the resonance, we studied the electromagnetic spatial profiles of the structure. Figure 3.12 shows the fields distribution at the middle nickel plane at the resonant wavelength of the structure with D = 270 nm. Both the electric and magnetic fields are confined inside the particles in presence of nickel around them. It is therefore reasonable that the wavelength of resonance increases with D. Larger diameters imply larger cavities where the radiation is confined hence shifting the resonant mode towards larger wavelengths.
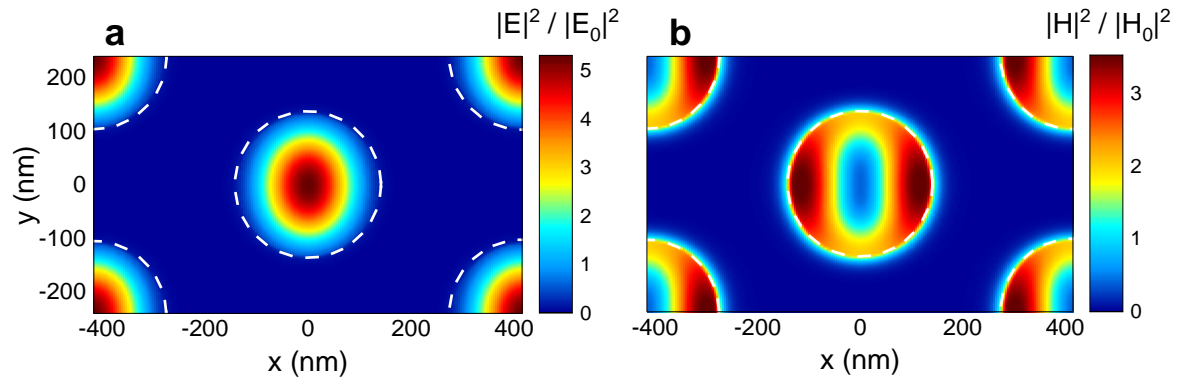
Figure 3.12 Normalized **a** electric and **b** magnetic field intensities of the multilayered structure at the nickel middle plane for the minimum reflection (λ = 616 nm). The electric field was **y** polarized. The unit cell corresponds to L = 480 nm, D = 270 nm, 50 nm thick Au layers and 70 nm thick Ni spacer. White dashed lines indicate the particles edge.

3.4.2 Double fishnet metamaterials

Following the nickel removal and transfer to glass substrates, the samples were measured in transmission T and reflection R. Figure 3.13 shows the extinction spectra (Ext=1-T-R) of double fishnet structures featuring different combinations of D and w. Closer examination of the spectra enabled us to identify the role played by the particles diameter and the gap width, revealing a main extinction peak that shifts as a function of these two parameters. Figure 3.13a and b illustrate how for a fixed gap of 25 nm, the resonance blue shifts from 920 to 890 nm when increasing the diameter of the particles. In contrast, when keeping D = 300 nm constant (Figure 3.13 b and c), decreasing the gap from 25 to 15 nm redshifts the feature towards 970 nm. The trend is also confirmed when keeping w = 15 nm fixed and increasing D to 350 nm, which blue shifts the resonance to 920 nm (Figure 3.13c and d).

In depth examination of the simulated curves pointed out a slight decrease in diameter and gap width after immersion in HNO_3, as observed by SEM. The broadening of the measured spectra with respect to the calculations is attributed to some experimental fluctuations of D and w over 100 μm length scales, this is, the spot size of the measurements. Such fluctuations are quantified in the form of error ranges. The errors of the particles size correspond to the standard deviation of the mean value, obtained from the SEM image analysis. The errors of the gap widths were obtained from simulations whose resonance was within the full width at half maximum of the experimental peak. In spite of this, a fairly good agreement between numerical and experimental results is observed.
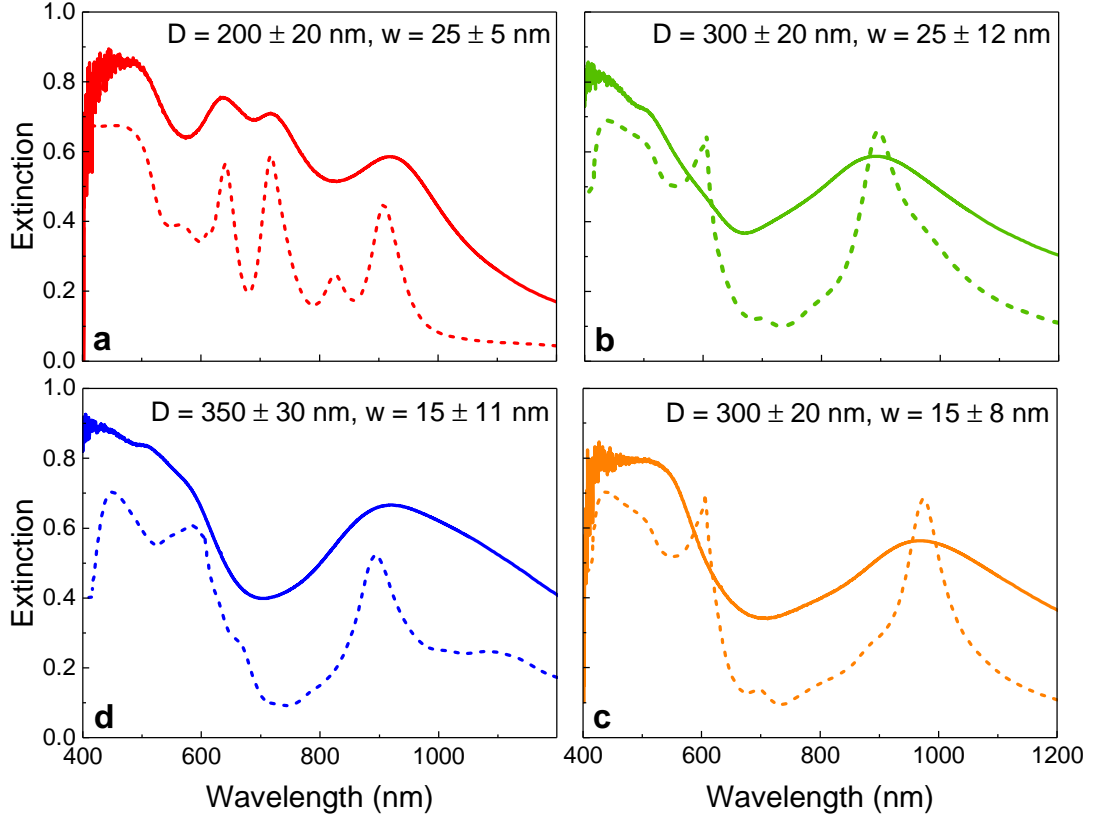
Figure 3.13 Experimental (solid lines) and simulated (dashed lines) extinction spectra of double fishnet structures with **a** D = 200 ± 20 nm and w = 25 ± 5 nm, **b** D = 300 ± 20 nm and w = 25 ± 12, **c** D = 300 ± 20 nm and w = 15 ± 8 nm, **d** D = 350 nm ± 30 nm and w = 15 ± 11 nm.

3.5 Properties of double fishnet metamaterials

3.5.1 Effective parameters

The effective refractive indices n_{eff} of the structures were extracted from the simulated complex reflection and transmission coefficients. The Appendix describes the employed retrieval method based on the effective medium approximation[40,41] and taking into account the anisotropy of the system caused by the substrate.[42,43] Figure 3.14 summarizes the real parts of the refractive indices for all the fabricated structures. The values vary from positive to negative as a function of D and w, both acting as turning knobs of our design. In particular, the sample with the largest diameter (D = 350 nm) exhibits a positive n_{eff} over the whole range of interest despite its small w of 15 nm. The refractive index can approach zero values for the double fishnet structure with D = 300 nm and w = 25 nm (n_{eff} = 0.50 at 855 nm), and for the one with D = 300 nm and w = 15 nm (n_{eff} = -0.16 around 970 nm). Negative refractive indices are also within reach for fishnets with the appropriate structural parameters. This is the case for the metamaterial

with D = 200 nm and w = 25 nm, which exhibits a minimum value of -1.0 at 945 nm and is well below zero over a broad spectral range of 100 nm width.
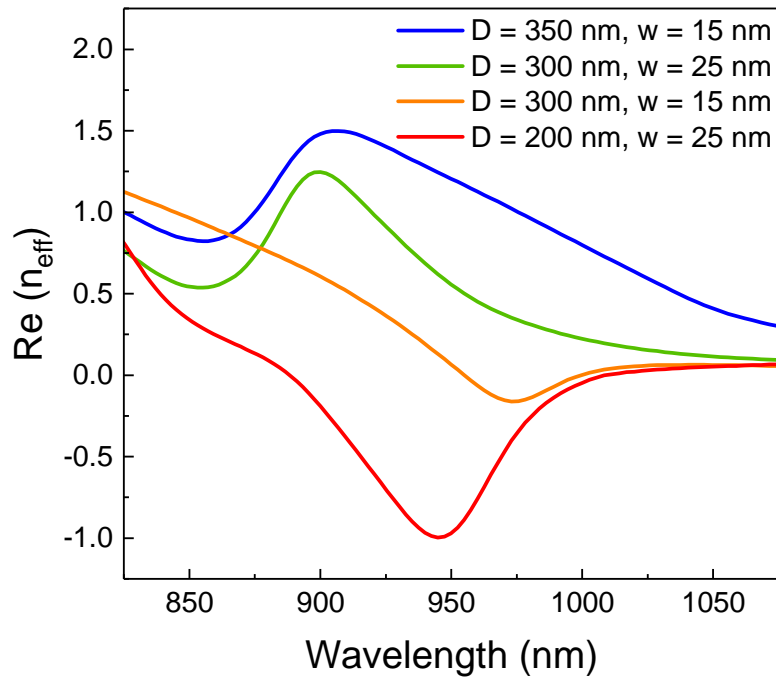
Figure 3.14 Real part of the refractive indices extracted from the numerical reproduction of the experimental data.

The major effective properties of the sample exhibiting -1 refractive index are presented in Figure 3.15. The retrieval method is as well explained in the Appendix. The reasonably high imaginary part of the effective refractive index (Figure 3.15a) likely originates from the inherent metallic absorption in the gold layers. Consequently, the FOM gets a maximum value of around 0.3 (Figure 3.15b). The losses could be eventually compensated by including a gain medium within the gap, which would give a higher FOM.[21,44]

The break of symmetry coming from the substrate is revealed by a non-zero magnetoelectric coupling ξ, also known as bianisotropy parameter (Figure 3.15c). As a consequence, the effective impedance z adopts different values depending on the propagation direction of the light. Figure 3.15d shows the real and imaginary parts of z for light impinging from the air (solid curved) and from the substrate (dashed curves). The real and imaginary parts of the effective permittivity and permeability are shown in Figure 3.15e and f, respectively. Focusing on the real parts, we can observe that whereas ε gets negative values over the whole range, μ remains positive. We have therefore made a single-NIM working in the near-infrared region.
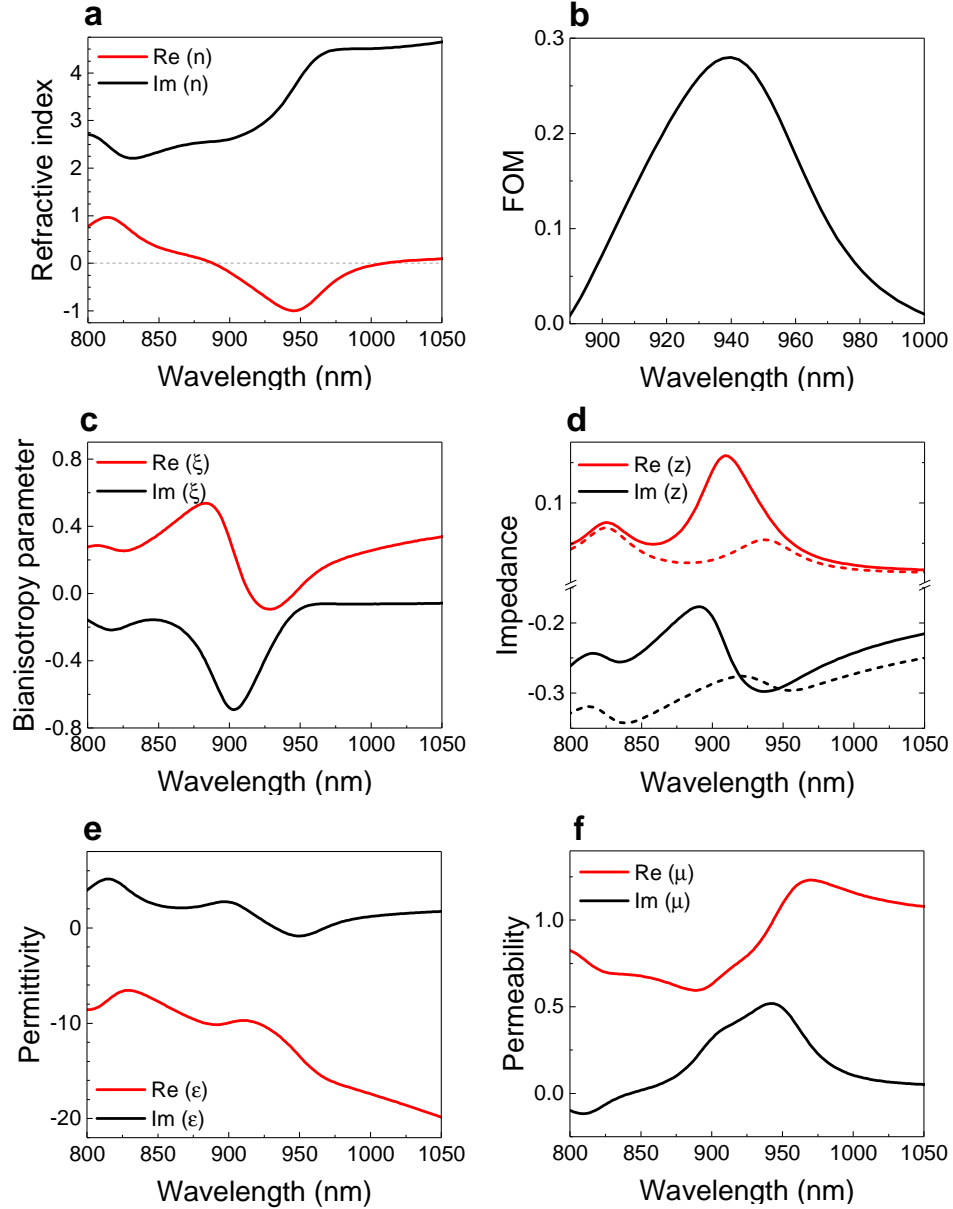
Figure 3.15 Retrieved effective parameters of the double fishnet showing -1 refractive index. **a** Refractive index. **b** Figure of merit of the negative region. **c** Magnetoelectric coupling parameter. **d** Impedance values for light impinging from air (solid lines) and from the substrate (dashed lines). **e** Electric permittivity. **f** Magnetic permeability.

In order to understand the correlation between the retrieved effective parameters and the extinction resonance at this region (Figure 3.13a), the electromagnetic distribution was calculated at the extinction maximum (λ = 920 nm) for the two planes depicted in Figure 3.16a. At the air middle plane between the gold layers, the electric field presents a polarization dependent dipole around the particles (Figure 3.16b), in contrast with what was found in the presence of nickel, where the field remained confined in the dielectric spheres. Moreover, a new magnetic resonance is found in both

x and y directions at the middle plane between the particles (Figure 3.16c). Such resonance can be explained when looking at the electrical current flow within the metamaterial. Antisymmetric currents are created in the metallic layers along the y direction between the particles as illustrated in red arrows in Figure 3.16e. These current loops are induced by the GSPs propagation at the air-gold internal interfaces.[29] The electric field pointing at opposite directions generates a magnetic dipole parallel to the x direction and confined in the dielectric spacer as can be observed in Figure 3.16e. Consequently, the magnetism of our structures, and therefore the refractive index, strongly depends on the gap width, in agreement with the theory explained in Section 3.2.
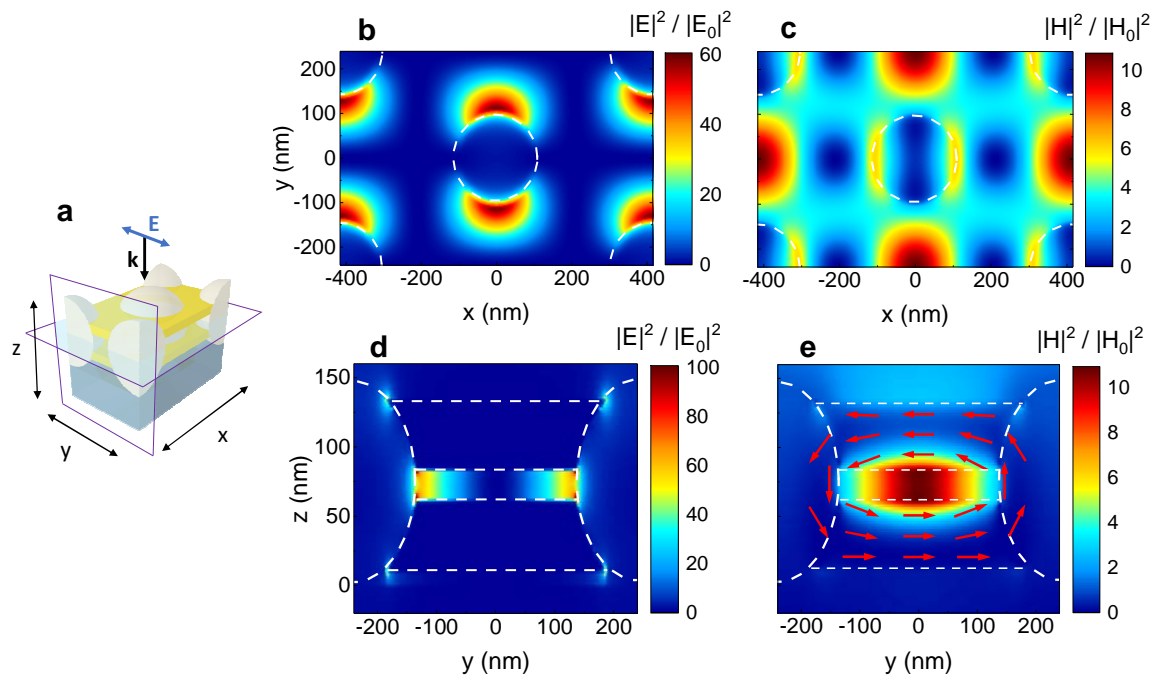
Figure 3.16 a Unit cell of the simulated system with the mapped planes, where E denotes the polarization of the electric field and k the direction of the incident wave. Electromagnetic fields distribution of the -1 refractive index metamaterial at **b,c** the sketched horizontal plane, and **d,e** at the vertical plane. The simulations were done at the resonant wavelength of 920 nm. Red arrows represent the direction of the electric field. White dashed lines are a guide for the eyes outlining the different surfaces.

Considering this dependence, more negative values of the permeability could be obtained by properly controlling this resonance. For instance, enlarging the gap width while still exciting GSPs, would increase the overall effective magnetic response of the structure.[45] However, the structure would exhibit shorter resonant wavelengths, approaching to significant less negative values of the permittivity, what could hamper

the achievement of negative n_{eff}. An alternative method would be stacking several MIM cavities where the individual magnetic resonances couple to each other giving rise to a stronger magnetic response.[46]

3.5.2 Verification by Fresnel modelling

According to the effective medium theory, an ideal homogeneous slab characterized by the retrieved effective parameters would macroscopically behave as the original complex structure. For such verification, we numerically replaced our structures by films exhibiting their effective properties (Figure 3.17a) and obtained the extinction spectra at normal incidence. This calculation was done by making use of the Fresnel equations, which describe the reflection and transmission of light at the interface between different media.[47] Denoting by 1, 2 and 3 the three media involved (air, effective medium and glass substrate), the reflectivity R and transmissivity T at normal incidence can be expressed as:

$$R = \left| \frac{r_{12} + r_{23}e^{2i\beta}}{1 + r_{12}r_{23}e^{2i\beta}} \right|^2 \tag{3.5}$$

$$T = \frac{\eta_3}{\eta_1} \left| \frac{t_{12}t_{23}e^{i\beta}}{1 + r_{12}r_{23}e^{2i\beta}} \right|^2 \tag{3.6}$$

where the propagation phase β inside the metamaterial depends on its refractive index n_{eff} and thickness d as

$$\beta = \frac{2\pi}{\lambda} n_{eff} d \tag{3.7}$$

Taking into account that in our materials $\mu \neq 1$, the Fresnel coefficients r_{ij} and t_{ij} have to be expressed as a function of the admittance η_i and not just as a function of the refractive index as commonly described.

$$\eta_i = \frac{1}{z_i} = \sqrt{\frac{\varepsilon_i}{\mu_i}} \tag{3.8}$$

$$r_{ij} = \frac{\eta_i - \eta_j}{\eta_i + \eta_j} \tag{3.9}$$

$$t_{ij} = \frac{2\eta_i}{\eta_i + \eta_j} \tag{3.10}$$

Figure 3.17b-e presents the comparison between the extinction calculated via the Fresnel equations and the experimental data of each sample. The optical properties are well reproduced in all the cases, which confirms the validity and success of our retrieval procedure.
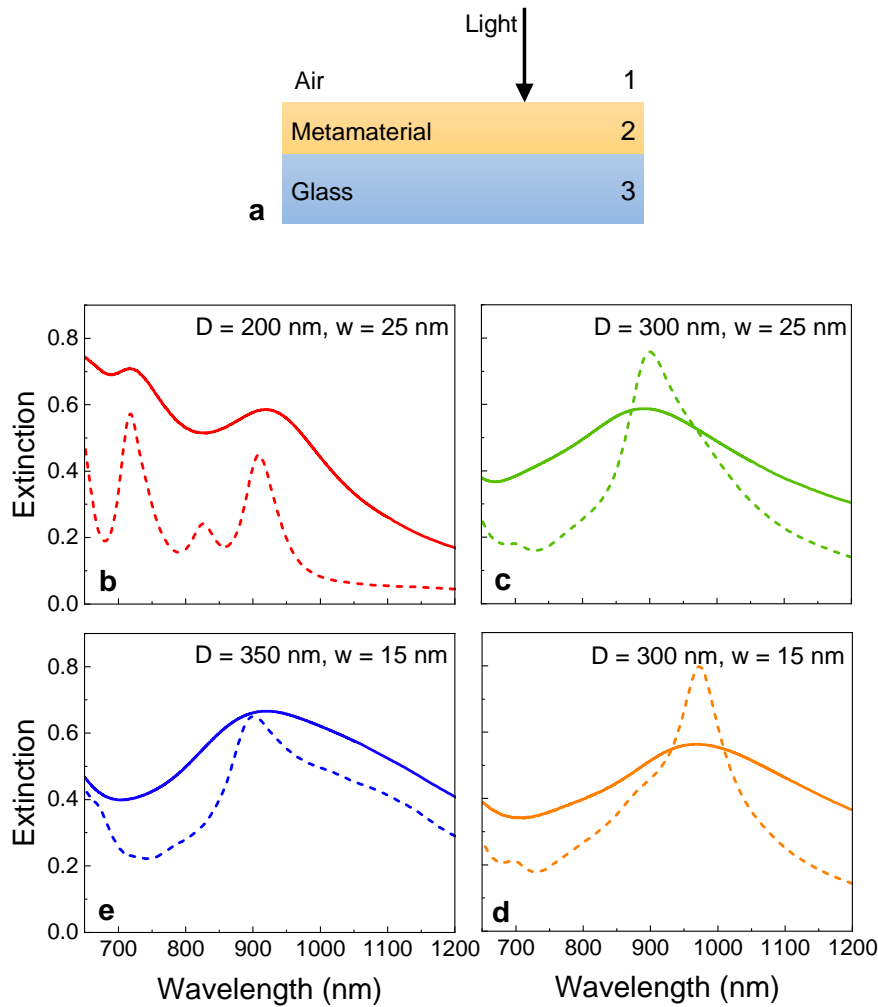
Figure 3.17 a Scheme of the effective system adopted for Fresnel modelling. Experimental (solid lines) and calculated (dashed lines) extinction spectra of samples with **b** D = 200 nm and w = 25 nm, **c** D = 300 nm and w = 25 nm, **d** D = 300 nm and w = 15 nm, **e** D = 350 nm and w = 15 nm.

3.5.3 Negative refraction in a metamaterial prism

To better illustrate the behavior of light through the metamaterial exhibiting n_{eff} = -1, an ideal prism composed of several layers of the basic structure was numerically modelled. The prism was placed between absorbing walls in a waveguide configuration so that it would not act as a single scattering structure.[48] Figure 3.18a shows how the light front propagates through the NIM at λ = 945 nm, this is, where the more negative n_{eff} value appears. As can be observed, the light front bends oppositely

to the conventional direction described by Snell's law. Negative refraction occurs after passing through the metamaterial. Moreover, close view of the electric field evolution through the dielectric spheres (Figure 3.18b) shows the phenomenon of negative phase propagation, as expected in a negative-index metamaterial. The two movies of these effects can be found in the Supporting Information of ref [49].
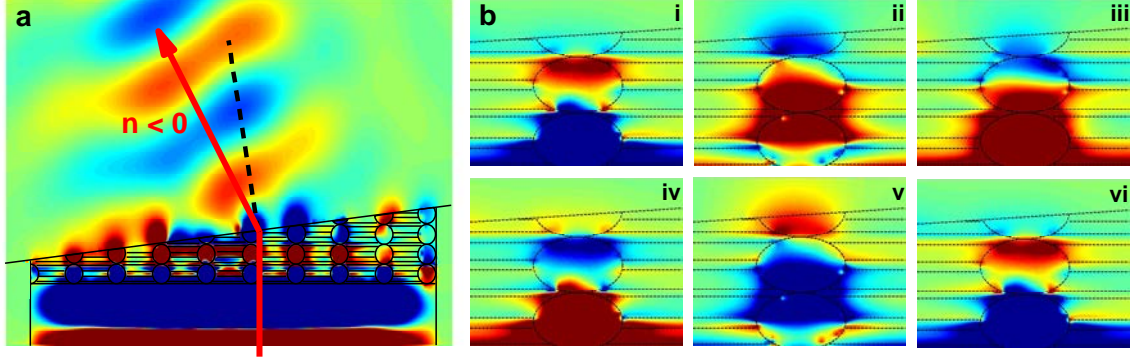
Figure 3.18 Simulated electromagnetic behavior of a prism composed of several layers of the fishnet metamaterial. **a** Electric field propagation at the resonant wavelength. The black dashed line represents the normal vector of the prism and the red line the direction of the light front. **b** Evolution of the electric field phase within the metamaterial.

3.5.4 Angle dependence of the operation wavelength

Since the magnetic response of the structures is linked with the excitation of SPPs, oblique angles of incidence will change the momentum matching relation. Therefore, the resonance might vary its spectral position with the incident angle. The optical response of the metamaterial exhibiting n_{eff} = -1 was numerically obtained for planar waves impinging onto the structure at oblique incidence. Figure 3.19 presents the evolution of the extinction with the angle of incidence for transverse electric (TE) and transverse magnetic (TM) polarizations. Both cases present the same spectral response at normal incidence, the resonant wavelength behind the negative index being located at λ = 920 nm. As the incident angle increases, this resonance shifts towards higher wavelengths in line with previous works.[24,50,51] However, it is interesting to note that in these studies the angle dependence was only present in TM mode. In contrast, our fishnet structures exhibit as well this dispersion in TE configuration. This is likely because of the hexagonal symmetry, where the unit vectors of the array differ from the two perpendicular polarizations. As a result, both oblique TM and TE modes can excite the GSP resonance behind the negative refractive index.
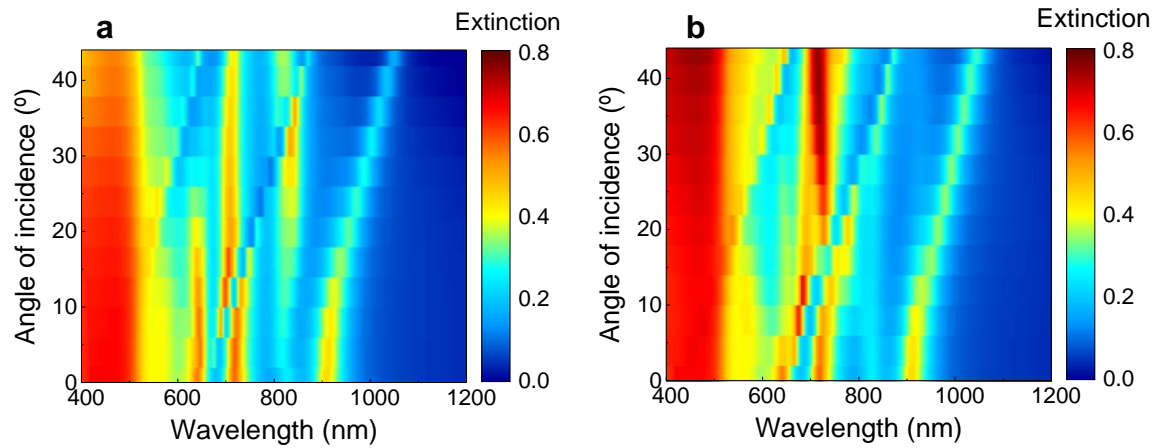
Figure 3.19 Extinction versus wavelength and incident angle of the metamaterial presenting -1 refractive index for **a** TE and **b** TM polarizations.

3.6 Conclusions

A new design of double fishnet metamaterials has been fabricated by nanosphere lithography and electrochemical deposition over large surfaces. The proper control of the temperature and time during oxygen plasma etching enabled the production of highly ordered non-closed-packed colloidal templates of different diameters. Such architectures were successfully employed for the infiltration of sacrificial nickel and gold layers around the particles. By finely adjusting the electrodeposition time, we fabricated several colloidal monolayers embedded in nickel-gold-nickel-gold stacks, where the two gold layers were placed symmetrically with respect to the equatorial axis of the monolayer. The selective dissolution of the nickel parts led to double-fishnet metamaterials made of two layers of gold separated by an air cavity and perforated by the dielectric particles. Besides, the use of a nickel-coated substrate from the beginning enabled transferring the metamaterial structures to transparent substrates for their detailed optical characterization. From the experimental point of view, this approach provide a very good control over the geometrical features so that the final properties of the structures can be easily tuned.

The fishnet-like samples exhibited extinction resonances in the NIR that varied as a function of the diameter of the particles and the air gap width between the metallic layers. The good agreement between the optical measurements and the simulated spectra throughout the fabrication process attested the successful control over the structures as well as the reliability of the calculations.

From the latter, the effective optical properties of the structures were retrieved, demonstrating that we were experimentally able to tailor the refractive index from positive to near-zero and even negative values. The minimum achieved corresponded to a single-NIM with -1 effective refractive index around 940 nm, with negative values over a 100 nm wide spectral band and a maximum FOM of 0.3. Electromagnetic field distributions confirmed that the nature of this phenomenon is related with the excitation a magnetic resonance within the dielectric gap.

The optical spectra of our materials were well reproduced by a simple Fresnel modelling, ensuring the validity of our calculations. Finally, further simulations confirmed that the metamaterial can lead to negative refraction and negative phase propagation, with a dependence on the angle of incidence.

In conclusion, we have developed an effective bottom-up route for the low-cost and up-scalable fabrication of negative index metamaterials working in the near-infrared region.

3.7 References

1.   A. M. Urbas et al. Roadmap on optical metamaterials. *J. Opt.* **2016**, *18*, 093005.

2.   V. Ponsinet et al. Self-assembled nanostructured metamaterials. *EPL* **2017**, *119*, 14004.

3.   M. Mayer, M. J. Schnepf, T. A. F. Konig and A. Fery. Colloidal self-assembly concepts for plasmonic metasurfaces. *Adv. Opt. Mater.* **2019**, *7*, 1800564.

4.   S. Mühlig et al. A self-assembled three-dimensional cloak in the visible. *Sci. Rep.* **2013**, *3*, 2328.

5.   V. Many et al. High optical magnetism of dodecahedral plasmonic meta-atoms. *Nanophotonics* **2018**, *8*, 549–558.

6.   R. Paniagua-Domínguez, F. López-Tejeira, R. Marqués and J. A. Sánchez-Gil. Metallo-dielectric core-shell nanospheres as building blocks for optical three-dimensional isotropic negative-index metamaterials. *New J. Phys.* **2011**, *13*, 123017.

7.   J. Cheng et al. GoldHelix: Gold nanoparticles forming 3D helical superstructures with controlled morphology and strong chiroptical property. *ACS Nano* **2017**, *11*, 3806–3818.

8.   S. Vignolini et al. A 3D optical metamaterial made by self-assembly. *Adv. Mater.* **2012**, *24*, 23–27.

9.   M. Stefik, S. Guldin, S. Vignolini, U. Wiesner and U. Steiner. Block copolymer self-assembly for nanophotonics. *Chem. Soc. Rev.* **2015**, *44*, 5076–5091.

10.   M. Kim, J. Kim and M. Allen. Nanopatterned surfaces based on template-assisted multilayer electrodeposition. *Small* **2015**, 1912–1918.

11.   X. Wang et al. Hyperbolic-by-design self-assembled metamaterial based on block copolymers lamellar phases. *Opt. Laser Technol.* **2017**, *88*, 85–95.

12.   M. C. Gwinner et al. Periodic large-area metallic split-ring resonator metamaterial fabrication based on shadow nanosphere lithography. *Small* **2009**, *5*, 400–406.

13.   K. Cho, G. Loget and R. M. Corn. Lithographically patterned nanoscale electrodeposition of plasmonic, bimetallic, semiconductor, magnetic, and polymer nanoring arrays. *J. Phys. Chem. C* **2014**, *118*, 28993–29000.

14.   Y. Cai, Y. Cao, P. Nordlander and P. S. Cremer. Fabrication of split-rings via stretchable colloidal lithography. *ACS Photonics* **2014**, *1*, 127–134.

15.   K. Tanikawa et al. Fabrication of peelable thin films containing crescent-shaped split-ring resonators for three-dimensional optical metamaterials. *Opt. Mater. Express* **2017**, *7*, 1.

16.   X. Zhou, Q. H. Fu, J. Zhao, Y. Yang and X. P. Zhao. Negative permeability and subwavelength focusing of quasi-periodic dendritic cell metamaterials. *Opt. Express* **2006**, *14*, 7188.

17.   X. Zhao. Bottom-up fabrication methods of optical metamaterials. *J. Mater. Chem.* **2012**, *22*, 9439–9449.

18.   K. Lodewijks, N. Verellen, W. Van Roy, G. Borghs and P. Van Dorpe. Self-assembled hexagonal double fishnets as negative index materials. *Appl. Phys. Lett.* **2011**, *98*, 091101.

19.   Z. Zhou et al. Broad-range electrically tunable plasmonic resonances of a multilayer coaxial nanohole array with an electroactive polymer wrapper. **2017**.

20.   B. Gong et al. A visible metamaterial fabricated by self-assembly method. *Sci. Rep.* **2014**, *4*, 4713.

21.   S. Li et al. A green-light gain-assisted metamaterial fabricated by self-assembled electrochemical deposition. *Appl. Phys. Lett.* **2013**, *103*, 181910.

22.   J. Valentine, S. Zhang, T. Zentgraf and X. Zhang. Development of bulk optical negative index fishnet metamaterials: Achieving a low-loss and broadband response through coupling. *Proc. IEEE* **2011**, *99*, 1682–1690.

23.   J. B. Pendry, L. Martín-Moreno and F. J. García-Vidal. Mimicking surface plasmons with structured surfaces. *Science* **2004**, *305*, 847–848.

24.   A. Mary, S. G. Rodrigo, F. J. García-Vidal and L. Martín-Moreno. Theory of negative-refractive index reponse of double-fishnet structures. *Phys. Rev. Lett.* **2008**, *101*, 103902.

25.   S. G. Rodrigo. Optical properties of nanostructured metallic systems: Studied with the finite-difference time-domain method, University of Zaragoza, 2012.

26.   S. Ramo, J. R. Whinnery and T. Van Duzar. *Fields and waves in communication electronics*; USA and Canada, 1994.

27.   C. L. C. Smith, N. Stenger, A. Kristensen, N. A. Mortensen and S. I. Bozhevolnyi. Gap and channeled plasmons in tapered grooves: A review. *Nanoscale* **2015**, *7*, 9355–9386.

28.   E. N. Economou. Surface plasmons in thin films. *Phys. Rev.* **1969**, *182*, 539–554.

29.   R. Ortuño, C. García-Meca, F. J. Rodríguez-Fortuño, J. Martí and A. Martínez. Role of surface plasmon polaritons on optical transmission through double layer metallic hole arrays. *Phys. Rev. B* **2009**, *79*, 075425.

30.   T. W. H. Oates et al. Oblique incidence ellipsometric characterization and the substrate dependence of visible frequency fishnet metamaterials. *Opt. Express* **2012**, *20*, 11166.

31.   J. Yang. Theoretical studies of optical fishnet metamaterials, University of Paris-Sud, 2012.

32.   F. D. Egitto. Plasma etching and modification of organic polymers. *Pure Appl. Chem.* **1990**, *62*, 1699–1708.

33.   C. T. Bauer et al. Size and shape evolution of PS particle layers during etching. *Bioinspired, Biomim. Nanobiomaterials* **2013**, *2*, 130–140.

34.   N. Vogel, S. Goerres, K. Landfester and C. K. Weiss. A convenient method to produce close- and non-close-packed monolayers using direct assembly at the air-water interface and subsequent plasma-induced size reduction. *Macromol. Chem. Phys.* **2011**, *212*, 1719–1734.

35.   A. Plettl et al. Non-close-packed crystals from self-assembled polystyrene spheres by isotropic plasma etching: Adding flexibility to colloid lithography. *Adv. Funct. Mater.* **2009**, *19*, 3279–3284.

36.   J. Rieger. The glass transition temperature of polystyrene. *J. Therm. Anal.* **1996**, *46*, 965–972.

37.   M. Heim, S. Reculusa, S. Ravaine and A. Kuhn. Engineering of complex macroporous materials through controlled electrodeposition in colloidal superstructures. *Adv. Funct. Mater.* **2012**, *22*, 538–545.

38.   H. Zheng et al. Morphological design of gold nanopillar arrays and their optical properties. *J. Phys. Chem. C* **2016**, *120*, 1178–1185.

39.   H. Zheng. Design and bottom-up fabrication of nanostructured photonic / plasmonic materials, University of Bordeaux, 2016.

40.   X. Chen, T. M. Grzegorczyk, B. I. Wu, J. Pacheco and J. A. Kong. Robust method to retrieve the constitutive effective parameters of metamaterials. *Phys. Rev. E* **2004**, *70*, 016608.

41.   D. R. Smith, D. C. Vier, T. Koschny and C. M. Soukoulis. Electromagnetic parameter retrieval from inhomogeneous metamaterials. *Phys. Rev. E* **2005**, *71*, 036617.

42.   Z. Li, K. Aydin and E. Ozbay. Determination of the effective constitutive parameters of bianisotropic metamaterials from reflection and transmission coefficients. *Phys. Rev. E* **2009**, *79*, 026610.

43.   S. Yun et al. Experimental verification of substrate-induced bianisotropy in optical metamaterials. *Appl. Phys. Lett.* **2013**, *103*, 233109.

44.   S. Xiao et al. Loss-free and active optical negative-index metamaterials. *Nature* **2010**, *466*, 735–740.

45.   P. Ding et al. Numerical simulations of terahertz double-negative metamaterial with isotropic-like fishnet structure. *Photonics Nanostructures - Fundam. Appl.* **2009**, *7*, 92–100.

46.   J. Zhou, T. Koschny, M. Kafesaki and C. M. Soukoulis. Negative refractive index response of weakly and strongly coupled optical metamaterials. *Phys. Rev. B* **2009**, *80*, 1–6.

47.   M. Born and E. Wolf. *Principles of optics. Electromagnetic theory of propagation, interference and diffraction of light*, 7th ed.; Cambridge University Press, UK, 2002.

48.   J. L. Garcia-Pomar and M. Nieto-Vesperinas. Transmission study of prisms and slabs of lossy negative index media. *Opt. Express* **2004**, *12*, 2081.

49.   M. Gómez-Castaño et al. Tunable index metamaterials made by bottom-up approaches. *Nanoscale Adv.* **2019**, *1*, 1070–1076.

50.   A. Minovich et al. Tilted response of fishnet metamaterials at near-infrared optical wavelengths. *Phys. Rev. B* **2010**, *81*, 1–6.

51.   S. S. Kruk, D. A. Powell, A. Minovich, D. N. Neshev and Y. S. Kivshar. Spatial dispersion of multilayer fishnet metamaterials. *Opt. Express* **2012**, *20*, 15100–15105.

Chapter 4

Fishnet metamaterials by soft nanoimprint lithography

4.1 Introduction

Soft nanoimprint lithography has been proven as a powerful technique for the development of plasmonic devices such as structural colour filters,[1] directional light emitters,[2] biosensing platforms,[3] or metamaterials.[4] Thanks to its easy, large-scale and low-cost operation, NIL technology has led to a broad variety of high performance metamaterials and metasurfaces, including chiral structures,[5] superabsorbers[6] and NIMs made of different geometries and materials.[7] Several works can be found in the literature regarding the fabrication of SRRs by NIL and metal evaporation. The good adaptability of these techniques to different configurations gave rise to circular,[8] U-shaped[9] and L-shaped[10] designs working at the NIR region. Tamioka et al.[11] developed a different approach based on the combination of nanoimprint lithography with electrodeposition. In this way, the metallic parts were directly deposited in between the template following its shape and avoiding any post-transfer of the structures.

Fishnet structures have been as well accomplished making use of soft nanoimprinting. Chanda et al.[12] showed for the first time the potential application of NIL to these metamaterials. Their method was based on the deposition of metal-insulator-metal unit cells over rectangular patterns and subsequent transfer printing to flexible substrates. The relatively large periodicity of the structures (850 nm) led to NIMs working over a broad spectral range in the deep near-infrared, with refractive index up to -7.8 and FOM close to 8. Working at the same spectral region, Bergmair et al. proposed an approach based on multitransfer printing for piling up several layers.[13] Sharp et al. developed a method where a SiC stamp pressed under high pressure against a continuous multilayered stack displaced part of the structure and led to the apertures of the fishnet design.[14] The structures exhibited a refractive index of the order of -5 operating in the NIR with FOMs around 3. The first achievement of a fishnet

metamaterial made by NIL working in the visible was obtained by Gao et al.[4] thanks to the employ of 300 nm pitch gratings, with a minimum value of -0.73 refractive index at 710 nm and FOM of 4. By optimizing the previous method of Chanda et al.,[12] they carried out a multilayer deposition on top of a pattern followed by lift-off and removal of the excess material. These examples are summarized in the overview graph of the main fishnet metamaterials fabricated to date (Figure 1.14 from Chapter 1).

Despite the scalability of these works, they involve several steps and still make use of top-down deposition methods that can increase the costs and hamper the mass manufacturing. From the optical point of view, NIMs working in the visible range with strong negative indices are still lacking for the eventual implementations in optical devices. Besides, it is worth noting that obtaining NIMs with a negligible angular dependency remains a daunting challenge but would lead to significant improvement for light directionality.
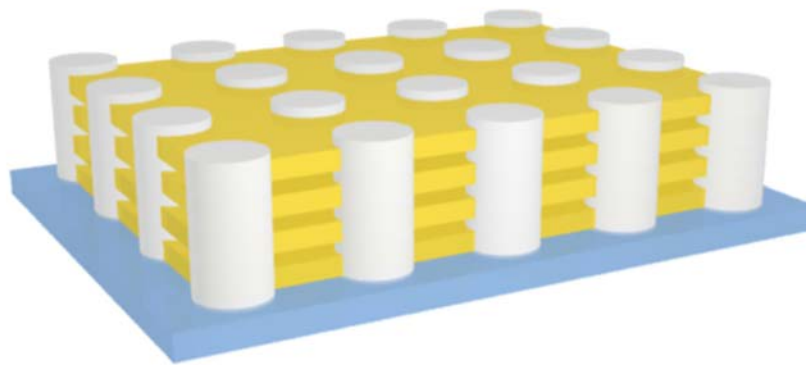

Figure 4.1 Illustration of the proposed multilayered fishnet structure combining nanoimprinting lithography and electrodeposition.

This chapter aims at developing a new approach for the straightforward fabrication of multilayered fishnet metamaterials. To do so, we will combine the scalable techniques of soft nanoimprinting and electrodeposition. The targeted geometry is illustrated in Figure 4.1. A squared array of cylindrical pillars behaves as template for flat gold layers separated by air gaps, being the whole system placed on top of a transparent substrate. We engineer constituent dimensions such as lattice spacing, pillars diameter, gold layers and gaps widths to attain strong refractive indices ranging from the NIR to the visible. We study experimentally and theoretically the optical properties of the metamaterials, from the influence of the number of metallic layers to the angular response. Finally, we demonstrate the accessibility to the air gaps by studying the

performance of the metamaterials as optical sensors when infiltrating different liquids within the metallic layers.

4.2 Fabrication of fishnet metamaterials by soft nanoimprinting

Multilayered fishnet metamaterials were fabricated over centimeter-sized areas by the versatile combination of soft nanoimprint lithography and metallic electrodeposition. The procedure followed for the fabrication of the metamaterials is summed up in Figure 4.2. The following sections will describe each fabrication step.
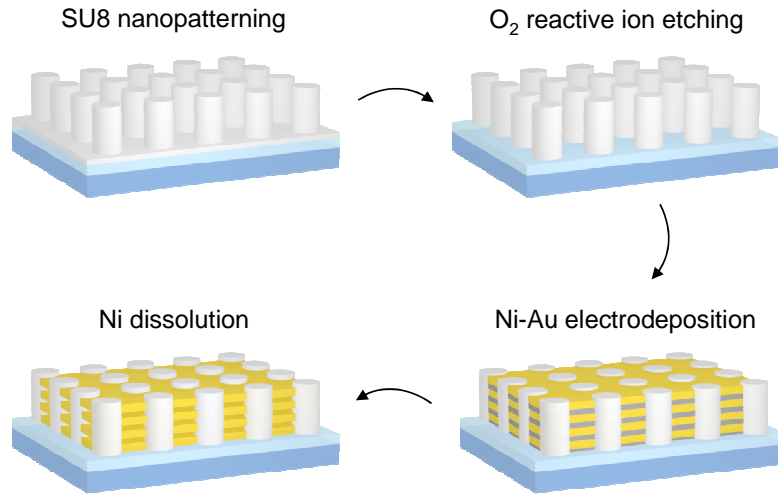
Figure 4.2 Scheme of the fabrication process of fishnet metamaterials based on soft nanoimprinting and electrodeposition.

4.2.1 Preparation of periodic arrays of pillars

Two-dimensional templates of pillars were prepared by patterning a SU8 thin layer according to the protocol described in Chapter 2. In brief, a hard-PDMS mold of holes is pressed against a SU8 layer heated above its glass transition temperature. The photoresist fills the mold adopting the negative shape and is then cooled down. The nanopattern is fixed by cross-linking the photoresist with UV light and a post-baking step. In this project, we made use of squared arrays of cylindrical pillars with lattice parameters (*L*) of 500, 400, 300 and 200 nm in order to obtain structures working over a broad spectral range.

Substrate choice

Two types of substrates were investigated as WE for the electroplating stage and the eventual transfer to transparent surfaces. Placing the metamaterials on transparent

substrates will enable the full characterization of their optical properties. Firstly, trying to optimize the fabrication process followed in Chapter 3, we made use of 100 μm thick nickel strips (Alfa Aesar). After the electrodeposition step, these bulk pieces would completely dissolve, leading to transferable membranes onto different substrates. Thanks to this method, we could simplify the detachment from the original substrate, avoiding issues like a strong physical adhesion or the possible break of the structures.

As an alternative, we used glass slides coated with a transparent conducting oxide (TCO). These materials are of great interest in optoelectronics because of their low electrical resistance and still high transparency.[15,16] In our case, it allows us to directly fabricate the multilayer structure on transparent surfaces without the need of exchanging the substrate. Hence, the quality of the structures over large surfaces would be preserved. From the TCOs available, we made use of indium doped tin oxide (ITO, Ossila) because of its smoother surface and widespread use in optoelectronic devices.[17,18] Figure 4.3 presents two samples with a SU8 periodic array of pillars printed on top of the two substrates.
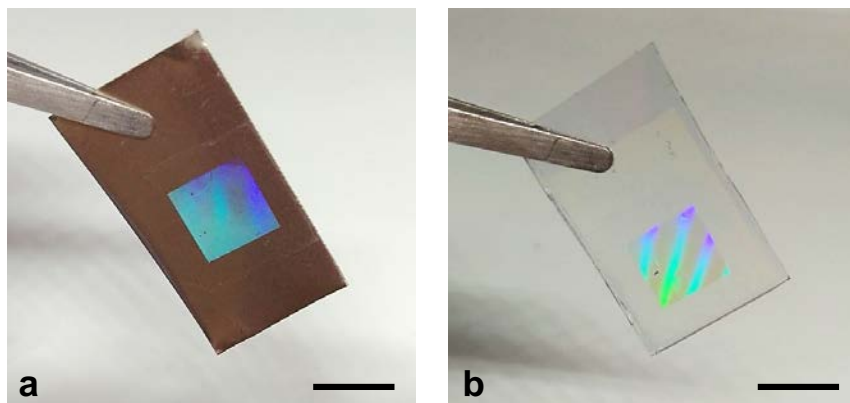
Figure 4.3 Photographs of patterns of 500 nm periodic pillars printed on SU8 on top of **a** nickel strip and **b** ITO coated glass. Scale bars: 1 cm.

Removal of the residual layer by RIE

The imprinting process is characterized by the formation of a residual layer between the patterned surface and the substrate. If additional fabrication steps are planned, it is usually necessary to remove this residual layer to reach the substrate and isolate the features within the array. In our case, uncovering the conductive substrate was a crucial step for the correct operation of electrodeposition. The most suitable etching technique strongly depends on the material to remove and the desired final shape of the structures. As discussed in Section 3.3.1, the most straightforward approach

when working with organic materials is the oxygen plasma treatment. In the case of spheres, an isotropic plasma cloud was ideal for a homogeneous reduction of the particles diameter. However, when working with two-dimensional patterns, a controlled anisotropic treatment is preferred to preserve the aspect ratio of the features. Reactive ion etching (RIE) enables a high control on the directionality of the generated plasma species. Ions and radicals are accelerated by an electric field towards the target substrate, enhancing the etching process in the vertical axis and, therefore, minimizing the variation of the initial shape. An oxygen RIE treatment was the most appropriate step for removing the SU8 residual layer under the pillars.
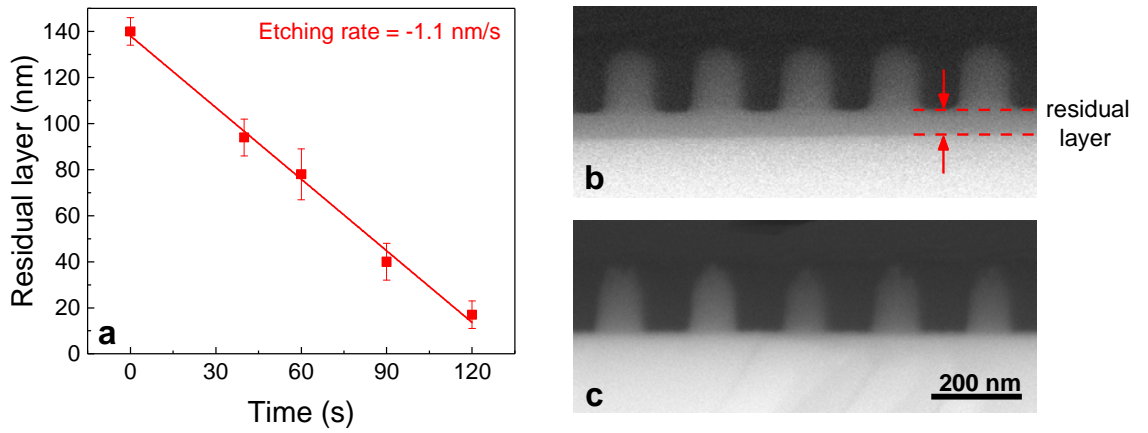
Figure 4.4 a Residual layer thickness as a function of the oxygen RIE time. SEM images of 200 nm pitch pillars **b** before and **c** after the etching process.

We carried out the experiments at the clean room of the Catalan Institute of Nanoscience and Nanotechnology (ICN2), using a PlasmaPro Cobra 100 equipment from Oxford Instruments. SU8 residual layers were etched using 25 sccm of O_2 under a pressure of 25 mTorr and a plasma power of 50 W. The sample stage was backside cooled to maintain a constant temperature during the process. The etching rate (1.1 nm/s) was previously determined from different etching times over patterns with L = 500 nm with an initial residual layer of 140 nm (Figure 4.4a). The etching time was adjusted for each batch of samples, whose residual layer was 40-70 nm depending on the pattern. Although the etching rate can vary with the density of the array because of the proximity between pillars, such quantity was taken as a valid approximation for very thin residual layers independently of the pattern features. Figure 4.4b and c show a periodic array of pillars with L = 200 nm before and after the RIE process. Even though

the pillars are slightly shrunk at the top nanometers, it is proved that the diameter width is mainly well conserved.

### 4.2.2 Multilayer electrodeposition through two-dimensional templates

The removal of the residual layer gave rise to periodic arrays of isolated dielectric pillars on top of conductive substrates. Similarly to Chapter 3, these structures can be used as templates for the alternating electrodeposition of sacrificial nickel and gold layers. These multilayer stacks will be the base for the final fishnet structure sustained by the SU8 pillars. In the case of colloidal templates, a symmetric design regarding the z axis implied the initial deposition of a supporting nickel layer around the particles. In the current case, given the lack of symmetry in such direction, the multilayered geometry could be accomplished by directly electroplating a first gold layer.

Some works have studied the current-time variation when electroplating across two-dimensional templates. In the case of growing nanowires, a drastic current change is observed after complete filling the nanoholes, coming from a rapid increase of the electroactive area.[19] However, the deposited thickness is difficult to control when working with the opposite template: open surfaces patterned with pillars. In such case, the pillar surface density is not sufficiently large to observe a clear current variation when exceeding the template high. The layers instead will practically grow like on a flat surface.

Electrodeposition on nickel strips

Initial tests over unpatterned Ni strips showed that gold deposition did not take place until applying a reduction potential of -0.9 V, above our usual voltage of -0.7 V. Such absolute increase manifested a lower chemical affinity between the gold electrolyte and the nickel foils. Since gold morphology is very sensitive to the deposition conditions, applying higher potentials could provoke the formation of rough surfaces or even hierarchical structures.[20,21] Instead, we first deposited a 10 nm thick Ni adhesive layer at the usual conditions (-0.9 V), followed by the deposition of Au at -0.7 V. In this way, the morphological properties of the gold layers were preserved to be the same as in previous experiments. However, the same procedure through our templates presented an inhomogeneous distribution at the microscale. This result was ascribed to the high roughness of nickel strips, which could increase the hydrophobicity of the substrates. Considering that our electrolytes were aqueous-based solutions, the low wettability of

the substrates could affect the homogeneity of the deposits. For this reason, the samples were treated for 3 min with UV-activated ozone to render the surface more hydrophilic and let immersed for 15 min in the bath prior the deposition to increase its diffusion through the template.
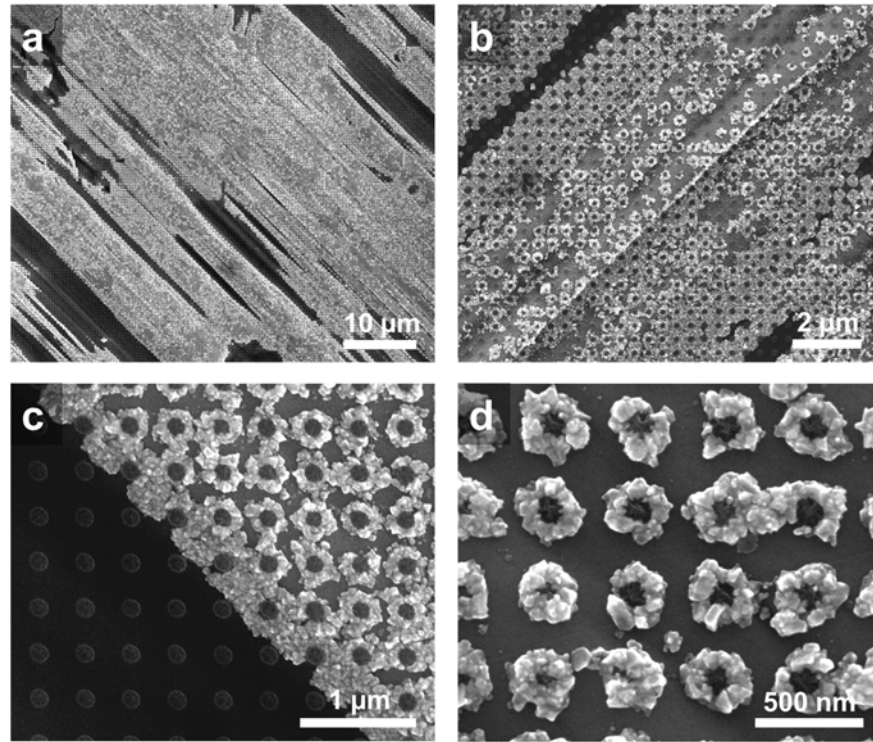
Figure 4.5 SEM images after Ni-Au electrodeposition through 400 nm periodic arrays of pillars on top of nickel strips. **a** Long range view of the sample surface. **b** Image showing the blend between continuous and ring-like deposits. **c** Close view of the two types of defects found across the sample: uncovered areas and rings around the pillars. **d** Metallic rings surrounding the pillars.

Despite these optimizations, the electrodeposition of Ni-Au films still exhibited non-negligible defects along the surface that could complicate the optical characterization. First, there existed an absence of coating along micrometer lengths (Figure 4.5a). This lack of deposit was due to an inhomogeneous SU8 residual layer caused by the inherent roughness of the nickel strips. As a result, the applied RIE time was not long enough to remove the underlayer across the entire surface. More important was the discontinuity of the layers observed in Figure 4.5b and c. While some regions presented a flat deposit, others were characterized by the formation of gold nanorings around the pillars (Figure 4.5d). The inhomogeneous morphology could reflect the low wettability of the surface, which led to a discontinuous deposition. The formation of metallic rings can be explained as a preferential nucleation at the pillars edges. Since the

electrodeposition cannot take place under the pillars, the electrical density increases right at the edges of the features.[22,23] This effect along with the hydrophobicity of the substrate could explain the lack of deposit in between the pillars.

Although interesting for other structures and applications, the formation of nanorings made unfeasible the proper fabrication of a multilayered structure. We concluded that if one desires a continuous and homogeneous layer infiltrated through a template, hydrophilic and flat surfaces are preferentially needed.

Electrodeposition on ITO coated glasses

Alternatively to nickel strips, ITO coated glasses were investigated as WE for the template-assisted electrodeposition. Despite its conductive properties, ITO presents higher resistance than metals (15 Ω/sq), what leads to the formation of isolated gold nanoparticles when electrodepositing at RT.[24] Higher electrolyte temperatures can increase the adatoms diffusion on the working electrode, leading to larger grains and smoother surfaces.[25] Based on previous works,[26] denser deposits were obtained when reducing gold at -0.9 V at 55 °C. However, they still formed non-continuous coatings for thickness of about 200 nm. Taking into account that our multilayered structure is based on 50 nm thick gold layers, these conditions were not suitable for our design. Again, a sacrificial nickel adhesive layer was first electrodeposited through the templates to ensure a homogeneous deposit.
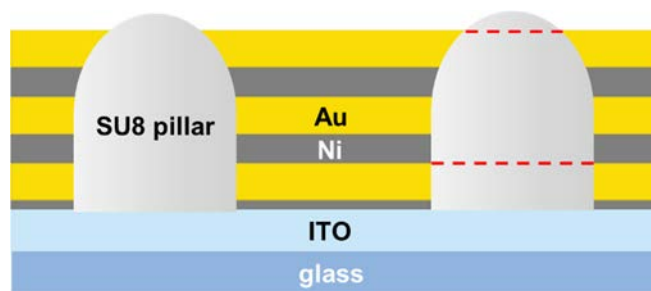
The multilayer electrodeposition through pillar arrays placed on ITO substrates was performed as follows. The sample was let in 55 °C hot nickel bath for 10 minutes. This period ensured the electrolyte diffusion through the template. A thin layer of approximately 10 nm was then electrodeposited at -0.9 V at the same temperature. Having successfully deposited a homogeneous adhesive film, the rest of layers could be nicely electrodeposited following our usual experimental conditions. In particular, alternating layers of gold and nickel were electrodeposited at RT at -0.7 V and -0.9 V, respectively. It is worth noting that the samples were always let immersed for 10 minutes in the electrolytes before the depositions in order to assure the homogeneity across the surface. After each step, they were rinsed in water for cleaning. The deposition rate for each metal was determined by SEM analysis on several pattern samples, being 2.9 ± 0.2 nm/s for nickel deposited at 55 °C, 1.1 ± 0.1 nm/s for nickel deposited at RT and 0.65 ± 0.06 nm/s for gold. The last two results manifest higher values than growth rates on unpatterned surfaces. Such effect can be attributed to the higher electrical density at

the proximity of the electroactive areas. Given the impossibility of reducing on the dielectric pillars, the ions migrate towards the closer uncovered surfaces, what increases the deposition rate. Based on this, the template favors the creation of more compact layers than an unpatterned surface.
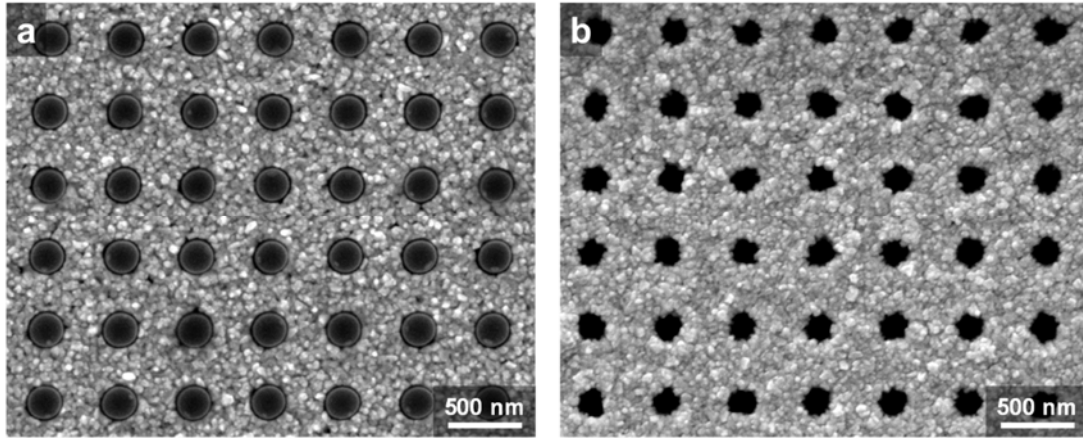
Figure 4.6 SEM images of 500 nm periodic templates after electrodepositing **a** the first gold layer and **b** four gold layers separated by nickel spacers.

Figure 4.6a presents the successful growth of the first nickel-gold layers deposited on ITO embedding 500 nm periodic pillars. The contrast with the deposition on nickel strips confirms the importance of the surfaces wettability. The formation of continuous layers on the ITO substrate enabled the multilayer deposition across the template height. With a similar grain morphology, the main difference after electrodepositing one and four gold layers lies on the smaller apertures obtained for the latter (Figure 4.6b). This observation indicates that the metallic stack has reached the top of the pillars. Specifically, from close examination of Figure 4.4c, one can notice that the shape of the pillars is not exactly cylindrical but rather domed at the top. This structural modification resulted from the RIE step. The metallic films at this location, therefore, present narrower holes than at the bottom part of the template (Figure 4.7).

Figure 4.7 Scheme of the multilayered metallic stack embedding the dielectric pillars. Red dashed lines mark the diameter of the pillars at the first and last gold layers as observed by SEM.

It is important to note that electrodepositing beyond the pillars height would eventually close the holes since the growth would not encounter any template limitation. In order to prevent the fishnet design, the amount of layers deposited through each template was varied based on the height of the patterns. We used two types of templates according to their height:

o Arrays with L = 200 and 300 nm were 150 nm tall and served for the infiltration of up to 3 gold layers with 45 nm thickness, always separated by 15 nm thick sacrificial Ni layers.

o Arrays with L = 400 and 500 nm were 330 nm high and enabled the deposition of even 4 gold layers with a thickness of 50 nm, separated by 30 nm Ni layers.
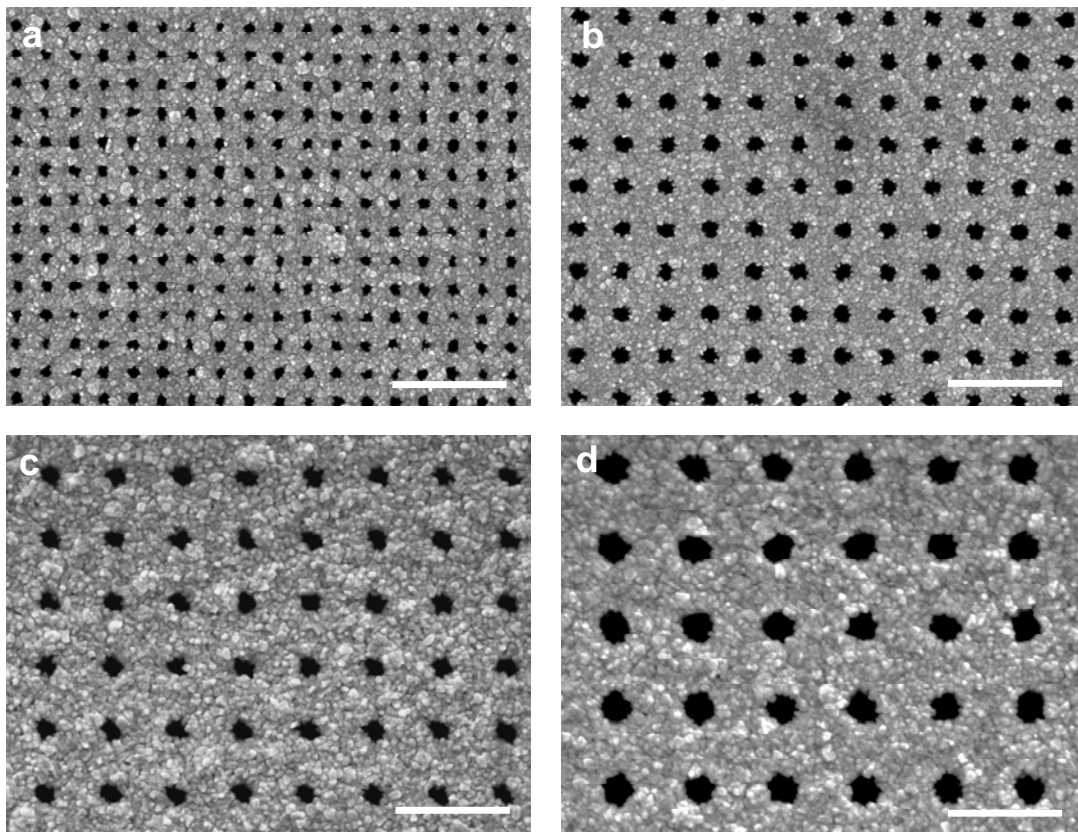
Figure 4.8 SEM top views of the multilayered metallic stacks with the maximum number of gold layers for **a** 200 nm, **b** 300 nm, **c** 400 nm and **d** 500 nm lattice spacing. Scale bars: 1 μm.

In our design, gold layers of around 50 nm thickness were considered as an appropriate value for, first, achieving homogeneous and continuous deposits and, second, for providing a good GSP coupling as presented in Chapter 3. The thickness of the nickel layers was chosen considering that wider gaps led to NIMs working at shorter

wavelengths (equation 3.3). For this reason and taking into account the experimental restrictions in terms of available height, nickel layers were grown as thick as possible. Figure 4.8 compares the structures with the maximum number of layers for each template used in this work. A very similar morphology is obtained in all the cases in spite of the space reduction between the pillars. Thus, our method based on using ITO as WE and first depositing a Ni adhesive layer effectively worked over a wide range of periodicities. These structures attest to the compatibility of electrodeposition through NIL templates.

4.2.3 Nickel dissolution

Sacrificial nickel layers were dissolved by immersion in 10 wt% HNO_3 for 15 min, cleaned in deionized water and dried by air blowing. Using ITO substrates during the electrodeposition avoided the need of transferring the structures to transparent substrates for their optical characterization. In this way, the quality, size and homogeneity of the structures were highly preserved. Figure 4.9 presents images of the samples obtained after nickel removal.
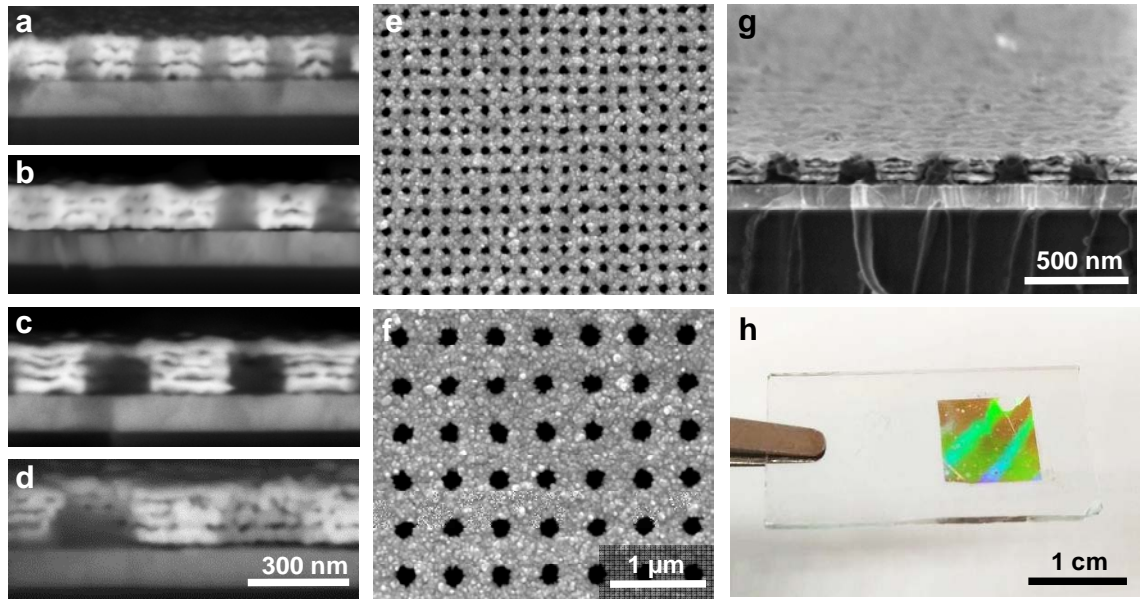
Figure 4.9 SEM cross-sectional views of MIM fishnet metamaterials with the maximum number of gold layers for **a** L = 200 nm, **b** L = 300 nm, **c** L = 400 nm and **d** L = 500 nm. Top views of structures with **e** L = 200 nm and **f** L = 500 nm at the same stage. **g** Tilted perspective of 400 nm pitch fishnet metamaterial with 4 gold layers. **h** Photograph of a L = 500 nm fishnet metamaterial after nickel dissolution.

Figure 4.9a-d shows the SEM side view from samples with different lattice parameters. Although sometimes collapsed after cutting the samples, once can easily identify the gold layers separated by air gaps and supported by the SU8 pillars. The gap widths were found to be slightly smaller than the nominal Ni thickness. This was attributed to a thinner deposit that estimated or to a small fall of the gold layers when removing the nickel supports. Top view SEM images from the structures with L = 200 and 500 nm with 3 and 4 gold layers, respectively, are shown in Figure 4.9e and f. The tilted view of a fishnet structure of L = 400 nm with 4 gold layers is presented in Figure 4.9g and illustrates the good quality of the samples. This is indeed perceived just by naked eye observation of the iridescent large area samples (Figure 4.9h).

We can conclude that we have successfully developed a new straightforward method for the fabrication of large area multilayered fishnet metamaterials. Our approach is strongly compatible with different structural dimensions such as the lattice, the diameter or number of layers. Table 4.1 summarizes the geometrical parameters of all the fabricated samples according to the scheme presented in Figure 4.10.
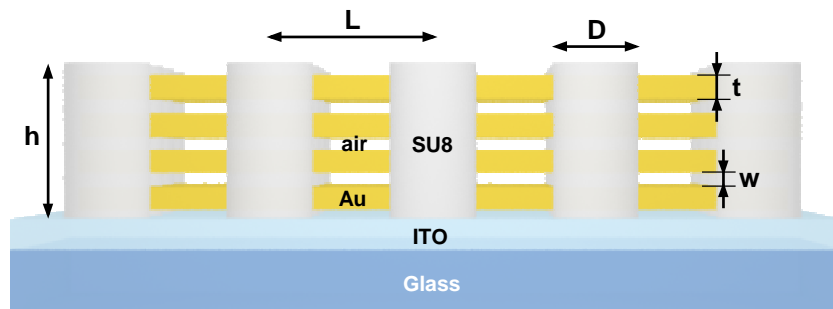
Figure 4.10 Scheme of the fabricated samples denoting their composition materials and geometrical parameters. L stands for lattice spacing, D for pillars diameter, h for pillars height, t for metal thickness and w for gap width.

Table 4.1 Geometrical features of the fabricated structures.

L (nm)	D (nm)	h (nm)	t (nm)	w (nm)	#Au layers
200	85	150	45	15	2, 3
300	115	150	45	15	2, 3
400	180	330	50	25	2, 3, 4
500	210	330	50	25	2, 3, 4

4.3 Optical characterization of multilayered fishnet metamaterials

The previous section proved the feasibility of fabricating fishnet structures featuring several layers over different templates. In order to study their optical properties and understand the dependence with the features dimensions, the samples were characterized in transmission T and reflection R. The spectroscopic properties were measured at normal incidence by FTIR.

Given the anisotropy caused by the substrate, reflectance spectra were compared for light impinging from the top and bottom sides of samples made of L = 500 nm. As presented in Figure 4.11a, when illuminated from top, the reflectivity of the samples increases with the number of layers while losing definition of the optical features. Such observations can be explained when analyzing in detail our samples. First, an increase in the number of layers could bring about higher reflectance values because of the larger amount of metal within the structure. Second, since the first light-matter interaction takes place at the top gold layer, any morphological variation at this point could lead to noticeable spectral modifications. As previously discussed, the pillars become narrower at the top part, leading to larger metallic surfaces and thus, higher reflectivity. More important is the loss of definition with the number of layers, whose explanation can be found at the scattering caused by the gold layers roughness.
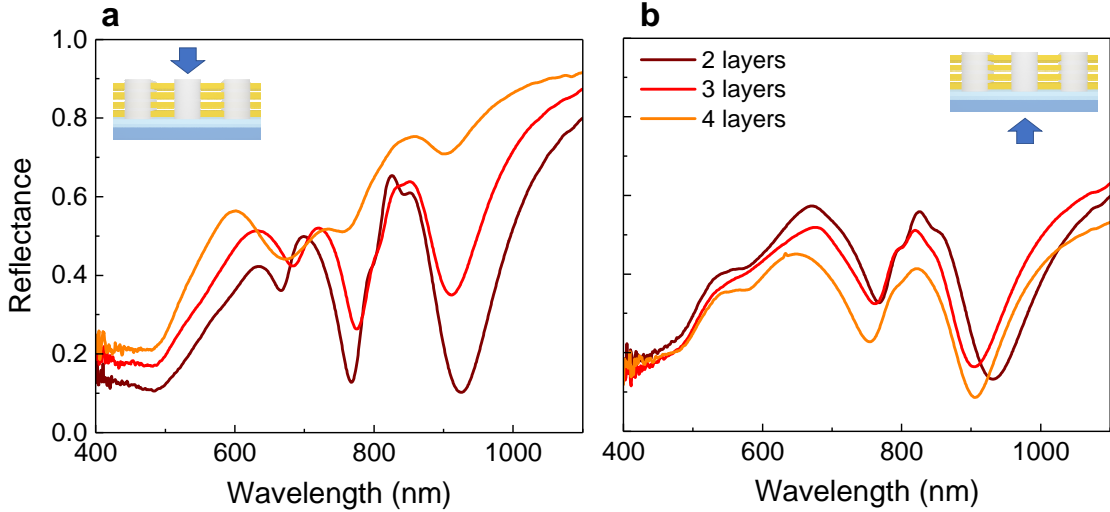
Figure 4.11 Reflectance spectra of multilayered fishnet structures with L = 500 nm measured **a** from top and **b** bottom sides.

Analogous results were obtained when measuring from the bottom side (Figure 4.11b). The first observation is the signal attenuation coming from the absorption

through the ITO layer.[27] In contrast with the previous configuration, an increase of the number of layers does not imply higher reflectance values. This indicates that such increase was not mainly related with the number of layers but rather with the metal fraction of the top layer. The similarity of R spectra for all the samples when measuring from bottom corroborates this statement since all the structures present the same base diameter and, hence, same metal fraction where the first light-matter interaction occurs. The main contrast might be the better definition of the curves. Given the lower roughness of ITO when compared with the electrodeposited layers, the first gold interface is smoother than the others. As a result, the light is less scattered than in the former configuration and, therefore, the optical features are better defined.

Considering that we aimed to numerically reproduce as accurately as possible our experimental results, hereafter we mainly worked with the spectra collected from the bottom because of the higher resolved curves. Spectra acquired from the top were also taken as control measurements and compared with the corresponding simulations. Transmission spectra were as well measured in both configurations and presented identical curves, in agreement with the reciprocity dictated by Fresnel laws (Section 3.5.2).

Figure 4.12 presents the transmission and reflection measurements (left) for each batch of samples with the corresponding simulations (right). The experimental curves are representative spectra of the homogeneous optical response along the surface. FDTD simulations based on the parameters specified in Table 4.1 reproduced well both the position and intensity of the experimental curves, thus corroborating the quality of the final structures. In the case of L = 200, 300 nm, the spectra were fitted to 45 ± 7 nm thick gold layers and 14 ± 4 wide gaps, where the error ranges correspond to the standard deviation from the average fitted values. For structures with L = 400, 500 nm, the spectra were fitted to 50 ± 5 nm thick gold layers and gap widths of 27 ± 3 nm. The first observation from the optical response reveals two main resonances for all the fishnet structures except for the samples with lattice parameter L = 200 nm, whose first resonance likely falls within the gold absorption band. The resonance redshifts when increasing the periodicity of the structures. This behavior is ascribed to the excitation of plasmonic resonances in a metallic grating, where the resonant wavelength scales with L. The disagreement of L = 300 nm with this trend indicates that other geometrical dimensions must be taken into account when analyzing the peaks position.
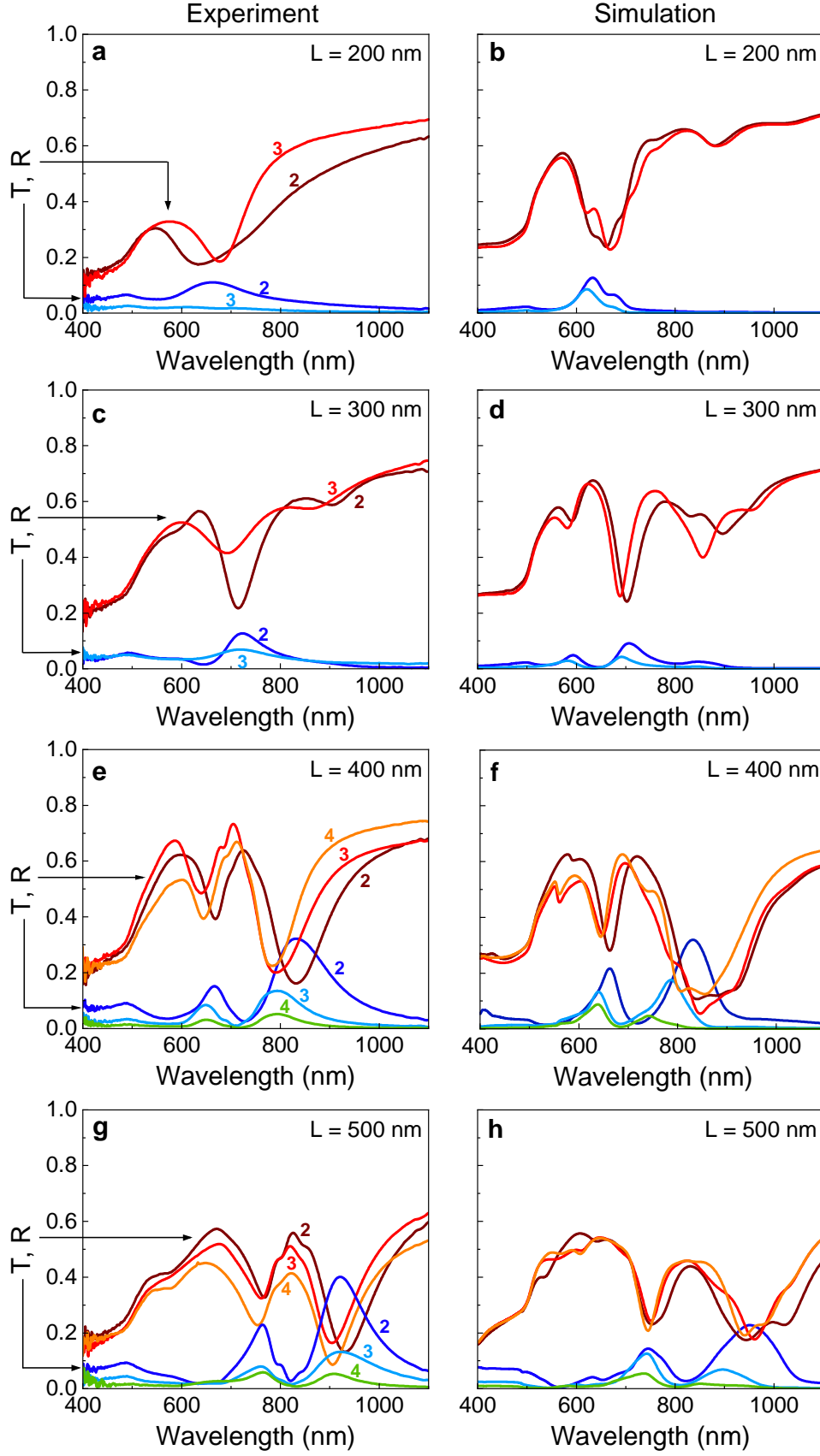
Figure 4.12 Measured (left) and simulated (right) spectra of fishnet metamaterials with lattice parameters of **a,b** 200 nm; **c,d** 300 nm; **e,f** 400 nm and **g,h** 500 nm. The numbers indicate the amount of gold layers present in each sample.

To investigate the physical origin of these resonances, we studied the electromagnetic fields distribution in a fishnet metamaterial of L = 500 nm composed by 4 layers (orange curve in Figure 4.12h). As presented in Figure 4.13, the low wavelength peak is characterized by an EM confinement within the pillars and the SPP excitation at the Au-ITO interface. Thus, the substrate material and the cylinders diameter mainly govern the resonant wavelength.
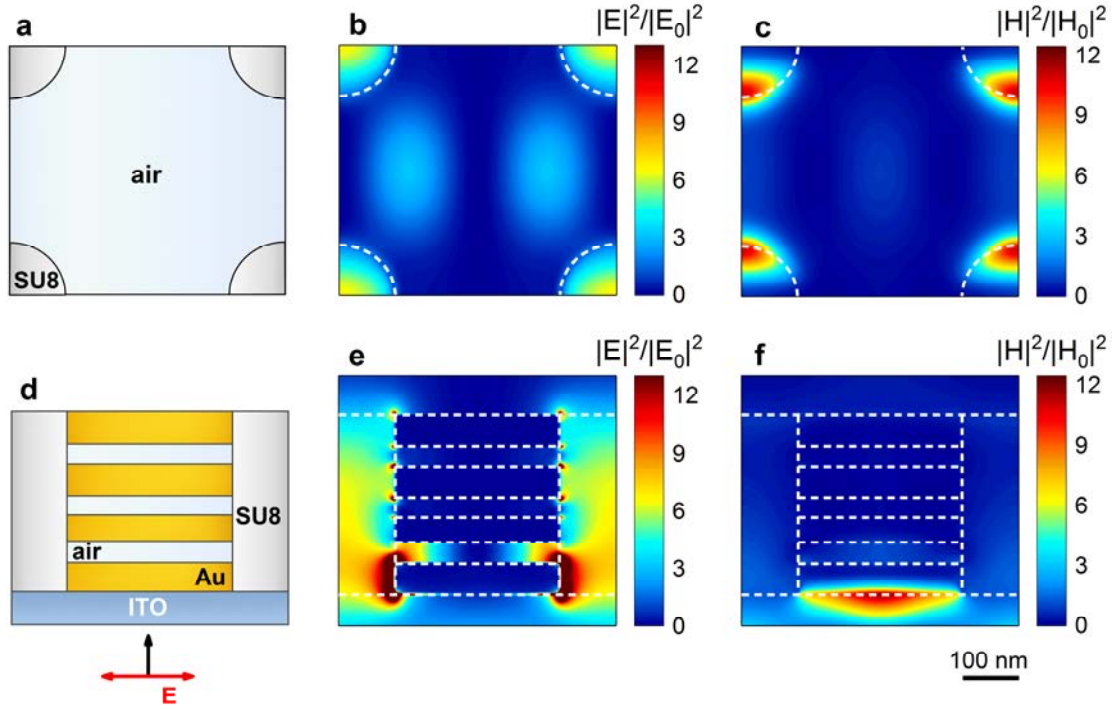
Figure 4.13 Schemes of the simulated structure at **a** the middle air gap plane and **d** the cross-sectional plane parallel to E polarization. **b-f** Normalized EM intensities at the low resonant wavelength (λ = 745 nm) at both planes of a fishnet metamaterial made of L = 500 nm and 4 layers. White dashed lines delimit the materials surfaces.

On the contrary, the EM profiles found at the second peak (Figure 4.14) highly resemble the distributions observed for double fishnet metamaterials made with PS spheres (Figure 3.16 from Chapter 3). The electric field concentrates at the Au-SU8 interfaces in the same direction as the electric field polarization (Figure 4.14b,e). The magnetic profiles indicate, first, a dependence on the pillars separation (Figure 4.14c) and second, the existence of a strong magnetic confinement in the dielectric gaps (Figure 4.14f). As previously explained, this EM distribution is responsible of the negative-index phenomenon in fishnet designs, where magnetic dipoles are induced in the dielectric layers thanks to the excitation of GSPs. Therefore, from the spectra presented in Figure 4.12, the resonances of interest for NIMs are the high wavelength peaks.

The relation with the pillars diameter in both EM distributions explains why samples with L = 300 nm present resonant wavelengths comparable with the ones of larger periodicities. When analyzing these designs, one should have in mind not only the lattice parameter of the grating but also the lateral dimension of the features. Calculating the ratio D/L from the values given in Table 4.1, it is found that geometries with L = 200, 400 and 500 nm present a ratio of the order of 0.43, while the design with L = 300 exhibits a lower ratio of 0.38. Larger diameters would have implied a ratio in line with the other periodicities and, moreover, shorter resonant wavelengths as demonstrated in Section 3.2.
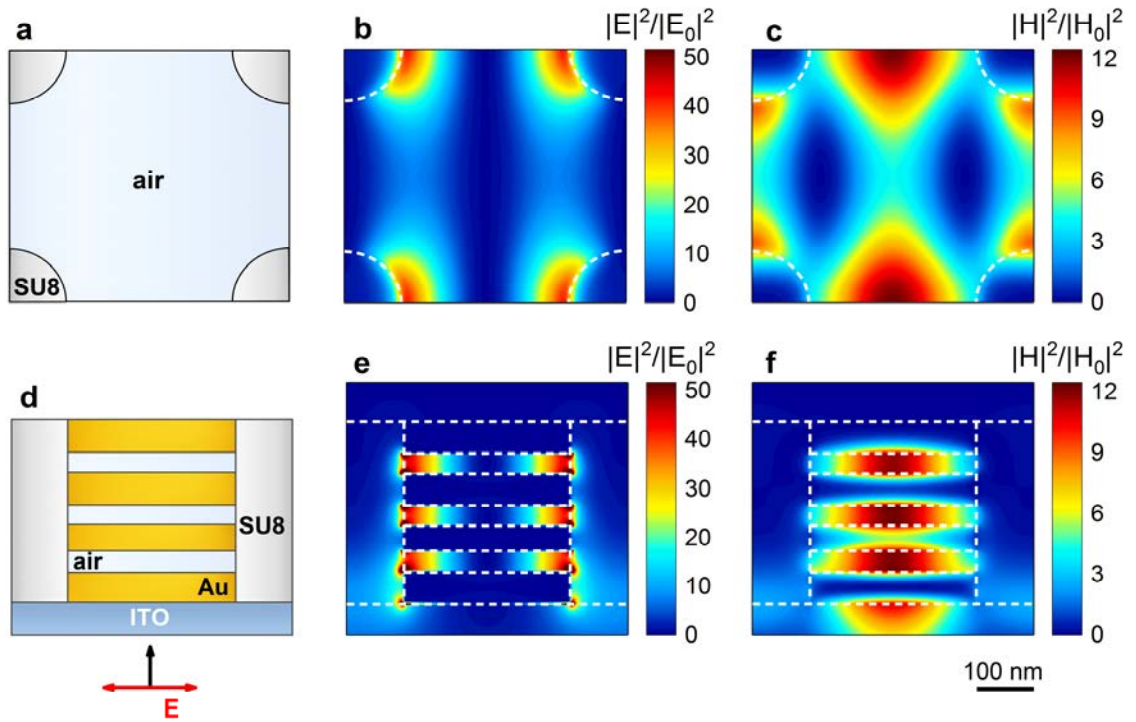
Figure 4.14 Schemes of the simulated structure at **a** the middle air gap plane and **d** the cross-sectional plane parallel to E polarization. **b-f** Normalized EM intensities at the high resonant wavelength (λ = 981 nm) at both planes of a fishnet metamaterial made of L = 500 nm and 4 layers. White dashed lines delimit the materials surfaces.

## 4.4 Effective properties of multilayered fishnet metamaterials

4.4.1 Effective parameters

The effective parameters of the fabricated structures were retrieved from the simulated complex transmission and reflection coefficients as described in the Appendix. We made use of the effective medium approximation[28,29] and considered the anisotropy of the structures caused by the substrate.[30,31]

Refractive index

Figure 4.15 presents the real part of the effective refractive index n_{eff} for each batch of samples along with the FOM of each metamaterial. Negative indices are found at the high wavelength resonance, confirming that the magnetic confinement found in the air gaps leads to this extraordinary property. As foreseen in the spectra, the operation region mainly depends on the lattice parameter of the metamaterial, shifting to longer λ as the periodicity increases. In opposition, the negative band blue shifts when increasing the number of layers. Thanks to our broad range of structures and the proper relation between L and D, we successfully obtained metamaterials working from the visible to the NIR range.
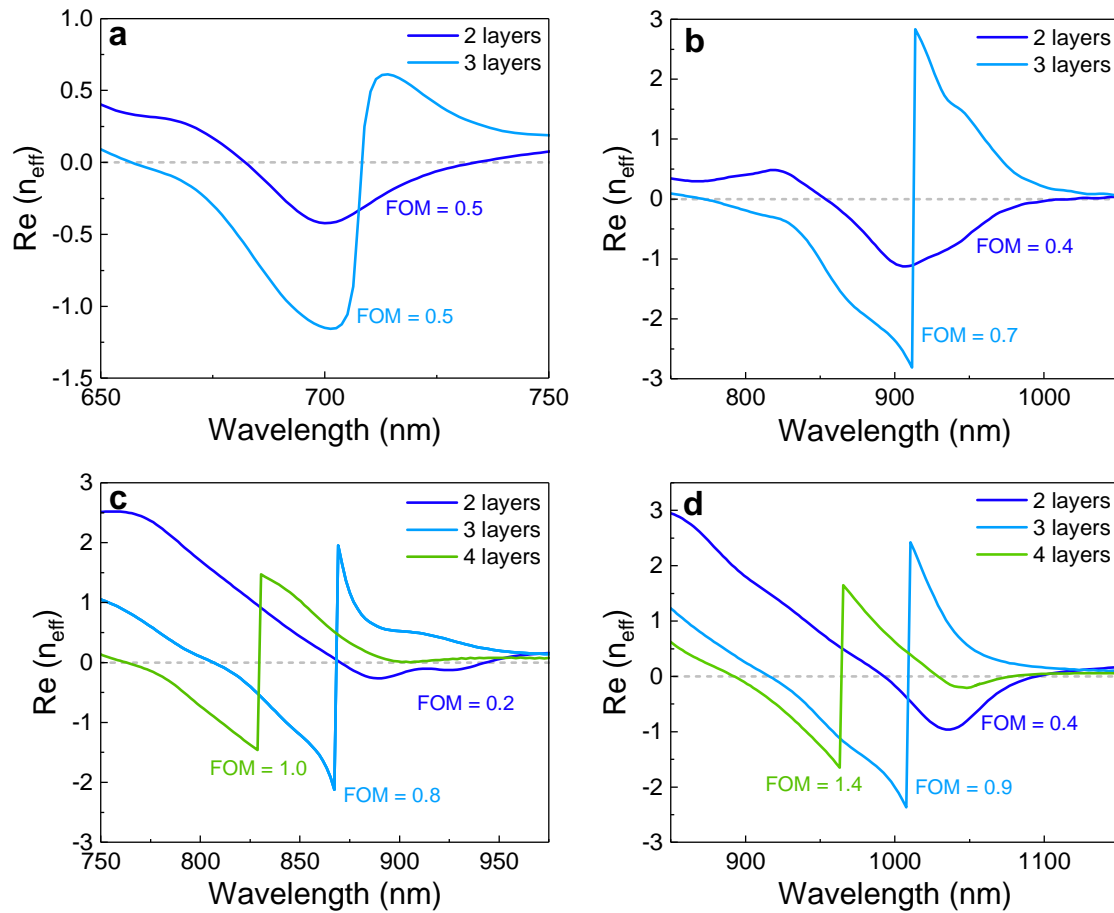
Figure 4.15 Effective refractive indices of all the fabricated samples retrieved from simulations. The lattice spacing corresponds to **a** 200 nm, **b** 300 nm, **c** 400 nm and **d** 500 nm.

In the visible, the minimum achieved is n_{eff} = -1.2 (λ = 700 nm), arising from the structure with L = 200 nm and 3 gold layers with 15 nm wide gaps (Figure 4.15a). We should emphasize the fact that large area NIMs working at this region are scarce because of the complex fabrication process at this scale.[4,7] In the NIR, we achieved values up to

-2.8 at λ = 910 nm (Figure 4.15b) or -2.1 at λ = 870 nm (Figure 4.15c), within the first telecommunication window. The achievement of such strong values has been rarely reported in this region, with similar results only at longer wavelengths.[12,32,33]

Figure of merit

The FOM improvement when increasing the number of layers is known to happen due to the shift of the minimum real part from the maximum imaginary part of n_{eff}.[34,35] Moreover, a gradual increase of the FOM is observed as L becomes larger, as plotted in Figure 4.16. This relation manifests the complex task of designing and fabricating efficient NIMs working at visible wavelengths, where the metal losses become more relevant.
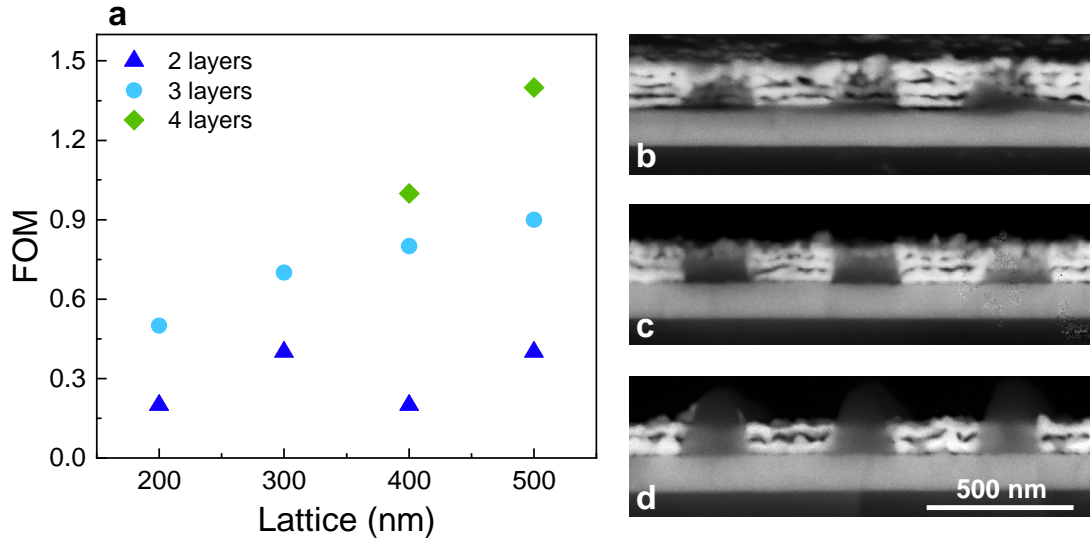
Figure 4.16 a Figure of merit of the NIMs as a function of their lattice parameter. SEM images of fishnet structures with L = 500 nm and **b** four gold layers, **c** three layers and **d** two layers.

Permittivity and permeability

Figure 4.17 presents the effective permittivity and permeability obtained from the retrieval procedure. The positive values of the permeability along with the permittivity being negative classify our metamaterials as single-NIMs, where n_{eff}< 0 is attained with just one of these parameters below zero. It is worth noting that in all the cases the permeability differs from 1 at the operation region, implying a magnetic response at NIR and visible wavelengths. The permeability is also found to decrease with the number of layers up to near-zero values like in the cases of the largest L with more than two gold layers (Figure 4.17f and h). The combination of the latter with near-zero permittivities (Figure 4.17g) leads to the interesting subgroup of near-zero metamaterials. These

systems also attract high interest in the community because of the small light phase variation within the structure, what enables phenomena such as radiation patterning or spontaneous emission manipulation.[36,37]
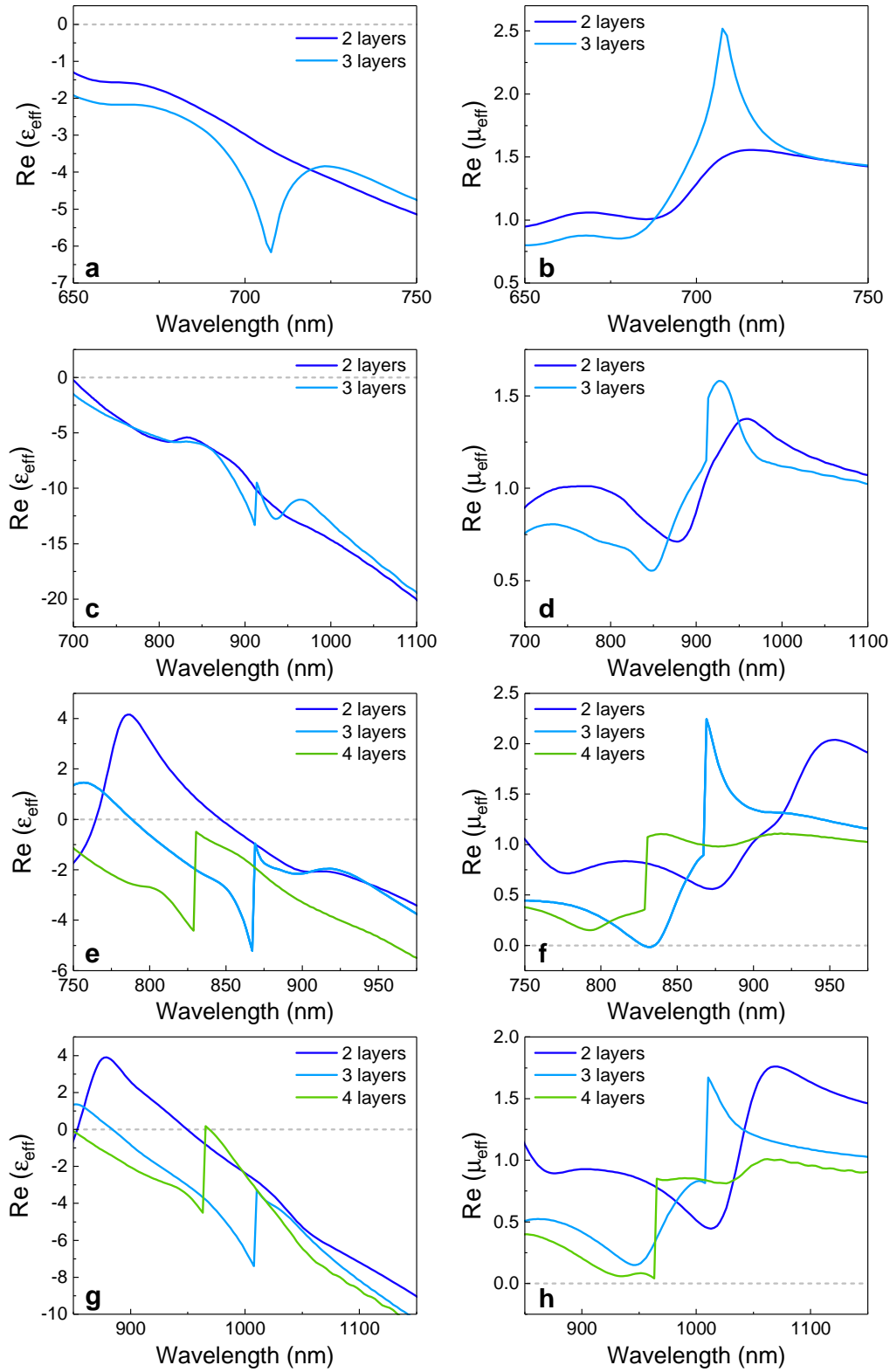
**Figure 4.17** Real parts of the effective permittivity (left) and permeability (right) for samples with periodicities of **a,b** 200 nm, **c,d** 300 nm, **e,f** 400 nm and **g,h** 500 nm.

4.4.2 Change of branch in the refractive index

When light propagates in a periodic structure, an infinite number of modes is excited for a given wavelength. Among them, the mode with the lowest absorption governs the optical response.[38] This is the reason why the refractive index in periodic structures, does not depend only on the wavelength but also on the propagating mode. In the case of fishnet metamaterials with more than two metallic layers, the two branches observed for n_{eff} (Figure 4.15) represent the change on the dominant mode propagating inside the system. This was studied in a fishnet metamaterial with L = 400 nm and 4 gold layers by analyzing the EM distributions below and above the refractive index discontinuity found at λ = 829 nm (Figure 4.18).
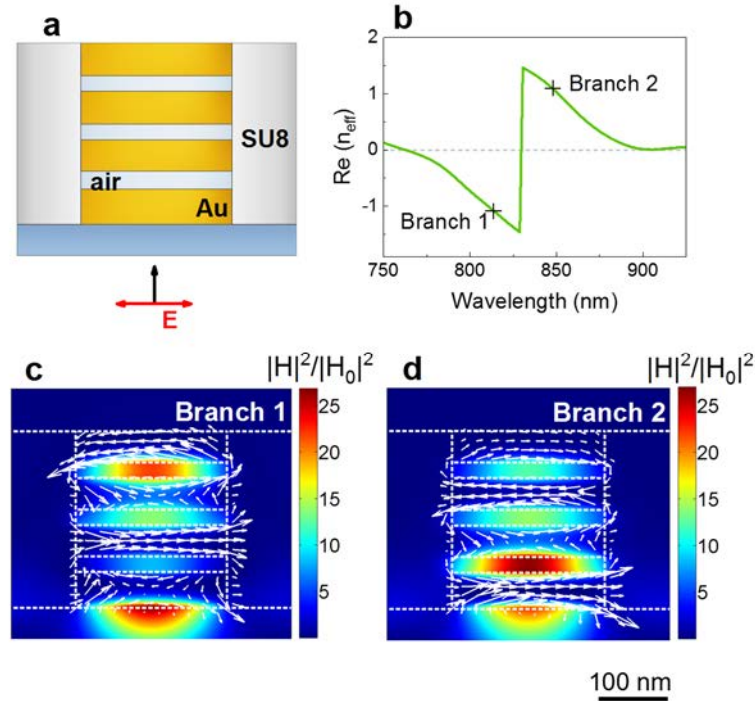
Figure 4.18 a Cross-sectional scheme of the simulated structure. **b** Effective refractive of the fishnet metamaterial made by L = 400 nm and 4 gold layers. Magnetic field profiles at **c** branch 1, where n_{eff}< 0, and at **d** branch 2, where n_{eff} > 0. White arrows show the electric current density.

On one hand, when n_{eff} < 0 (branch 1), the top and middle air gaps exhibit in-phase contouring current vectors, leading to in-phase magnetic dipoles at these locations, with a strong enhancement at the top gap. On the other hand, when n_{eff} > 0 (branch 2), the magnetic field is mainly concentrated in the bottom space, with contouring current loops being in phase for the bottom and middle gaps. Therefore, a change in propagating mode is perceptible in the magnetic profile as well as in the direction of the antisymmetric currents generated in the gold-air interfaces.

4.4.3 Angular dependence of the working wavelength

Figure 4.15 showed that the position of the negative index band depends on the number of layers that compose the structure. For a given lattice, a blue shift appeared when increasing the amount of layers. Former works have discussed the dependence of the effective properties on the metamaterial thickness, this is, on the number of MIM cavities composing the structure.[35,39,40] It has been shown that by reaching a minimum number of stacked layers, the multilayered fishnet metamaterial converge to the so-known bulk metamaterial regime.[34,41]
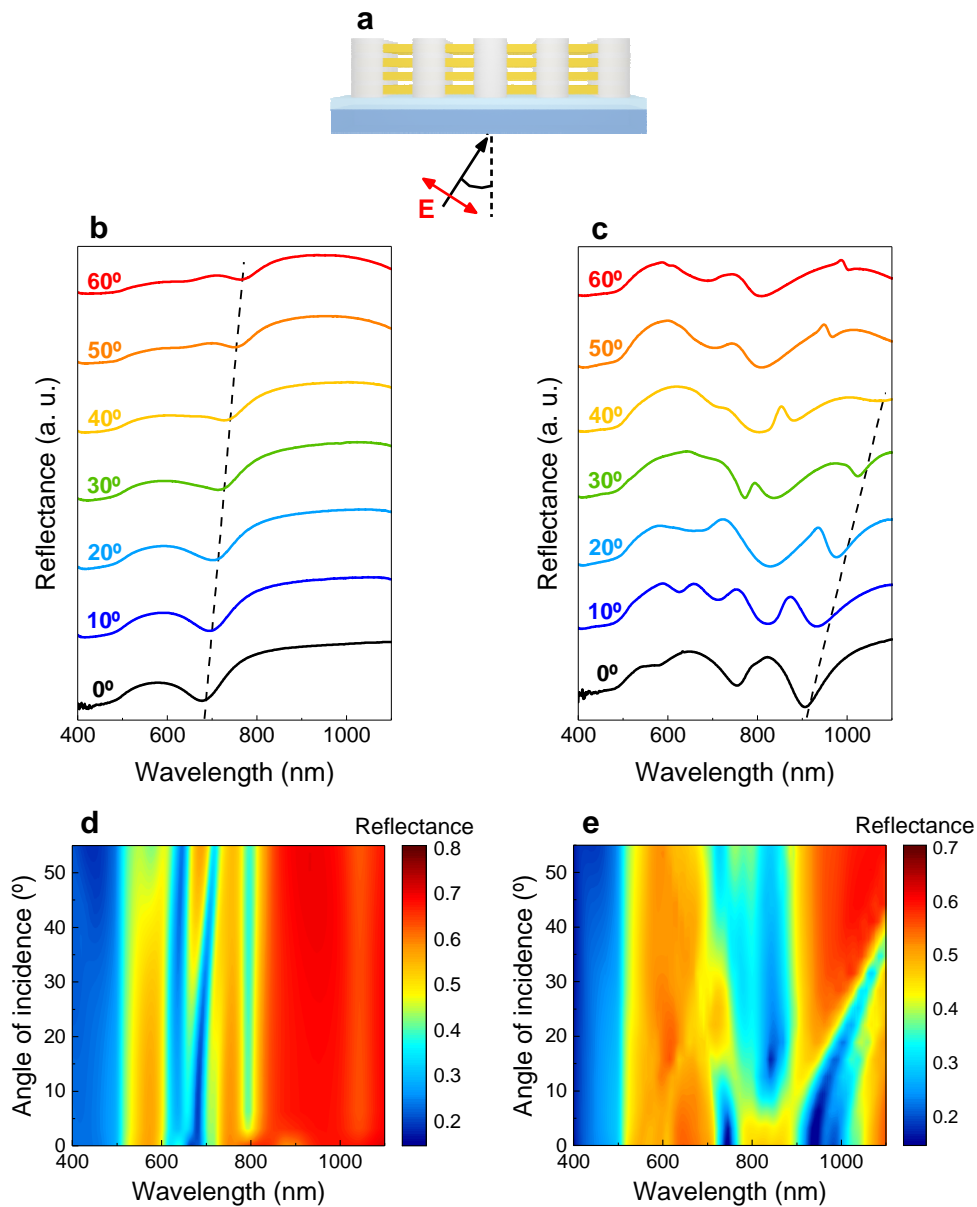
Figure 4.19 a Scheme of the TM oblique excitation. Experimental reflectance spectra collected in this mode for different incident angles in fishnets with **b** L = 200 nm with 3 gold layers and **c** L = 500 nm with 4 gold layers. Dashed lines are a guide to the eye indicating the evolution of the GSP resonance. **d,e** Calculated angular dispersions for the same structures and configuration.

At this limit, metamaterials present unambiguous effective properties independently of the number of unit cells or the angle of incidence, exhibiting weak angular dispersion. The small shift of the band observed in Figure 4.15a,b for L = 200 nm and 300 nm suggests that the structures are approaching to the bulk limit with just 3 gold layers, this is, two MIM cavities.

We tested this assumption by measuring reflection from the samples with light impinging at 0º, 10º, 20º, 30º, 40º, 50º and 60º. Reflectance in TM mode is expected to be highly sensitive to the angle of incidence because of the change in the E field direction respect to the surface plane (Figure 4.19a). Figure 4.19b and c show the angle-resolved reflection measurements taken under TM configuration for the fishnet structures with L = 200 nm and 3 gold layers and L = 500 nm and 4 gold layers, respectively. For the largest periodicity, a clear redshift of the GSP resonance is observed in line with the results developed in Chapter 3 and in previous works.[35,42] Such behavior has been found to come from the electromagnetic field delocalization across the gaps and interaction between adjacent cells (Figure 4.20). As a result, the coupling energy of the GSP mode decreases for higher incident angles and thus, the resonant wavelength redshifts.[43]
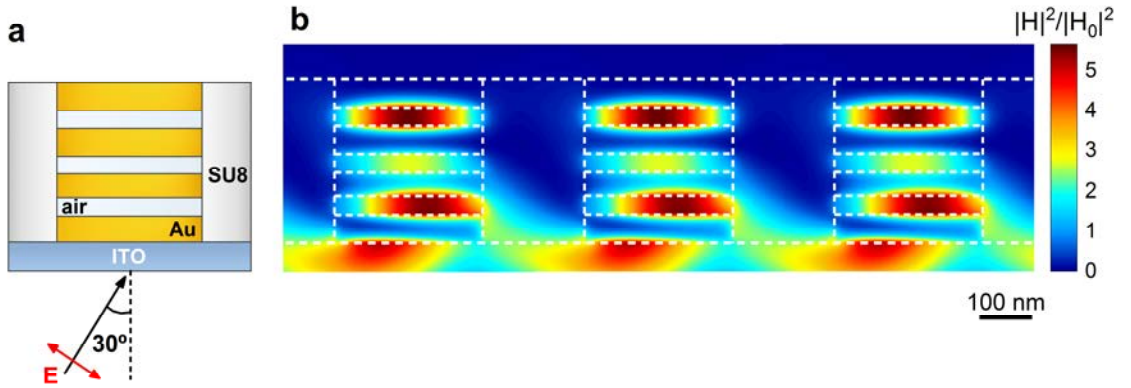
Figure 4.20 a Scheme of the simulated structure in TM configuration, being 30º the incident angle from air. **b** Normalized magnetic intensity at the gap resonant wavelength of three adjacent cells, showing the electromagnetic coupling between them. The lattice corresponds to 500 nm.

In contrast, the sample with the smallest periodicity (L = 200 nm) presents weak angular dispersion, outlining the robustness of this structure with the angle and, therefore, its close convergence to a bulk metamaterial. The trends observed for both structures are supported by the angular dispersion obtained from the simulations, which present a very good agreement with the measurements (Figure 4.19d,e).

Both measurements and simulations for the TE mode (Figure 4.21) show no significant changes in the GSP resonance since the direction of the E field remains constant with respect to the structure as the angle increases.
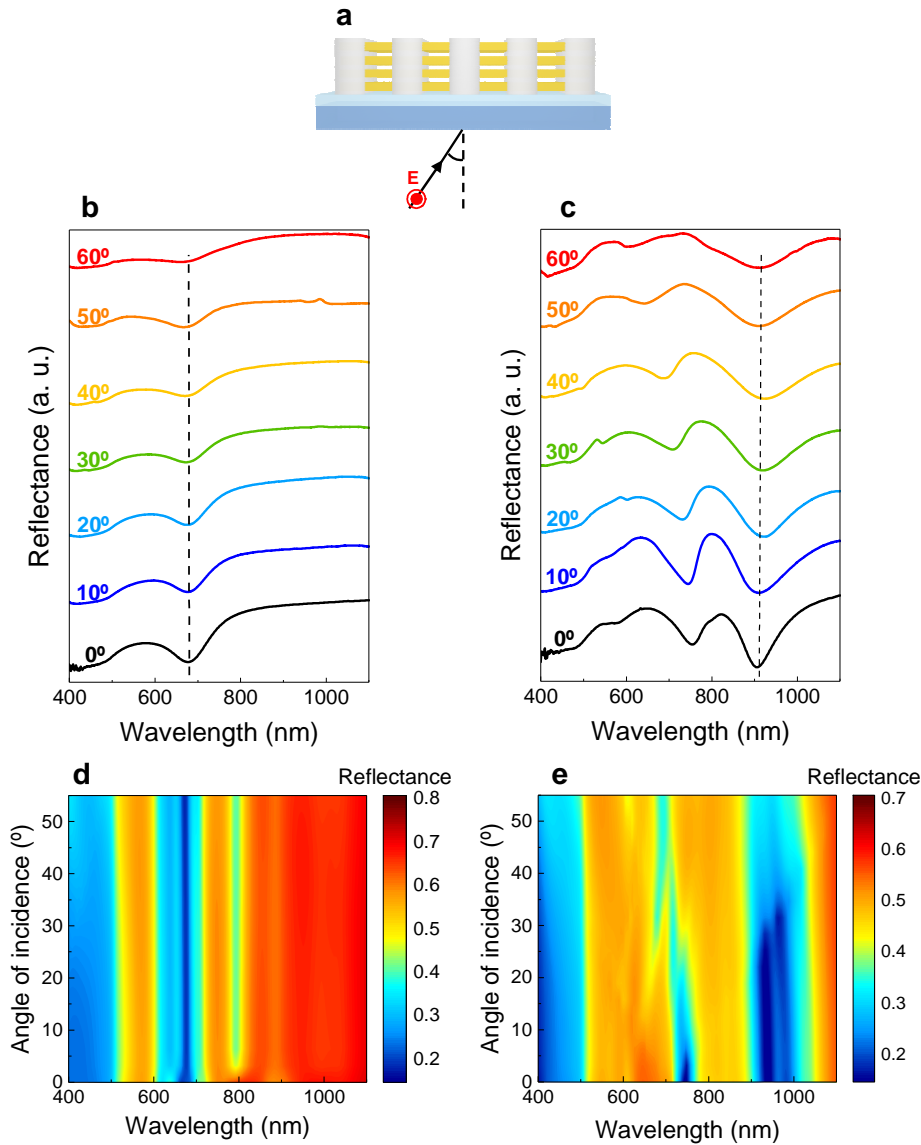
Figure 4.21 a Scheme of the TE oblique excitation. Experimental reflectance spectra collected in this mode for different angles for fishnet metamaterials with **b** L = 200 nm with 3 gold layers and **c** L = 500 nm with 4 gold layers. Dashed lines are a guide to the eye indicating the evolution of the GSP resonance. **d,e** Calculated angular dispersions for the same structures and configuration.

4.5   Fishnet metamaterials as refractive index sensors

Optical sensors are acquiring great attention in technology for their ability of transducing refractive index changes into chemical, biological or food modifications.[44] Plasmonic structures stand out in this field because of the strong EM enhancement at the resonant wavelengths, which are highly sensitive to any variation in the surrounding

medium. Several works have published in the recent years the fabrication and characterization of plasmonic structures serving as refractive index sensors. Examples of diverse geometries include MIM gratings,[45] metal dimers,[46] graphene-metal hybrid systems[47] or even NIMs made from split-ring resonators.[48]

In a common fishnet design, the system is composed by a stack of metal and dielectric layers, drilled with air apertures. Our systems, in contrast, present a different structure where the apertures are made of a solid material and the dielectric spacers correspond to air gaps. This unique structure can be understood as a porous material that allows the infiltration of different media through the gold layers. As a proof of concept, here we explore the opportunity of tuning the optical response of the metamaterials when infiltrating liquid media in between the metallic layers. Since the achievement of negative refractive index relies on the high EM confinement at the air gaps, the optical properties of the structures are expected to strongly depend on the medium placed at this location.[45,49]

Liquids covering a broad range of refractive index n were chosen in order to study the dependence of the GSP resonance with the dielectric medium embedded. In particular, me made use of water (n = 1.33), isopropanol (n = 1.38), cyclohexane (n = 1.42), toluene (n = 1.49) and chlorobenzene (n = 1.53). For these measurements, a drop of the liquid of interest was placed on top of a glass slide and covered by the sample facing down so that the fluid penetrated through the layers (Figure 4.22). The whole system was then placed in the FTIR setup for reflection measurements. After the spectra collection, the samples were rinsed with isopropanol and dried with air blowing.
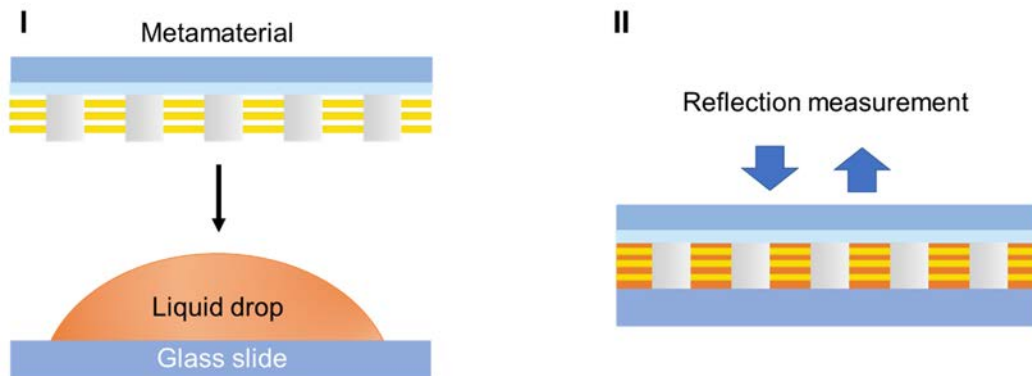
Figure 4.22 Scheme of the liquid infiltration experiment. **I** Fishnet metamaterials are placed facing down on a liquid covered glass slide. **II** After infiltration through the air gaps, reflection spectra of the whole system are collected.

Figure 4.23 presents the wavelength dependence of the limit samples of (a,c) L = 200 nm and (b,d) L = 500 nm. A redshift is observed when increasing the refractive index of the dielectric spacer, implying a redshift as well on the negative n_{eff} operation region. This trend is in good agreement with equation (3.2), which indicates that in the linear approximation the vacuum wavevector is inversely proportional to the refractive index of the spacer. Consequently, the resonant wavelength scales with the index of this layer. It is interesting to note that while this equation presents a linear relationship, our experiments follow a polynomial curvature. This is ascribed to a non-linear dependency over broad index ranges such as ours, in line with other studies about the surface plasmon resonance dependency with bulk solutions.[50,51]
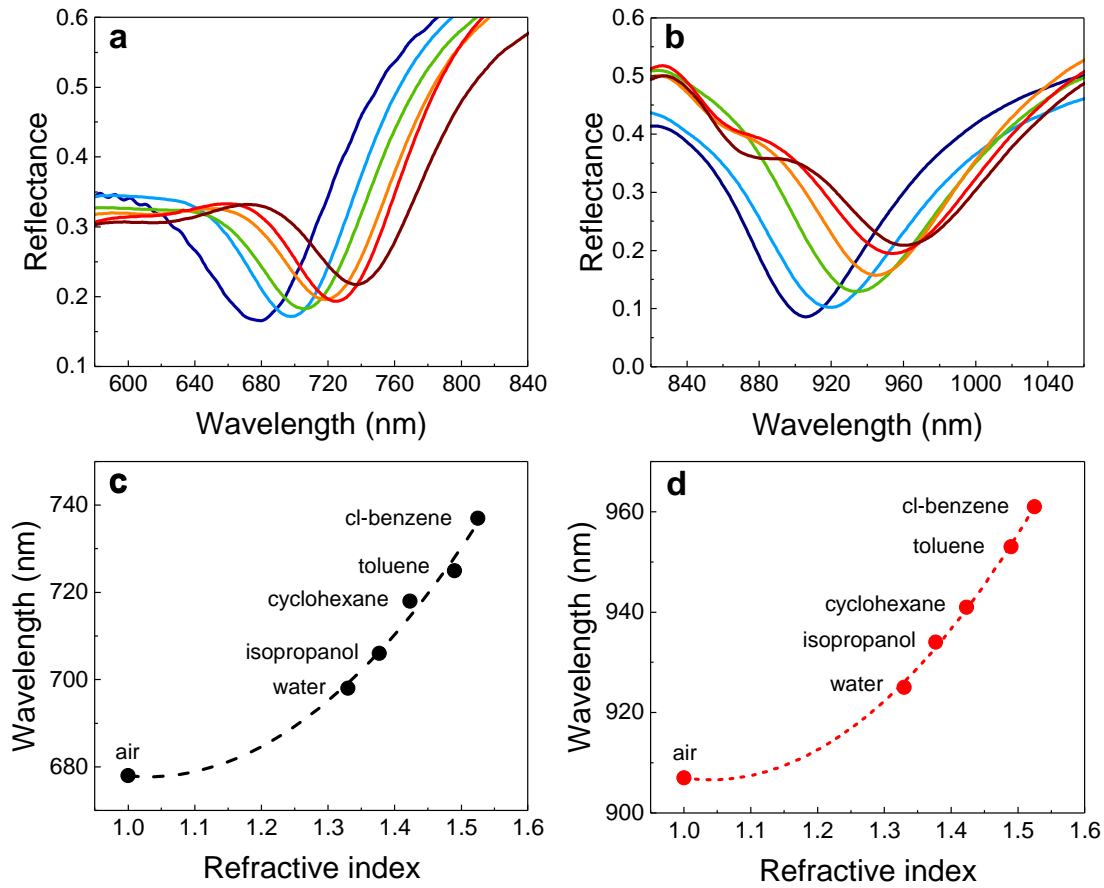
Figure 4.23 Reflectance spectra of fishnet metamaterials made of **a** L = 200 nm with 3 gold layers and **b** L = 500 nm and 4 gold layers separated by air (dark blue) or infiltrated by water (cyan), isopropanol (green), cyclohexane (orange), toluene (red) and chlorobenzene (brown). **c,d** Resonant wavelength as a function of the refractive index of the liquids for the same structures. Dashed curves describe a second order polynomial fitting.

The wavelength shift observed when infiltrating different optical media suggests the capability of these structures for refractive index (RI) optical sensing. Three parameters are commonly used to characterize RI sensors: sensitivity (S), figure of merit (F) and quality factor (Q-factor), defined as:

$$S = \frac{\Delta\lambda}{\Delta n} \qquad (4.1)$$

$$F = \frac{S}{FWHM} \qquad (4.2)$$

$$Q - \text{factor} = \frac{\lambda}{FWHM} \qquad (4.3)$$

The sensitivity is the ratio of the change in resonant wavelength $\Delta\lambda$ to the bulk RI variation Δn, usually expressed as a function of refractive index units (RIU). The figure of merit of a sensor reflects is selectivity, defined as the normalization of the sensitivity divided by the full width at half maximum (FWHM) of the resonant dip. The Q-factor is a measurement of the resonance sharpness and, therefore, of its definition. From a linear fit of the wavelength shift at high index media (Figure 4.24), the sensitivity to surrounding medium changes was found to be 190 nm/RIU and 180 nm/RIU for metamaterials with L = 200 nm and L = 500 nm, respectively. The figure of merit was calculated at each point, giving an average value of F = 2 in both cases. Lastly, Q-factors of 7 and 11 were obtained for fishnets with L = 200 and 500 nm, respectively.
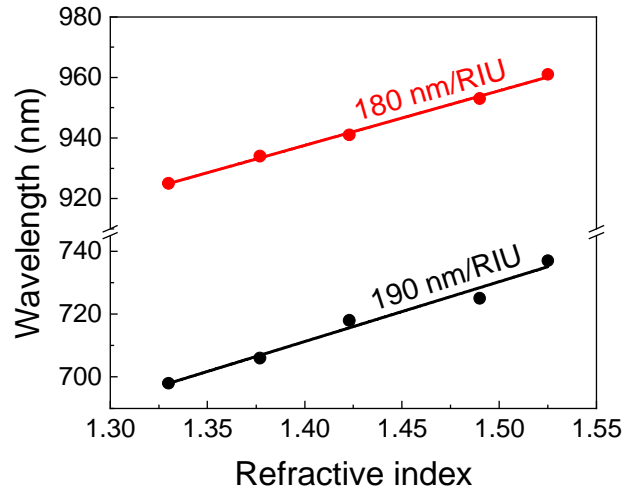
Figure 4.24 Evolution of the resonant wavelength with the refractive index of the infiltrated solvents for structures with (black) L = 200 nm and 3 gold layers and (red) L = 500 nm and 4 gold layers.

These values are in line with those obtained by other plasmonic RI sensors working at optical wavelengths,[52,53] except in our case, the platforms exhibit the particularity of a negative index of refraction. Our results are of great relevance for the scalable development of both negative index metamaterials and GSP-optical sensors,

being the first fishnet structure applied to this domain. In future experiments, the media sensitivity combined with the negative index of the structures could lead to tunable flat lenses.

As preliminary results of the change in the negative band, Figure 4.25 shows the effective refractive index of the metamaterial with L = 200 nm filled with air, water and chlorobenzene. The values were retrieved by fitting the measurements shown in Figure 4.23. As observed, the negative index decreases and the operation band shifts to longer wavelengths when infiltrating higher RI media within the metamaterial. Thus, these systems would enable focusing light at different wavelengths or focal lengths depending on the embedded liquid.
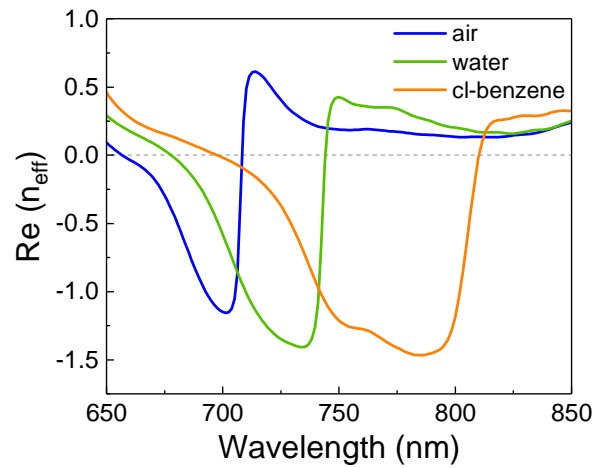
Figure 4.25 Effective refractive index of the fishnet metamaterial made of L = 200 nm with 3 gold layers when embedded in air, water and chlorobenzene.

4.6 Conclusions

In this chapter, we have developed a novel design of large area fishnet metamaterials based on nanoimprinting lithography and electrodeposition. The optimization and appropriate etching of the residual layer enabled the fabrication of two dimensional arrays of isolated dielectric pillars. Two types of substrates were investigated as working electrodes for the electrodeposition, demonstrating that high wettable surfaces are advantageous for obtaining planar layers infiltrated through the pillars. ITO substrates served as efficient substrates for the homogeneous deposition of multilayered Ni-Au stacks over patterns with different lattice parameters. The chemical dissolution of the nickel parts gave rise to the final design of multilayered fishnet metamaterials over transparent surfaces.

Our versatile approach allows tuning different structural parameters such as the lattice spacing, pillar diameter or number of metallic layers. Furthermore, our fabrication process involves 4 simple steps and produces metamaterials on a conductive transparent substrate ready for device implementation.

The fabricated structures displayed optical resonances at wavelengths ranging from the NIR to the visible, depending on the geometrical parameters of the features and in good agreement with the simulations. Electromagnetic fields distributions showed that among the exhibited resonances, the largest wavelengths corresponded to the expected excitation of gap surface plasmons in between the metallic layers.

Strong negative refractive indices were obtained from the careful fitting of reflectance and transmittance spectra, achieving a minimum value of -1.2 in the visible for structures made with 200 nm pitch pillars and -2.8 in the NIR for structures of 300 nm pitch. The figures of merit were found to increase with the number of layers composing the metamaterial. Electromagnetic profiles demonstrated that the refractive index discontinuity obtained for multilayered structures was due to a change on the spatial mode propagating through the structure. The operation bands shifted to shorter wavelengths when increasing the number of layers. This behavior was noticeably weaker in the case of the smallest pitches (L = 200 nm) because of the approach to the bulk metamaterial regime. Such property was corroborated by the negligible angular dispersion of their spectroscopic properties, in contrast with the behavior displayed by the largest lattice structures (L = 500 nm).

Lastly, we studied the accessibility to the porosity of our metamaterials by infiltrating different optical media in between the metallic layers. The resonant wavelength exhibited a polynomial dependence with the refractive index of the filling liquid that could be approximated to a linear relationship at the highest indices. At this region, the structures presented performance capabilities close to the reported values in the literature, making our metamaterials potential sensing platforms. Our results report for the first time the application of large area fishnet metamaterials as optical sensors and pave the way for the implementation of metamaterials in optoelectronic devices.

In conclusion, we have developed a cost effective and up scalable approach for the fabrication of multilayered fishnet metamaterials operating at visible and NIR wavelengths with promising properties as optical sensors.

4.7 References

1.   Y. K. R. Wu, A. E. Hollowell, C. Zhang and L. Jay Guo. Angle-insensitive structural colours based on metallic nanocavities and coloured pixels beyond the diffraction limit. *Sci. Rep.* **2013**, *3*, 1–6.

2.   G. Lozano, G. Grzela, M. A. Verschuuren, M. Ramezani and J. G. Rivas. Tailor-made directional emission in nanoimprinted plasmonic-based light-emitting devices. *Nanoscale* **2014**, *6*, 9223–9229.

3.   J. Zhu et al. Low-cost flexible plasmonic nanobump metasurfaces for label-free sensing of serum tumor marker. *Biosens. Bioelectron.* **2020**, *150*, 111905.

4.   L. Gao et al. Nanoimprinting techniques for large-area three-dimensional negative index metamaterials with operation in the visible and telecom bands. *ACS Nano* **2014**, *8*, 5535–5542.

5.   K. Dietrich et al. Elevating optical activity: Efficient on-edge lithography of three-dimensional starfish metamaterial. *Appl. Phys. Lett.* **2014**, *104*.

6.   P. Molet et al. Ultrathin semiconductor superabsorbers from the visible to the near-infrared. *Adv. Mater.* **2018**, *30*, 1–6.

7.   G. Yoon, I. Kim and J. Rho. Challenges in fabrication towards realization of practical metamaterials. *Microelectron. Eng.* **2016**, *163*, 7–20.

8.   C. Fan et al. Wafer-scale fabrication of metal nanoring and nanocrescent arrays from nanoimprinted nanopillar arrays. *J. Micro/Nanolithography, MEMS, MOEMS* **2017**, *16*, 033501.

9.   G. J. Sharp, A. Z. Khokhar and N. P. Johnson. Fabrication of 70 nm split ring resonators by nanoimprint lithography. *Metamaterials VII* **2012**, *8423*, 84230H.

10.   W. Wu et al. Midinfrared metamaterials fabricated by nanoimprint lithography. *Appl. Phys. Lett.* **2007**, *90*, 1–4.

11.   T. Tomioka, S. Kubo, M. Nakagawa, M. Hoga and T. Tanaka. Split-ring resonators interacting with a magnetic field at visible frequencies. *Appl. Phys. Lett.* **2013**, *103*, 1–5.

12.   D. Chanda et al. Large-area flexible 3D optical negative index metamaterial formed by nanotransfer printing. *Nat. Nanotechnol.* **2011**, *6*, 402–407.

13. I. Bergmair et al. Single and multilayer metamaterials fabricated by nanoimprint lithography. *Nanotechnology* **2011**, *22*, 325301.

14. G. J. Sharp, S. I. Khan, A. Z. Khokhar, R. M. de la Rue and N. P. Johnson. Negative index fishnet with nanopillars formed by direct nano-imprint lithography. *Mater. Res. Express* **2014**, *1*, 045802.

15. M. Morales-Masis, S. De Wolf, R. Woods-Robinson, J. W. Ager and C. Ballif. Transparent electrodes for efficient optoelectronics. *Adv. Electron. Mater.* **2017**, *3*.

16. R. A. Afre, N. Sharma, M. Sharon and M. Sharon. Transparent conducting oxide films for various applications: A review. *Rev. Adv. Mater. Sci.* **2018**, *53*, 79–89.

17. F. Li et al. Semitransparent inverted polymer solar cells employing a sol-gel-derived TiO_2 electron-selective layer on FTO and $MoO_3/Ag/MoO_3$ transparent electrode. *Nanoscale Res. Lett.* **2014**, *9*, 1–5.

18. A. Way et al. Fluorine doped tin oxide as an alternative of indium tin oxide for bottom electrode of semi-transparent organic photovoltaic devices. *AIP Adv.* **2019**, *9*.

19. T. M. Whitney, J. S. Jiang, P. C. Searson and C. L. Chien. Fabrication and magnetic properties of arrays of metallic nanowires. *Science* **1993**, *261*, 1316–1319.

20. W. Ye, J. Yan, Q. Ye and F. Zhou. Template-free and direct electrochemical deposition of hierarchical dendritic gold microstructures: Growth and their multiple applications. *J. Phys. Chem. C* **2010**, *114*, 15617–15624.

21. H. Zheng, R. M. Almeida, T. Rivera and S. Ravaine. Fabrication of broadband omnidirectional non-reflective gold surfaces by electrodeposition. *Adv. Device Mater.* **2015**, *1*, 11–16.

22. R. Ji, W. Lee, R. Scholz, U. Gösele and K. Nielsch. Templated fabrication of nanowire and nanoring arrays based on interference lithography and electrochemical deposition. *Adv. Mater.* **2006**, *18*, 2593–2596.

23. J. García et al. Fabrication and modeling of integrated micro-thermoelectric cooler by template-assisted electrochemical deposition. *ECS J. Solid Sci. Technol.* **2017**, *6*, N3022–N3028.

24.   V. Q. Nguyen, D. Schaming, P. Martin and J. C. Lacroix. Large-area plasmonic electrodes and active plasmonic devices generated by electrochemical processes. *Electrochim. Acta* **2015**, *179*, 282–287.

25.   M. Aliofkhazraei. *Electroplating of Nanostructures*; IntechOpen, Iran, 2015.

26.   J. Elias et al. Electrodeposition of gold thin films with controlled morphologies and their applications in electrocatalysis and SERS. *Nanotechnology* **2012**, *23*.

27.   D. Zhang and Y. Tang. Enhancing light reflective properties on ITO glass by plasmonic effect of silver nanoparticles. *Results Phys.* **2017**, *7*, 2874–2877.

28.   X. Chen, T. M. Grzegorczyk, B. I. Wu, J. Pacheco and J. A. Kong. Robust method to retrieve the constitutive effective parameters of metamaterials. *Phys. Rev. E* **2004**, *70*, 016608.

29.   D. R. Smith, D. C. Vier, T. Koschny and C. M. Soukoulis. Electromagnetic parameter retrieval from inhomogeneous metamaterials. *Phys. Rev. E* **2005**, *71*, 036617.

30.   Z. Li, K. Aydin and E. Ozbay. Determination of the effective constitutive parameters of bianisotropic metamaterials from reflection and transmission coefficients. *Phys. Rev. E* **2009**, *79*, 026610.

31.   S. Yun et al. Experimental verification of substrate-induced bianisotropy in optical metamaterials. *Appl. Phys. Lett.* **2013**, *103*, 233109.

32.   S. Zhang et al. Experimental demonstration of near-infrared negative-index metamaterials. *Phys. Rev. Lett.* **2005**, *95*, 137404.

33.   G. Dolling, C. Enrich, M. Wegener, C. M. Soukoulis and S. Linden. Low-loss negative-index metamaterial at telecommunication wavelengths. *Opt. Lett.* **2006**, *31*, 1800–1802.

34.   J. Zhou, T. Koschny, M. Kafesaki and C. M. Soukoulis. Negative refractive index response of weakly and strongly coupled optical metamaterials. *Phys. Rev. B* **2009**, *80*, 1–6.

35.   S. S. Kruk, D. A. Powell, A. Minovich, D. N. Neshev and Y. S. Kivshar. Spatial dispersion of multilayer fishnet metamaterials. *Opt. Express* **2012**, *20*, 15100–15105.

36. I. Liberal and N. Engheta. Near-zero refractive index photonics. *Nat. Photonics* **2017**, *11*, 149–158.

37. I. Liberal and N. Engheta. Zero-index structures as an alternative platform for quantum optics. *Proc. Natl. Acad. Sci. U. S. A.* **2017**, *114*, 822–827.

38. S. Zhang et al. Optical negative-index bulk metamaterials consisting of 2D perforated metal-dielectric stacks. *Opt. Express* **2006**, *14*, 6778–6787.

39. C. García-Meca, R. Ortuño, F. J. Rodríguez-Fortuño, J. Martí and A. Martínez. Double-negative polarization-independent fishnet metamaterial operating in the visible spectrum. *Opt. Lett.* **2009**, *34*, 1603–1605.

40. Y. Liang, Z. Yu, N. Ruan, Q. Sun and T. Xu. Freestanding optical negative-index metamaterials of green light. *Opt. Lett.* **2017**, *42*, 3239–3242.

41. J. Valentine, S. Zhang, T. Zentgraf and X. Zhang. Development of bulk optical negative index fishnet metamaterials: Achieving a low-loss and broadband response through coupling. *Proc. IEEE* **2011**, *99*, 1682–1690.

42. A. Minovich et al. Tilted response of fishnet metamaterials at near-infrared optical wavelengths. *Phys. Rev. B* **2010**, *81*, 1–6.

43. J. Marae-Djouda et al. Angular plasmon response of gold nanoparticles arrays: approaching the Rayleigh limit. *Nanophotonics* **2017**, *6*, 279–288.

44. J. A. Jackman, A. R. Ferhan and N. Cho. Nanoplasmonic sensors for biointerfacial science. *Chem. Soc. Rev.* **2017**, *46*, 3615.

45. Z. Liang et al. Plasmonic metamaterial using metal-insulator-metal nanogratings for high-sensitive refraction index sensor. *Results Phys.* **2019**, *15*, 102602.

46. B. Gerislioglu et al. Monolithic metal dimer-on-film structure: New plasmonic properties introduced by the underlying metal. *Nano Lett.* **2020**.

47. W. Wei et al. Graphene/Au-enhanced plastic clad silica fiber optic surface plasmon resonance sensor. *Plasmonics* **2018**, *13*, 483–491.

48. X. Xu et al. Flexible visible–infrared metamaterials and their applications in highly sensitive chemical and biological sensing. *Nano Lett.* **2011**, *11*, 3232–3238.

49. R. Yahiaoui, A. C. Strikwerda and P. U. Jepsen. Terahertz plasmonic structure with enhanced sensing capabilities. *IEEE Sens. J.* **2016**, *16*, 2484–2488.

50.   B. Liedberg, I. Lundstrom and E. Stenberg. Principles of biosensing with an extended coupling matrix and surface plasmon resonance. *Sensors Actuators B* **1993**, *11*, 63–72.

51.   L. S. Jung, C. T. Campbell, T. M. Chinowsky, M. N. Mar and S. S. Yee. Quantitative interpretation of the response of surface plasmon resonance sensors to adsorbed films. *Langmuir* **1998**, *14*, 5636–5648.

52.   Y. Lee, S. Kim, H. Park and B. Lee. Metamaterials and metasurfaces for sensor applications. *Sensors* **2017**, *17*, 1726.

53.   Y. Xu et al. Optical refractive index sensors with plasmonic and photonic structures: Promising and inconvenient truth. *Adv. Opt. Mater.* **2019**, *7*, 1801433.

Chapter 5

Nanostructured metallic surfaces for enhanced molecular emission

5.1 Introduction

In the previous chapters, we have shown the feasibility of obtaining large-area and high quality nanostructured patterns at low-cost processing. Inspired by the accurate control and reproducibility of these structures, this chapter aims at developing nanostructured surfaces for exploring the interplay between quantum emitters and the photonic environment.

An interesting aspect of quantum emitters is the possibility of enhancing their spontaneous emission rate when placed in a resonant cavity.[1] This enhancement of the light matter interaction will greatly improve the effectiveness of fluorescence-based technologies such as bioimaging,[2] optical communications,[3] energy conversion[4] or quantum information.[5]

A singular phenomenon for enhancing the spontaneous emission rate is the collective optical response of an ensemble of quantum emitters, first introduced by Dicke.[6,7] When a dense collection of emitters interacts with the same light field, it responds collectively and coherently to the excitation. This is called superradiance effect. In this situation, both the emission rate and the field intensity are boosted when compared with a set of independent emitters.

Since the collective radiation relies on the interaction with a common field, an electromagnetic resonance would reinforce the cooperativity by promoting long-range interactions.[8] In 2009, Pustovit et al. theoretically demonstrated that this collective response of emitters could be enhanced by coupling them with plasmons.[9] Since then, several plasmonic systems have been discussed for their potentialities to achieve collective emission. Examples include metallic nanowaveguides, nanoparticles or metamaterials.[10-14] Experimentally, many works have reported the enhancement of both the luminescent signal and decay rates when placing quantum emitters in the proximity

of metallic structures. Typically, these systems avoid the direct adsorption of the emitters to the metallic surface because of the quenching effects, e.g., reduction of both the decay lifetime and intensity due to ohmic losses in the metals.[15]

For instance, Fauche et al. studied the decay rate of dye molecules grafted to core-shell metal-dielectric nanoparticles, showing a clear dependence of the rates on the dielectric shell thickness and the number of emitters.[16] Hoang et al. also found a significant enhancement of the intensity and emission rates of quantum dots in presence of metal colloidal nanocubes.[17] Shestakov et al. showed that the de-excitation lifetime of luminescent Ag nanoclusters was influenced by a plasmon energy exchange with other surrounding Ag nanoparticles.[18] Although not referred in these terms, other authors have as well studied the modification of the spontaneous emission of emitters placed near plasmonic arrays. Examples include periodic nanopatterns of rods or squares made by e-beam lithography,[19,20] or holey arrays made by the low-cost approach of nanosphere lithography.[21]
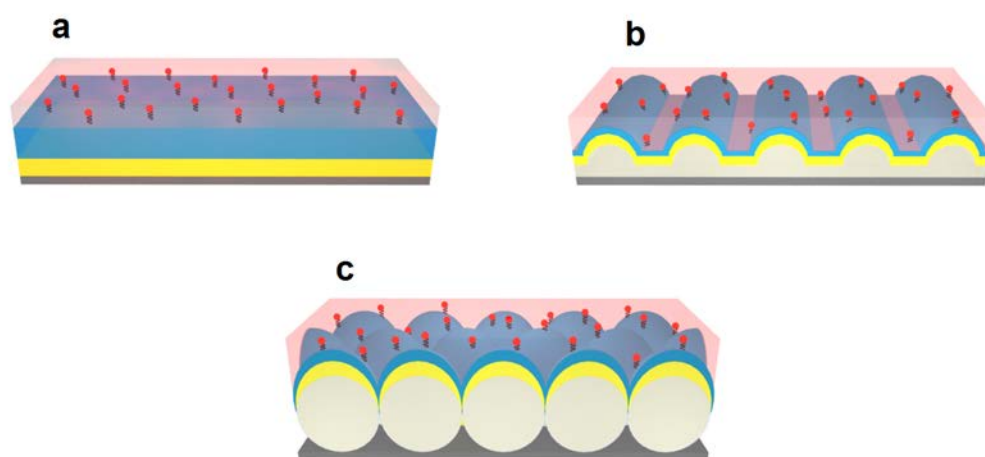
Figure 5.1 Schemes of the proposed surfaces for studying collective spontaneous emission. **a** Flat mirror. **b** One-dimensional plasmonic array. **c** Two-dimensional plasmonic array.

Along this chapter, we design three types of metallic substrates for studying the collective optical response of an ensemble of fluorophores. Our structures consist of flat, one- and two-dimensional patterned metallic surfaces, covered by a dielectric spacer on top of which the dye molecules are deposited (Figure 5.1). Starting with the flat configuration, we study the collective decay rate evolution as a function of the dielectric layer thickness. Later, we take advantage of nanoimprinting and colloidal lithography for creating large-area plasmonic arrays serving as superradiance platforms. The proper

design of these structures enables the excitation of plasmonic resonances close to the emission wavelength of the dyes that can enhance their spontaneous emission.

This work is the product of an on-going collaboration with Dr Renaud Vallée from CRPP, Dr Maxim Shukarev from the Arizona State University and the Microelectronics Laboratory from the Autonomous University of Madrid (UAM). I was specifically involved in the fabrication, optical characterization and fluorescence lifetime measurements of these structures.

5.2 Fluorescent dye

The effect of metallic boundaries was studied on the emission of Atto 655 organic fluorophores (Sigma Aldrich, 634 g/mol). These red emitting dyes are commonly used in fluorescence imaging[22,23] because of their high performance characteristics at wavelengths where the autofluorescence of the samples is drastically reduced. They present strong absorption (1.25×10^5 M^{-1} cm^{-1}), high fluorescence quantum yield (0.3) as well as high thermal- and photo-stability. Their maximum peaks of absorption and emission appear around 660 and 680 nm, respectively (Figure 5.2). For this reason, the molecules will be excited with a pulsed laser operating at 654 nm (see Chaper 2 for further details). Besides, we will engineer the resonant wavelength of the plasmonic arrays to occur near the emission maximum in order to induce the plasmonic superradiance effect.
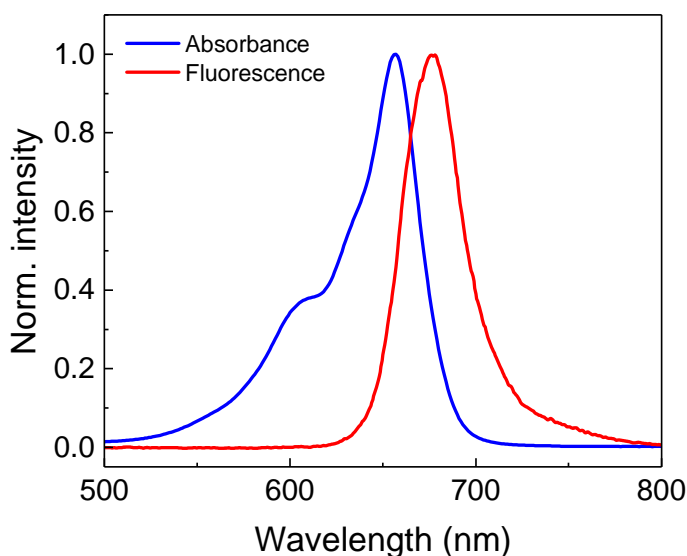

Figure 5.2 Absorbance and fluorescence spectra of Atto 655 molecules diluted in ethanol.

5.3 Flat metallic surface

A pioneering experiment of the spontaneous emission modification of a quantum emitter was carried out by Drexhage et al.[24] They investigated the influence of a planar metallic surface on the emission lifetime of a single Er^{3+} ion. It was shown that the decay rate oscillated with the distance to the metallic surface because of the interference between the emitted light from the ion and its reflection from the mirror. Since then, the oscillatory effect has been extensively studied and reproduced in analogous systems including quantum dots or fluorescent dyes.[25-27] This phenomenon is not limited to a single emitter but is rather expected to happen as well with clusters nearby a metallic boundary.[28] In this section, we study the fluorescence decay rate evolution of ensembles of dye molecules as a function of their separation from the metal surface.

5.3.1 Fabrication method

The proposed samples were fabricated as shown in Figure 5.3. In summary, a flat gold surface is covered by a silicon dioxide (SiO_2, silica) layer with a well controlled thickness. Such film works as a thoroughly regulated spacer between the metallic mirror and a post deposited molecular layer of Atto 655 fluorophores, avoiding quenching effects. A layer of polymethyl methacrylate (PMMA) is finally deposited on top of the structure to fix the position of the dyes and provide similar electromagnetic boundary conditions on both sides of the molecular layer.[29]
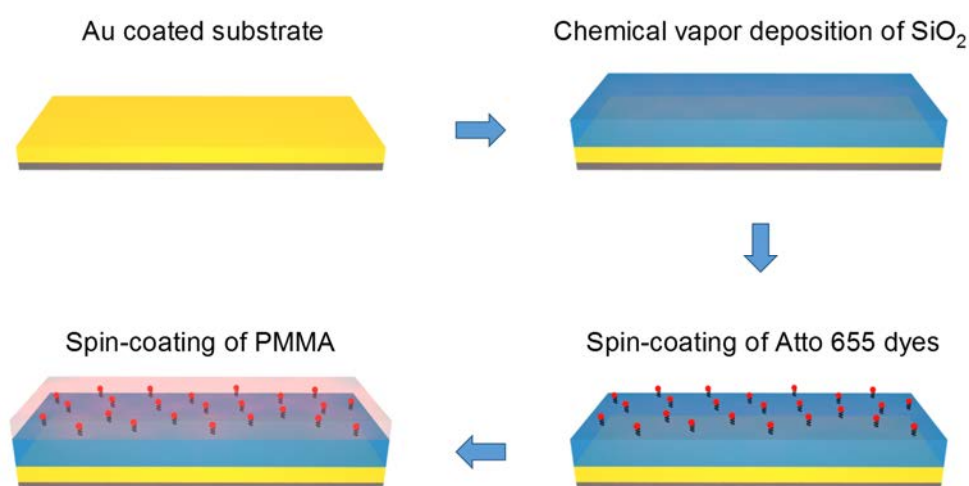
Figure 5.3 Scheme of the fabrication process of ensembles of molecular emitters placed in front of a flat metallic surface.

Gold substrate

Commercial gold films of 150 nm thickness and 1 cm² were taken as mirror substrates because of their high reflectivity at the dyes emission wavelength and because of the chemical inertness of this material, which made it compatible with the further fabrication steps.

Chemical vapour deposition of SiO₂

The deposition of the well-controlled silica spacer was performed during a collaboration stay at the Microelectronics Group of UAM. A broad range of SiO_2 thicknesses were deposited on top of the gold substrates by chemical vapour deposition enhanced by electron cyclotron resonance (CVD-ECR). CVD consists in the controlled chemical reaction of volatile precursors in vacuum, leading to thin and homogeneous deposits of the reacted species. In the case of CVD-ECR, a plasma of the gases is created by electron cyclotron resonance for promoting the deposition process. This technique enables low deposition temperatures and good mechanical and optical properties of the layers.[30]

We used a PlasmaQuest 357 equipment. SiO_2 layers were deposited by reacting 60 scmm of silane (SiH_4) diluted in 5% Ar and 70 sccm of O_2. The process was performed at RT with a microwave power of 1000 W and a working pressure of 10^{-6} mbar. The growth rate, determined by ellipsometry from initial trials, corresponded to 17.0 ± 0.3 nm/min. The accurate control over the deposited thickness allowed us to obtain dielectric spacers ranging from 20 to 680 nm, in steps of 60 ± 2 nm thickness.

Spin-coating of Atto 655 molecules

For the deposition of the Atto 655 molecular layer, the dyes were diluted in ethanol at concentrations of 10^{-8} and 10^{-7} M. They were deposited by spin-coating following a literature protocol for single molecule detection, avoiding molecular aggregates.[31] Aliquots of 20 µL were poured onto the SiO_2/Au samples, completely covering the surface, and spun at 3000 rpm for 20 s. For reference measurements, the same procedure was carried out on previously cleaned glass substrates.

The density of this molecular layer can be calculated from the amount of molecules dispersed on a given surface. We estimated this quantity with control experiments over large area substrates, avoiding any border effect. Specifically, spin-coatings of 20 µL of ethanol on a Si wafer expanded over areas of about 2.5 cm in radius r. Knowing the

number N of molecules present in the initial volume and the covered area A, one can determine the molecular surface density. Then, assuming a monolayer distribution of the molecules, the thickness t of the deposit can be considered as the molecule size, which for organic dyes is typically below 3 nm.[32,33] From these values and equation (5.1), we can estimate molecular densities ρ_m of 3×10^{22} m^{-3} and 3×10^{23} m^{-3} for ensembles of molecules deposited from 10^{-8} and 10^{-7} M solutions.

$$\rho_m = \frac{N}{At} = \frac{N}{(\pi r^2)t} \tag{5.1}$$

Spin-coating of the PMMA top layer

A final thin PMMA layer was deposited on top of the fluorescent dyes to fix their position. PMMA was chosen as material because of its easy deposition and similar refractive index than the silica layer (n_{SiO_2}=1.46, n_{PMMA}=1.45), avoiding surface effects on the molecular dipoles as well as undesirable reflection at the interface.

PMMA powder (Sigma Aldrich, $M_w \sim 150000$) was diluted in acetone at 1:120 weight ratio and spin-coated on top of the fluorophores at 3000 rpm for 30 s. These conditions ensured a film of 50 nm thickness.

## 5.3.2 Fluorescent decay in absence of metallic boundary

The emission properties of the structures were investigated by time-resolved fluorescence microscopy in close collaboration with Dr Renaud Vallée. As described in Section 2.6.3, a pulsed laser operating at 654 nm was normally focused on the sample surface. The emitted fluorescence was then collected through the same objective and sent to the detector for the following reconstruction of the decay profiles.

Figure 5.4 shows the decay profile of Atto 655 molecules deposited on a reference glass substrate from a concentration of 10^{-8} M in ethanol, which corresponds to a molecular density of 3×10^{22} m^{-3}. The intensity I of the signal presents a clear single exponential decay in time t of the form:

$$I(t) = Ae^{-\gamma t} + C \tag{5.2}$$

where A is the intensity factor, C accounts for background noise and γ corresponds to the decay rate. This γ value was found to be 0.27 ± 0.01 ns^{-1}, in good agreement with the lifetime values reported in absence of a metallic structure.[27,34] The monoexponential decay is characteristic of non-aggregated molecules and reflects an independent emission of the dyes. Larger concentrations, typically above 3×10^{24} m^{-3}, lead to non-

exponential decays, evidencing the aggregation of molecules on the glass surface. This situation was avoided in the following experiments in order to clearly study the influence of the metallic surface on the collective behavior of emitters, not due to the properties of aggregates.
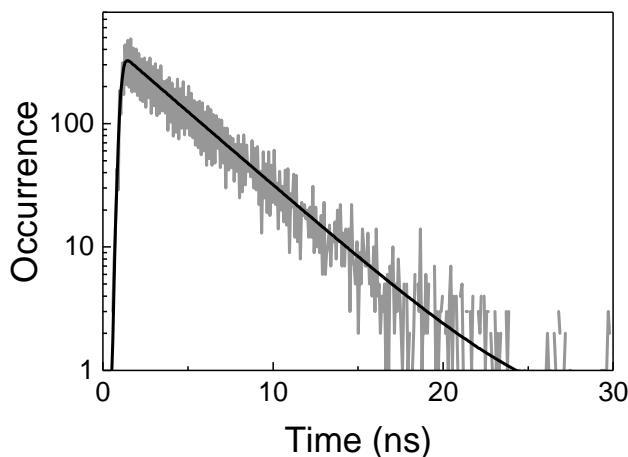
Figure 5.4 (Grey) Semi-logarithmic decay profile of 3×10^{22} m^{-3} Atto 655 molecules deposited on a bare glass substrate and covered with 50 nm thick PMMA layer. (Black) Monoexponential fit of the decay.

5.3.3 Collective interference

Figure 5.5 presents decay profiles of different concentrations of Atto 655 molecules deposited at various distances (SiO$_2$ thickness) from the gold mirror. A common deviation from the above mentioned single exponential decay is perceptible. In this case, a biexponential function of the form

$$I(t) = I_L e^{-\gamma_L t} + I_S e^{-\gamma_S t} + C \tag{5.3}$$

convoluted to the instrumental response of the setup provided a good fitting of the decay profiles. Such expression represents the two regimes observed in the profiles: the first decline dominated by a large decay rate γ_L and the second slope, dominated by a small decay rate γ_S. The rest of coefficients (I_L, I_S and C) are just fitted for the respective intensity factors and background noise.

When comparing samples with the same density of molecules such as Figure 5.5a, b or Figure 5.5c, d, one notices that both decay rates (inserted in the figures) vary with the thickness of the SiO$_2$ layer. Furthermore, samples with the same silica thickness but different molecular density present an increase of the large decay rate when going from lower to higher concentrations (Figure 5.5b and c, respectively). Therefore, the decay rates depend on both the spacer thickness and the density of fluorophores.

117
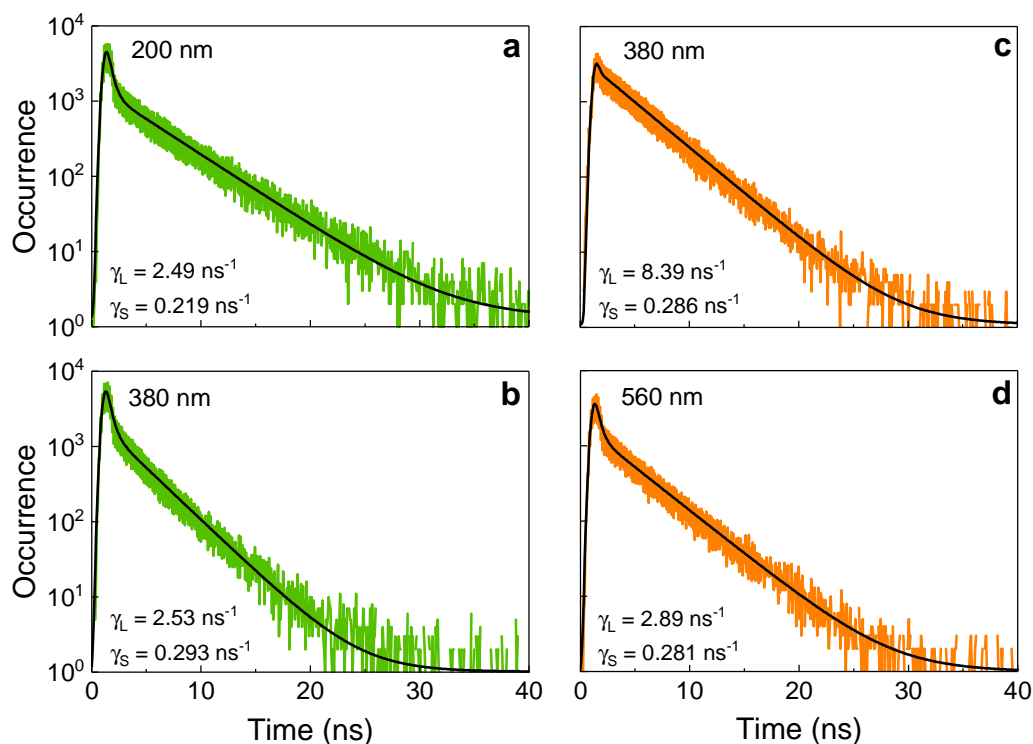
Figure 5.5 Semilogarithmic decay profiles of samples with molecular densities of **a,b** 3×10^{22} m^{-3} (green) and **c,d** 3×10^{23} m^{-3} (orange). The SiO$_2$ layer thicknesses separating the molecules from the gold mirror are **a** 200 nm, **b** 380 nm, **c** 380 nm and **d** 560 nm. The black lines represent the biexponential fit to each decay. The insets correspond to the large (γ_L) and small (γ_S) decay rates extracted from the fits to each sample.

Figure 5.6 better exhibits such dependencies, presenting the decay rates evolution with the SiO$_2$ thickness for the two molecular densities studied. The error bars shown in this figure are standard deviations of various measurements performed on the samples and do not reflect the setup time resolution. The experimental points of γ_L were fitted by a sinusoidal signal, while γ_S points were fitted by a damped sinusoid. The oscillating period, related to the emission wavelength of the dyes and the refractive index of the surrounding medium,[26] found in Figure 5.6a was used as a fixed parameter for the three other fits. It should be noted that the large decay rates exhibited in Figure 5.6b are on the edge of the time resolution of the setup. As such, not all the decay profiles could be fitted appropriately and the amplitude of the sinusoid in this figure was merely adjusted by hand, which makes it more a guide to the eye than a fit.

The small decay rates (Figure 5.6c and d) exhibit damped oscillations with the distance as already observed for similar single molecule experiments.[24] These observations result from the interference of the signals between an emitter and its image

from the mirror. As the distance increases, the interference is attenuated and the decay rate recovers the reference value of 0.27 ns^{-1} measured on bare glass (Figure 5.4). This spatial modulation is as well observed for the large decay rates but, remarkably, is not damped over the observed distance. Furthermore, one notices immediately the increase of this rate γ_L while going from lower to higher concentrations (Figure 5.6a and b, respectively), a feature not observed for the γ_S. This rapid behavior for γ_L indicates the existence of a collective relaxation phenomenon. Thus, the interference behavior is not limited to individual molecules but is also seen in the collective regime with a notable absence of damping.
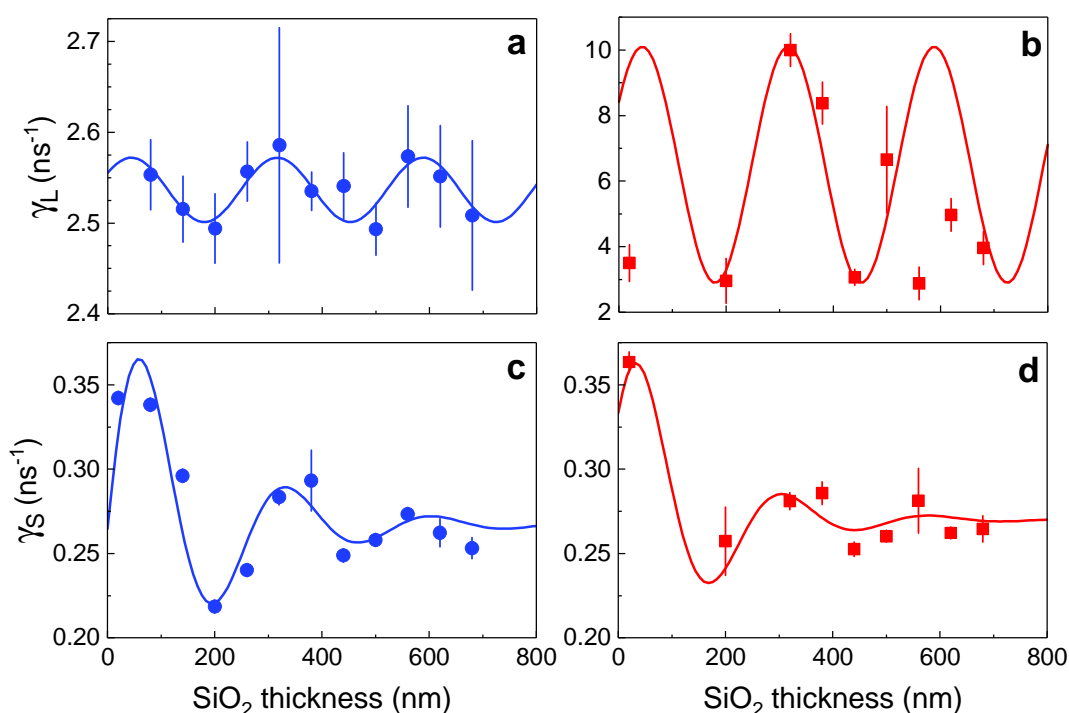
Figure 5.6 Experimental (dots) and fitted (lines) decay rates as a function of SiO$_2$ spacer thickness. **a,b** Evolution of the large decay rate γ_L for molecular densities of 3×10^{22} m^{-3} and 3×10^{23} m^{-3}, respectively. **c,d** Evolution of the short decay rate γ_S for the same densities.

5.3.4 Theoretical model

The collective response of the systems was theoretically modelled by Dr Sukharev, from the Arizona State University. The electrodynamics of molecule-to-molecule interactions were described by the Maxwell-Bloch equations considering the molecules as two-level emitters.[35] The excited state population exhibited an exponential decay profile with time, from where the decay rates were obtained. It should be noted that in

these calculations, the emitters are taken to oscillate in phase, leading to a fully coherent response and, thus, representing the large decay rate of the experiments.

Figure 5.7a shows the dependence of this decay rate γ with the density of molecules for three thicknesses of the fluorophore layer. The SiO_2 spacer is kept at 300 nm. It is seen that the decay rate linearly scales with the molecular density, as expected in the collective spontaneous emission regime.[7] Figure 5.7b shows the decay rate as a function of the SiO_2 spacer for three thicknesses of the molecular layer, with a density of molecules of 3×10^{23} m^{-3}. As can be observed, the spatial oscillations obtained from the simulations are in excellent agreement with the experimental results for the large decay rates shown in Figure 5.6a and b. The overestimation of the numerical values is likely because, in the simulations, all the molecules are perfectly aligned parallel to the interface and to each other. For an isotropic molecular system, averaging over all orientations of the dipoles amounts to multiple by 1/3,[36] which is remarkably close to the experiments. In addition, the simulations consider an ideal collective response, where the intrinsic emission disorder of the experiment is not included. In fact, the presence of an incoherent component in the measurements may explain why a perfect destructive interference is not observed. Nevertheless, we can conclude that the lifetime modulation, long known for individual emitters, is experimentally observed and theoretically corroborated for ensembles of molecules collectively interacting.
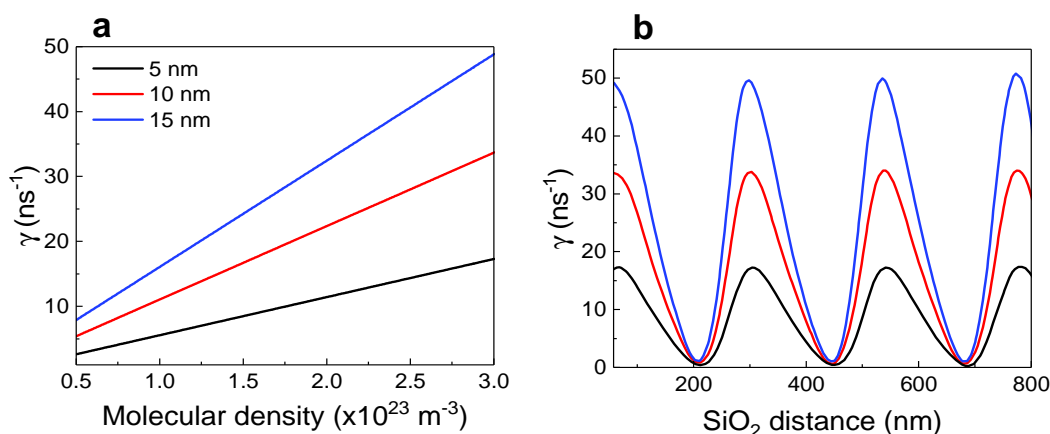

Figure 5.7 a Simulated large decay rate as a function of the molecular density for three different thicknesses of the molecular layer. The thickness of the spacer layer was kept to 300 nm. **b** Spatial dependence of the large decay rate on the thickness of the SiO_2 spacer for the same three thicknesses of the molecular layer. The molecular density is 3×10^{23} m^{-3}.

5.4 One-dimensional plasmonic arrays as superradiance platforms

In the previous section, we have demonstrated the collective response of an ensemble of molecules placed in front of a flat metallic surface. Here, we design a higher dimensional metallic structure sustaining plasmon resonances as potential platforms for the plasmonic superradiance effect.

We designed one-dimensional (1D) plasmonic arrays, this is, metallic gratings of periodic lines supporting SPPs as depicted in Figure 5.8. NIL enabled the fabrication of high quality and homogeneous patterns of horizontal lines while working over large-area surfaces and short time periods. This base structure was then covered with a gold thin layer and a well-defined thickness of aluminium oxide (Al_2O_3, alumina) working as spacer. On top of the metal/dielectric structures, Atto 655 fluorophores and a thin layer of PMMA were deposited as detailed in Section 5.3.1.

We will now focus on the intricacies of the fabrication of these structures and the optical properties that derive from them. The proper control over the features will lead to optimized structures for enhancing the fluorescence of the dyes.
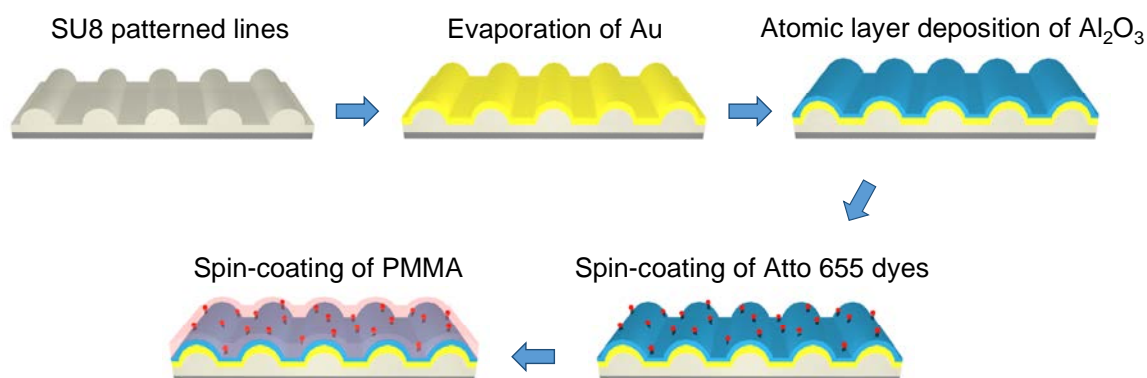
Figure 5.8 Schematic fabrication process of one-dimensional plasmonic arrays serving as superradiance platforms.

5.4.1 Shallow lines patterning

Taking into account the targeted design of Figure 5.8, a corrugated metallic surface would be accomplished if the gold deposition is performed onto shallow periodic lines. Otherwise, using deep patterns as base template, the deposition would create discontinuous metallic layers, being the metal mainly deposited on the top and bottom parts of the features. During this work, we developed a simple method for adapting initial 350 nm deep patterns to shallow templates without passing through complex

engraving or etching steps. Unlike a conventional hot embossing process, we imprinted a SU8 layer below its glass transition temperature T_g so that the photoresist did not completely filled the mold, reducing the height of the obtained features (Figure 5.9).

PDMS mould

SU8 layer

Substrate
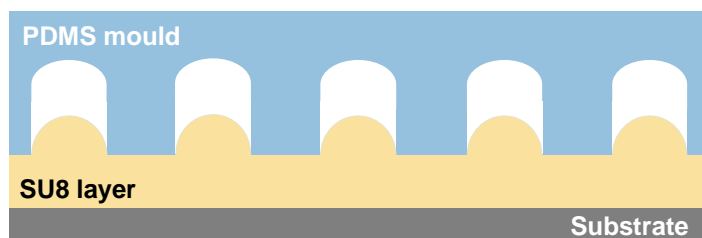
Figure 5.9 Scheme of the limited infiltration of the SU8 photoresist through the mold when imprinting below its T_g.

The detailed procedure for obtaining shallow lines was as follows. First, a SU8 layer of about 200 nm was spin-coated on a Si substrate. A pre-patterned hard-PDMS mold of lines with 400 nm pitch, 200 nm width and 350 nm height was used as stamp (Figure 5.10a). For the imprinting process, it was pressed onto the SU8/Si sample at 40 °C and 5 bar of pressure for 30 minutes. SEM analysis determined that the printed lines were 62 ± 5 nm high; this is, 5 times shorter than the ones of the initial pattern (Figure 5.10b, c). Higher temperatures risked to produce taller features because of the close proximity to the glass transition temperature of the SU8 photoresist (T_g = 55 °C). In contrast, lower pressures such as 3 bar or shorter times such as 15 min, gave rise to even shallower lines. These structures were discarded because of the likely loss of definition of the features with the further deposits.
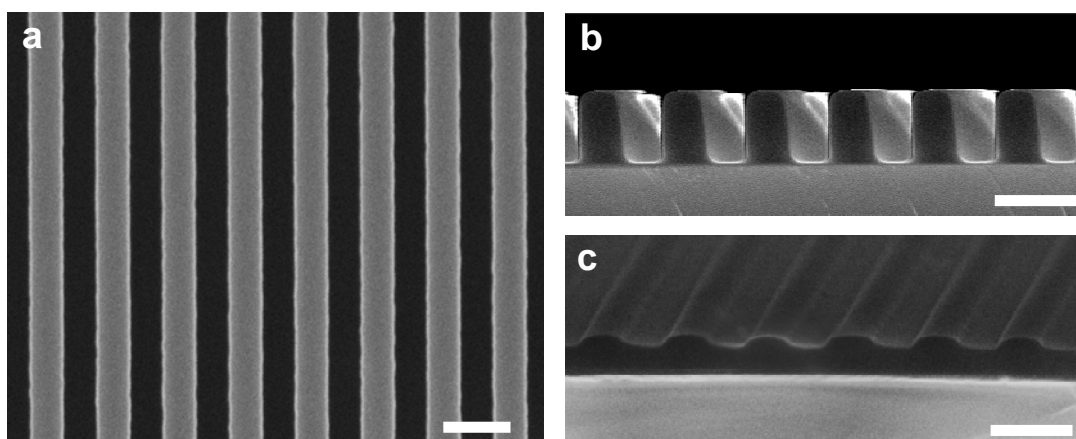

Figure 5.10 a SEM top view of the initial silicon master of 400 nm periodic lines. **b** Cross-sectional view of SU8 lines imprinted by hot embossing. **c** Cross-sectional view of 60 nm deep periodic lines imprinted below the SU8 T_g. Scale bars: 400 nm.

Having checked the success of this controlled imprinting process, we made use of the great advantage of NIL and replicated this shallow pattern on several stamps of hard-PDMS as detailed in Chapter 2. The fact of working with numerous stamps significantly accelerated the fabrication process and enabled the production of a large number of samples for the subsequent studies. Finally, the PDMS molds were conventionally printed onto 90 nm thick SU8 layers deposited on glass substrates. This step led to our final one-dimensional templates of 400 nm pitch and approximately 60 nm deep periodic lines.

5.4.2 Corrugated metallic surface

The 1D plasmonic structure was accomplished by evaporating 50 nm of gold on top of the patterns. This deposition method uses a resistive heat source to evaporate a solid material in a vacuum environment. The material vapour traverses the chamber and finally condenses in form of thin film on the cold substrate. We used a MBraun thermal evaporator working at 10^{-6} mbar with a controlled deposition rate of 0.6 Å/s, monitored by a quartz crystal microbalance. Again, we chose gold as metal because of its good plasmonic excitation and chemical stability.
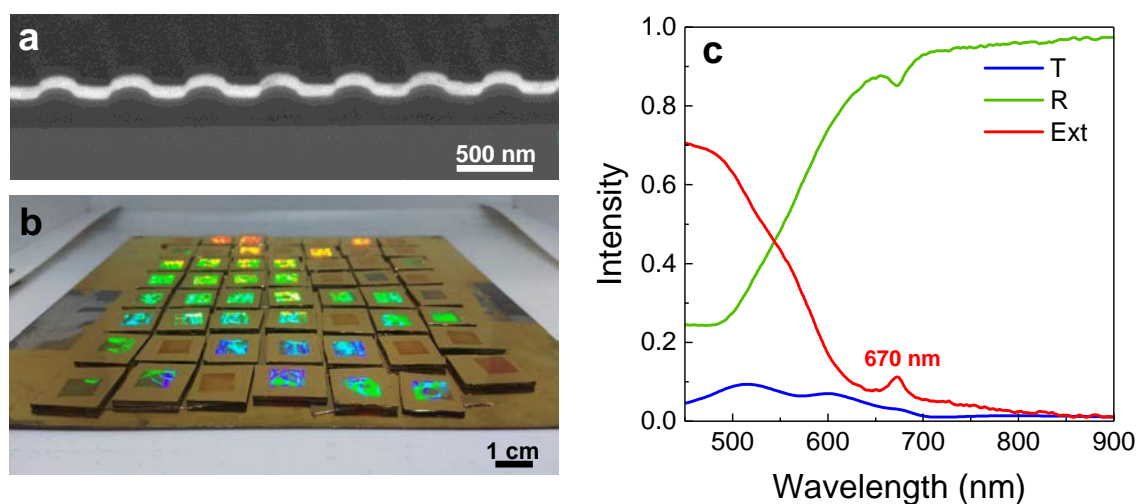
Figure 5.11 a SEM cross-sectional view of 400 nm shallow periodic lines covered with 50 nm thick Au layer. **b** Photograph of the fabricated samples right after gold evaporation. **c** Transmittance (T), reflectance (R) and extinction (Ext) spectra of Au coated-SU8 lines on glass substrates.

Figure 5.11a presents the accomplished plasmonic grating of periodic SU8 lines covered by a highly continuous gold layer. Figure 5.11b shows the samples after the metal deposition process, which enhanced the iridescence of the arrays. As can be observed in Figure 5.11c, the structures follow the spectroscopic properties of a flat gold

thin film with a noticeable extinction peak at 670 nm. Making use of the momentum matching equation for exciting surface plasmons in linear gratings (eq. 1.15), we can ascribe this peak to a SPR at the gold-SU8 interface.

Dielectric-coated metal gratings

We made use of the atomic layer deposition (ALD) technique to deposit the dielectric spacer between the plasmonic grating and the dyes. The principle of ALD relies on the sequential pulsing of precursor vapours with intermediate purging periods. In each independent pulse, the vapour molecules react with the surface in a self-limiting manner, ensuring that the reaction stops once all of the reactive sites on the substrate are filled. Each reaction then forms about one atomic layer. This technique stands out for providing highly thickness control and conformal deposits, this is, adapted to the shape of the features.

We deposited Al_2O_3 layers of 5, 10, 15, 20 and 25 nm using a Savannah200, Cambridge Nanotech equipment. Water and trimethylaluminum (TMA) were used as precursor gases of Al_2O_3 with open valve times of 0.05 and 0.10 s respectively, followed by 65 s pump time, which led to 1.1 Å/cycle. The chamber was kept at 150 °C during the deposition process, which did not affect the cured SU8 or gold features.
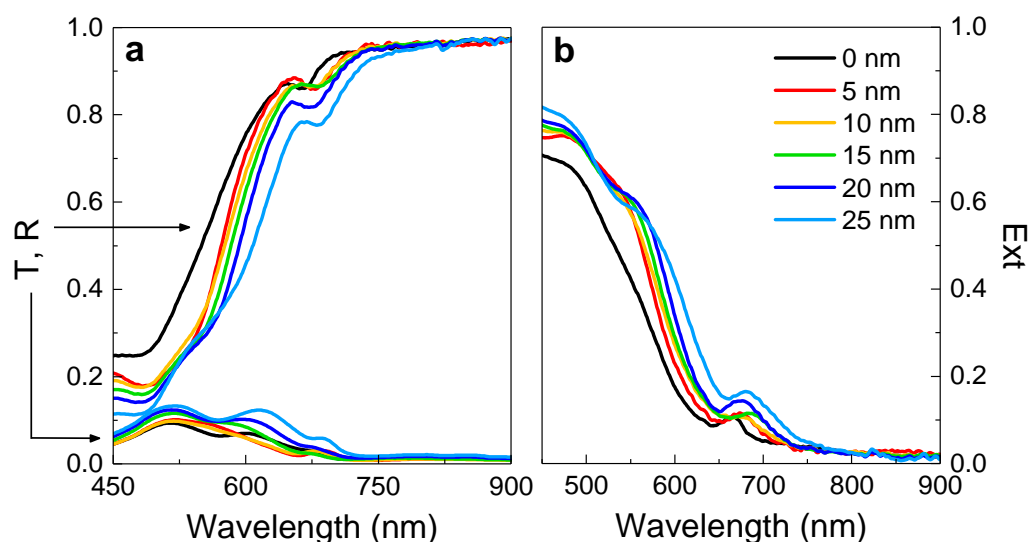
**Figure 5.12 a** Transmittance, reflectance and **b** extinction spectra of 2D plasmonic lines covered with different thickness of Al_2O_3.

Figure 5.12 presents the transmittance, reflectance and extinction (T, R, Ext) spectra of plasmonic arrays of lines after the deposition of different thicknesses of alumina. For reference, the spectra of the metallic array without dielectric on top are shown as well in

black. Small redshifts of the resonant extinction peak are observed due to the increase of the refractive index at the top of the gold layer. It is worth mentioning that although the SPR is excited at the internal gold surface, the thin thickness of this layer enables the energy transfer and propagation of the SPP at the Al_2O_3-Au frontier, too.[37,38] The position of this EM resonance matching the emission peak of the dyes makes it suitable to enhance the emitters de-excitation.

5.4.3 Fluorescent decay evolution with the spacer thickness

Atto 655 fluorophores were finally spin-casted on top of the Al_2O_3 coated metallic gratings as previously described. Similarly, a PMMA cover was deposited on top of the ensembles of molecules.
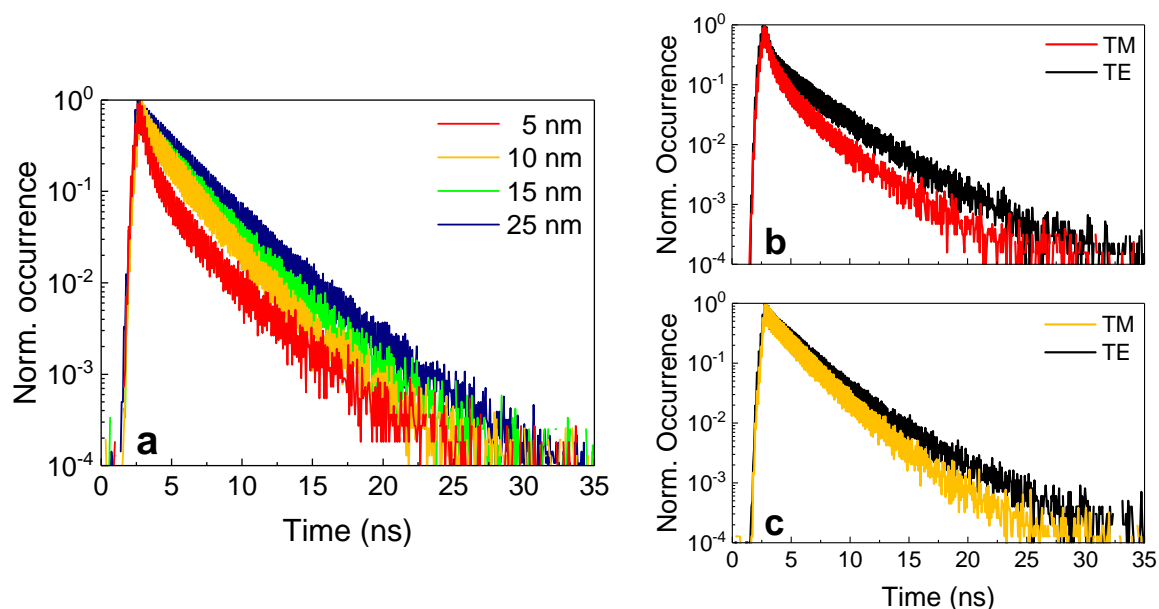
Figure 5.13 a Normalized decay profiles of 10^{-8} M Atto 655 molecules deposited at different spacer distances from the plasmonic 1D grating, measured in TM polarization. Comparison of the decay profiles in TM and TE configurations for spacer thicknesses of **b** 5 nm and **c** 10 nm.

Figure 5.13 presents preliminary fluorescence decay profiles of structures with 10^{-8} M concentration of dyes in solution. Polarizing the excitation light perpendicularly to the grating (TM mode), we observe that the relaxation gets faster as the emitters are closer to the metal surface (Figure 5.13a). This manifests a decay rate enhancement arising from the plasmonic structure. The decay profile corresponding to 20 nm of alumina is not shown because of its similarity with the 25 nm spacer decay. This may suggest that above 20 nm, the fluorophores do not experience any plasmonic interaction due to the attenuation at these distances. Moreover, the deviations from a single bi-

exponential decay, significantly at 5 nm, suggest the existence of several fluorescence regimes: the single molecule, where the emitters relax independently; the collective de-excitation, this is, the superradiance phenomenon; and some intermediate behaviors. As described in previous studies, these rates would be accelerated by a plasmonic resonance.[16,21,39]

Interestingly, for the lowest spacer thicknesses (5 and 10 nm), the parallel polarization (TE) presents larger relaxation times than the TM (Figure 5.13b,c). Such observation confirms the presence of a plasmon-enhanced fluorescence since in this type of gratings the SPPs are typically excited in TM mode. Nonetheless, an accurate analysis of the decay profiles together with a comparison to numerical models should be done in the future to better understand these observations.

5.5 Two-dimensional plasmonic arrays as superradiance platforms

The possibility of achieving plasmonic superradiance was also explored with the design of two-dimensional plasmonic arrays (Figure 5.14). For this purpose, we made use of colloidal lithography, which enabled a low-cost and fast fabrication process of hexagonal templates. Similarly to the earlier structures, the patterns were covered with a gold thin layer and different thicknesses of a dielectric spacer in order to study the influence of this separation on the fluorescence decays of Atto 655 dyes. The molecules and the PMMA layer were spin-casted as previously detailed.
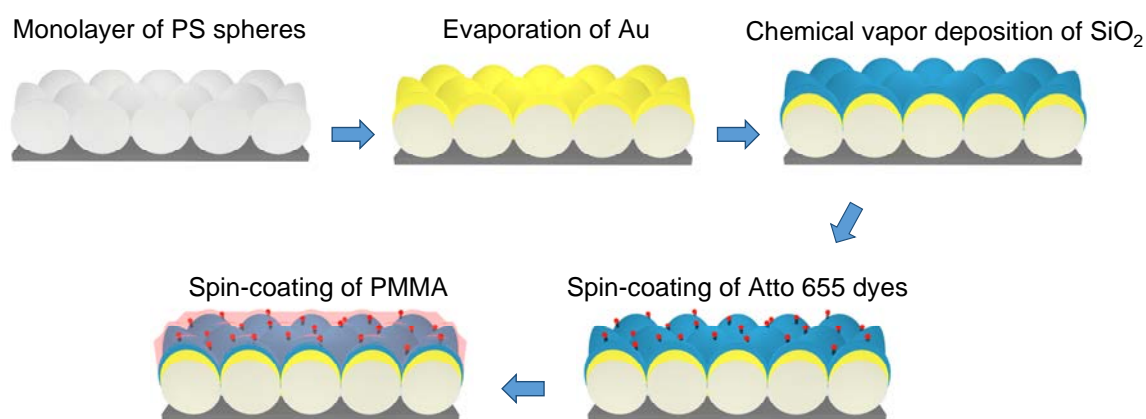
Figure 5.14 Schematic fabrication process of two-dimensional plasmonic arrays serving as superradiance platforms.

5.5.1 Metal-coated colloidal monolayers

Colloidal monolayers of 480 nm large PS beads were prepared on cleaned glass substrates following the self-assembly procedure described in Chapter 2. A gold layer of 50 nm thickness was deposited on top of the monolayers by thermal evaporation in a similar manner as formerly detailed. Figure 5.15a and b show the resulting structure, which is composed by metallic half-shells covering the top surface of the particles.
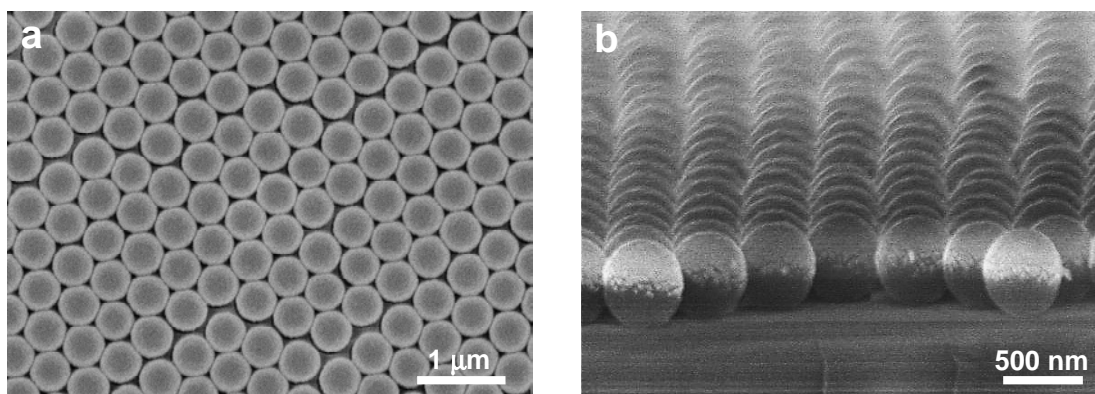
Figure 5.15 a Top-view and **b** cross-section SEM image of a gold-coated colloidal monolayer of PS particles.

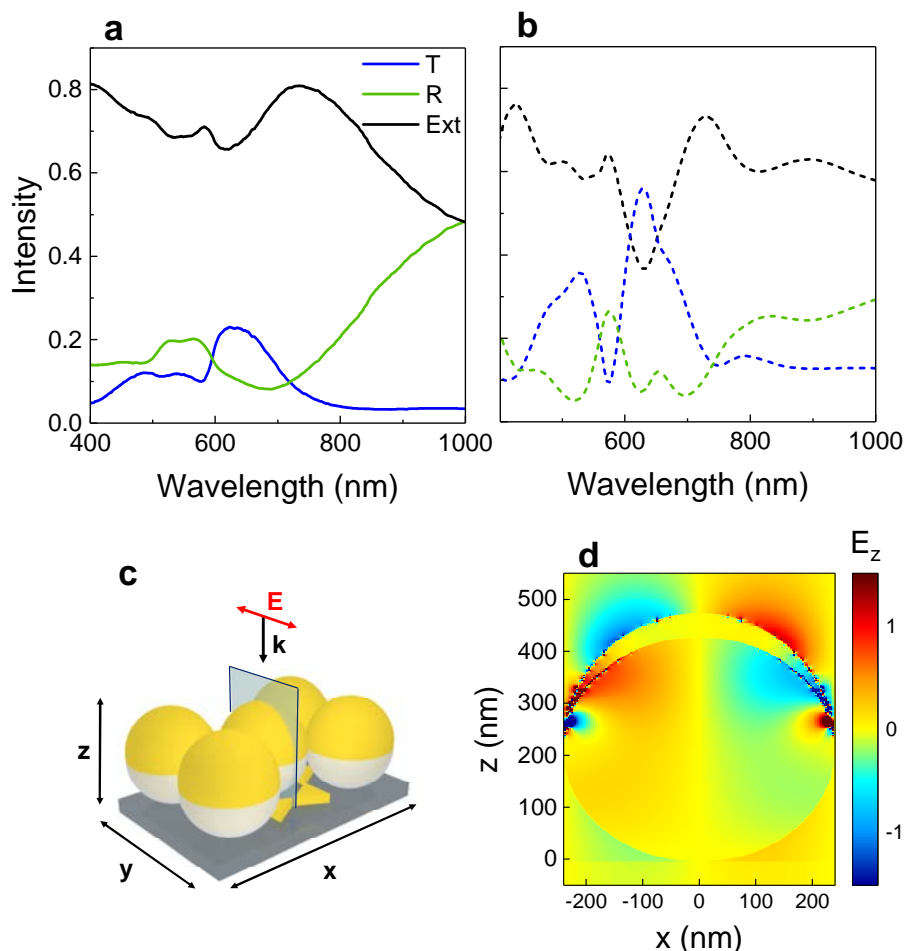Visible spectra of the metal-coated colloidal monolayers were measured and well reproduced by FDTD simulations (Figure 5.16a,b). The unit cell of the calculations was composed of close-packed 480 nm large spheres with a gold half-shell of 50 nm height. Gold triangular prisms, formed in between the particles during the deposition, were also included with a side length of 135 nm and 40 nm thickness (Figure 5.16c).

The lower transmittance found for the measurements could be ascribed to the packing defects of the monolayer. Specifically, the deposition of larger gold areas around the particles could considerably reduce the overall transmittance while increasing the reflectance. In spite of this, the experimental optical features are in very good agreement with the numerical calculations. The small extinction peak at 580 nm is known to be a hybrid plasmon-photonic mode coming from the waveguided mode in the dielectric monolayer and the SPP at the metal-PS interface.[40] Given the overlapping of the main extinction peak (λ = 730 nm) with the Atto 655 fluorescence, we focused on this resonance. The E_z field distribution at this wavelength shows periodic lobes along the metallic half-shells that indicate the excitation of SPPs propagating through the array (Figure 5.16d).[41] Besides, the tapered profile of the shells at the edges of the cover leads to a strong EM enhancement in between the particles. Thus, the plasmonic nature of this

resonance together with its wavelength, could reinforce the cooperative emission of the dyes.

Figure 5.16 a Measured and **b** simulated transmission, reflection and extinction spectra of gold-coated colloidal monolayers. **c** Unit cell scheme of the simulated structure. **d** Distribution of the z-component of the electric field at the maximum extinction of 730 nm.

Dielectric-metal-coated colloidal monolayers

Dielectric layers of SiO_2 ranging from 5 to 25 nm thickness were deposited by CVD under the same conditions than for the flat metallic structures. Despite the generation of a plasma oxygen during the process that could etch the PS spheres, the integrity of the monolayer was preserved thanks to the instrumental distance from the plasma and the shield provided by the gold layer. Figure 5.17a, b show two examples of the successful deposition of SiO_2 on top of the metal-coated monolayers. Although for 25 nm of silica (Figure 5.17b) one can distinguish a reduction of the particles size at the bottom, it is also manifested that the quality of the monolayer and the gold shells are maintained. Therefore, combining colloidal self-assembly with thermal evaporation and chemical

vapour deposition we fabricated large-area two-dimensional dielectric-metal arrays with a high structural control.
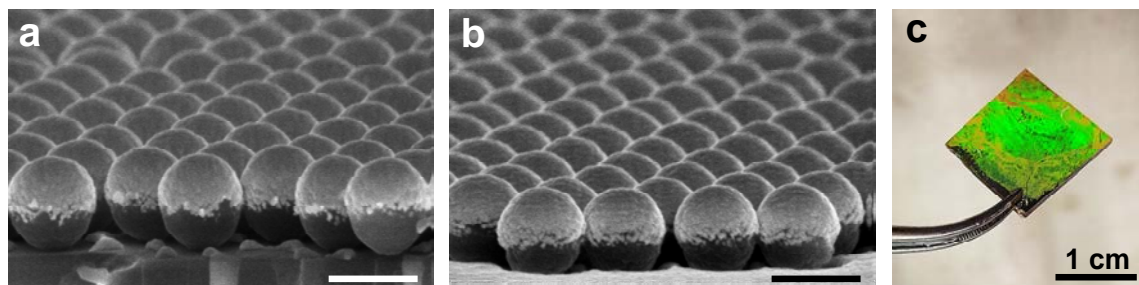
Figure 5.17 SEM pictures of SiO$_2$/Au coated colloidal monolayers. The thickness of the dielectric spacer is **a** 15 nm and **b** 25 nm. **c** Photograph of one of the centimeter-sized samples.

The spectra after the SiO$_2$ deposition show a drastic reduction of the overall transmission and an increase of the reflectance around 550 nm (Figure 5.18). This could come from the multiple reflections occurring at the SiO$_2$ interfaces because of the refractive index mismatch. As a result, the main extinction peak is blue-shifted in average to 720 nm, closer to the maximum emission wavelength of the dyes. It is interesting to note that the initial extinction peak of 580 nm becomes a dip with the dielectric coating, decreasing its intensity with the thickness. Such behavior could indicate the attenuation of the plasmon-photonic hybrid mode. However, further simulations should be performed to fully understand this effect.
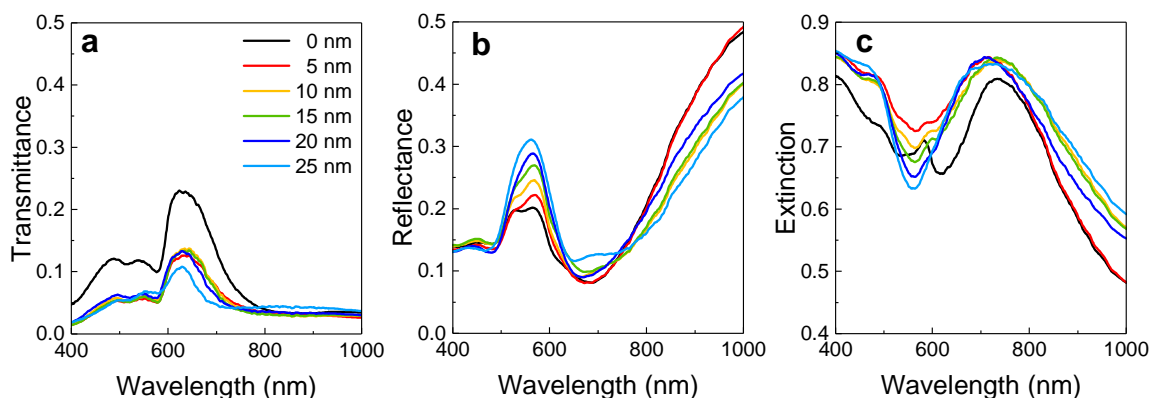
Figure 5.18 a Transmittance, **b** reflectance and **c** extinction spectra of SiO$_2$/Au coated colloidal monolayers, with different thicknesses of the silica layer. For comparison, the spectra of the Au coated monolayer have been included.

5.5.2 Fluorescence decay evolution with the distance

The dielectric-metal hexagonal arrays were finally coated with Atto 655 dyes and a thin PMMA layer as detailed for the former structures. Figure 5.19 shows the first results

of the measured fluorescence decays, from an initial dyes concentration of 10^{-7} M. A clear shortening of the lifetime relaxation is observed as decreasing the distance from the metallic surface, which reflects a plasmonic enhancement of the fluorescence rate. Moreover, the decays present non-exponential profiles that indicate the presence of both coherent and decoherent optical responses mediated by the spatial and spectral overlays with the plasmon resonance. Compared to the modulation observed for the plasmonic lines (Figure 5.13), the decays are much more monoexponential and shorter for the design based on colloidal monolayers. This suggests a better coupling between the fluorophores and the plasmons sustained by the structures, with more intense EM fields at the dyes location.

Further analysis of these results, comparison to numerical models and studies of the effect of the emitters concentration will be done in the near future to understand the effectiveness of the plasmon-mediated superradiance. In addition, an eventual future project could study the influence of the extinction deep observed at short wavelengths on the behavior of dyes emitting in this region.
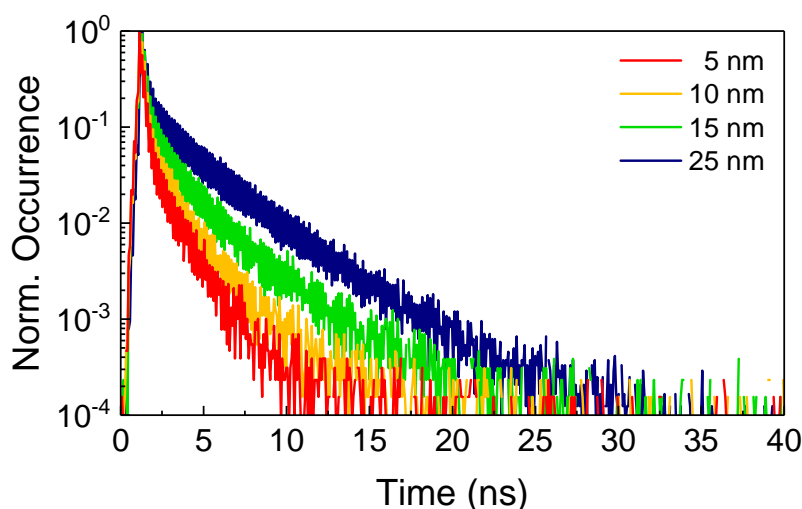
Figure 5.19 Semi-logarithmic decay profiles of 10^{-7} M Atto 655 molecules deposited at different distances (silica thicknesses) from the plasmonic 2D colloidal crystal.

5.6 Conclusions

In this chapter, we have fabricated and characterized different metallic surfaces as platforms for the observation of collective spontaneous emission of Atto 655 molecules. Starting with a flat mirror, we have both experimentally and theoretically demonstrated that the de-excitation of ensembles of molecules strongly depends on the distance from the metal and the emitters concentration, as a result of interference effects. Two distinct

decay rates have been experimentally and theoretically identified. First, a small decay rate, exhibiting damped oscillations with the distance from the mirror was ascribed to single molecule fluorescence. In contrast, the large decay rate presented similar oscillations but without damping and was strongly dependent of the fluorophores concentration, which confirmed it collective nature.

With the aim of extending these studies, we have designed two types of nanostructured metallic substrates for studying the plasmonic superradiance phenomenon. First, we have fabricated large-area plasmonic gratings of lines by nanoimprint lithography. We have adapted the conventional protocol to the fabrication of shallow periodic arrays of lines. The proper choice of the periodicity together with the deposition of a thin gold layer have enabled the excitation of SPPs at the emission wavelength of the dyes. After depositing nanometric dielectric spacers, we have observed that the fluorescence decay rates of the dyes increase in the proximity of the metal, evidencing the plasmon-enhanced effect. Furthermore, the noticeable non-exponential profile observed at short distances suggests the achievement of a plasmon-mediated collective response.

Finally, large-area two-dimensional plasmonic arrays have been successfully fabricated based on colloidal self-assembly. The optical responses of the metal-coated monolayers have been very well reproduced by numerical simulations, which also showed the existence of a strong plasmonic resonance around the gold half-shells. The electromagnetic enhancement has been used for promoting the fluorescence decay rate of dyes separated by dielectric spacers from the metal. The decay profiles showed a clear shortening of the emission lifetime when approaching the metallic surface, confirming the influence of the plasmonic resonance on the fluorescence. Like in the former case, the non-exponential profiles might be ascribed, with further analysis, to the phenomenon of plasmonic superradiance.

In summary, we have developed very efficient metal-based nanostructured surfaces for investigating the enhancement of collective molecular emission. This work is on its infancy and detailed analysis and comparison with appropriate numerical models have to be performed in the future to grasp of the involved phenomena.

5.7 References

1.   E. M. Purcell. Spontaneous emission probabilities at radio frequencies. *Phys. Rev.* **1946**, *69*, 681.

2.   O. S. Wolfbeis. An overview of nanoparticles commonly used in fluorescent bioimaging. *Chem. Soc. Rev.* **2015**, *44*, 4743.

3.   E. Desurvire and J. R. Simpson. Amplification of spontaneous emission in erbium-doped single-mode fibers. *J. Light. Technol.* **1989**, *7*, 835–845.

4.   F. Sgrignuoli et al. Purcell effect and luminescent downshifting in silicon nanocrystals coated back-contact solar cells. *Sol. Energy Mater. Sol. Cells* **2015**, *132*, 267–274.

5.   O. Gazzano and G. S. Solomon. Toward optical quantum information processing with quantum dots coupled to microstructures. *J. Opt. Soc. Am. B* **2016**, *33*, C160–C175.

6.   R. H. Dicke. Coherence in spontaneous radiation processes. *Phys. Rev.* **1954**, *93*, 99–110.

7.   M. Gross and S. Haroche. Superradiance: An essay on the theory of collective spontaneous emission. *Phys. Rep.* **1982**, *93*, 301–396.

8.   P. Lalanne, W. Yan, K. Vynck, C. Sauvan and J. P. Hugonin. Light interaction with photonic and plasmonic resonances. *Laser Photonics Rev.* **2018**, *12*, 1700113.

9.   V. N. Pustovit and T. V. Shahbazyan. Cooperative emission of light by an ensemble of dipoles near a metal nanoparticle: The plasmonic Dicke effect. *Phys. Rev. Lett.* **2009**, *102*, 077401.

10. D. Martín-Cano, L. Martín-Moreno, F. J. García-Vidal and E. Moreno. Resonance energy transfer and superradiance mediated by plasmonic nanowaveguides. *Nanoletters* **2010**, *10*, 3129–3134.

11. T. Iida. Control of plasmonic superradiance in metallic nanoparticle assembly by light-induced force and fluctuations. *J. Phys. Chem. Lett.* **2012**, *3*, 332–326.

12. R. Fleury and A. Alu. Enhanced superradiance in epsilon-near-zero plasmonic channels. *Phys. Rev. B* **2013**, *87*, 201101.

13.   Y. Li and C. Argyropoulos. Controlling collective spontaneous emission with plasmonic waveguides. *Opt. Express* **2016**, *24*, 26696.

14.   I. Protsenko, S. Zhang, A. Uskov, X. Chen and H. Xu. Plasmonic superradiance of two emitters near metal nanorod. *Proc. SPIE 10118, Adv. Photonics Quantum Comput. Mem. Commun. X* **2017**, 1011811.

15.   P. Anger, P. Bharadwaj and L. Novotny. Enhancement and quenching of single-molecule fluorescence. *Phys. Rev. Lett.* **2006**, *96*, 113002.

16.   P. Fauche. Plasmonic superradiance in metallo-dielectric nanohybrids, University of Bordeaux, 2016.

17.   T. B. Hoang et al. Ultrafast spontaneous emission source using plasmonic nanoantennas. *Nat. Commun.* **2015**, *6*, 7788.

18.   M. V. Shestakov, E. Fron, L. F. Chibotaru and V. V. Moshchalkov. Plasmonic Dicke effect in Ag-nanoclusters-doped oxyfluoride glasses. *J. Phys. Chem. C* **2015**, *119*, 20051–20056.

19.   E. Wientjes, J. Renger, A. G. Curto, R. Cogdell and N. F. van Hulst. Nanoantenna enhanced emission of light-harvesting complex 2: The role of resonance, polarization, and radiative and non-radiative rates. *Phys. Chem. Chem. Phys.* **2014**, *16*, 24739.

20.   T. Leisner, O. Kostiucenko, J. R. Brewer, H. Rubahn and J. Fiutowski. Nanostructure induced changes in lifetime and enhanced second-harmonic response of organic-plasmonic hybrids. *Appl. Phys. Lett.* **2015**, *107*, 251102.

21.   N. Michieli, B. Kalinic, C. Scian, T. Cesca and G. Mattei. Emission rate modification and quantum efficiency enhancement of Er^{3+} emitters by near-field coupling with nanohole arrays. *ACS Photonics* **2018**, *5*, 2189–2199.

22.   S. Van de Linde, R. Kasper, M. Heilemann and M. Sauer. Photoswitching microscopy with standard fluorophores. *Appl. Phys. B* **2008**, *93*, 725–731.

23.   H. Kim, M. H. Cho, H. S. Choi, B. Il Lee and Y. Choi. Zwitterionic near-infrared fluorophore-conjugated epidermal growth factor for fast, real-time, and target-cell-specific cancer imaging. *Theranostics* **2019**, *9*, 1085–1095.

24. K. H. Drexhage, M. Fleck, H. Kuhn, F. P. Schafer and W. Sperling. Beeinflussing der fluoreszenz eines europium-chelates durch einen spiegel. *Ber. Bunsenges. Phys. Chem* **1966**, *70*, 1179.

25. J.-Y. Zhang, X.-Y. Wang and M. Xiao. Modification of spontaneous emission from CdSe/CdS quantum dots in the presence of a semiconductor interface. *Opt. Lett.* **2002**, *27*, 1253–1255.

26. A. Kwadrin and A. F. Koenderink. Gray-tone lithography implementation of Drexhage's method for calibrating radiative and nonradiative decay constants of fluorophores. *J. Phys. Chem. C* **2012**, *116*, 16666–16673.

27. N. Karedla et al. Single-molecule metal-induced energy transfer (smMIET): Resolving nanometer distances at the single-molecule level. *ChemPhysChem* **2014**, *15*, 705–711.

28. R. Brechbühler et al. Two-dimensional Drexhage experiment for electric- and magnetic-dipole sources on plasmonic interfaces. *Phys. Rev. Lett.* **2018**, *121*, 113601.

29. R. Vallée et al. On the role of electromagnetic boundary conditions in single molecule fluorescence lifetime studies of dyes embedded in thin films. *Chem. Phys. Lett.* **2001**, *348*, 161–167.

30. L. Martinu, O. Zabeida and J. E. Klemberg-Sapieha. Plasma-enhanced chemical vapor deposition of functional coatings. *Handb. Depos. Technol. Film. Coatings* **2010**, 392–465.

31. Y. Wang, X. Wang, S. K. Ghosh and H. P. Lu. Probing single-molecule interfacial electron transfer dynamics of porphyrin on TiO$_2$ nanoparticles. *J. Am. Chem. Soc.* **2009**, *131*, 1479–1487.

32. O. Schulz et al. Tip induced fluorescence quenching for nanometer optical and topographical resolution. *Opt. Nanoscopy* **2013**, *2*, 1.

33. B. Pedras. *Fluorescence in Industry*; Springer, Switzerland, 2019.

34. V. Buschmann, K. D. Weston and M. Sauer. Spectroscopic study and evaluation of red-absorbing fluorescent dyes. *Bioconjug. Chem.* **2003**, *14*, 195–204.

35. M. Gómez-Castaño et al. Energy transfer and interference by collective electromagnetic coupling. *Nanoletters* **2019**, *19*, 5790–5795.

36.   M. Sukharev and A. Nitzan. Optics of plasmon-exciton nanomaterials. *J. Phys. Condens. Matter* **2017**, *29*, 443003.

37.   P. Berini. Long-range surface plasmon polaritons. *Adv. Opt. Photonics* **2009**, *1*, 484–588.

38.   B. Xiao, S. K. Pradhan, K. C. Santiago, G. N. Rutherford and A. K. Pradhan. Topographically engineered large scale nanostructures for plasmonic biosensing. *Sci. Rep.* **2016**, *6*, 24385.

39.   H. Yin et al. Plasmon enhanced quantum dots fluorescence and energy conversion in water splitting using shell-isolated nanoparticles. *Nano Energy* **2017**, *42*, 232–240.

40.   C. Farcau, M. Giloan, E. Vinteler and S. Astilean. Understanding plasmon resonances of metal-coated colloidal crystal monolayers. *Appl. Phys. B* **2012**, *106*, 849–856.

41.   C. Farcau. Metal-coated microsphere monolayers as surface plasmon resonance sensors operating in both transmission and reflection modes. *Sci. Rep.* **2019**, *9*, 3683.

Chapter 6

General conclusions and perspectives

6.1 Conclusions

The works developed during this thesis have been motivated by the design and large-area fabrication and characterization of plasmonic nanostructures displaying unusual electromagnetic phenomena. Principally, we have tackled the cost-effective manufacture and analysis of negative-index metamaterials working at optical wavelengths; namely, fishnet metamaterials. Secondly, we have addressed the fabrication of nanostructured metallic platforms for the enhancement of collective spontaneous emission. The most significant contributions to the fields of metamaterials and enhanced spontaneous emission are given below.

6.1.1 Negative-index fishnet metamaterials

Along this thesis, we have proposed alternative designs of fishnet metamaterials where the common metal-insulator-metal stack was composed of gold layers and air cavities. This approach has been demonstrated to be highly compatible with low-cost fabrication techniques such as colloidal lithography, soft nanoimprinting and electrodeposition. Specifically, centimeter-sized arrays of colloidal monolayers and pillars have served as templates for the electrodeposition of alternating metallic layers.

Fishnet metamaterials based on colloidal lithography

Combining colloidal lithography and electrodeposition, we have first fabricated metallic stacks of gold and sacrificial nickel layers embedding non-close-packed monolayers of polystyrene particles. By dissolving the nickel parts, we have demonstrated the feasibility of obtaining transferable double fishnet metamaterials made of gold and air, where the particles work as both dielectric perforations and supports of the layers.

These metamaterials exhibited optical resonances in the near-infrared that were easily tailored with the diameter of the particles or the air gap width between the two

gold layers. The electromagnetic distribution at these wavelengths showed the excitation of a magnetic resonance within the gap, coming from the coupling of surface plasmons propagating at the gold-air interfaces. This artificial magnetism together with the electric response of the metal layers gave rise to tunable effective refractive indices as function of the geometrical parameters. Specifically, we were able to tune the refractive index from positive to near-zero and negative values, achieving a record value of -1 at 940 nm with an entirely bottom-up fabrication process.

Further analysis such as an effective medium modelling or a metamaterial prism verified the reliability of the metamaterial design and the calculations done for retrieving the effective parameters.

### *Fishnet metamaterials based on soft nanoimprinting*

These results were extended to metamaterials made from nanoimprinted patterns and electrodeposition. Based on the previous method, we developed a straightforward fabrication process of multilayered fishnet metamaterials made of dielectric pillars supporting several stacks of gold-air-gold layers. Moreover, we demonstrated the adaptability of the process to transparent conductive substrates, ready for a metamaterial device implementation.

The multilayered fishnet structures displayed optical resonances ranging from visible to near-infrared wavelengths. The position of the response was governed by structural parameters such as the periodicity, diameter of the pillars or number of metallic layers. Strong negative refractive indices were obtained at these resonances, with minimum values of -1.2 at 700 nm and -2.8 at 910 nm.

We found that increasing the number of layers brought about significant improvements for optical metamaterials such as higher figures of merit or shorter operation wavelengths. This blue shift was noticeably weaker for the smallest pitches because of its close convergence to the bulk metamaterial regime. The negligible angular dispersion of this structure corroborated such statement.

Finally, we demonstrated the possibility of tuning the optical response of our metamaterials when infiltrating different liquids in the air cavities. Increasing the refractive index of the filling medium, the resonant wavelength was found to move to larger wavelengths, with attractive capabilities for optical sensing.

As proof of the impact of our metamaterials to the current research progress, Figure 6.1 compares the major results of this thesis with the state of the art at the beginning of the project. Making use of up-scalable techniques, this work has established new large-area fabrication procedures of fishnet metamaterials with properties comparable or even superior than the ones obtained by common short-range methods.
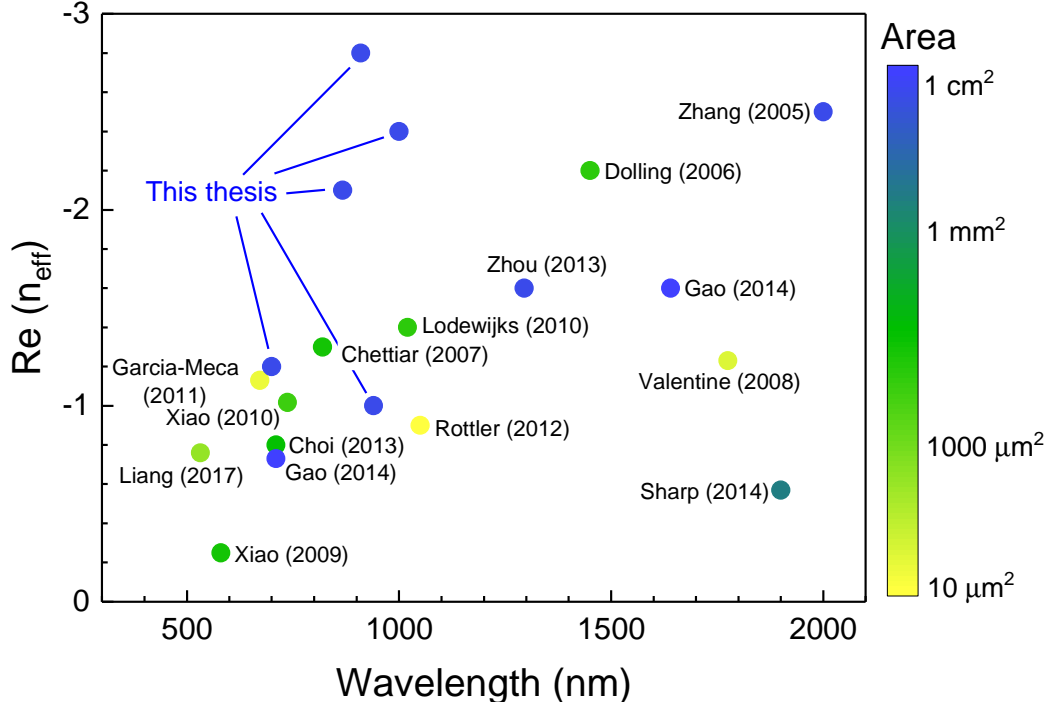
Figure 6.1 State of the art at the end of this thesis. Main fishnet metamaterials fabricated to date as a function of the strongest effective refractive index n_{eff}, the operation wavelength and the area.

6.1.2 Enhanced spontaneous emission

We have developed various metallic nanostructured platforms for the observation of collective molecular emission. In a flat metal-dielectric design, the emission rate of molecular assemblies depended on the distance to the metallic surface, with spatial oscillations arising from constructive/destructive interferences. The emission decay presented two regimes: a small decay rate coming from single molecule fluorescence and a large decay rate arising from the collective relaxation.

This study inspired the design of one- and two-dimensional plasmonic arrays for promoting the collective emission phenomenon of superradiance. Nanoimprinting and colloidal lithography enabled the fabrication of large-area metal-dielectric platforms displaying plasmonic resonances nearby the emission wavelength of the fluorophores. Preliminary characterization showed the increase of the decay rates when reducing the

distance of the molecules to the metallic surfaces, evidencing the influence of the plasmonic resonances on the fluorescence rate. The bi-exponential decay profiles found at short distances suggest the excitation of a plasmon-mediated collective response. Further analysis will be performed in the near future to understand the nature of such enhanced behavior.

6.2   Perspectives

The methods and structures engineered along this thesis pave the way for the device implementation of negative-index metamaterials, experimental study of collective emission phenomena or the development of further intriguing plasmonic designs by cost-effective routes. In this section, some interesting continuations of the thesis are presented.

6.2.1 Fishnet design

The losses of negative-index metamaterials are considerably reduced in multilayered designs, as proved by the fishnet structures developed by nanoimprint lithography. This improvement could be applied to the fishnet designs made by colloidal lithography by depositing several nickel-gold layers around the particles that would finally lead to multilayered gold-air-gold cavities.

Replacing the gold layers by less lossy metals such as silver would also reduce the absorption within the metamaterials. A detailed study of the optimum conditions for electrodepositing silver in homogeneous films would be the basis for the new fishnets. Special attention should be paid to the roughness of the deposits since the performance of the final metamaterial strongly depends on the uniform separation between the metallic layers. Moreover, the dissolution step based on nitric acid might be highly controlled in order not to dissolve the silver parts.

Considering the negative-index bands achieved with each lattice parameter by nanoimprinting, we can think about a centimeter-size gradient metamaterial. This would consist on imprinting side by side various patterns, from the smallest to the largest periodicity, and following the same electrodeposition protocol. The whole structure might work as flat lens for different wavelengths.

Inspired by the accessibility to the air gaps, the response of fishnet metamaterials could be interestingly controlled by filling the cavities with liquid crystals. We could

tune the negative-index bands by heating the system or applying a bias through the ITO and top gold layer. The alignment changes would vary the refractive index of the liquid crystals, enabling the modulation of the metamaterial response.

6.2.2 Superradiance platforms

As previously discussed, further analysis will be done in the near future regarding the ensembles of molecules placed near plasmonic arrays. The enhancement of singular and collective emission will be thoroughly studied when varying the distance to the metallic surfaces as well as the concentration of molecules.

These works might be extended to other types of emitters such as quantum dots. In the same way, we could study the dependence of their emission rate with the distribution on the plasmonic surfaces. These investigations will contribute to the experimental study of plasmonic superradiance in multiple systems.

6.2.3 Further photonic and plasmonic systems

The methods established along this thesis also broaden the possibilities to explore in the fields of nanofabrication, photonics and plasmonics.

For instance, we could combine colloidal lithography and nanoimprinting by replicating a monolayer of polystyrene particles. This would give rise to PDMS large-area patterns of bowls or domes ranging from microns to a hundreds of nanometers. The possibility of repeatedly imprinting these low-cost patterns implies a significant progress for surface nanostructuration, avoiding the use of multiple samples or engraving steps.

Working with hydrophobic substrates such as the nickel strips discussed in Chapter 4, we could study the achievement of metallic nanorings in pillar-based templates. These systems have demonstrated potential properties for catalysis, sensing or enhanced spectroscopies.[1,2]

Finally, one could take advantage of the flexibility of the PDMS stamps to obtain asymmetric patterns via elongation of the mold.[3] Preliminary results based on stretched patterns of pillars and electrodeposition have shown the achievement of arrays of metallic wavy lines (Figure 6.2). These unusual shapes are due to the distinct residual layers formed in x and y directions when stretching the patterns, preventing the metallic deposition in one of the axis. Optical characterization will be done in future works in order to unravel the electromagnetic properties that these structures can provide.
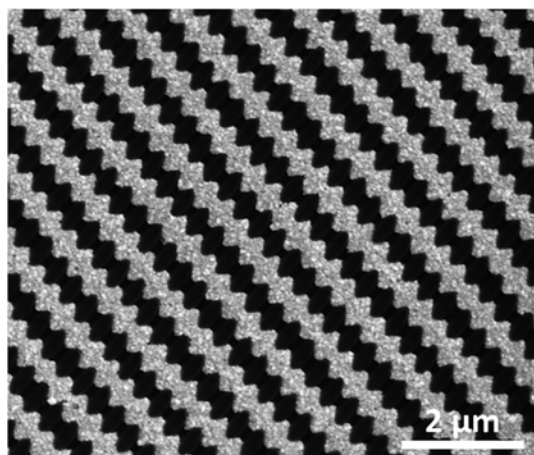
Figure 6.2 SEM image of gold wavy lines. The sample was fabricated by imprinting a 60% stretched PDMS mold onto SU8, removing a few nanometers of residual layer by RIE and electrodepositing gold through the template.

6.3 References

1.   A. Genç et al. Hollow metal nanostructures for enhanced plasmonics: Synthesis, local plasmonic properties and applications. *Nanophotonics* **2017**, *6*, 193–213.

2.   X. Liu, W. Liu and B. Yang. Highly ordered 3D-silver nanoring arrays (3D-AgNRAs) for refractometric sensing. *J. Mater. Chem. C* **2019**, *7*, 7681–7691.

3.   L. Liu et al. A programmable nanoreplica molding for the fabrication of nanophotonic devices. *Sci. Rep.* **2016**, *6*, 22445.

Appendix

Retrieval of effective parameters

The effective properties of the samples were retrieved from FDTD simulations and making use of the homogenization method, this is, describing the metamaterials as effective media. One of the most common methods for obtaining the macroscopic properties relies on the complex transmission and reflection electric fields, known as scattering parameters or simply S-parameters.[1,2]

Given the asymmetry of our systems caused by the substrate under the metamaterial, the S-parameters differ depending on the side of illumination. As a result, two simulations have to be done for retrieving the effective parameters (Figure A.1): one where light impinges from the top of the structure and one where light comes from the bottom, which corresponds to the substrate in our case.
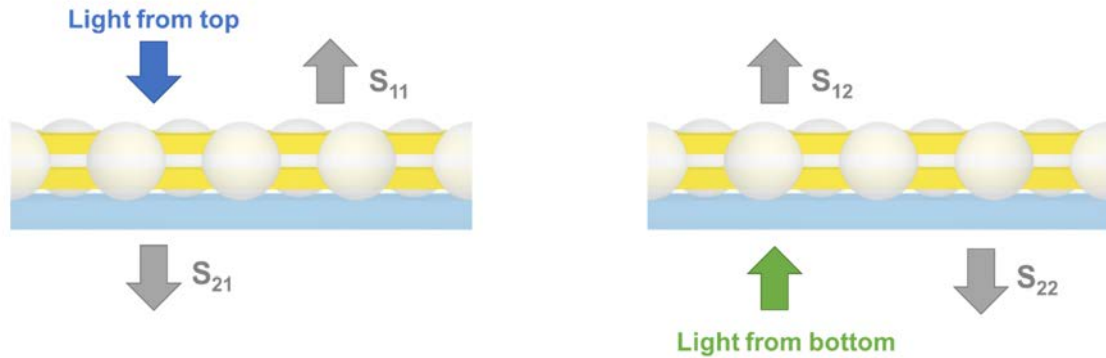
Figure A.1 Scheme of the two simulations performed for the retrieval in a double-fishnet metamaterial made by colloidal lithography.

The associated four S-parameters can be obtained from the reflected, transmitted and incident electric fields (E_r, E_t, E_i) as:

$$S_{11} = E_r / E_{i_{top}} \tag{A.1}$$

$$S_{21} = E_t / E_{i_{top}} \tag{A.2}$$

$$S_{22} = E_r / E_{i_{bottom}} \tag{A.3}$$

$$S_{12} = E_t / E_{i_{bottom}} \tag{A.4}$$

Figure A.2b and c show the calculated amplitudes and phases of the S-parameters for the double-fishnet metamaterial made by colloidal lithography displaying -1 refractive index (Section 3.5). This sample will serve as example for illustrating the retrieval procedure used along the thesis with fishnet metamaterials. Whereas the transmission curves present a similar behavior because of the reciprocity of transmitted light, the reflection amplitudes and phases are different and manifest the substrate-induced anisotropy.
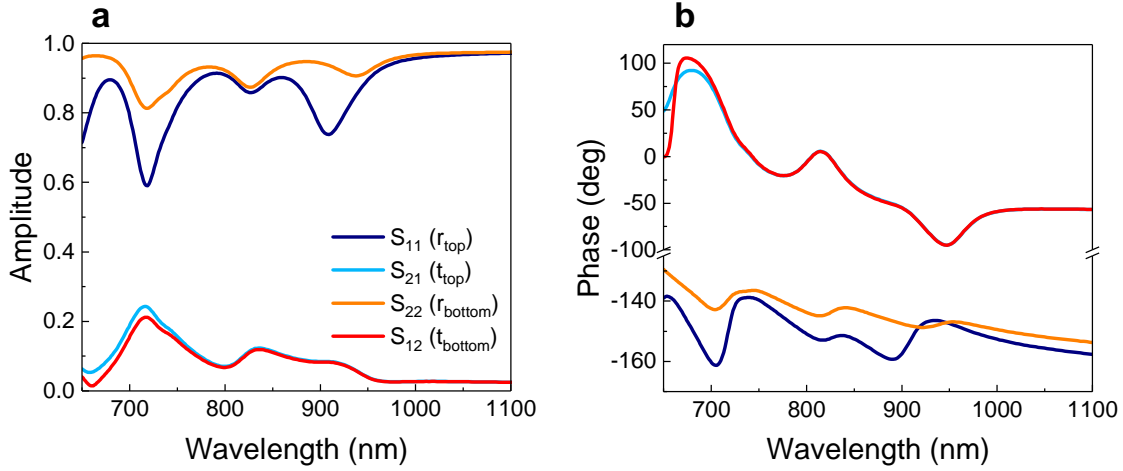
Figure A.2 a Amplitudes and **b** phases of the simulated S-parameters for the double-fishnet metamaterial with -1 refractive index made by colloidal lithography.

The effective properties were calculated according to the procedure reported by Li et al.[3] If the asymmetry of the system is omitted, the effective refractive index n can be obtained from:

$$\cos(nkd) = \frac{1 - S_{11}^2 + S_{21}^2}{2S_{21}} \tag{A.5}$$

where k is the wavenumber of light in free space and d is the thickness of the metamaterial without involving the substrate. However, since the reflection coefficients S_{11} and S_{22} are different, this equation must be corrected to:

$$\cos(nkd) = \frac{1 - S_{11}S_{22} + S_{21}^2}{2S_{21}} = X \tag{A.6}$$

where the averaged term $S_{11}S_{22}$ has been included. Isolating $n = n' + in''$ and expressing the arccosine function in its logarithmic form we get[4]

$$n' = \frac{1}{kd}\left[\text{Im}\left\{\ln\left(X \pm i\sqrt{1-X^2}\right)\right\} + 2\pi m\right] \tag{A.7}$$

$$n'' = \frac{-1}{kd}\text{Re}\left\{\ln\left(X \pm i\sqrt{1-X^2}\right)\right\} \tag{A.8}$$

where m is an integer denoting the branch index of n'. From these equations, first, the signs of the square roots were chosen considering that in a passive medium the imaginary part must obey $n'' > 0$. Second, the branch m was chosen so that it verified the Kramers-Kronig relations, where n' is related to n'', ensuring the validity of the retrieved effective index.[5]

Figure A.3 shows the real part of n for the top and bottom incidences (equation (A.5)), as well as the corrected value based on equation (A.6). As observed, the effective index differs in minimum value and band width from the individual values extracted from top and bottom illumination. Hence, one should not neglect this correction for retrieving a valid effective refractive index.
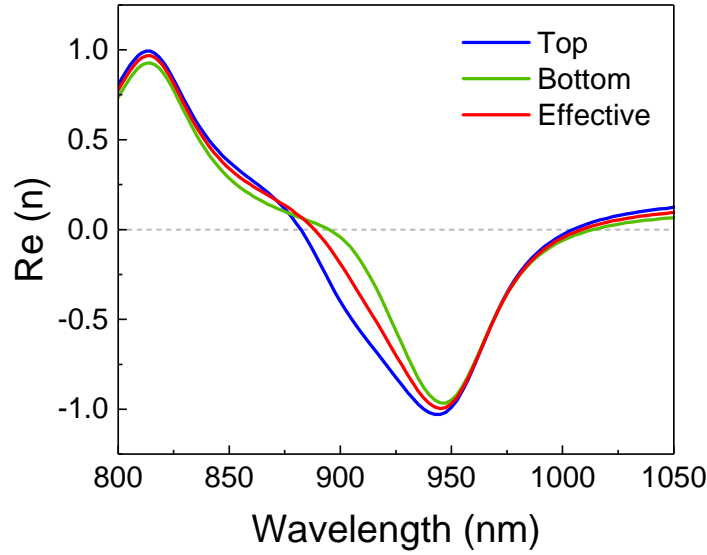
Figure A.3 Real part of the effective refractive index when light impinges from top, from bottom and after the correction made considering both results.

For comparison, Figure A.4 presents the effective refractive index for the same structure with and without substrate, showing that a freestanding membrane would exhibit a larger negative refractive index over a blue-shifted band and a higher FOM. Previous works have shown that these differences arise from a magnetoelectric coupling at the resonant wavelength induced by the substrate, namely bianisotropy.[6] This implies that the wave propagation in the metamaterial is described by the permittivity ε, the permeability μ and an additional bianisotropy parameter ξ, whose value manifests the magnetoelectric coupling strength. These properties can be derived from the refractive index and S-parameters as:
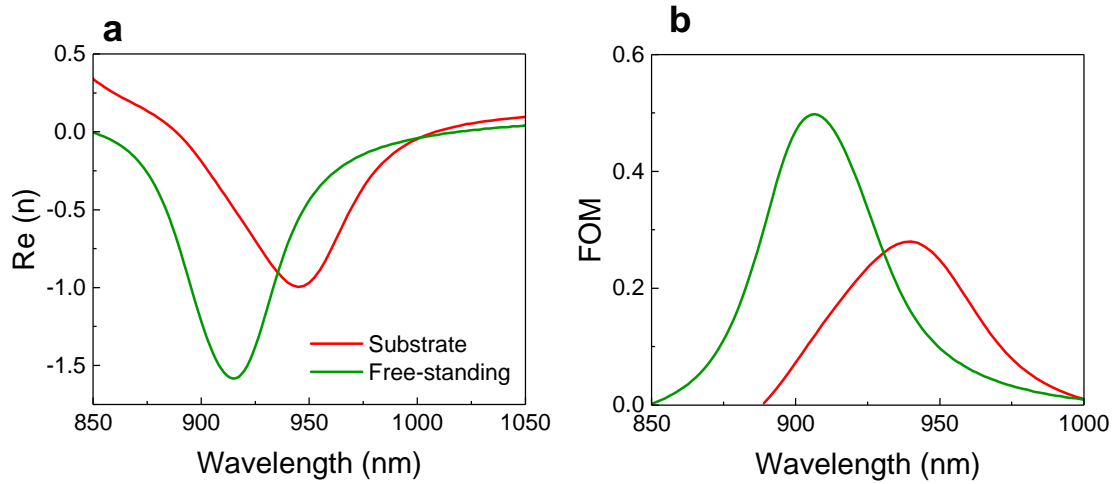
$$\xi = \left(\frac{n}{-2\sin(nkd)}\right)\left(\frac{S_{11} - S_{22}}{S_{21}}\right) \tag{A.9}$$

$$\mu = \left(\frac{in}{\sin(nkd)}\right)\left(\frac{2 + S_{11} + S_{22}}{2S_{21}} - \cos(nkd)\right) \tag{A.10}$$

$$\varepsilon = \frac{(n^2 + \xi^2)}{\mu} \tag{A.11}$$

In addition, the existence of a magnetoelectric coupling affects the impedance z in the sense that two values are obtained, depending on the direction of the incoming light.

$$z_{\pm} = \frac{\mu}{n \pm i\xi} \tag{A.12}$$

Figure A.4 a Real part of the effective refractive index and **b** figure of merit of the double-fishnet metamaterial with and without substrate underneath.

References

1. D. R. Smith, D. C. Vier, T. Koschny and C. M. Soukoulis. Electromagnetic parameter retrieval from inhomogeneous metamaterials. *Phys. Rev. E* **2005**, *71*, 036617.

2. E. J. Rothwell, J. L. Frasch, S. M. Ellison, P. Chahal and R. O. Ouedraogo. Analysis of the Nicolson-Ross-Weir method for characterizing the electromagnetic properties of engineered materials. *Prog. Electromagn. Res.* **2016**, *157*, 31–47.

3. Z. Li, K. Aydin and E. Ozbay. Determination of the effective constitutive parameters of bianisotropic metamaterials from reflection and transmission coefficients. *Phys. Rev. E* **2009**, *79*, 026610.

4.   X. Chen, T. M. Grzegorczyk, B. I. Wu, J. Pacheco and J. A. Kong. Robust method to retrieve the constitutive effective parameters of metamaterials. *Phys. Rev. E* **2004**, *70*, 016608.

5.   Z. Szabó, G. Park, R. Hedge and E.-P. Li. A unique extraction of metamaterial parameters based on Kramers–Kronig relationship. *IEE Trans. Microw. Theory Tech.* **2010**, *58*, 2646–2653.

6.   S. Yun et al. Experimental verification of substrate-induced bianisotropy in optical metamaterials. *Appl. Phys. Lett.* **2013**, *103*, 233109.

Scientific contributions

Publications derived from this thesis

1. M. Gómez-Castaño, H. Zheng, J.L. García-Pomar, R. Vallée, A. Mihi and S. Ravaine. Tunable index metamaterials made by bottom-up approaches. *Nanoscale Adv.* **2019**, *1*, 1070-1076.

2. M. Gómez-Castaño, A. Redondo-Cubero, L. Buisson, J.L. Pau, A. Mihi, S. Ravaine, R. Vallée, A. Nitzan and M. Sukharev. *Nano Lett.* **2019**, *19*, 5790-5795.

3. M. Gómez-Castaño, J.L. García-Pomar, L.A. Pérez, S. Shanmugathasan, S. Ravaine and A. Mihi. Electrodeposited negative index metamaterials with visible and near infrared response. *Adv. Opt. Mater.* **2020**, accepted.

Conference presentations

1. M. Gómez-Castaño, C. Matricardi, R. Vallée, A. Mihi and S. Ravaine. Gold nanopillar arrays as SERS-active platforms, *Surface Enhanced Raman Scattering – SERS: Faraday Discussions*, Glasgow (UK), August **2017**, Poster.

2. M. Gómez-Castaño, R. Vallée, A. Mihi and S. Ravaine. Bottom-up fabrication of double fishnet metamaterials working at visible and near infrared frequencies, *5th LAPHIA Symposium*, Bordeaux (France), December **2017**, Poster.

3. M. Gómez-Castaño, R. Vallée, A. Mihi and S. Ravaine. Bottom-up fabrication of double fishnet metamaterials, *11th International Conference on Nanophotonics*, Wroclaw (Poland), July **2018**, Talk.

4. M. Gómez-Castaño. Metamaterials for negative refraction: Making a perfect lens, *7th Interdisciplinary Meeting of Predoctoral Researchers (JIPI)*, Barcelona (Spain), February **2019**, Talk.

5. M. Gómez-Castaño, J.L. García-Pomar, R. Vallée, A. Mihi and S. Ravaine. Tunable index metamaterials made by bottom-up approaches, *Colloidal Science and Metamaterials 2019*, Paris (France), February **2019**, Talk.

6. M. Gómez-Castaño, H. Zheng. J.L. García-Pomar, R. Vallée, A. Mihi and S. Ravaine. Tunable index metamaterials made by bottom-up approaches, *8th International Conference on Spectroscopic Ellipsometry*, Barcelona (Spain), May **2019**, Poster.

7. M. Gómez-Castaño. Tunable index metamaterials made by bottom-up approaches, *JPhD - 4th Scientific Meeting of BCN-c Students*, Barcelona (Spain), June **2019**, Best poster contribution award.

8. M. Gómez-Castaño, J.L. García-Pomar, R. Vallée, A. Mihi and S. Ravaine. Negative-index metamaterials made by low-cost approaches, *10th META Conference*, Lisbon (Portugal), July **2019**, Invited talk.

9. J.L. García-Pomar, M. Gómez-Castaño, C. Matricardi and A. Mihi, Large area and low cost metasurfaces and metamaterials, *Nanophotonics and Micro/Nano Optics International Conference*, Munich (Germany), September **2019**, Talk.

10. M. Gómez-Castaño, J.L. García-Pomar, L.A. Pérez, S. Shanmugathasan, S. Ravaine and A. Mihi, Electrodeposited negative index metamaterials with visible and near infrared response, *Photonics Online Meetup*, June **2020**, Poster.

Titre : Métamatériaux optiques : conception, fabrication à grande échelle et caractérisation

Résumé : Les métamatériaux sont des matériaux structurés artificiellement, soigneusement designés pour obtenir des réponses électromagnétiques inobservables dans la nature, telles qu'un indice de réfraction négatif. Le but de cette thèse est le développement de métamatériaux optiques à grandes échelles pouvant être incorporés au sein de dispositifs réels. En combinant la lithographie colloïdale avec l'électrodéposition, nous avons réalisé par voie ascendante des métamatériaux de type « fishnet » faits de couches d'or et air, présentant un indice de réfraction qui varie entre valeurs positives et négatives dans le proche infrarouge. Des multicouches de type fishnet ont aussi été fabriquées en couplant la lithographie par nanoimpression et l'électrodéposition. Nous avons analysé en détail les réponses optiques de ces structures, qui présentent des valeurs négatives d'indice de réfraction du visible au proche infrarouge. Leur performance comme capteurs optiques a été étudiée via leur infiltration par différents liquides. Les différentes techniques d'élaboration précitées ont également été utilisées pour fabriquer des substrats métalliques nanostructurés afin d'étudier l'émission spontanée collective d'ensembles de molécules fluorescentes.

Mots clés : métamatériaux, indice de réfraction négatif, lithographie colloïdale, lithographie par nanoimpression, électrodéposition, plasmonique, émission spontanée

---

Title: Optical metamaterials: design, up-scalable fabrication and characterization

Abstract: Metamaterials are artificially structured materials, thoroughly designed for achieving electromagnetic properties not observed in nature such as the negative refractive index. The purpose of this thesis is the development of up-scalable optical metamaterials that can be easily incorporated into actual devices. By combining colloidal lithography and electrodeposition, we report an entirely bottom-up fishnet metamaterial made of gold and air layers. A proper theoretical and experimental design gives rise to tunable refractive index, from positive to negative values in the near infrared. This structure is extended to multilayered fishnet metamaterials made by nanoimprint lithography and electrodeposition. We thoroughly analyze the optical response of the structures, which lead to strong negative index from the visible to near infrared. Their performance as optical sensors is studied when infiltrating different liquids through the air cavities. These techniques are used to fabricate nanostructured metallic substrates for studying the collective spontaneous emission of fluorescent molecules.

Keywords: metamaterials, negative refractive index, colloidal lithography, nanoimprint lithography, electrodeposition, plasmonics, spontaneous emission